

GMOX

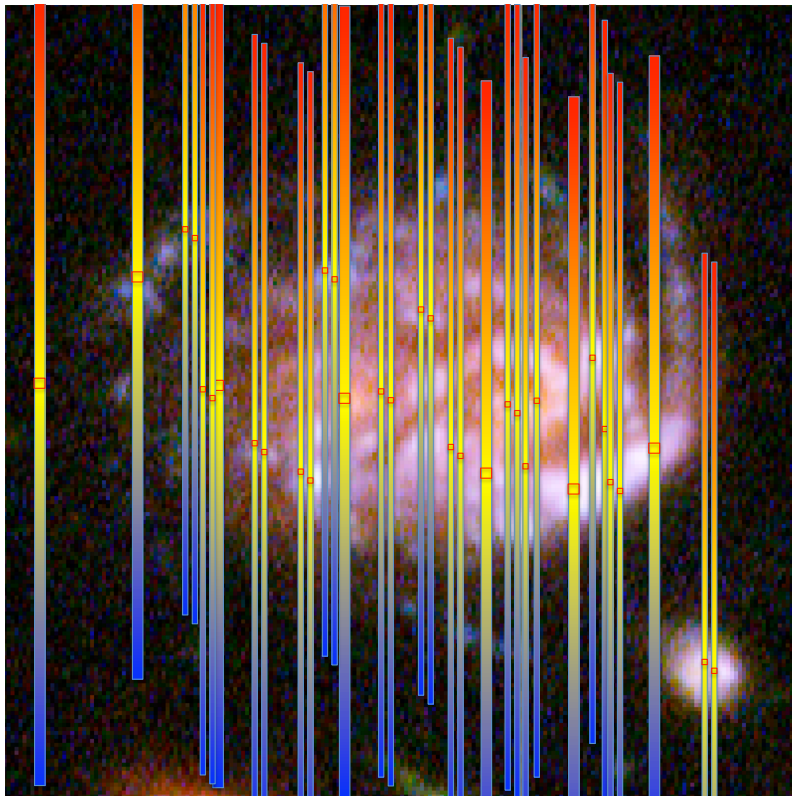
GEMINI MULTI-OBJECT EXTRA-WIDE-BAND SPECTROGRAPH

A FEASIBILITY STUDY FOR A 4th GENERATION GEMINI INSTRUMENT

PRESENTED BY:

M. ROBERTO (JHU & STSCI, PRINCIPAL INVESTIGATOR),
T. HECKMAN (JHU), S. SMEE (JHU), Z. NINKOV (RIT),
M. GENNARO (STSCI), R. BARKHOUSER (JHU)
AND THE GMOX SCIENCE TEAM

Final Report – October 25, 2015



REVISIONS:

Revised October 26, 2015 (RevA)

Revised October 26, 2015 (RevB)

CONTENTS

A	EXECUTIVE SUMMARY	1
B	INTRODUCTION	3
B.1	GEMINI AND THE GIFS REQUEST FOR PROPOSAL	3
B.2	FROM THE REQUIREMENTS TO GMOX	4
B.3	INTRODUCING GMOX	4
B.4	GMOX AND THE GEMINI-STAC PRINCIPLES	5
B.5	SUMMARY: GMOX'S UNIQUE STRENGTHS	9
C	SCIENCE CASE: RESOLVING GALAXIES THROUGH COSMIC HISTORY	11
C.1	GMOX SCIENCE TEAM	11
C.2	TEN KEY SCIENCE QUESTIONS ADDRESSED BY GMOX	12
C.3	SETTING THE STAGE	13
C.4	COSMIC HISTORY: 3.5 GYR OF GROWTH	15
C.4.1	DARK AGES AND POPULATION III OBJECTS	17
C.4.1.1	OPEN PROBLEMS	17
C.4.1.2	OBSERVATIONAL NEEDS	18
C.4.1.3	GMOX REQUIREMENTS	19
C.4.2	REIONIZATION AND EARLY GALAXY FORMATION	20
C.4.2.1	OPEN PROBLEMS	20
C.4.2.2	OBSERVATIONAL NEEDS	22
C.4.2.3	GMOX REQUIREMENTS	23
C.4.3	GALAXY BUILDING EPOCH	26
C.4.3.1	OPEN PROBLEMS	26
C.4.3.2	OBSERVATIONAL NEEDS	26
C.4.3.3	GMOX REQUIREMENTS	26
C.4.4	"HIGH NOON" OF COSMIC HISTORY	28
C.4.4.1	OBSERVATIONAL NEEDS	28
C.4.4.2	GMOX REQUIREMENTS	28
C.4.5	CLUSTERS OF GALAXIES	30
C.4.5.1	OPEN PROBLEMS	30
C.4.5.2	OBSERVATIONAL NEEDS	30

c.4.5.3	GMOX REQUIREMENTS	30
c.5	COSMIC HISTORY: 10 GYR OF DECLINE	32
c.5.1	GALACTIC-SCALE STAR FORMATION	32
c.5.1.1	OPEN PROBLEMS	32
c.5.1.2	OBSERVATIONAL NEEDS	33
c.5.1.3	GMOX REQUIREMENTS	34
c.5.2	MASSIVE STAR FORMATION IN LOCAL GROUP DWARFS	36
c.5.2.1	OPEN PROBLEMS	36
c.5.2.2	OBSERVATIONAL NEEDS	36
c.5.2.3	GMOX REQUIREMENTS	36
c.5.3	GLOBULAR CLUSTERS	38
c.5.3.1	OPEN PROBLEMS	38
c.5.3.2	OBSERVATIONAL NEEDS	39
c.5.3.3	GMOX REQUIREMENTS	40
c.5.4	FORMATION AND EVOLUTION OF THE GALACTIC BULGE	41
c.5.4.1	OPEN PROBLEMS	41
c.5.4.2	OBSERVATIONAL NEEDS	41
c.5.4.3	GMOX REQUIREMENTS	41
c.5.5	YOUNG STELLAR CLUSTERS	43
c.5.5.1	OPEN PROBLEMS	43
c.5.5.2	OBSERVATIONAL NEEDS	44
c.5.5.3	GMOX REQUIREMENTS	45
c.5.6	STAR FORMATION AND CIRCUMSTELLAR DISCS	47
c.5.6.1	OPEN PROBLEMS	47
c.5.6.2	OBSERVATIONAL NEEDS	49
c.5.6.3	GMOX REQUIREMENTS	49
c.6	LSST TRANSIENTS	51
c.6.1	GMOX CAPABILITY FOR LSST FOLLOW-UP OBSERVATIONS	51
c.6.1.1	OBSERVATIONAL NEEDS	55
c.6.1.2	GMOX REQUIREMENTS	55
D	SCIENCE REQUIREMENTS	56
E	GMOX CAPABILITIES	57
E.1	EXPOSURE TIME CALCULATOR	57
E.2	SENSITIVITY ESTIMATES	58
E.3	EXAMPLES OF GMOX GUARANTEED TIME PROGRAMS	61
E.3.1	GALACTIC OUTFLOWS	61
E.3.2	EXOPLANETS IN THE GALACTIC BULGE	62
E.3.3	EXTREME HORIZONTAL BRANCH STARS IN GLOBULAR CLUSTERS	63

E.3.4	YSOs IN THE MAGELLANIC CLOUDS	65
E.4	GMOX IN THE CONTEXT OF OTHER MAJOR FACILITIES	65
F	CONCEPT OF OPERATIONS	69
F.1	GEMINI AO AND GMOX	69
F.2	NORMAL SEEING CONDITIONS, PARTIAL AO CORRECTION	71
F.3	POOR/BAD SEEING CONDITIONS	72
F.4	EXCELLENT SEEING CONDITIONS, FULL AO CORRECTION	72
F.5	OBSERVING MODES	73
F.6	HADAMARD TRANSFORM SPECTROSCOPY	76
F.7	CALIBRATION STRATEGY	77
G	TECHNICAL REQUIREMENTS AND A FEASIBLE INSTRUMENT DESIGN	81
G.1	TOP-LEVEL REQUIREMENTS	81
G.2	INSTRUMENT DESIGN	81
G.2.1	ADAPTIVE OPTICS MODES	81
G.2.1.1	GMOX WITH GEMS	81
G.2.1.2	GMOX WITH ALTAIR	87
G.2.2	OPTICAL DESIGN	87
G.2.2.1	FORE-OPTICS	89
G.2.2.2	REIMAGERS	90
G.2.2.3	DIGITAL MICROMIRROR DEVICE	91
G.2.2.4	OFF-AXIS SCHMIDT COLLIMATORS	94
G.2.2.5	SPECTROSCOPIC CHANNELS	94
G.2.2.6	SLIT-VIEWING CHANNELS	94
G.2.3	OPTICAL PERFORMANCE	94
G.2.3.1	THROUGHPUT	100
G.2.3.2	DMD CONTRAST	100
G.2.4	MECHANICAL DESIGN	104
G.2.4.1	THE LOWER BENCH	107
G.2.4.2	THE UPPER BENCH	108
G.2.4.3	THE NEAR INFRARED CRYOSTAT	109
G.2.4.4	OPTICAL MOUNTS	114
G.2.4.5	DETECTOR MOUNTS	117
G.2.4.6	FLEXURE	118
G.2.4.7	INSTRUMENT INTEGRATION	118
G.2.5	ELECTRICAL DESIGN	120
G.2.5.1	ELECTRONICS FOR INSTRUMENT CONTROL AND MONITORING	121
G.2.5.2	DETECTOR READOUT SYSTEM	123
G.2.5.3	DETECTORS FOR THE VISIBLE SCIENCE ARMS: CCDs	123

G.2.5.4	CCD READOUT ELECTRONICS	125
G.2.5.5	NEAR IR ARM DETECTORS; HgCdTe DETECTORS	126
G.2.5.6	NEAR INFRARED DETECTOR READOUT ELECTRONICS	127
G.2.5.7	SLIT-VIEWING CAMERA DETECTORS	127
G.2.5.8	SLIT-VIEWING CAMERA READOUT ELECTRONICS	130
G.2.5.9	DMD ELECTRONICS	130
G.2.5.10	COMMERCIAL VERSUS CUSTOM BOARDS	131
G.2.6	INSTRUMENT SOFTWARE DESIGN	132
G.2.6.1	OVERVIEW OF CONTROL SOFTWARE ARCHITECTURE	132
G.2.6.2	COMMUNICATIONS	133
G.2.6.3	DMD CONTROL SOFTWARE	133
G.2.6.4	DETECTOR READOUT SOFTWARE	134
G.2.6.5	DEVELOPMENT TOOLS	134
G.2.7	DATA REDUCTION SOFTWARE CONSIDERATIONS	135
G.2.8	PERFORMANCE TRADES	135
G.2.8.1	FIELD OF VIEW	135
G.2.8.2	NIR DETECTOR SELECTION	135
G.2.9	TECHNICAL RISKS	135
H	PROJECT MANAGEMENT ASPECTS	138
H.1	COST ESTIMATE	138
H.1.1	DESCOPE OPTIONS	140
H.1.1.1	DEFER OR ELIMINATE THE K-BAND	140
H.1.1.2	DEFER OR ELIMINATE H AND K BANDS	140
H.1.1.3	ELIMINATE SIMULTANEOUS COVERAGE IN THE NIR	140
H.1.1.4	RESTRICT AO FEEDBACK TO THE NIR ARM	141
H.1.1.5	DEFER OR ELIMINATE THE BLUE ARM	141
H.2	ESTIMATED SCHEDULE	142
H.3	WORK BREAKDOWN STRUCTURE	142
H.4	RISK MANAGEMENT	142
H.4.1	MANAGING TECHNICAL RISKS	144
H.4.2	MANAGING COST RISKS	146
H.4.3	MANAGING SCHEDULE RISKS	148
H.4.4	MANAGING STAFFING RISKS	150
H.5	FACILITY REQUIREMENTS	151
H.6	REQUIRED SKILL-SETS	152
H.6.1	SCIENCE SKILLS	152
H.6.2	TECHNICAL SKILLS	153
H.6.3	MANAGEMENT SKILLS	154

H.7	LONG-LEAD PROCUREMENTS	154
I	PROJECT REVIEW	155
I.1	STUDY SCHEDULE	155
I.2	STUDY COST	155
I.3	STUDY LEVEL OF EFFORT	156
I.4	GMOX COST ESTIMATE: STUDY VERSUS THE PROPOSAL	156
I.5	GMOX SCHEDULE: STUDY VERSUS THE PROPOSAL	156
I.6	IS GMOX FEASIBLE?	156
J	ACKNOWLEDGMENTS	158

A EXECUTIVE SUMMARY

We present the Feasibility Study of **GMOX**, the **Gemini Multi-Object eXtra-wide-band** spectrograph, as the 4th generation Gemini facility instrument. We envision GMOX as a spectrograph covering the entire optical/near-IR wavelength range accessible from the ground (**from $\sim 3500 \text{ \AA}$ in the U-band up to $2.4 \mu\text{m}$ in the K-band**) with resolving power $R \simeq 5,000$, adequate to mitigate the effect of telluric airglow lines. Using existing Micro Electro Mechanical Systems (MEMS) technology, GMOX can simultaneously acquire **hundreds of spectra** of faint sources in crowded fields with unparalleled spatial resolution. GMOX optimally adapts to **both seeing-limited and diffraction-limited conditions** provided by ALTAIR and GeMS at Gemini North and South, respectively. On a large fraction of nights, these systems deliver nearly diffraction-limited imaging in the near-IR ($\lambda/D = 50 \text{ mas}$ at $2 \mu\text{m}$) and exquisite, seeing-limited images across the visible. Fed by GeMS (f/33), GMOX can synthesize slits as small as 40mas (corresponding to a single HST/WFC3 CCD pixel) over its entire $85'' \times 45''$ field of view, reaching the ultimate sensitivity to point sources while resolving structures smaller than 300 pc across the observable Universe. Both the slit and field size double at the native f/16 focal ratio of Gemini.

Resolving galaxies through cosmic time is the key science driver for GMOX. Space telescopes like the HST, JWST and WFIRST have the capability of resolving typical galaxies at any redshift. Thanks to HST, we have learned that imaging alone is not adequate to disentangle the physical processes leading to the formation, growth and evolution of galaxies over time, both intrinsic (bursts of star formation, activity of central black holes,...) and extrinsic (mergers, feedback,...). Ground based spectroscopy in the seeing-limited regime provides integrated information that is often misleading, as galaxies are not homogeneous: individual sub-regions are dominated by different processes. The problem is exacerbated by the need to analyze statistically significant samples of galaxies in different environments and at different redshifts, from the voids and supervoids, to the sheets and filaments, up to the richest and densest clusters. **Adaptive optics on 8m class telescopes could play a crucial role** if equipped with a spectrograph delivering pin-point accuracy, comparable to the diffraction limit of the telescope, flexibility to adapt to the actual AO performance, extremely large wavelength coverage and extensive multi-object capability. The combination of these requirements is prohibitive for multi-object spectrographs or integral field units. GMOX is the first instrument with such a capability, complementing JWST/NIRSpec below $1 \mu\text{m}$ and with superior spatial and spectral resolution up to $2.5 \mu\text{m}$. Its versatility will enable exciting discoveries in many fields of astrophysics, from studies of individual, isolated faint sources to the analysis of highly crowded fields such as globular clusters, the Galactic Bulge, the Magellanic Clouds, nearby galaxies and galaxy clusters. We expect GMOX to become the **ideal workhorse instrument for Gemini**, highly requested and extremely productive in all observing conditions. Future facilities like LSST will also dramatically increase the demand for **spectroscopic followup**; GMOX will allow Gemini to play a critical role in this field well over the next decade.

GMOX is comprised of three arms: **Blue, Red and Near-IR** observing the same field through dichroic mirrors. The split focal planes are reimaged onto three **Digital Micromirror Devices (DMDs)** of the latest generation, commercially available; each DMD covers the field with 2048×1080 mirrors of $13.7 \mu\text{m}$ size, sampling at **$0.083''/\text{mirror}$ at f/16 and $0.040''/\text{mirror}$ at f/33 (GeMS)**. Each mirror can be individually tilted by $\pm 12^\circ$; those tilted in the "ON" state reflect the light to the **spectroscopic channel**, acting as slits. The multitude of other mirrors left in the "OFF" state project an image of the field to an ancillary **imager for slit acquisition, AO tip-tilt control, or parallel deep imaging**. The Near-IR arm is split into three channels, dedicated to the YJ, H and K-bands. With a total of 2 large format CCDs and 3 H4RG IR detectors, the full spectra of all selected sources are simultaneously collected, each spanning about 25,000 pixels.

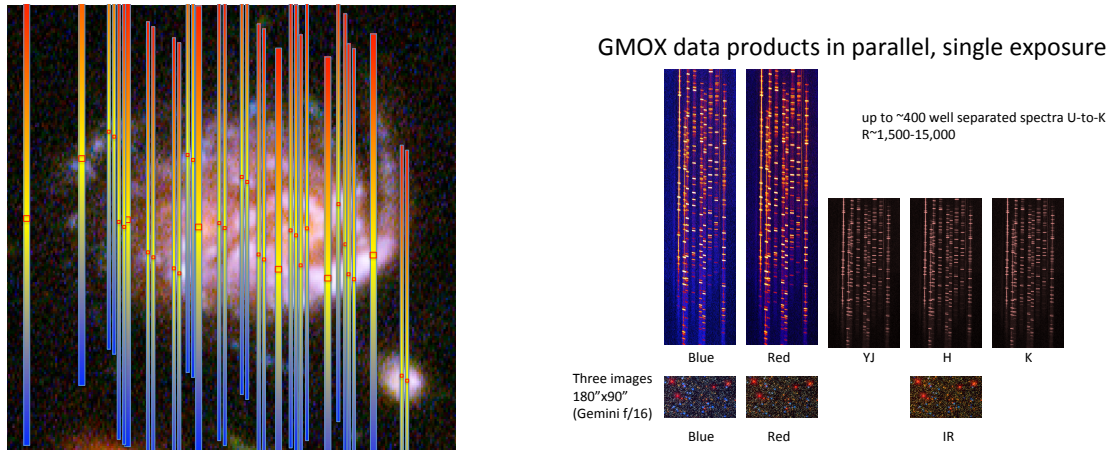


Figure 1: Left: A $10'' \times 10''$ portion of the Hubble Ultra Deep Field, with a prominent dual-nucleus galaxy. The image is rendered with the original 50 mas pixel sampling of ACS/WFC (courtesy Z. Levay, STScI). The vertical bars are intended to represent the spectra that can be obtained by GMOX, with smallest apertures comparable to the pixels of the HST cameras. This $10'' \times 10''$ field is approximately 150 times smaller than the actual field of view of GMOX, at Gemini f/16. Right: a sketch of the data obtained by GMOX at each pointing. Five detectors capture the full wavelength range from U to K, each one dispersed over about 25,000 pixels, for hundreds of targets spread over the GMOX field of view.

Our conservative estimates show that under normal seeing conditions GMOX approaches Signal-to-Noise=5 at $J_{AB} \simeq 22$ in 1000s, per resolution element. With Adaptive Optics, the capability of using ultra-narrow slits with minimal sky background allows GMOX to reach unprecedented sensitivity across its entire spectral range. The possibility of defining slit widths by multiples of 83 mas (at f/16) or 40 mas (at f/33 of GeMS) is, in fact, critical. **GMOX can instantaneously and optimally synthesize slits** that with any other approach would be completely impractical to handle, especially given the sensitivity of an AO-fed system to the weather conditions. GMOX removes the need for pre-imaging weeks in advance and fully relaxes the requirements on long-term stability of the focal plane, while allowing real-time monitoring of the perfect slit alignment during the longest integrations. With AO, it enables adapting the slit width (and therefore the spectral resolution) to the quality of the PSF across the field. It enables tip-tilt control on fainter natural stars observed in white light within the field to maximize Strehl ratio and extend AO correction well into the visible range. It enables wide-field Integral Field Spectroscopy through the use of Hadamard transforms. As accurate slit positioning is nearly instantaneous, GMOX is extremely efficient even for the simplest, single source observations: the target can be acquired with a mouse click, regardless of its position in the field. Pointing corrections, blind offsets, etc., are no longer needed.

GMOX leverages previous studies to bring this technology to fruition for future space missions. Our team has unique experience with DMD technology, having built two DMD-based instruments, and experience in general with the concept, construction and operations of major instrumentation for ground-based and space observatories. We have crafted a well defined instrument concept for GMOX, one that addresses all critical technical considerations. We believe that GMOX will deliver unique science and superior performance (field size, wide-band coverage and sensitivity) at a lower cost than any competing IFU or multi-slit spectrograph.

B INTRODUCTION

B.1 GEMINI AND THE GIFS REQUEST FOR PROPOSAL

The Feasibility Study for GMOX presented in this document responds to the principles listed in the Gemini Instrument Feasibility Study (GIFS) - Request for Proposal for the next facility instrument. The twin Gemini telescopes represent the largest observing facility accessible to the entire US astronomical community, as well as to the other member states. To satisfy the needs of a such a large constituency, they must enable the most demanding research programs in almost every field of observational astronomy. In planning a future facility instrument for Gemini, extreme **versatility** is thus the first key requirement for a workhorse instrument. At the same time, to be competitive, a Gemini facility instrument must also offer some **unique observing capability** that optimally exploits the characteristics of the telescopes. Both Gemini telescopes have been designed with ultimate performance in the IR in mind, with the lowest possible emissivity at the expense of a relatively modest field of view. Both are now equipped with state-of-the-art adaptive optics systems, in particular Gemini South has the only Multi-Conjugate AO (MCAO) system currently offered to general observers, GeMS. A facility instrument exploiting these unique capabilities, together with conventional seeing-limited conditions, would enable new and exciting discoveries.

Synergy with other observing capabilities must also be taken into account. With the advent of a new generation of large facilities performing wide-field imaging surveys (DES, Pan-STARRS, Sky Mapper, VISTA, LSST, Euclid, WFIRST), the need for deep and efficient spectroscopic follow-up is becoming critical for almost every field of astrophysics. The National Research Council (NSF) **Report of the Astro2010 Decadal Survey's Panel on Optical and Infrared Astronomy from the Ground**[1] asserts the need for

“Massively multiplexed optical/NIR spectrographs and spectroscopic surveys on 4 to 8-m telescopes to map large-scale structure for the study of dark energy and cosmology, measure the evolution of galaxies across redshift and environment using spectral diagnostics, and to study the chemical and dynamical history of the Milky Way with large spectroscopic samples of stars. Several SFPs [Science Frontiers Panels] identified the need for surveys at least an order or magnitude larger than those currently underway; such surveys require new instrumentation for either fully or highly dedicated facilities as well as large survey teams”.

More recently, the NSF report **Optimizing the US Ground-Based Optical and IR Astronomy System**[2] issued the following guidelines:

- *The National Science Foundation should support the development of a wide-field, highly multiplexed spectroscopic capability on a medium- or large-aperture telescope in the Southern Hemisphere to enable a wide variety of science, including follow-up spectroscopy of Large Synoptic Survey Telescope targets. Examples of enabled science are studies of cosmology, galaxy evolution, quasars, and the Milky Way.*
- *The National Science Foundation should work with its partners in Gemini to ensure that Gemini South is well positioned for faint-object spectroscopy early in the era of Large Synoptic Survey Telescope operations, for example, by supporting the construction of a rapidly configurable, high-throughput, moderate-resolution spectrograph with broad wavelength coverage.*

We believe that this last recommendation could have been more ambitious. Gemini can play a unique role in the next decade, complementary to JWST, LSST and the future 30-meters telescopes,

if equipped with a facility class spectrograph combining very-wide-band coverage and multiplexing capability with the sensitivity and spatial resolution provided by an extreme Adaptive Optics system, a technology for which Gemini currently plays a leading role. A facility instrument with all these characteristics, joined to ease of operations for immediate **follow-up of transients and targets of opportunity**, would allow the large Gemini astronomical community to advance in **completely unexplored territories, enabling transformational science** in fields ranging from Solar System studies to the nature of the early galaxies at the edge of the Universe.

Such an instrument does not exist, nor is it planned at any other major facility. However, we have identified a viable, low risk path to build it, and we are presenting the concept in response to this Gemini Request for Proposals.

B.2 FROM THE REQUIREMENTS TO GMOX

In developing GMOX, we have been guided by a key science theme that will play a dominant role in astrophysical research for the foreseeable future: **Resolving galaxies through cosmic time**, ideally suited to the strengths of the Gemini telescopes and to the STAC principles of this call. Our exercise led to the following list of top-level requirements:

1. A spectrograph with **wide spectral coverage**, from the UV to the near-IR (NIR) to capture all major spectroscopic tracers of star formation from the local Universe to high redshift galaxies, with resolution adequate to work effectively between the telluric OH lines; we have set as baseline $R \simeq 5,000$.
2. **High observing efficiency**, i.e. high throughput and substantial multi-object capability to justify long integrations on a multitude of faint targets.
3. The capability of exploiting **all seeing conditions**, including the best ones delivered by the extreme AO systems of Gemini, exploiting the full AO corrected field of view. This translates to **extreme accuracy and versatility of the slit alignment mechanism**.
4. Minimal overheads: aligning hundreds of slits with pinpoint accuracy means that slits must be **configurable in a fraction of a second**, matching the source position and width to the actual acquisition image while monitoring in real time the perfect alignment for deep, hour long exposures; this requirement is naturally satisfied by a MEMS device.

The main instrument layout and parameters have been derived from these top-level requirements, taking into account the constraints provided by the telescope design, including the AO systems, and the status of current technology (detector size and performance, MEMS availability and size). The resulting design is introduced hereafter.

B.3 INTRODUCING GMOX

The GMOX concept breaks the standard paradigm where Multi-Object-Spectrographs are optimal for wide-field coverage and Integral-Field-Units (IFUs) are optimal when fine spatial sampling is needed. By exploiting existing Micro Electro Mechanical Systems (MEMS) technology, in particular commercially available Digital Micromirror Devices (DMDs) used as slit selectors, it is possible to build a spectrograph with very-wide bandpass coverage, from U to K like the VLT/X-shooter, as well as with multi-object capability, unique spatial resolution and very high sensitivity. The latter two can be achieved by optimal exploitation of the Gemini AO systems: ALTAIR at Gemini-North

or, even better, the MCAO system GeMS at Gemini-South. The combination of wide spectral coverage, multi-object-capability, spatial resolution and sensitivity guaranteed by GeMS would put GMOX in its own new, unique class.

A schematic optical layout for GMOX is presented in Figure 2, with the main parameters summarized in Table 1. Light coming from the telescope (i.e. from the top in the figure) is split by two dichroics into three arms: the Blue arm, for the wavelength range approximately 3500-5900Å, the Red arm, for the wavelength range approximately 5900-9800Å, and the IR arm for the wavelength range 9800-24000Å. Each arm has reimaging optics that project the focal plane onto a DMD of 2048 × 1080 tiny mirrors, each one capable of deflecting the light $\pm 12^\circ$. The reflected beams are first captured and corrected by an off-axis system, then reimaged to either an imaging camera (OFF mirrors) or to a spectrograph (ON mirrors) to take, simultaneously, hundreds of spectra at $R \simeq 5,000$. In the case of the IR arm, the spectra are so long that three different detectors are required: one for the YJ, H, and K bands, respectively.

A single DMD mirror, at the standard f/16 focal length of Gemini, corresponds to a slit width of 83 mas, and 40 mas at the f/33 of GeMS. This is the size of e.g. a pixel of the highest resolution camera currently operating on the Hubble Space Telescope, WFC3-UVIS. We define the GMOX nominal slits using three, four and five mirrors for the IR, Red and Blue channels, respectively, corresponding to 0.25, 0.33 and 0.41 arcsec slits, but any combination is possible. With these slits the resolving power is approximately $R = \lambda/\Delta\lambda = 5000$ with about 3 pixel/slit sampling at the detector; different combinations span the range from $R = 25,000 - 15,000$ for single mirrors slits to $R \simeq 1250 - 2000$ with 1" slits. The field of view of 171" × 90" (at f/16) matches the 3.1' unvignetted field of Gemini.

The capability of adjusting the slit position and width by multiples of 83 mas (40 mas at GeMS) allows GMOX to exploit all seeing conditions, including the best possible delivered by the extreme AO systems of Gemini, matching the variations across the corrected field of view. In background limited conditions, the Signal-to-Noise ratio scales as $\sqrt{\tau}/d_{slit}$, where τ is the system throughput and d_{slit} is the width of a square slit; for point sources, a 30% throughput loss due the presence of a complex AO system like GeMS is compensated by using slits smaller by 17%; as slits get narrower the sensitivity to point sources increases. By exploiting the diffraction limited performance in the near-IR ($\lambda/D \simeq 50$ mas at 2 micron) delivered by Gemini AO systems, the sensitivity gain provided by GMOX can be substantial, especially in the IR.

Using the imaging channels, GMOX can optimally configure all slits in a fraction of a second, adapting the slit position and width to the actual image quality, variable across the field in the case of AO, and monitoring in real time the perfect alignment for deep, hour long exposures. GMOX can also provide tip-tilt guiding on field sources, optimal to reach the highest Strehl ratios, with improved sensitivity as the imaging channels can tip-tilt in "white light" with wider bandpass while still reflecting the light of the target sources to the spectrograph.

B.4 GMOX AND THE GEMINI-STAC PRINCIPLES

We developed GMOX's concept taking into account the principles set by the Gemini Science and Technology Advisory Committee (STAC) in their 2012B report on feasibility design studies, [3]. In particular:

1. *"The instrument should be a workhorse instrument, meaning that it has broad scientific appeal and enables a wide range of science cases."*

GMOX is the ultimate workhorse instrument. It provides parallel spectroscopic and imaging capabilities, from the U to the K-band. Spectroscopy can be performed on a single object

Parameter	Gemini North & South, no AO (f/16) Gemini North, ALTAIR LGAO (f/16)	Gemini South, GEMS MCAO (f/33)
Field of View	171" × 90"	85" × 45"
DMD mirror scale	83 mas/mirror	40 mas/mirror
Nominal slit width		
Blue Arm:	0.42" (5 mirrors)	0.20" (5 mirrors)
Red Arm:	0.33" (4 mirrors)	0.16" (4 mirrors)
NIR Arm - YJ channel:	0.25" (3 mirrors)	0.12" (3 mirrors)
NIR Arm - H channel:	0.25" (3 mirrors)	0.12" (3 mirrors)
NIR Arm - K channel:	0.25" (3 mirrors)	0.12" (3 mirrors)
GMOX Arms/Channels		
Blue Arm:	3500 < λ < 5890Å, R=4500	
Red arm:	5890 < λ < 9700Å, R=4500	
NIR arm - YJ channel:	0.97 < λ < 1.35 μ m, R=3800	
NIR arm - H channel:	1.46 < λ < 1.81 μ m, R=4500	
NIR arm - K channel:	1.93 < λ < 2.45 μ m, R=4500	
Nr. of dichroics	4 (Blue arm, Red arm, YJ-band, H-band)	
Nr. of DMDs	3 (Blue, Red, NIR arms)	
DMD type	Cinema 2K, 2048 × 1080 mirrors	
DMD mirrors	13.0 μ m side, 13.7 μ m center-to-center	
Detectors:	Blue , Red: 2 CCDs E2V290-99, 9216 × 9232 pixels NIR: 3 FPAs, model H4RG-10, 4096×4096 pixels	
GMOX spatial scale:	90" × 90" over 1350 × 1350 pixels	
Sampling	Blue and Red Arm: 3 pixel/nominal slit width NIR Arm (all channels): 2.75 pixel/nominal slit width	
Max nr. of spectra	≈ 200 – 500, depending on slit size and separation	
Slit-viewing cameras	Blue, Red: 2 Andor sCMOS (4096 × 4096 × 12 μ m) NIR: 1 H2RG (2048 × 2048 × 18 μ m) 1 pixel per DMD mirror (all arms)	

Table 1: GMOX baseline parameters.

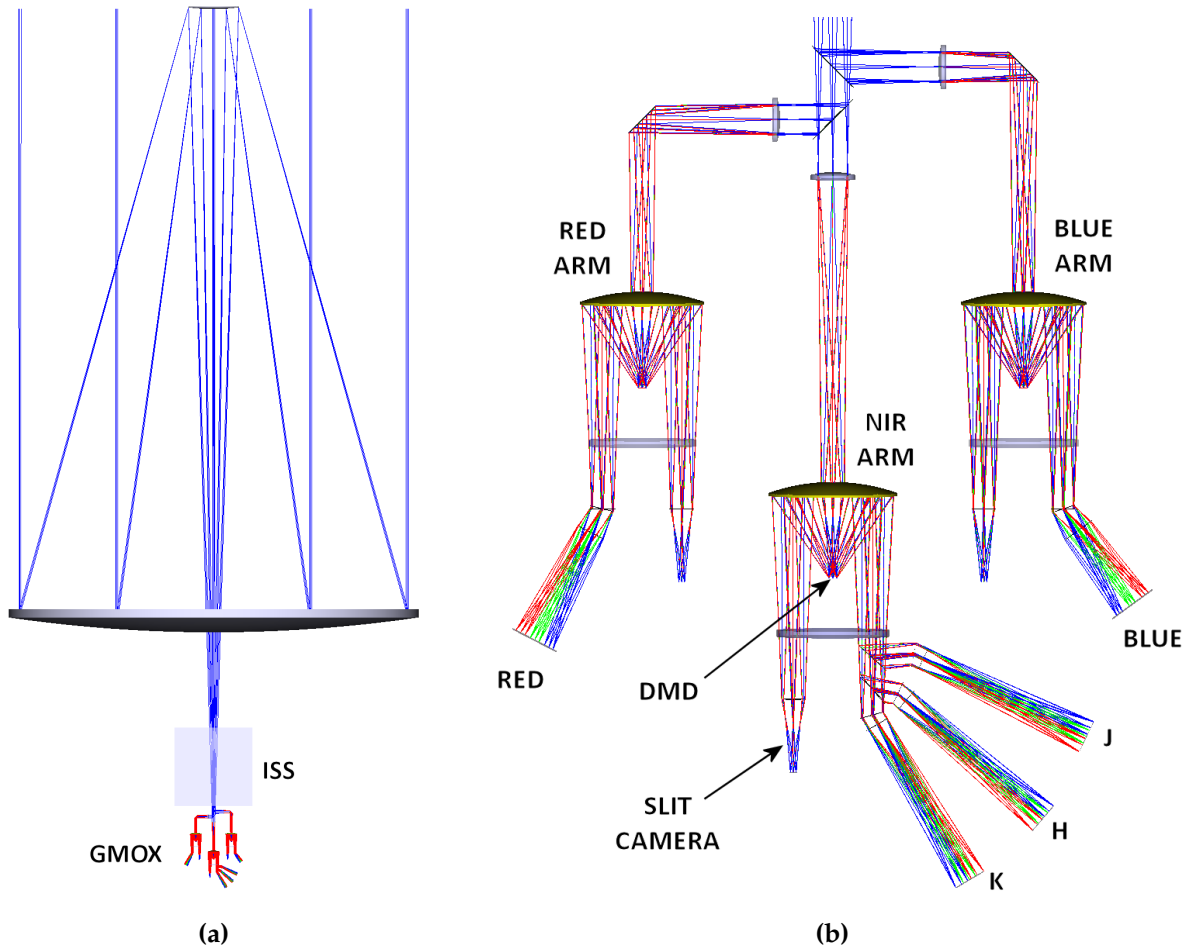


Figure 2: Simplified optical concept for GMOX. (a) GMOX on Gemini, shown beneath an ISS-sized cube for scale. (b) Schematic layout of the GMOX 3-arm concept, unfolded for clarity. Roughly to scale.

or on multiple objects, up to several hundreds, with every slit optimally and nearly instantaneously positioned to maximize throughput. The full spectrum of each source falls on about 25,000 pixels at $R \simeq 5,000$. Imaging can be performed on three band-passes in parallel. GMOX can exploit any level of seeing and adapt to non-uniform PSFs varying across the field. In standard seeing limited conditions, GMOX is more capable, versatile, and efficient than any other existing or planned wide-band mid-resolution spectrograph. Fed by the ALTAIR or GeMS AO systems, GMOX can use extremely narrow slits to reach unprecedented sensitivity levels. Using Hadamard Transform Spectroscopy, GMOX can also operate in integral field mode over its large field of view with performance comparable to state-of-the-art IFUs.

2. *The proposals should be science driven and include science cases. Science cases that provide synergies with new capabilities coming online (e.g. LSST, JWST, ALMA, etc) are highly desirable, especially including capabilities needed to follow up survey discoveries.*

We have been guided by a well defined, compelling science theme that will remain central to astrophysics in the years to come: *Resolving Galaxies Through Cosmic History*. We

have elaborated a variety of science cases to illustrate how GMOX can carry out an enormous range of programs, as appropriate for a facility instruments. These include unique observations exploiting Gemini extreme-AO capabilities. The wide band-pass coverage, the possibility of working under any seeing condition, the ultimate rapidity of slit configuration, and the parallel imaging capability also make GMOX ideal for immediate followup of new discoveries made by other observatories, LSST in particular.

3. *The instrument should fit within the technical constraints of the Gemini telescopes as they now exist.*

GMOX can be mounted at both Gemini-North and Gemini-South; it can operate in seeing limited conditions as well as with any level of Adaptive Optics correction, while matching the allocated space envelope, weight, position of center of mass and all other requirements posed to new Gemini instrumentation. Moreover, GMOX is ready to exploit any further upgrade of the AO systems without modifications. Demand may eventually arise for doubling GMOX, having a version at each Gemini telescope!

4. *The expected cost of the instrument shall be capped at a cost that is to be determined as part of the process of defining the RfP.*

We have made an effort to keep GMOX within the cost cap of the RfP; our cost estimate compares favorably with other instruments of similar scale. The addition of contingency, however, puts GMOX well above the cost cap. We are presenting descope options but the exceptional advantages offered by the baseline deserve a **reconsideration of the initial cost cap**. This would be consistent with Recommendation 4b of the Optimizing the U.S. Ground-Based Optical and Infrared Astronomy System report: *“The National Science Foundation should work with its partners in Gemini to ensure that Gemini-South is well positioned for faint-object spectroscopy early in the era of Large Synoptic Survey Telescope operations, for example, by supporting the construction of a rapidly configurable, high-throughput, moderate-resolution spectrograph with broad wavelength coverage”*.

5. *The technical risk of the instrument should be modest, i.e. the success of the instrument should not depend upon some not-yet-proven technology.*

For GMOX we have assumed in our baseline the 4K IR detectors under development e.g. for WFIRST and the latest generation of CCDs. The instrument, however, can be built using existing detectors with some compromise in performance and efficiency. DMDs have been built in tens of millions of parts for the consumer market, are extremely reliable and have already been used in astronomical instruments by our team. All optical elements have modest size. Overall, **the technical risk of GMOX is low**. Details are provided in the second part of this document.

6. *The instrument should be highly efficient, maintaining the 8-m aperture advantage.*

GMOX boosts efficiency by splitting the beam in 3 arms for optimal throughput with dedicated coatings, and through the capability of optimally aligning slits and their width “on the fly” for hundred of sources observed in parallel over a very wide spectral range. Even in seeing limited conditions, the efficiency gain with respect to single object spectrographs

like VLT/X-shooter in crowded fields (all fields are crowded in deep observations!) may be **higher by a factor of a few hundreds**.

7. *Although proposals for all instruments fitting these criteria will be fully considered, it is the majority opinion of the STAC that a wide-bandwidth moderate-resolution spectrograph is likely to prove most compelling.*

GMOX is by the design a wide-bandwidth, moderate-resolution spectrograph. It is also multi-object, with extensive parallel imaging capability, and AO capable.

B.5 SUMMARY: GMOX'S UNIQUE STRENGTHS

In summary, there are two key factors that make GMOX rather unique: a) the capability of taking wide-band spectra of multiple targets in crowded fields; and b) the capability of using extremely narrow slits.

To map the parameter space uniquely probed by GMOX we can consider three different cases for each factor. For the source density we can distinguish between:

- Crowded fields, with several tens or even hundreds of sources per square arcminute. Examples are: Clusters of Galaxies, Nearby Galaxies, Magellanic Clouds, Globular Clusters, Galactic Bulge, Galactic Young Clusters.
- Rich fields, with a few tens of sources per square arcminute. Examples: Outskirts of globular clusters, Orion Nebula.
- Sparse fields, i.e. a few targets, or possibly just one target per square arcminute. These are the cases typically accessible by conventional long-slit spectrographs. Examples: Rare primordial galaxies, targets of opportunity, field brown dwarfs.

while for the spatial resolution we can distinguish between:

- Diffraction-limited mode, with Extreme AO delivering $\lambda/D \simeq 0.05''$ in the near-IR. Needed to resolve substructures in galaxies, extremely crowded fields (LMC, nearby galaxies,...) spectroscopy of faint targets.
- Seeing-enhanced mode, with AO providing a significant reduction of the seeing-limited PSF, achieving e.g. $\text{FWHM} \simeq 0.25''$. Standard observing mode for GMOX, appropriate for fields not crowded, target of opportunity followup etc.
- Ordinary seeing conditions, with $\text{FWHM} \simeq 0.8'' - 1''$. Targets requiring low spectral resolution.

These cases can be arranged in a 3×3 table that graphically captures the regimes where GMOX has **UNIQUE** capabilities, where GMOX is not unique but definitely more **EFFICIENT** than other instruments with comparable capabilities, and where GMOX simply replicates capabilities offered by other **COMMON** instruments.

FWHM	Crowded Field	Rich Field	Sparse
0.05''	UNIQUE	UNIQUE	EFFICIENT
0.25''	UNIQUE	EFFICIENT	COMMON
1''	EFFICIENT	COMMON	COMMON

Table 2

In general, GMOX has rather unique capabilities when one has to operate in crowded/rich fields with extreme spatial resolution to avoid confusion or to pinpoint key targets. The Hubble Legacy Archive provides us with thousands of exciting fields falling within this category. As the target density or the requirement on spatial resolution decrease, instruments like MOSFIRE or KMOS are a viable alternative, and the choice of instruments becomes richer as one decreases the source density and/or the requirement on the spatial resolution. Still, even in this case GMOX provides strong advantages from the point of view of ease of operations and wide-spectral coverage.

C SCIENCE CASE: RESOLVING GALAXIES THROUGH COSMIC HISTORY

C.1 GMOX SCIENCE TEAM

- T. Heckman (JHU, Science Team Lead): Galaxies
- M. Gennaro (STScI, Science Team Deputy): Resolved Stellar Populations
- A. Adamo (Stockholm University): Star clusters formation
- G. Becker (UC Riverside): High redshift Quasars
- A. Bellini (STScI): Globular Clusters
- L. Bianchi (JHU): Resolved Stellar Populations
- A. Bik (Stockholm University): Massive Stars
- R. Bordoloi (MIT): Circumgalactic Medium
- A. Calamida (STScI): Globular Clusters
- D. Calzetti (UMass): Star Formation in the Local Group
- G. De Rosa (STScI): AGN and high redshift Universe, calibrations
- S. Deustua (STScI): Calibration program
- J. Kalirai (JHU, STScI): Resolved Stellar Populations
- J. Lotz (STScI): clusters of galaxies
- J. MacKenty (STScI): Galaxies, DMD operations
- C. F. Manara (ESA): Circumstellar discs
- M. Meixner (JHU, STScI): Resolved Stellar Populations
- C. Pacifici (STScI): Galaxy Evolution
- M. Robberto (JHU, STScI): Local Star Formation
- E. Sabbi (STScI): Massive Star Clusters
- K. Sahu (STScI): Galactic Bulge, planets
- J. Tumlinson (STScI): Galaxy Evolution

C.2 TEN KEY SCIENCE QUESTIONS ADDRESSED BY GMOX

1. How rapid and patchy was the process of **reionization of the Universe**? Which sources are responsible for it?
2. When did the **first stars** appear and what has been their role in **ending the Dark Ages**?
3. How did **Super Massive Black Holes** form? What are their seeds?
4. How do **Galaxies** build up their stellar mass?
5. What is the relation between star formation and **AGN** ?
6. What is the origin of multiple stellar populations in **Globular Clusters**?
7. Is the **Initial Mass Function** Universal?
8. What are the connections between host galaxy properties, star Formation Rate density and **Cluster Formation, evolution and disruption**?
9. How does feedback from **Massive Stars** affect their birth environments?
10. What is the main driver of **Circumstellar Disks** evolution and dispersal?

C.3 SETTING THE STAGE

Cosmic Dawn, New Worlds, and Physics of the Universe are the three overarching science themes envisioned in the 2010 NRC Decadal Survey report *New Worlds, New Horizons in Astronomy and Astrophysics* [NWNH, 1]. Transformational science in these fields requires synergistic use of both ground-based and space-based observatories with highly dedicated instruments spanning all wavelength ranges. The theme of New Worlds drives, e.g., the development of high-contrast coronagraphic imagers and spectrographs to directly resolve planets and map the structure of protoplanetary disks. The theme of New Physics drives, e.g., the design of wide-field surveys both in imaging and spectroscopy to investigate weak lensing and baryon acoustic oscillations.

In this study we mostly concentrate on the first theme, Cosmic Dawn. Thanks to the exquisite resolving power of the Hubble Space Telescope, in combination with photometric data from the Spitzer Space Telescopes, we are now pushing the observational frontier beyond $z \simeq 10$, corresponding to ~ 400 Myr after the Big Bang. With nearly 1000s likely detected galaxies at $z > 6$, including about 20 credible candidates at $z \sim 9 - 11$ we can for the first time **probe the growth and evolution of galaxies from the reionization epoch to the present.**

Galaxies grow with time and space telescopes like the HST, and in the future JWST and WFIRST, can spatially resolve any average galaxy across the visible universe. Thanks in particular to the HST, we have learned that galaxies are not homogeneous even at the highest redshifts, but grow mainly by hierarchical merging; their formation, growth and evolution is regulated by a variety of factors, both intrinsic (bursts of star formation, activity of central black holes,...) and extrinsic (mergers, feedback,...) that still need to be interpreted in a coherent, comprehensive framework capable of explaining the observed variety of systems. Ground based spectroscopy, in the seeing-limited regime, provides integrated information that is often misleading, as different regions can be dominated by different physical processes and stellar populations. The problem is exacerbated by the need to analyze statistically significant samples of galaxies in different environments and at different redshifts, from the voids and supervoids, to the sheets and filaments, up to richest and densest clusters.

Resolving galaxies through cosmic time is the main science objective of our proposal. An instrument like GMOX, capable of observing hundreds of sources in parallel over 4 decades of the electromagnetic spectrum using slits as small as 1/25th of an arcsecond, can write new chapters in our quest for understanding how the first galaxies formed, how they assembled and controlled their stellar mass, fed their central black holes and generally evolved to create the rich phenomenology we observe in our local Universe, harboring stars and planetary systems germane to our own existence.

GMOX can pinpoint and collect deep spectra of regions with angular size as narrow as the spatial resolution of the Hubble Space Telescope (Figure 1). As shown in Figure 3, GMOX's 83 mas slit size ($f/16$), matching the 2-micron diffraction limit of Gemini (50 mas), resolves the scale of the inner Solar System at the distance of the Orion Nebula, 1/50th of a parsec at the distance of the LMC, half a parsec everywhere in the Local Group, 750 pc at redshift $z \simeq 1.5$. Beyond this distance the physical spatial resolution increases again with the angular distance, i.e. **GMOX can resolve spatial scales less than 750 pc at all cosmological distances.** (Fig. 4). GMOX can thus spatially resolve any average galaxy in the observable Universe, according to the measured size-redshift relation (Fig. 5). At GEMS ($f/32$) the minimal slit size is narrower by a factor of 2. The potential is enormous. Exploiting galaxy clusters like MS 1358.4+6245 [4], capable of gravitationally magnifying a $z = 4.92$ background galaxy by a factor 5 to 100, depending on the individual lensed image, one can analyze bursts of star formation in regions the size of a globular cluster, about 10 pc, at the age of formation of globular clusters, about 1 Gyr after the Big Bang!

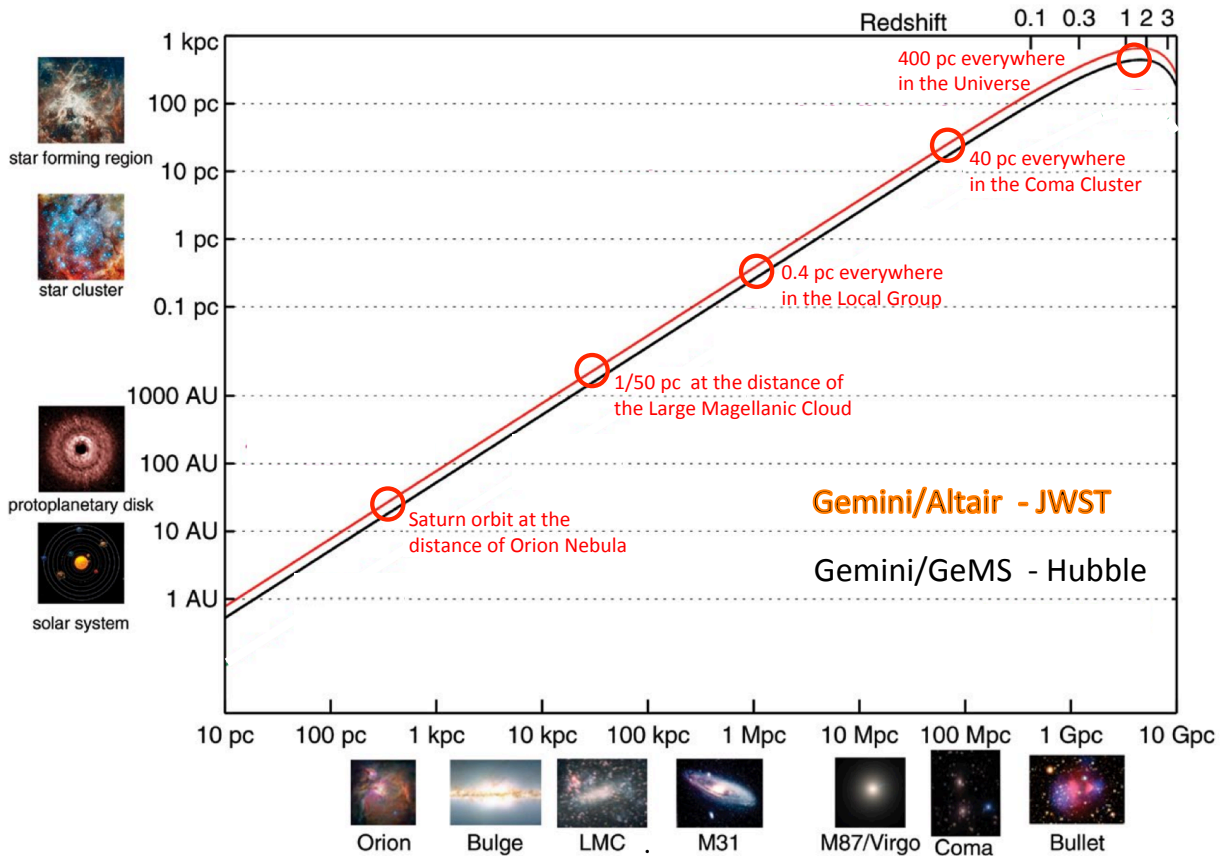


Figure 3: GMOX’s capability to synthesize slits matching the diffraction limit of an 8m telescope allows one to analyze the physical status of compact regions across cosmic distances. The angular slit widths of GMOX at Gemini with ALTAIR and GeMS are marked in magenta and black, respectively; they are close to the diffraction limit at $\lambda = 2\mu\text{m}$ of the $D = 6.5$ m JWST telescope and of the $D = 2.4$ m Hubble. Major resolution thresholds are marked by red circles. (adapted from Fig. 4.1 of “From Cosmic Birth to Living Earth”, AURA Report, 2015)

It is obvious that an instrument with these capabilities, standing above its predecessors in nearly all performance metrics based on combinations of sensitivity, angular resolution, wavelength coverage and multiplexing capability, has **great scientific potential for almost any field of astronomy**. The history of astronomy shows that when there is a breakthrough in observing capabilities new discoveries are made that eclipse the results of science cases planned years in advance. Bearing in mind this lesson, the purpose of this section is to identify a range of scientific topics in which GMOX is likely to enable major advances. We have mostly focused on cases where GMOX can contribute with stand-alone programs, but LSST follow-up observations have also been considered. The themes reflect, to some degree, the scientific interests of our science team and mostly derive from extensive experience with the HST. We devote one section to each topic, ordered approximately by cosmic time.

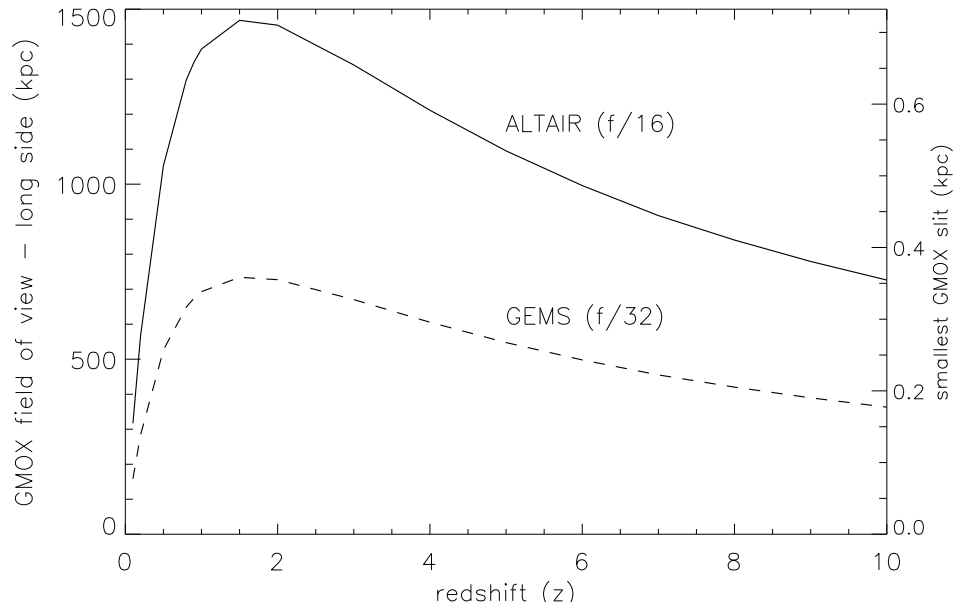


Figure 4: The nominal field of view of GMOX is $170.66'' \times 90''$ at $f/16$ and $85''$ at GEMS ($f/32$). These angular sizes corresponds to a comoving distance (left axis) that varies with redshift. The minimal size, corresponding to one “open” micromirror, is also plotted on the right vertical axes. We assumed $H_0 = 69.6$ km/s, $\Omega_m = 0.286$ and a flat Universe.

C.4 COSMIC HISTORY: 3.5 GYR OF GROWTH

The key science case leading to the concept of GMOX is the study of the formation and evolution of galaxies through the analysis of their single components. This theme can only be briefly summarized for the purposes of this document.

Galaxy evolution can be divided in 4 historic phases, up to the “present epoch” at $z < 1$:

1. The first 500 Myr of cosmic history, corresponding to $z > 10$. In the early stages of the so-called “Dark-Ages” galaxies begin to form in dark matter halos created by initial density fluctuations in the primordial Universe. The first stars appear, starting the reionization of the Universe and producing the first metals.
2. The epoch of reionization, completed about one billion years after the Big Bang, corresponding to about $6 < z < 10$. In this epoch mini-halos expand and merge while the early compact embryos of present day galaxies are assembled. Super Massive Black Holes also have formed by the end of this phase.
3. The second billion years of cosmic history, $3 < z < 6$, where the stellar mass of the Universe grows from $\sim 1\%$ of its present value to $\sim 10\%$ with significant enhancement of heavy elements. Globular Clusters and the Milky Way Bulge are formed.
4. The “high noon”, between 2 and 6 billion years of cosmic history ($1 < z < 3$), when galaxies build about 75% of their stellar mass as the star formation efficiency reaches a maximum about 3.5 Gyr after the Big Bang.

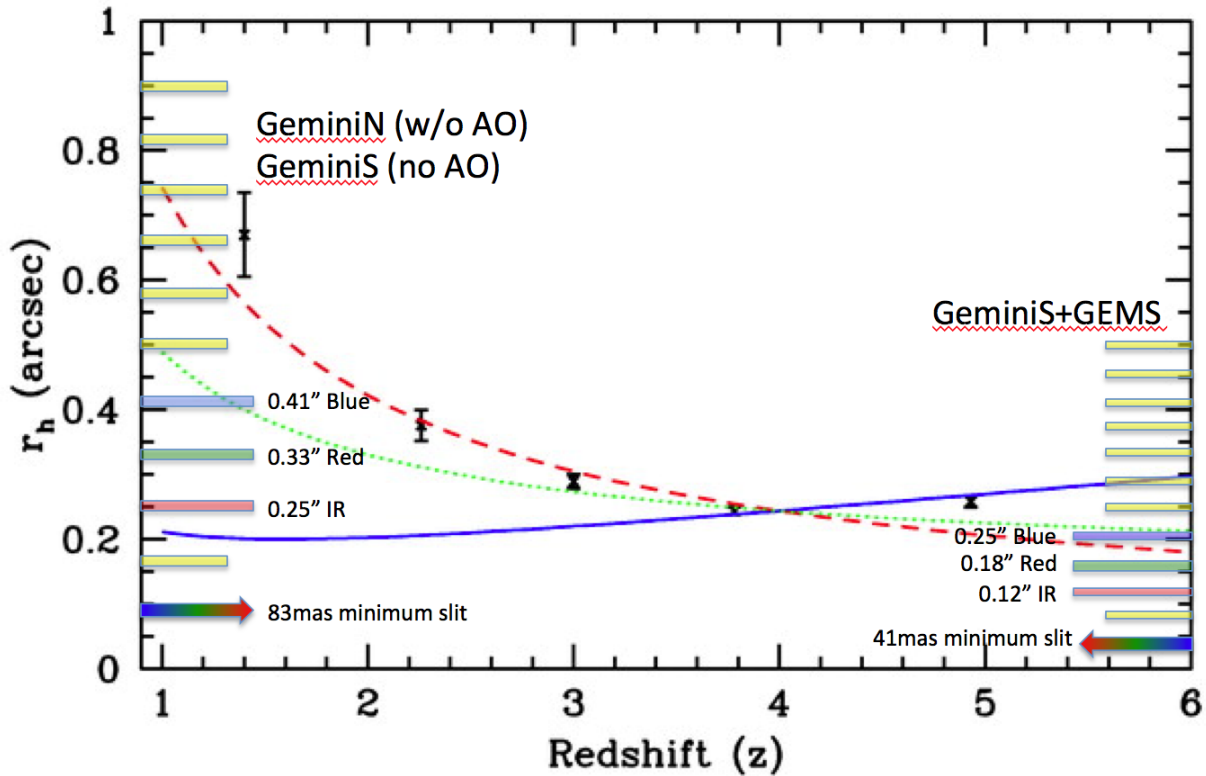


Figure 5: Size vs. redshift relation for Galaxies at $z > 1$ derived from the Hubble deep fields. The solid blue curve shows the expected trend in the WMAP cosmology if physical (proper) sizes do not evolve. The dashed red curve shows the trend if sizes evolve as $H^{-1}(z)$, and the dotted green curve shows $H^{-2/3}(z)$. The bars at the sides represent the slit sizes that GMOX can synthesize at $f/16$ (left) and at $f/32$ (right). The red, green and blue bars represent the nominal slits corresponding to a resolving power $R=5,000$. The colored arrows indicate the minimal slit width for the two configurations, (adapted from Ferguson et al. ApJ 600:L107-L110, 2004).

Because of cosmological redshift, these phases can be associated to different spectroscopic tracers of ionized hydrogen. This is indicated in Fig. 6, providing a visual guide to the following sections where we briefly examine each cosmic phase separately.

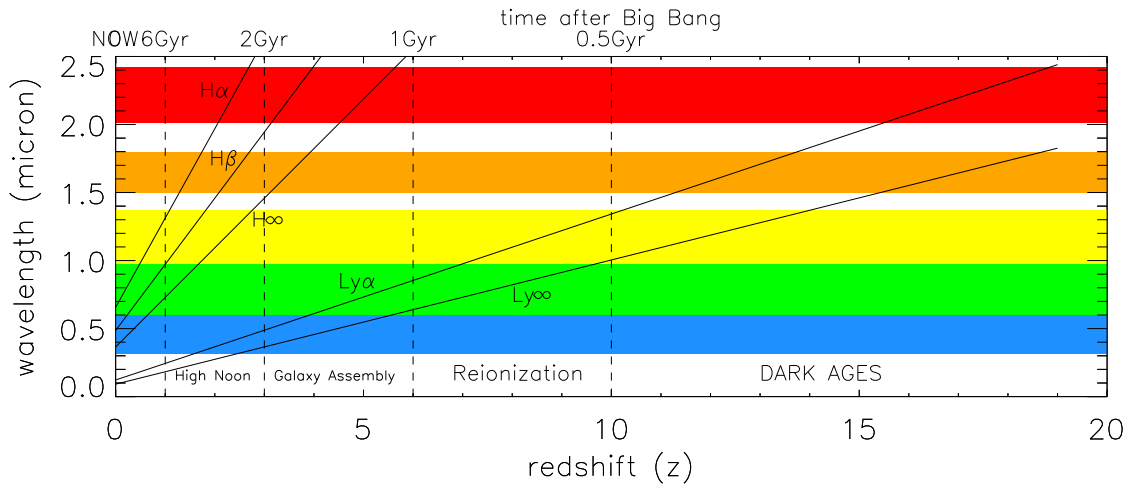


Figure 6: Illustration of how the main recombination lines of hydrogen scan the spectral range covered by GMOX as a function of cosmological redshift z . The colored bands refer to GMOX’s Blue arm (blue), Red arm (green), NIR arm-J channel (yellow), NIR arm-H channel (orange) and NIR arm-K channel (red).

C.4.1 DARK AGES AND POPULATION III OBJECTS

C.4.1.1 OPEN PROBLEMS

The “Dark Ages”, i.e. the time interval between cosmic recombination ($t \simeq 0.4$ Myr after the Big Bang, $z \simeq 1100$) and the beginning of reionization ($t \simeq 500$ Myr, $z \simeq 10$), is the ultimate frontier of observational astronomy. Models predict that following recombination, the first dark matter halos begin to form driven by the density fluctuations imprinted in the primordial Universe. These halos grow by accretion increasing their virial temperature while the expanding neutral Universe cools down. Eventually the environment becomes cool enough that H_2 can radiate, allowing density to increase, up to the appearance of the first Population III (Pop III) stars at $z \sim 20 - 50$. These pure H-He stars are likely very massive, and are obvious candidates for beginning the reionization of the Universe and the first metal enrichment. We don’t know when they formed, how many, their initial mass function, the clustering properties, the lifetime, the efficiency of production and escape of hard-UV photons. The first galaxy seeds may appear soon after the first stars, still at redshift $z > 10$. Finding these primordial objects, either as massive hypergiants, clusters or galaxy embryos, is a holy grail of present day astrophysics. Analyzing them is the main science driver of the James Webb Space Telescope.

At $z > 10$ the Universe is still opaque to $Ly\alpha$ radiation. Thus, the search for primordial objects has to be done using the Lyman-break technique beyond $\simeq 1 \mu m$, mostly with HST/WFC3-IR. Deep HST imaging in the F125W, F140W and F160W filters has provided so far only two candidates: the CLASH object in cluster MACS0647 [5] and the UDF j-39546284 object [6]. While the former appears to be multi-lensed and compatible with a geometrical solution for its $z \sim 10.8$ redshift and lens model, the second, initially found as a F125W

Key Questions:

- How did reionization occur? Was it a fast or a slow process?
- How patchy was the reionization process?
- How much did pop III stars contribute to reionization?

dropout, has been later classified as a F140W dropout [7], that would push it at $z \sim 11.7$. However, its relatively bright flux and the fact that it is marginally resolved by HST suggests that this system may actually be a strong line emitter at $z \sim 2 - 3$.

C.4.1.2 OBSERVATIONAL NEEDS

Extremely-high redshift objects are expected to be faint and rare, and therefore their search will probably remain a prerogative of JWST, with substantial investment of observing time. Predictions are model dependent, for example Robertson et al. [8] estimate that JWST/NIRCam may return 5 galaxy candidates at $z > 10$ over its ~ 10 arcmin² field. Projects like LSST, with the capability of reaching a shallower limiting depth $z \simeq 26.2$ mag can probe into the bright tail of this redshift range, providing a few hundreds of bright candidates ($M_{AB} \simeq 25$) across the sky. Spectroscopic confirmation will be needed to discriminate against low redshift sources, as samples of Lyman dropouts identified using broad near-IR filters have low- z interlopers caused by the Balmer/4000Å jump (cold stars and brown dwarfs may also be contaminants, depending on the filter set used).

Deep spectroscopic observation may require substantial investment of exposure time [27 hours have been used by the MUSE team on VLT to reach a limiting flux 1×10^{-19} erg s⁻¹ cm⁻² arcsec⁻², 9]. Detecting very-high redshift candidates discovered by JWST will require reaching $M_{AB} \simeq 28 - 29$ in the near-IR with SNR $\simeq 1$ per resolution element, in order to detect the Ly-break and the UV continuum after rebinning. Exposures requiring several nights, possibly with AO, would still be comparable to the amount of time effectively invested by JWST to discover the candidates in a combination of IR photometric bands. Multiplexing capabilities seem needed to justify those substantial investments of observing time. They would be extremely useful when high- z candidates are found near to the critical line of lensing foreground clusters, as in the case of MACS0647, as one can acquire wide-band spectra of hundreds of lensing and lensed galaxies, complementing JWST imaging and photometry at longer wavelengths. Reconstructing the full spectral energy distributions of all sources in the field of galaxy clusters adds enormous value to the deepest spectroscopic observations of individual sources at extreme redshifts (see also Section C.4.5 on galaxy clusters).

At near-IR wavelengths, spectral resolution $R \simeq 5,000(10,000)$ is needed to cover about 80% (90%) of the near-IR spectral range accessible from the ground without being impacted by strong sky emission lines. The spectra would confirm the presence of the Lyman break in the near-IR and the lack of lines in the blue continuum. While rest frames optical emission lines would be displaced at wavelengths longer than $\simeq 3 \mu\text{m}$, in the JWST regime, a spectral range including the K-band may allow detection of CIV $\lambda 1549$ at $z \lesssim 14.49$ and CIII] $\lambda 1909$ at $z \lesssim 11.6$, tracers of metal-enriched systems. Wide wavelength coverage is also vital to reject low- z contaminants through their [OIII] $\lambda 5007$ and H β $\lambda 4862$ emission (observable at $z \lesssim 3.8$ and $z \lesssim 3.9$ respectively). Another key observational tracer is the HeII $\lambda 1640$ line, a tracer of Pop III stars. With 10% of the strength of Ly α line, the detection of this line provides the strongest evidence in support of the evanescent (a few Myr) Pop III sources.

C.4.1.3 GMOX REQUIREMENTS

Parameter	Value	Justification
Bandpass	NIR	To observe UV and optical rest-frame lines of high- z candidates and remove low- z interlopers
Resolving Power	3000-5000	To remove telluric lines
Field of View	$\sim 1 \text{ arcmin}^2$	To observe whole lens-clusters when studying background high- z lensed candidates
Slit width	$\lesssim 0.3''$	To reduce background to reach faint objects
Multiplexing Capability	> 3 sources	To observe objects lensed multiple times
Observing Efficiency	Simultaneous coverage of the NIR bands	To maximize the outcome of very long exposures necessary to follow-up high redshift candidates

Table 3: Summary of requirements for case C.4.1

C.4.2 REIONIZATION AND EARLY GALAXY FORMATION

C.4.2.1 OPEN PROBLEMS

As the Universe expands, the fraction of ionized atoms increases due to the Lyman continuum photons of primordial sources. This process is controlled by a few key parameters: the star formation rate density, ρ_{SFR} [$M_{\odot} \text{ yr}^{-1} \text{ Mpc}^{-3}$], the rate of ionizing photons produced per unit mass ξ_{ion} [$\text{s}^{-1} M_{\odot}^{-1}$], and the fraction of those photons that escape to ionize the neutral intergalactic medium, f_{esc} . The product of these three values determines the fraction of ionized hydrogen in the Universe.

The estimate of ρ_{SFR} relies on the luminosity functions of galaxies observed at high redshifts, either in their rest-frame UV or IR, extrapolated beyond our current sensitivity levels. The fact that the visibility of the Ly α line drops significantly beyond redshift $z = 6$ indicates that at that redshift, about 1 Gyr after the Big Bang, reionization is nearly complete. The problem is to explore beyond this limit to understand how reionization occurred.

At redshift $z < 10$ the Ly-break enters the visible range while Ly α shifts to the J-band (Fig. 6). Ground-based facilities therefore start to play a major role, complementary to HST and Spitzer, and, in the future JWST. So far, more than 1000 candidates have been found using HST data (Fig. 8), but only 20 galaxies have been spectroscopically confirmed at $z > 6.5$ [with the record holder being at $z = 8.7$, 10] almost exclusively on the basis of the presence of Ly α emission at $\lambda \sim 1.1 \mu\text{m}$. Using MOSFIRE at Keck-1 with $0.7''$ slits and a dispersion of $\simeq 1.2 \text{ \AA pix}^{-1}$, [11] could not detect Ly α emission in any candidate at $z \sim 7 - 9$ down to median limiting fluxes of $0.4 - 0.6 \times 10^{-17} \text{ erg s}^{-1} \text{ cm}^{-2}$ (5σ), whereas a few detections would have been expected if the distribution of Ly α emission had been the same as at ~ 6 . High redshift galaxies are elusive. The scarcity of $z \sim 8$ galaxies suggests either a dramatic increase in Ly α optical depth or that the number of star forming galaxy increases rapidly at redshift ~ 7 .

Measures of the Thomson optical depth τ from Planck LFI polarization data, together with lensing and high-multipole temperature data, imply a reionization optical depth $\tau = 0.066 \pm 0.012$. This suggests that faint, star-forming galaxies are the main sources driving the reionization of the Universe, making reionization a quick process, with the Universe passing from 20% to 90% of ionized hydrogen in the 400 Myr between $6 < z < 9$ [8].

In this “late” scenario, Pop III stars may continue to form down to relatively low redshifts in isolated pockets of primordial gas, [12]. Source CR7 of Sobral et al. [13] is a Ly α emitter at redshift of $z = 6.604$ presenting only a narrow HeII $\lambda 1640$ emission line (no other lines detected) in its X-shooter spectrum, which covers the spectral range from the U to the K band. HST/WFC3 observations show that CR7 is indeed spatially separated between a very blue component, coincident with the Ly α and He II emission, and two red components ($\sim 5 \text{ kpc}$ away), which dominate the mass. These findings are consistent with theoretical predictions of a Pop III wave, with Pop III star formation migrating away from the original sites of star formation (Fig. 7). Finding Pop III systems may eventually be not too hard: we just need to look at redshift $6 < z < 10$!

While a number of observations favors a relatively late end to reionization ($z \sim 6 - 7$), the constraints are still quite weak. For example, the number density of star-forming galaxies at $z > 6$

Key Questions:

- When was the inter galactic medium reionized?
- What are the main contributors to reionization?
- How did feedback processes shape the first galaxies and their circum-galactic environments?

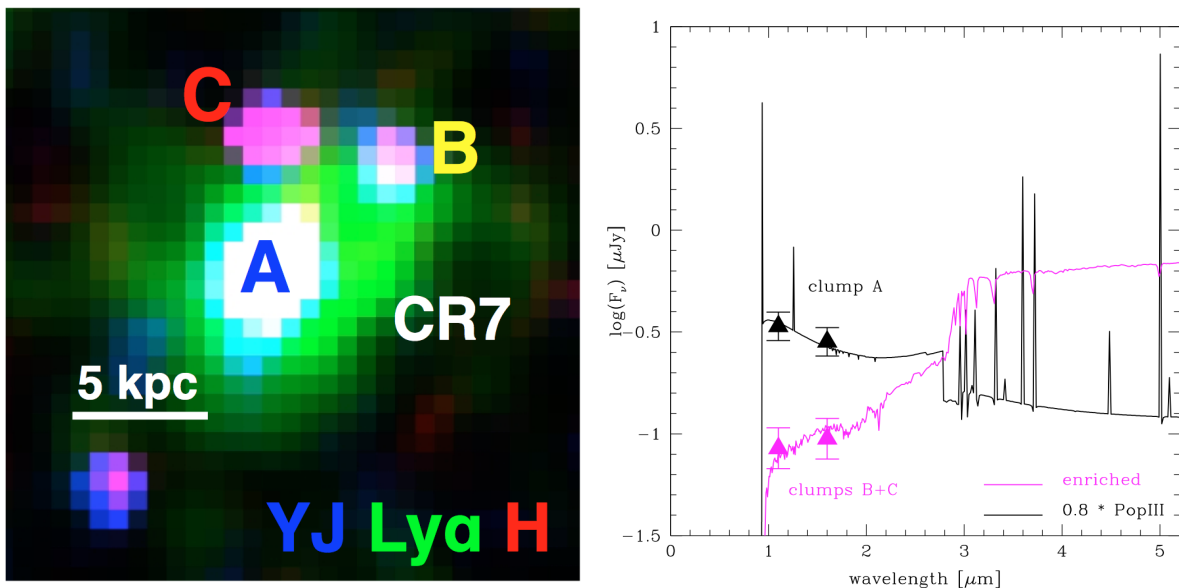


Figure 7: Left: reproduction of Fig.7 of Sobral et al. [13]; a false color composite of CR7 using NB921/Suprime-cam imaging ($\text{Ly}\alpha$) and two HST/WFC3 filters: F110W (YJ) and F160W (H). Component A dominates the $\text{Ly}\alpha$ emission and the rest-frame UV light, whereas the (likely) scattered $\text{Ly}\alpha$ emission seems to extend all the way to B and part of C. Right: reproduction of Fig.8 of Sobral et al. [13]; HST imaging in YJ and H allows one to model the resolved CR7 components with two very different stellar populations. While clump A is very blue and dominates the rest-frame UV flux, B+C are red and likely dominate the rest-frame optical and the mass. GMOX is designed to spectroscopically confirm this type of results.

appears to be uncomfortably low to produce the required number of ionizing photons unless the escape fraction of these photons is considerably higher than observed in galaxies at lower redshifts; on the other hand, faint galaxies could conceivably produce enough ionizing photons to complete reionization much earlier. Electron scattering optical depth measurements from Planck are consistent with late reionization, but these have large error bars. The declining fraction of galaxies that show $\text{Ly}\alpha$ in emission at $z > 6$ can be interpreted as evidence for scattering by neutral gas in the IGM; on the other hand, the sizes of the $\text{Ly}\alpha$ halos around these galaxies may simply be increasing with redshift, leading to slit losses and non-detections. A complementary approach to the study of reionization requires studying the intergalactic medium (IGM) to determine when and how it became reionized.

Quasar (QSO) spectra provide detailed information about the physical conditions of the IGM, and therefore play a central role in reionization studies. The structure of the $\text{Ly}\alpha$ forest generally confirms that reionization was largely completed by $z \sim 6$, although the final stages may extend to $z \sim 5$ [14, 15]. Damping wing absorption in the spectra of the first $z \sim 7$ QSO, ULAS J1120+0641, also appears to favor a significantly neutral IGM [16, 17], and hence a late end to reionization; however, it is only one object, and the damping absorption is subtle and difficult to measure.

At the same time, studies of QSO absorption lines can shed light on the formation of the first galaxies, constraining the effect of feedback processes at early cosmic times. The first attempts to study early metal enrichment and feedback at $z > 6$ have been made with optical and near-IR spectrographs such as X-shooter. These have demonstrated that metals are present in significant quantities at these redshifts, although in far less abundance than seen at later times. Current observations of metal absorbers traced by lines such as CIV, CII, OI, and MgII suggest a buildup of metals in the circum-galactic media of galaxies during the reionization epoch though from galac-

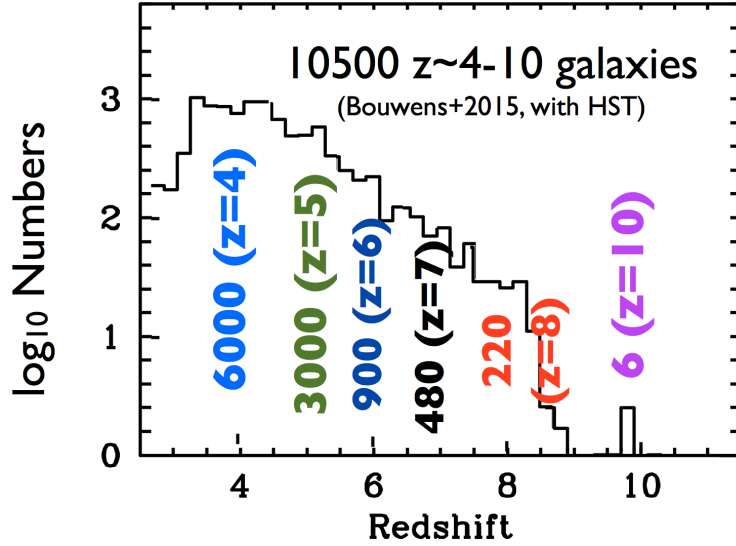


Figure 8: Number of galaxies per redshift bin identified using deep HST imaging surveys.

tic winds, i.e., feedback processes that are critical for shaping these early galaxies. The current statistics are still fairly sparse, however, and it is not yet clear how rapidly the metals accumulate, or what population of galaxies they trace.

Finally, observations of the CIV $\lambda 1549$ and MgII $\lambda 2798$ broad emission lines (redshifted in the NIR for QSOs at $z \sim 7$, place critical constraints on the mass of the black holes harbored in these powerful sources. Recent studies on the highest- z QSOs have shown that black holes with masses of $10^9 M_{\odot}$ are already in place when the Universe is less than 0.8 Gyr old [e.g., 16, 18, 19]. These findings pose serious issues on black hole seeds formation models. However, these results are based on the study of the brightest and highly accreting objects, and are most probable not representative of the whole QSO population.

Increasing the number of known QSOs at $z > 6$ (there are ~ 70 QSOs known at $z \gtrsim 5.7$) would greatly improve our understanding of reionization and early galaxy assembly. We may have only probed “the tip of the iceberg” of the high- z QSO population, the bright, rare end of a more common, fainter population. This situation is set to change over the next several years as new quasars over $6 < z < 9$ will be discovered by DES, VISTA, LSST, WFIRST, and other survey facilities.

C.4.2.2 OBSERVATIONAL NEEDS

So far, the analysis of spectral properties of distant galaxies has almost exclusively relied on SED fits to the HST photometry in the near-IR. Spectroscopy is needed to access the slope of the continuum: the UV galaxy luminosity has a spectral slope parameterized by $f_{\lambda} \propto \lambda^{-\beta}$. Typically, $\beta \simeq 2$ for star forming galaxies [20], and the spectrum is bluer, $\beta \sim 3$, for dust-free and primordial stellar populations, with some dependence on the initial mass function and the star formation history used to compute the spectral energy distribution.

There are also several key physical diagnostics of star formation and gas dynamics that are available in the rest-frame UV (e.g., Ly α , CIV, OVI,...) and that affect photometric analysis. Disentangling the effects of dust extinction from the contribution of emission lines to the underlying continuum is at the moment extremely difficult, given the uncertainties on the metallicity of these

early systems. Spectroscopy is needed to enable calibration corrections for the emission line fluxes as a function of redshift, improving both the stellar mass estimates and the characterization of how metallicity evolves with redshift. Spectroscopy is also essential to break the degeneracy in the SED fitting between massive/passive galaxies and star forming galaxies with strong emission lines, as both types tend to present similar signatures in broad-band photometry.

As we have seen in the previous section, spectroscopic follow up of high redshift QSOs provides a formidable tool for analyzing the structure of the Universe at these early cosmic times. Study of the IGM through QSO absorption lines requires sensitive ($\text{SNR} > 10$, and preferably > 20), moderate to high-resolution optical and near-IR spectra of larger samples of $z > 6$ QSOs than are currently available.

For reionization studies, the key observable is the strength and shape of the $\text{Ly}\alpha$ emission line. At $z > 7$ this requires near-IR spectra – primarily Y+J, but H and K are also critical for modeling the intrinsic, unabsorbed spectrum. Resolution of $R \sim 2000$ is sufficient, but $R > 4000$ is preferable for resolving discrete $\text{Ly}\alpha$ absorption lines in the QSO near zones, which affect the profile of the QSO $\text{Ly}\alpha$ emission. A sample size of $\sim 10 - 20$ QSOs at $z > 7$ would be excellent, which is in line with expectations from current NIR sky-surveys such as VISTA VHS. As discussed below, AO would be a major benefit for accessing faint targets, although smaller samples could be obtained in seeing-limited conditions.

Intervening metal absorption lines are intrinsically narrow, and so higher resolution is needed ($R > 4000$) to study metal enrichment of the IGM. High SNR is also needed to detect weak lines ($\text{SNR} > 20$). At $z > 6$, the lines of interest fall over observed wavelengths of $\lambda = 9000 \text{ \AA}$ up through K band, so having optical + IR coverage is optimal. Current samples meeting these criteria in the near-IR are restricted to 6-7 objects at $z \sim 6$; an increase to 20+ objects is therefore needed. Extending to redshifts $z \geq 7$ is also a high priority. Due to the resolution and SNR requirements, particularly for fainter targets, AO would be a major asset for the suppression of the sky background and to minimize the impact of read noise and dark current (i.e., minimize the footprint of the spectral trace).

In both cases, a southern location would be superior in order to follow up new high- z QSOs discovered in optical+IR sky surveys such as DES+VISTA, Pan-STARRS, and LSST, which are predominantly southern or equatorial. On longer term, targets will come from Euclid (all sky) and WFIRST (High Latitude Survey potentially in the south).

C.4.2.3 GMOX REQUIREMENTS

If Pop III objects can be found at lower redshift, a spectrograph with wide-band spectral coverage and high throughput at intermediate resolution is essential. The case of sources CR7 of Sobral et al. [13] is emblematic: they used X-shooter, SINFONI and FORS2 at VLT, and DEIMOS at Keck, together with the original discovery images of the HST. Very wide band spectroscopy with VLT/X-shooter, from U to K, has been necessary to search for the presence of any emission lines other than $\text{Ly}\alpha$ and the $\text{He II}\lambda 1646$ line associated to Pop III stars. X-shooter, on the other hand, has been incapable of **spatially resolving** the individual components of this source: high spatial resolution is therefore the logical requirement to make a step forward.

To analyze the UV slope, reaching the line-free continuum level of high-redshift galaxies in the near-IR, one has to use spectral resolution $R \gtrsim 3000$ to work between the OH lines. High throughput and the capability of synthesizing narrow slits are also required to boost sensitivity if AO are available. Study of the $\text{Ly}\alpha$ forest requires relatively high spectral resolution to disentangle metal lines, pushing again for spectroscopy with AO support to minimize losses and reach fainter sources. Field coverage of the order of a few arcmin is needed to map the $\text{Ly}\alpha$ absorption toward

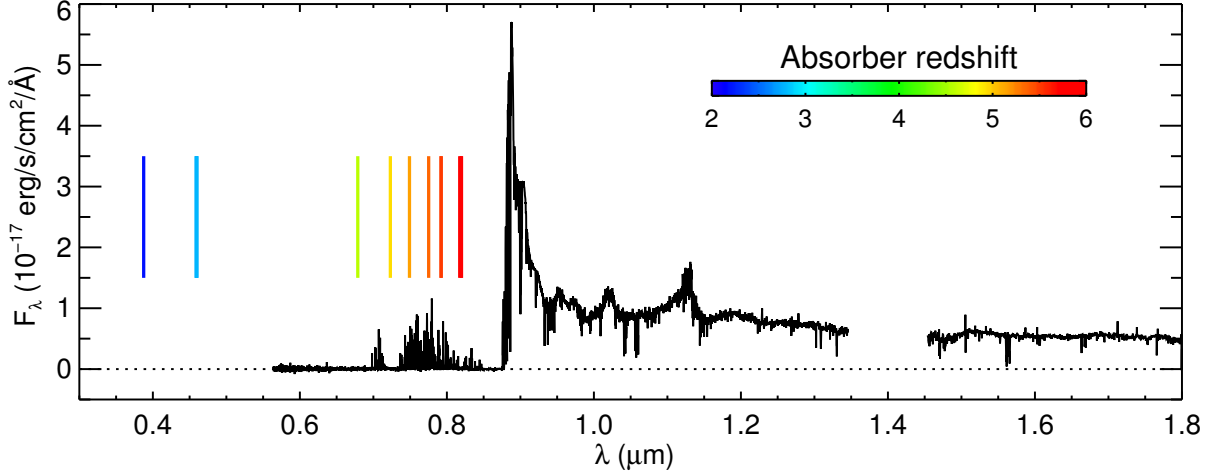


Figure 9: VLT/X-shooter spectrum of a quasar at $z = 6.3$. The Lyman- α forest is visible at $\lambda < 0.9 \mu\text{m}$, while metal absorption lines can be seen out into the near infrared. Wavelengths for Lyman- α at the redshifts of these absorbers, potentially corresponding to galaxies along the line of sight, are marked with vertical ticks.

lensed objects on scales the order of 1 Mpc (comoving). Multi-object capability is again needed to justify long exposure times on faint sources, noting that cosmic variance becomes stronger at high redshift, increasing both the local source density and the need to sample multiple regions. As GMOX can provide a very precise estimate of the distance of hundred of sources in a field, it may enable one to trace the high frequency structure of the early Universe, clarifying where the first galaxies formed within the clumps of cosmic-web.

GMOX has the potential to be transformative in the study of high- z QSOs, particularly if assisted by AO. Suppressing the sky background and minimizing the trace width on the detector will make it possible to obtain high-quality optical+NIR spectra of fainter objects than is currently possible with facilities such as VLT/X-shooter or Magellan/FIRE, hence enabling significantly larger samples to be obtained. The Vista VHS survey expects to uncover new QSOs at $z = 6 - 8$ down to $Y_{\text{AB}} = 21$. In AO mode it will be possible to obtain $\text{SNR} = 10$ spectra for such objects in 1.5 hours of exposure, and $\text{SNR} = 20$ in 5 hours. At $R \sim 5000$, GMOX will have sufficient resolution to study the IGM using the Ly α forest, as well as probe the environments of intervening galaxies through their metal absorption signatures.

High throughput and the ability to suppress sky emission using narrow slits and AO will boost sensitivity, allowing one to obtain high-quality spectra of quasars out to $z \sim 8 - 9$, even as their Ly α emission shifts into the infrared. Multiply lensed QSOs can thus be used to probe the spatial structure and correlation of the Ly α clouds, with their filamentary structure, providing unique insights into the growth of cosmic structures.

Parameter	Value	Justification
Bandpass	Y to K	To detect Ly α and metal lines (restframe UV) for $z \sim 7$ sources (YJ). To characterize their continuum slope (H+K). To observe HeII $\lambda 1646$ for Pop III stars.
Resolving Power	5000	To resolve Ly α absorbers, detecting weak lines between OH lines
Slit width	$\sim 0.2''$	AO-assisted to boost SNR of the faint high- z sources
Multiplexing Capability		
Observing Efficiency	simultaneous coverage of the NIR bands	To maximize the outcome of very long exposures necessary to follow-up high redshift candidates

Table 4: Summary of requirements for case [c.4.2](#)

C.4.3 GALAXY BUILDING EPOCH

C.4.3.1 OPEN PROBLEMS

Between $3 < z < 6$, in the second billion year of cosmic history, galaxies begin to take shape increasing their stellar mass significantly through minor and major mergers, and gas accretion. This rapid process is accompanied by a substantial increase in heavy elements abundances. For the majority of galaxies, the star formation rate is proportional to the stellar mass of the galaxy. Also, the star formation rate surface density is proportional to the gas surface density (the Schmidt-Kennicutt law). This relation has a slope γ connected to the underlying physics of the scaling between star formation and cold gas. However, the Schmidt-Kennicutt Law does not appear to be “scalable” at all gas surface densities. In particular, at low gas surface densities, the SFR seems to change more rapidly than at high gas surface densities. This non-linear dependence suggests that star formation may have different modes, depending on the stellar mass, the environment, and on the accretion history of the galaxy (see also Sect. C.5.1).

Λ CDM models show that mergers of small satellites into larger galaxies is one of the main mechanisms of the hierarchical galaxy assembly. This is supported by the direct observations of fossil tidal features in galaxy groups: streams, tails, and bridges trace interactions that may have occurred several Gyr earlier. Understanding the formation and erasure of structures during the build-up epoch, the efficiency of cluster formation and the link between clusters and stellar mass functions requires spectroscopic observations of resolved galaxies at redshifts $z > 3$.

Key Questions:

- Are there different modes of star formation through cosmic history, depending on the environment?

C.4.3.2 OBSERVATIONAL NEEDS

Observationally, at $z \sim 4$ the Balmer/4000Å break enters the K-band while the Lyman break swings the visible portion of the spectrum, allowing one to identify thousand of galaxies [21, 22, 23, 24]. Observing the features at UV and optical rest-frame wavelengths, one can select star-forming galaxies providing direct information on their most recent episodes of star formation. To assess the contribution of older stars, one has to move beyond $2\mu\text{m}$, to observe at near-infrared rest-frame wavelengths. While JWST will provide observations of such galaxies at long wavelengths, optical spectroscopy from the ground will be able trace their star formation rates in the last 100Myr, resolving localized starbursts. We expect that deep imaging of JWST/NIRCam will help to discover thousands of sources in this redshift range, calling for substantial parallel spectroscopic followup to derive precise redshifts and characterize the star formation activity, while eliminating low redshift interlopers.

C.4.3.3 GMOX REQUIREMENTS

The high density of sources in this redshift range is ideal for multi-object spectroscopy. GMOX must be able to cover deep fields of several arcmin² in a reasonable amount of time to match JWST/NIRcam search areas. This critical redshift range requires access to the full wavelength range, from the UV to the near infrared. GMOX must provide such a spectral range, covering from the U-band (where the Ly- α line becomes accessible at $z \sim 3$) to the K-band (where the [OII]

$\lambda 3727$ line, which is a tracer of star formation, is observable up to $z \sim 6$) in order to trace with continuity the evolution of star formation over the full redshift range. Resolution $R > 3,000$ provides accurate spectroscopic redshifts and assesses the contribution of line emission to the photometric fluxes for different classes of objects. Reaching the line-free continuum level of high redshift galaxies requires spectral resolution $R \gtrsim 4000$ to work between the OH lines. High throughput and the capability to synthesize narrow slits are also required to boost sensitivity. Study of the Ly α forest requires relatively high spectral resolution to disentangle metal lines.

Parameter	Value	Justification
Bandpass	U-to-K	To bracket the rest-frame spectra between the Lyman and Balmer break
Resolving Power	> 3000	To derive spectroscopic redshifts
	> 5000	To study Ly α forest To assess the contribution of line emission to the photometric fluxes for different classes of objects
Field of View	$\gtrsim 1 \text{ arcmin}^2$	To map the Ly α absorption toward lensed objects on scales of the order of 1 Mpc (comoving)
Slit width	$\lesssim 0.4(\text{UVIS})-0.25(\text{IR})$	To boost sensitivity, possibly with AO
Multiplexing Capability	10 – 50 targets/arcmin ²	High density of targets

Table 5: Summary of requirements for case C.4.3

C.4.4 “HIGH NOON” OF COSMIC HISTORY

Between $1 < z < 3$ galaxies experience a “growth spurt”, as the rate of mass buildup and AGN activity reaches its peak [25, 26]. To understand this phase of cosmic history we need to assess the spectral energy distribution of galaxies, not just as a whole, but spatially resolving their sub-structures. Since galaxies are not homogeneous, it is critically important to discriminate between stellar populations of different ages, their contribution to the mass of the galaxies, the history of star formation, and the dust properties within the galaxies.

C.4.4.1 OBSERVATIONAL NEEDS

The star formation rate can be traced by emission lines like $H\alpha$ and $[OII] \lambda 3727$ and by the rest-frame UV emission. Stellar masses can be derived by fitting the stellar continuum with spectral energy distribution models. From these synthetic spectra one can build a grid of observed stellar mass-to-light ratios as a function of $D(4000)$ (i.e. the ratio of the flux density at $3850,3950\text{\AA}$ to the flux density at $4000,4100\text{\AA}$; [27]), and the $H\delta$ absorption feature [28]. Having full access to different star formation rate indicators, consistently calibrated across a wide range of redshifts, would allow us to robustly derive how star formation changes within the galaxies.

Minor mergers can provide a significant increase in galaxy size without a substantial stellar mass increase, leaving a well defined compact core of older star [e.g. 29]; vice-versa, adiabatic expansion powered by large-scale mass loss such as AGN feedback [e.g. 30] can generate an expansion of the total stellar light profile. Discriminating between these two scenarios requires extreme AO to resolve galaxies bulges from disks, large field of view to compare several galaxies in a cluster and wide spectral coverage to map rest-frame indicators of stellar mass, age and star formation activity up to $z \sim 2$ (see contribution of S. Sweet at the 2015 Gemini Science Meeting).

Key Questions:

- What are the main drivers of the enhanced star formation activity?
- Why does star formation stop early in certain galaxies (“quenching”) without later resuming?
- Where are the low-mass galaxies predicted by Λ CDM models?
- What are the relations between star formation and AGNs?

At even lower redshifts, the capability of taking wide-band spectra with high spectral and spatial resolution allows one to probe the origin and kinematics of stellar populations in normal, starburst, interacting, and active galaxies. A $\simeq 0.1''$ resolving power can probe scales of $\sim 50\text{pc}$ at the distance of Coma cluster. Enabling massive spectroscopy of resolved stellar populations in the nearest galaxies will revolutionize our understanding of stellar populations and probe the relationship between super massive black holes and their host galaxy.

C.4.4.2 GMOX REQUIREMENTS

Moderate spectral resolution ($R \sim 4000$) is needed to resolve broad emission lines associated with central AGN activity (e.g. $H\alpha$, $H\beta$, CIV and MgII). The width of these broad emission lines combined with a measurement of the AGN continuum monochromatic luminosity can be used to estimate the mass of the powering black hole through scaling relations [e.g., 31]. Wide spectral coverage would allow one to track black-hole accretion and AGN activity throughout cosmic time. An instrument with such characteristics would be the perfect instrument to investigate the existing relation (if any) between AGN activity and galactic star formation.

Wide spectral coverage and $R \sim 4000$ from the UV to the near IR is needed to measure the intensity of nebular emission lines (e.g., [O II] $\lambda\lambda 3727, 3730$, H β , [O III] $\lambda\lambda 4960, 5007$, H α , [NII] $\lambda\lambda 6548, 6584$, and [SII] $\lambda\lambda 6717, 6731$), stellar continuum, and absorption features (e.g., Balmer lines, CaII H and K, Mgb) as galaxies evolve over this redshift range. Resolution of a few thousand allows resolving Hydrogen emission lines to measure star formation rate and Balmer decrement (H α /H β), which provides a direct measurement of dust attenuation. These can be analyzed to yield dynamical information on the evolution of the disks, giving new insights into the inflow of material onto galaxies and the processes controlling star-formation in galaxies.

The on-sky density of targets requires a multi-slit spectrograph. High spatial resolution is needed targeting single regions of enhanced star formation, measuring spectral variations across individual galaxies.

Resolving power $R \simeq 5000$ (60 Km/s nominal) corresponds to a few km/s when the spectra are cross correlated. With such velocity resolution, it will be possible to probe into the properties and kinematics of galactic companions, constraining the frequency of satellite accretion and their relevance in the build up in the galaxy size and stellar mass.

Parameter	Value	Justification
Bandpass	U-to-K	To study nebular emission at restframe optical
Resolving Power	$R > 2000$	To resolve H α -[NII] doublet
		To measure Star Formation Rate
		To measure Balmer decrement
Field of View	$R4000-5000$	To probe kinematics of components
	$\gtrsim 1$ arcmin ²	To measure AGN activity
Slit width	$\lesssim 0.4(\text{UVIS})-0.25(\text{IR})$	To map galaxies and their satellites
Multiplexing Capability	> 100 targets/arcmin ²	To resolve individual components
		To measure spatial variations across galaxies

Table 6: Summary of requirements for case [C.4.4](#)

C.4.5 CLUSTERS OF GALAXIES

C.4.5.1 OPEN PROBLEMS

Rich clusters of galaxies offer a unique opportunity to study the assembly and dynamics of the largest over-densities in the Universe, the impact of these environments on galaxy evolution, and the evolution of the background lensed galaxies. Detailed maps of the cluster galaxy dynamics can place additional constraints on the cluster dark matter profile, and help distinguish between recently accreted galaxies (which may be undergoing ram-pressure stripping, harassment, and triggered star-formation, [32, 33, 34]) and cluster relics (which may have assembled at $z > 1$ via multiple gas-poor mergers, [35, 36]). Mapping the outskirts of clusters will probe the large-scale filaments feeding the over-densities, and the evolution of galaxies in those filaments [37].

C.4.5.2 OBSERVATIONAL NEEDS

The HST CLASH survey [38] and Frontier Fields [39] have provided us with high angular resolution imaging of rich clusters at $z \gtrsim 0.3 - 0.6$. Cluster galaxies at these redshifts have many rest-frame optical spectroscopic tracers, including [OII]3727, Ca H+K 4000 Åbreak, $H\beta/[OIII]5007$, Mg b, NaI, [OI]6300, $H\alpha$, [NII], and [SiII]. By probing these features with $\sim 0.25''$ resolution, we can trace the chemical abundances of stars and gas, as well as central AGN activity, gas ionization, and star-formation rates on $\sim 1 - 3$ kpc scales for L^* and brighter galaxies. In the core of the Frontier Fields cluster Abell 2744 at $z = 0.308$, we find ~ 150 galaxies with $I < 22$ mag within the HST ACS field of view ($\sim 3.4' \times 3.4'$), [40]. High multiplexing capability over a comparable field of view is needed in order to be able to study all the cluster members.

Deep observations of strong-lensing clusters, such as the Frontier Fields, can also probe highly magnified galaxies beyond $z \sim 1$. Abell 2744 has ~ 10 $0.3 < z < 1.5$ background galaxies magnified to $I \sim 20 - 22$ mag, and other ~ 15 magnified to $I \sim 22 - 23$ mag. Spectroscopic z of these sources are powerful constraints on the lensing maps; moreover, their high magnifications (factors of $2 - 20$) allow detailed spectroscopic studies of galaxies at higher spatial resolution, fainter than those typically probed by blank field studies. [4] report the discovery of a $z = 4.92$ lensed galaxy in Abell 1703 magnified 25 times by cluster lensing: this means that GMOX at GEMS could probe structures as small as $\simeq 20$ pc when the Universe was 1 Gyr old!

Building [OII]3727 maps of $z \sim 1$ galaxies magnified by a factor of 3 would yield star-formation and kinematic maps on kpc scales. Deep “blind” observations of the cluster critical curves – regions of highest magnification – could potentially yield detections of intrinsically faint high-equivalent-width ($\gg 100$ Å) $Ly\alpha$ emitters at $z \gtrsim 3.5$ [41]. Although these detections will be rare, they will place important constraints on the $Ly - \alpha$ escape fractions of faint galaxies similar to those responsible for reionization.

Key Questions:

- How do galaxies form, evolve, and interact in clusters?
- What are the details of the dark matter distribution in galaxy clusters?

C.4.5.3 GMOX REQUIREMENTS

Deep spectra with resolution $R > 3000$ over a wide spectral range is needed to measure the redshift of both lensing and lensed objects. Multi-object capability ($\gtrsim 200$ sources) in fields of the

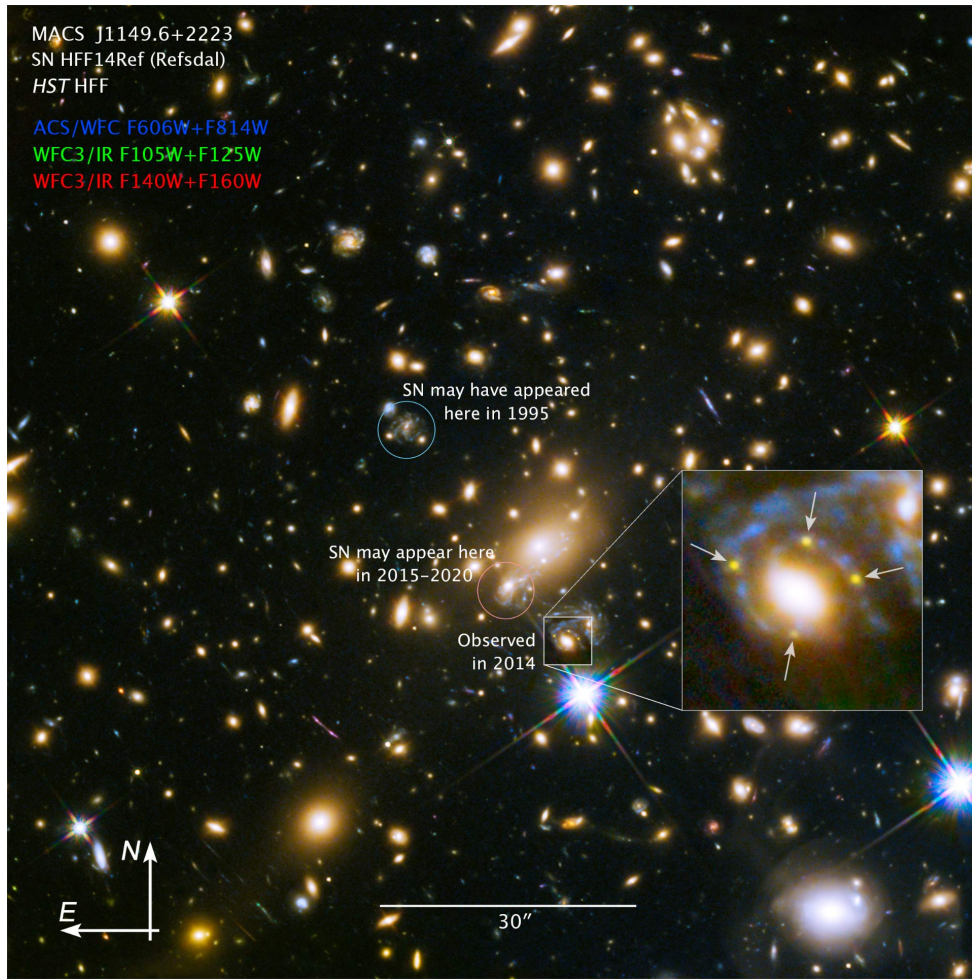


Figure 10: HST image of the galaxy cluster MACS J1149+2223 with an enlargement of the $z=0.54$ elliptical galaxy producing an Einstein cross of a $z=1.49$ supernova. The intensity of the 4 images is amplified by a factor $\simeq 20$ while the separation is about $2''$. Resolving Einstein crosses of this type is a requirement for GMOX.

order of an arcminute is needed to produce accurate dark matter maps. High spatial resolution (~ 100 mas) enables the study of lensed objects' structure.

Parameter	Value	Justification
Bandpass	U to K	Observation of UV and optical rest-frame lines up to $z \sim 0.6$
Resolving Power	> 3000	Redshift and chemical abundances
Field of View	$\sim 1 \text{ arcmin}^2$	Match the typical galaxy cluster size
Slit width	$\sim 0.2''$	Resolve structures in lenses objects
Multiplexing Capability	$\sim 100 \text{ targets/arcmin}^2$	Obtain spectra of each galaxy in the clusters

Table 7: Summary of requirements for case [c.4.5](#)

C.5 COSMIC HISTORY: 10 GYR OF DECLINE

Approximately 3.5 Gyr after the Big Bang, at $z \simeq 1.9$ the cosmic star-formation rate started to decline exponentially, with an e-folding timescale of 3.9 Gyr [42]; the Sun formed during this epoch, about 4.5 Gyr ago ($z = 0.44$), from the ashes of generations of more massive stars that had fully evolved through the previous 8 Gyr of cosmic history.

C.5.1 GALACTIC-SCALE STAR FORMATION

C.5.1.1 OPEN PROBLEMS

Star formation, the main process shaping galaxies from the cosmic dawn to present times, is *better described than understood* [43]. The missing link is the connection between the small scale of the single proto-star (~ 0.1 pc) and the large scale of extended star-forming structures and molecular complexes (several kpc). Galactic-scale star formation occurs in hierarchical structures of which bound star clusters occupy the densest peaks [44]. Star clusters can survive for even a Hubble time, as globular clusters, and provide a fossil record of the ancient star formation. The youngest massive clusters are easily detected to up to ~ 100 Mpc, and provide excellent tracers of current star formation. Hence, understanding cluster formation can provide a path for unraveling the physics of galactic-scale star formation, what regulates it, and its links to the properties and structures of the host galaxy.

Young star clusters (YSCs), i.e. bound or semi-bound systems younger than ~ 100 Myr, are excellent tracers of recent star formation in all galaxies, and many of their properties have been studied over the past 10-15 years [see e.g. 45, and references therein]; however a number of open questions remains. The reason why super-star-clusters, i.e. $\sim 10^6 M_{\odot}$ clusters, form in starburst galaxies (even dwarf ones) and mergers, but not in large spirals, remains a mystery, although the process is likely linked to ISM pressure and density [e.g. 46]. The cluster formation efficiency, i.e., the number of clusters formed per unit of star formation, appears to be a decreasing function of the star formation rate (SFR) surface density Σ_{SFR} , both locally and globally [45, Figure 1], but available data are scant in the key range of very high and very low Σ_{SFR} , where models and predictions can be discriminated [47]. Adding to the uncertainties in the fact that most of the properties of YSCs are derived under the assumption of a universal stellar Initial Mass Function (IMF), both at the low and high end, but evidence in this sense is contradictory [48, 49, 50, 51]

Key Questions:

- What are the connections between host galaxy properties, star formation rate density and cluster formation, evolution and disruption?
- What are the environmental dependencies of the upper end of the IMF?

The process of cluster disruption is also under hot debate. Two models have been put forward to explain the decline in number of bound clusters with age: mass independent disruption [MID, 52] stating that the disruption timescale does not depend on mass and environment and that the number of clusters decreases with time simply following a t^{-1} relation, and mass dependent disruption [MDD, 53] stating that the disruption of clusters depends on the initial mass of the cluster as well as on the environment of the cluster in the galaxy.

Another fundamental question that has not yet been definitively addressed is related to the presence or not of an upper-mass truncation in the young star cluster mass function. Such a

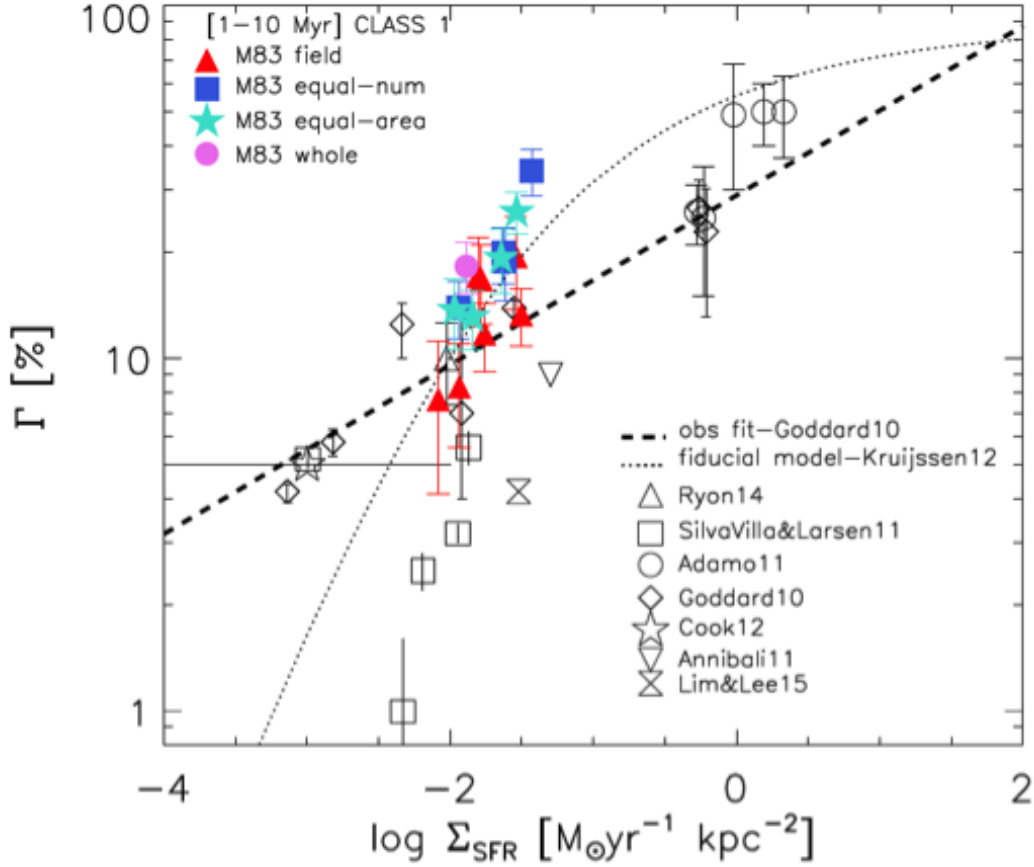


Figure 11: Left: The cluster formation efficiency Γ , i.e., the ratio of cluster formation rate to the star formation rate, as a function of the SFR surface density Σ_{SFR} , for galaxies and galactic regions [45, from]. Only clusters younger than 10 Myr are included. The low and high Σ_{SFR} regions of the plot are not well defined by current data due to the difficulty of accessing this portions of the parameter space: the low end Σ_{SFR} is populated by dwarf galaxies, which require sensitive instruments, and the high end is populated by starburst galaxies, which are rare.

truncation is present in globular cluster populations and seems to be related to the galaxy where the population has formed [54]. However the results of the cluster mass function analysis of young star cluster populations in local galaxies are still contradictory [55, 56].

c.5.1.2 OBSERVATIONAL NEEDS

Many key questions related to the formation and evolution of young star clusters have not yet been answered because of the limited information we can access with imaging data. Conditions for the formation of super star clusters, cluster formation efficiency, and the IMF are best investigated in the youngest among the YSCs, i.e. those that are younger than ~ 10 Myr. This is because the youngest among the clusters are still closely linked to their natal environment, which is needed to garner insights into the open problems above. As an example, in order to probe the universality (or not) of the stellar IMF at the high end, young massive ($M \gtrsim 20 M_{\odot}$) stars still need to be present, i.e., the cluster needs to be very young. Almost all galaxies contain YSC populations, but these are best observed in the local Universe, where the YSCs can be isolated and measured amidst the

galaxy background. However, starbursts and mergers are rare occurrences in the local Universe, thus placing a lower limit around ~ 100 Mpc in order to probe a large enough range of galactic environments (several ULIRGs and mergers are located within this volume).

The key parameters to understand cluster formation and evolution are their masses and ages. Typically the age and other properties of the young (< 500 Myr) clusters are determined by SED fitting of UV and optical images. However, the determination of the age is hampered by the degeneracy between the age and extinction, i.e. red clusters could be young and reddened or old and not reddened. Disentangling age from dust attenuation, requires U-to-J SEDs. The Dn(4000) feature is a powerful age indicator, when coupled with the long wavelength leverage up to J, required to derive the dust geometry (see Fig. 12). Extinction determination is further aided by the availability of multiple hydrogen recombination emission lines, e.g., $H\alpha$, $H\beta$, $P\beta$ [57]. Other age indicators will be observable thanks to the GMOX spectral coverage. For example, the He II 4686 (Wolf-Rayet feature) is created by Wolf-Rayet stars in clusters with typical ages of 4-6 Myrs, while the CO bandheads at $2.3 \mu\text{m}$ are caused by red super giants dominating the spectra after the WR stars have disappeared. Ionizing photon fluxes are also required to determine the shape of the high end of the IMF. Extensions to wavelengths longer than J are required when dealing with natal clusters (< 2 Myr) which are still very embedded. Finally, cluster ages, which are derived from model-matching, are sensitive to the cluster metallicity, implying that metallicity measurements are required for accurate age (and mass, which depends on the age) determinations.

Another important aspect which is still not fully constrained by observations is related to the effect of cluster feedback on the efficiency of gas removal from the region where the cluster has formed. Simulations are not able to remove gas from a cluster which has formed within a giant molecular cloud of $10^6 M_{\odot}$ [58]. However, observational census of very young clusters in local galaxies shows that the central clusters are able to remove the left-over gas. It remains still to be answered which form of feedback is the most efficient: radiation pressure from very young massive stars, or mechanical feedback from stellar winds and supernovae explosions. By studying the emission lines of the H textscii regions around these young stellar clusters, the cluster feedback can be studied in detail, using the detection of lines with different ionization potential (e.g. $H\alpha$, SII, SIII, OIII and lines produced by shocks from the supernova ejecta like FeII).

c.5.1.3 GMOX REQUIREMENTS

GMOX needs to be able to obtain high quality spectra of large samples of young clusters in local group galaxies, allowing age determination via spectral fitting techniques [59]. This will give a significant improvement in the accuracy over the photometric determinations by resolving the degeneracy between age and extinction. The high spatial resolution is needed to isolate individual clusters. GMOX should have high multiplexing capability (200 - 500) to allow the spectral age determination of large samples of clusters in galaxies allowing the study of the environmental dependencies of the cluster properties and survival rate. Multi-object capabilities are the only way to efficiently observe YSC populations in external galaxies, where several hundreds to a few thousand YSC can be included within a field-of-view of $\sim 1' \times 1'$.

To disentangle the age-extinction degeneracy, U-to-J coverage is needed. Masses are finally derived from the total flux at the long wavelengths ($> 7,000$ Angstrom, up to at least J-band). The broad wavelength coverage is also needed to enable age determination of clusters from 1 to up to ~ 10 Myr as several age dating features, emitted by stars of different ages, are covered in the spectrum: e.g. Balmer lines, Wolf-Rayet feature, CO-band heads (from red supergiants), Ca triplet, Mg lines.

The use of adaptive optics is essential for this study in order to identify and isolate the indi-

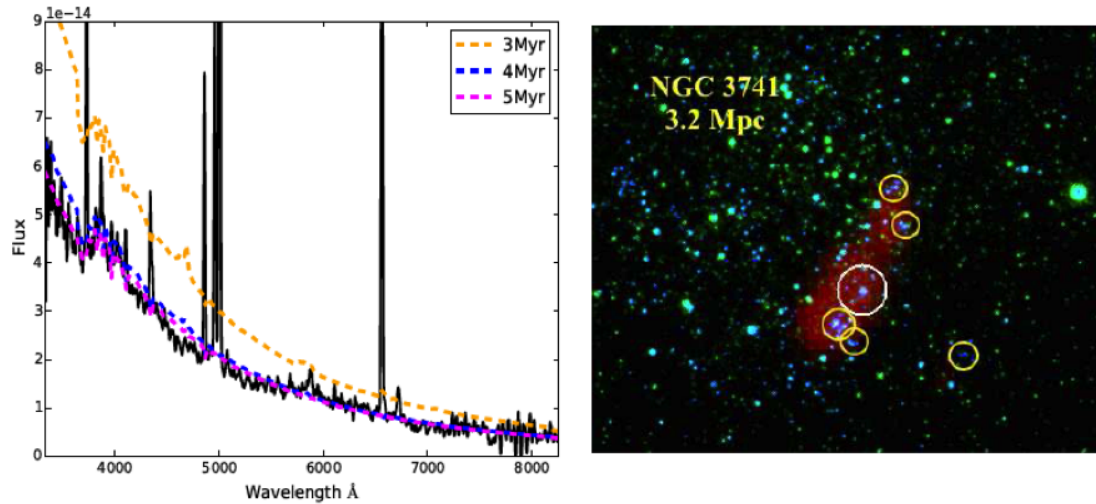


Figure 12: Left: Optical spectrum of a star cluster in a nearby dwarf galaxy, NGC3741 (shown at right, with a white circle), demonstrating how the wavelength coverage 3400-8000 is a minimal requirement to age-date clusters. Longer wavelength baselines are required in the presence of significant amounts of dust. Right: This color composite of NGC3741 shows that multi-object spectroscopy would be an efficient way to observe the clusters in this galaxy (yellow circles).

vidual clusters and to obtain as high a SNR as possible. A spectral resolution of 2000 is enough to identify the spectral features.

Parameter	Value	Justification
Bandpass	U-to-J	To disentangle the age-extinction degeneracy To derive masses
Resolving Power	$\simeq 5000$	To determine age from emission and absorption features
Field of View	$\sim 1' \times 1'$	To map resolved galaxies up to their outskirts
Slit width	$\sim 0.2''$	To resolve individual clusters
Multiplexing Capability	200-500 sources	To measure large samples of clusters in resolved galaxies

Table 8: Summary of requirements for case [c.5.1](#)

C.5.2 MASSIVE STAR FORMATION IN LOCAL GROUP DWARFS

C.5.2.1 OPEN PROBLEMS

The Local Group (LG) of galaxies offers the best opportunity to study massive stellar evolution and star formation (SF) in environments with a variety of properties, such as galaxy type, metallicity, gas density, dynamics and star formation history (SFH). SF modes and regulating factors as well as the interplay of stars and dust can be studied in detail given the vicinity of LG galaxies.[60] Ultimately, the resolved young populations of LG galaxies provide a crucial anchor point for the study of integrated properties of distant star forming galaxies. Given the typically low metallicities of dwarfs in the LG, they are ideal laboratories to study SF and evolution in conditions similar to the early Universe.

They are indeed very important for understanding the efficiency of metal enrichment of the interstellar medium, which might differ between the LG spirals (Milky Way and M31) and dwarfs. A question arises whether the observed low metallicity in dwarfs reflects a quiet SFH or their inefficiency in retaining and mixing their own nucleosynthetic products.

Key Questions:

- How does star formation proceed in low-metallicity environments?
- What factors determine the chemical history of dwarf galaxies?

C.5.2.2 OBSERVATIONAL NEEDS

Massive stars are usually born in dense stellar environments, making it quite challenging to perform spectroscopy of individual objects (Fig. 13). Adaptive optics can provide the angular resolution needed in such crowded fields. Accurate spectral typing and estimates of stellar parameters are needed to construct H-R Diagrams. From the latter it is possible to estimate stellar masses and ages, thus characterizing the upper-end of the IMF in low-metallicity environments and the recent SFH. Given the typical size of these dwarf galaxies on the sky, 10s to 100s hot massive stars are present within 1 square arcminute, the exact value depending on the target dwarf galaxy.

Other than the hot O and B stars, A-type supergiants can also be observed and their metallicities can be estimated from the many Fe lines available. These young stars reflect the *current* metallicity of their surroundings. Usually the star forming dwarf galaxies also present a number of cool red supergiants, which are slightly older than the hot OB stars. Covering the CaII triplet (8498, 8542, 8662 Å), visible in these stars, enables to estimate the metallicity of intermediate age populations and compare it to that of younger stars, thus quantifying their hosts' chemical enrichment.

C.5.2.3 GMOX REQUIREMENTS

Excellent image quality, typical of GLAO correction ($\simeq 0.3''$ in the visible) is needed to achieve the angular resolution needed to work in the crowded fields typical of nearby galaxies. A field of view of the order of 1×1 square arcmin is adequate to cover the typical extension of nearby dwarf galaxies. Medium resolution spectroscopy, $R \sim 3000$ is needed to show the presence of distinct populations, distinguishable by kinematics, metallicity and spatial distribution (as found e.g. in Sculptor Dwarf Spheroidal Galaxy but not in Carina).

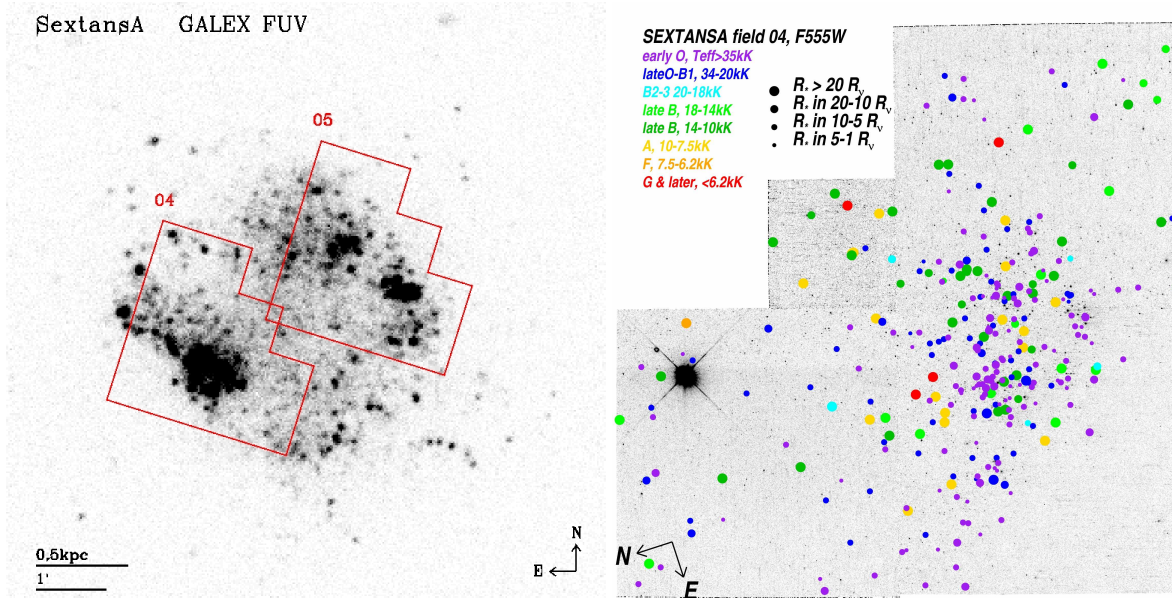


Figure 13: Left: GALEX image of the dwarf galaxy Sextans A, with the footprints of the HST/WFPC2 observations by [61, 62] superimposed. This galaxy represents a typical example of star-forming, low-metallicity, Local Group dwarf galaxy. Right: stellar temperature estimates from photometric SED fitting, by [61, 62]. HST observations like these can be used for GMOX target selection. The typical HST imaging cameras FoV can be covered with ~ 3 GMOX pointings.

Parameter	Value	Justification
Bandpass	U-to-H	To derive stellar parameters and reddening law
Resolving Power	$R \simeq 3000$	To differentiate distinct stellar populations
Field of View	$\gtrsim 1 \text{ arcmin}^2$	To match typical nearby dwarf galaxies sizes
Slit width	0.4 – 0.04	To reach faint sources in crowded fields with AO
Multiplexing Capability	$\simeq 100/\text{sq.arcmin}$	To get strong statistics on stellar populations

Table 9: Summary of requirements for case [c.5.2](#)

C.5.3 GLOBULAR CLUSTERS

C.5.3.1 OPEN PROBLEMS

One of the most-obvious assumptions made by astrophysics for over half a century was to consider globular clusters (GCs) as: “*the purest and simplest stellar populations we can find in nature*” [63]. However, in the last few years an overwhelming body of observational evidence, both photometric and spectroscopic, has shown that this old, simplistic paradigm can’t be applied to most (if not all) GCs, [64]. Multiple generations of stars in GCs are now the rule rather than the exception. *De facto*, a new era in GC research has started. In the local Universe, GCs do not appear to be brewing multiple generation of stars [65], so special conditions, encountered only in the early Universe, may be instrumental for the occurrence of the GC’s multiple population phenomenon. Ultimately, studying and understanding how multiple stellar systems were born and have evolved in GCs will help us shading light on the series of events that characterized the early childhood of the Universe. Formally, all GCs exhibit multiple main sequences (MSs), and the most reasonable explanation is that stars in each of these MSs are characterized by a different Helium abundances [66]. Helium abundance cannot be directly measured by spectroscopy, except for high temperature, highly evolved stars [67].

Key Questions:

- What is the origin of the multiple stellar populations observed in globular clusters?

Nevertheless, spectroscopic investigations of GCs have found large star-to-star variations in light-element (O, Na, Mg, Al and Si) abundances. These variations have distinct patterns: O and Mg abundances are positively correlated, and are anticorrelated with Na, Al and Si abundances. Such patterns leave little doubt about the chief nucleosynthesis culprit: high-temperature hydrogen fusion that includes CNO, NeNa, and MgAl cycles [68]. The main outcome of H burning, helium, is expected to be directly related to the observed chemical pattern of light elements in GCs. Stars on the MS that are highly enriched in He should have large depletions of O and Mg and large enhancements of Na and Al (possibly Si as well). In addition, first-generation stars are found to be O-rich, C-rich and N-poor. Conversely, second-generation stars, whose material has been CNO-cycle processed, are O-poor, C-poor and N-rich.

The kinematic properties of different stellar populations represent another key piece of the puzzle for a complete picture of the formation and evolutionary history of GCs. According to a number of different formation scenarios [69, 70, 71] second-generation (2G) populations should form more concentrated in the GCs inner regions, and then slowly diffuse towards the outskirts, preferentially along radial orbits [72]. Even if formation and early dynamics did not produce strong differences in the kinematic properties of 1G and 2G populations, the effects of the long-term evolution driven by two-body relaxation, combined with the predicted (and observed) differences in the spatial distribution of 1G and 2G stars, can still leave significant fingerprints in the current kinematic properties. However, line-of-sight velocities of GC stars have been measured so far only for the brightest giant stars. GMOX sensitivity and angular resolution will allow us to reach deep into the main sequence, giving us access to orders of magnitude more stars. Moreover, using only red giants represents a major limitation for studies focused on the global internal kinematics of GCs. In fact, because of the fast evolutionary timescale, giant stars have basically all the same dynamical mass, i.e. the mass of the current turn-off stars. It is only by reaching the main sequence that it would be possible to study the effects of energy equipartition, mass segregation and anisotropy [73]. When proper motions are also available for the same stars, GMOX line-of-sight velocities will allow us to constrain the 3D velocity and thus, the whole phase-space distribution

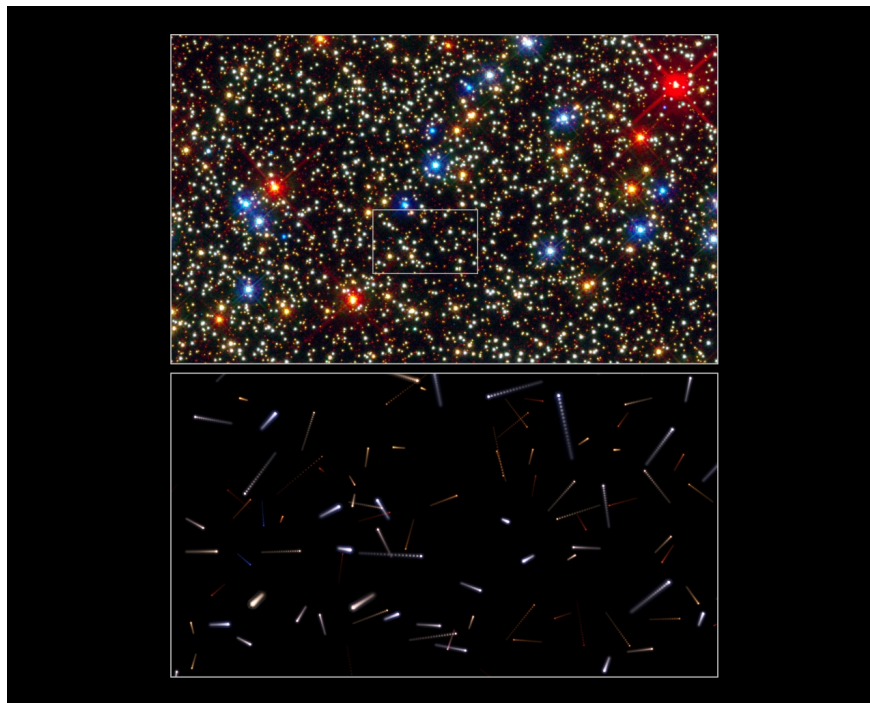


Figure 14: The upper panel shows a multi-color HST/WFC3 image of a field in the center of Omega Cen. The lower map shows the predicted positions of the stars highlighted by the white box. Each streak represents the motion of the stars over the next 600 years, sampled every 30 years. Radial velocity measures will allow one to reconstruct the 3d kinematics of the different stellar populations of the cluster.

functions, setting critical constraints on the dynamical and evolutionary status of the clusters. The core of GCs is the place where the most interesting dynamical interactions happen. Only state-of-the-art spectroscopy of faint stars in crowded fields will fully unlock these highly-demanding scientific investigations.

C.5.3.2 OBSERVATIONAL NEEDS

Multiobject spectroscopy in the full visible range and with the capability of operating in crowded fields is ideally suited for studies of globular clusters. The apparent half-mass radius of most galactic globular clusters is about 1 arcmin, so field of views of this order are adequate for measuring hundred of stars in a single exposure. Because of crowding, high angular resolution is mandatory to target single sources down to the very center of GCs.

Moderate resolving power ($R \gtrsim 3000$) from the near UV ($\lambda > 3400\text{\AA}$) to $1\ \mu\text{m}$ is adequate to obtain spectra of turnoff and sub-Giant Branch stars in Galactic globular clusters, targeting e.g. CN (3883 \AA) and CH (4305 \AA) molecular bands to derive nitrogen and carbon abundances. Spectral resolution $R > 5000$ is needed to explore the close link between He enhancement and the simultaneous depletion/increase in light elements of faint stars on different main sequences. These targets can be photometrically selected and then spectroscopically analyzed to infer their light-element abundances. Near-UV capability would be especially useful to directly measure key CNO-cycle molecular bands: NH ($\sim 3400\text{\AA}$), CN ($\sim 3800\text{\AA}$, $\sim 4150\text{\AA}$), and CH ($\sim 4300\text{\AA}$). Near infrared coverage is needed to constrain the possible occurrence of cool, low-mass companions that may contaminate the results. By using narrow slits to increase resolving power and exploiting the wide spectral coverage it is possible to measure line-of-sight velocities. It should be possible to

reaching the less massive MS stars and achieve higher precision than that achievable with proper motions from the Hubble Space Telescope.

c.5.3.3 GMOX REQUIREMENTS

GMOX must be capable of collecting accurate high-resolution spectra of a few hundred stars in a single pointing. The field of view should be at least 1 square arcminute. The spectral coverage should range from the near-UV to the near-IR, resolution $R > 3500$.

Parameter	Value	Justification
Bandpass	U-band	To determine CNO abundances
	Near-IR	To detect cool companions affecting v_{rad}
Resolving Power	$R \gtrsim 3500$	To resolve molecular bands
Field of View	$\simeq 1 \text{ arcmin}^2$	To cover the typical half-mass radius of most globular clusters
Slit width	$0.3'' - 0.04''$	To boost sensitivity and resolve individual targets in crowded fields
Multiplexing Capability	100 – 500 targets	To efficiently build rich statistical samples

Table 10: Summary of requirements for case [c.5.3](#)

C.5.4 FORMATION AND EVOLUTION OF THE GALACTIC BULGE

C.5.4.1 OPEN PROBLEMS

The Galactic bulge is the nearest spheroid and the only one for which we can access information from individual stars. Understanding the details of the Galactic bulge formation and evolution is therefore of great importance in both placing our own Milky Way in a broader, cosmological context and for testing our theories of galaxy assembly and evolution. Photometric studies of the bulge [74, 75, 76, 77] and stellar spectroscopy [78, 79, 80, 81, 82] point to a rapid bulge formation scenario from dissipational collapse or mergers: a *classical* Bulge. However, red clump star counts show that the bulge morphology is boxy/peanut-shaped [83, 84, 85], suggesting that the Bulge has formed by vertical heating of stars in the inner thick/thin disk, induced by the central bar [86, 87]: a *pseudo* Bulge.

C.5.4.2 OBSERVATIONAL NEEDS

To understand whether our bulge is a classical, pseudo or mixed-origin one, a combination of kinematic and chemical information is needed, across a large area. Access to the Calcium-Triplet spectral region is fundamental to characterize the chemical properties of bulge stars. This spectral region encompasses many Fe lines, as well as numerous α -elements lines (Mg, Si, Ti). Full spectral modeling allows the determination of [Fe/H] and [α /Fe], as demonstrated e.g. by [88] for the RAVE survey of the Galactic Disk using $\lambda = 8410 - 8795\text{\AA}$, $R \sim 7000$, $\text{SNR} > 30$ (we aim at $\text{SNR} > 70$). Line-of-sight velocities can be obtained by cross-correlation with template spectra; at our target SNR we expect uncertainties of ~ 1 km/s.

Existing surveys of the bulge are performed using fiber-fed spectrographs (FFSs). Given the high degree of crowding, FFSs are limited by the fiber size to observe bright sources, i.e. red giant and asymptotic branch stars. High angular resolution, like the one provided by the GeMS AO module, is needed if one wants to reach the yet unexplored main sequence regime. Moreover, for the same reason, all the existing surveys do not reach very close to the galactic midplane, while AO-capability could provide access to these most crowded regions. The BRAVA [89, 90, 91], ARGOS [92, 93, 94, 95] and GIBS [96] surveys use FFSs and have targeted red clump or brighter giants $-I_{\text{RC}}(AB) = 14.5 - 15.5$ mag, depending on extinction– in the Ca-Triplet region with resolving power between 6500 and 11000, and SNR of $\sim 50 - 80$. The APOGEE survey also uses FFSs but explores a different wavelength regime, the H-band, with a resolving power $R \sim 22500$ [97]. The aforementioned surveys observe ~ 100 targets per pointing, exploiting the large FFSs FoV. Large numbers of stars are needed to characterize the populations metallicity and velocity distribution function, their latitudinal and longitudinal dependencies, their higher moments.

Key Questions:

- How did the Milky Way Bulge form?
- Do we understand spheroids formation and evolution?

C.5.4.3 GMOX REQUIREMENTS

To be competitive with FFSs, GMOX needs to compensate for the smaller Gemini FoV by having a greater sensitivity, reaching much fainter targets in the same exposure time, thus still having several hundred possible targets per pointing (Fig. 16). This is certainly possible thanks to the

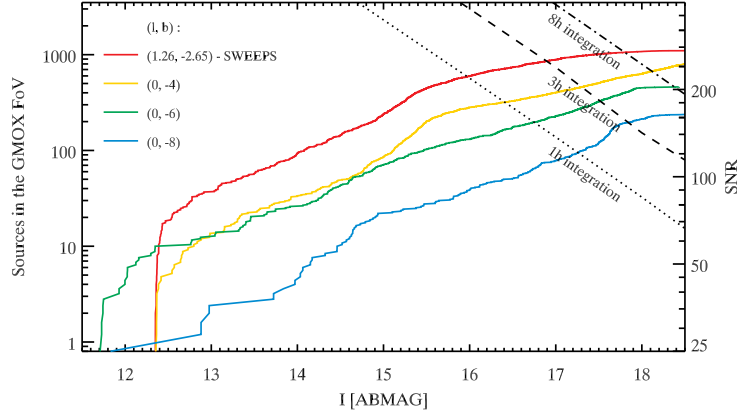


Figure 15: Source counts along different Galactic Bulge sightlines (color lines). The diagonal lines indicate the SNR per resolution element, at $\lambda = 8650\text{\AA}$. The star counts are estimated using near-infrared Vista-VVV data [98], converted to I band using stellar models by [99] (age = 10 Gyr, distance modulus = 14.5 mag). Extinction is estimated by fitting the J-K color of the red giant branch for each line of sight. Even for the less crowded fields, far from the Galactic midplane, GMOX will be able to observe ~ 100 sources at SNR=100 in just 1h.

combination of AO and DMDs. The requirement is for GMOX to reach SNR ~ 100 in 1 hour at $I(AB) \sim 17.5$ mag.

Spectral resolution $R \simeq 4,000$ is more than enough to measure radial velocities with $\sim \text{km/s}$ accuracy since numerous lines can be used for spectra cross-correlation. At this spectral resolution the Ca-Triplet region of the spectrum can be used for accurate metallicity estimates (± 0.2 dex). The Ca-Triplet region is also relatively free from telluric absorption and it encompasses several lines that can be used to measure elemental abundances, specially for α -elements. A large spectral coverage is needed to allow a full modeling of the stellar spectra, that takes into account not only the stellar parameters (T_{eff} , $\log g$, $[\text{Fe}/\text{H}]$) but also the foreground extinction. The latter is highly patchy towards Bulge sightlines and recent findings show that it cannot be modeled with a single-parameter standard extinction law [100].

Accessing the blue region of the spectrum is of high importance for a bulge survey, since it can help removing foreground dwarf stars contamination using gravity sensitive indicators such as the Mgb/MgH feature.

The ability to synthesize very narrow slits is fundamental to beat the effects of crowding, which are very severe towards the Galactic Bulge.

Parameter	Value	Justification
Bandpass	U-to-K	To determine T_{eff} , $[\text{Fe}/\text{H}]$, $[\alpha/\text{Fe}]$, gravities from giant to dwarf stars extinctions and remove foreground contaminants
Resolving Power	$R \simeq 4,000$	To measure v_{rad} with $\sim \text{km/s}$ accuracy To measure Ca-Triplet and other abundance diagnostics
Field of View	$1 - 5 \text{ arcmin}^2$	To have good statistics
Slit width	$0.4 - 0.04$	To beat crowding and increase sensitivity
Multiplexing Capability	$\simeq 100 - 500$ stars	To increase statistics in very crowded fields
Sensitivity	SNR=100 in 1hr at $I_{AB} = 17.5$	

Table 11: Summary of requirements for case C.5.4

C.5.5 YOUNG STELLAR CLUSTERS IN THE GALAXY AND IN THE MAGELLANIC CLOUDS

C.5.5.1 OPEN PROBLEMS

Young, massive stellar clusters in our Galaxy and in the Magellanic Clouds, close enough to be well resolved in their individual stellar components, are of prime interest for studying how stars form and understanding the role played by the environment. HST has produced spectacular images and large photometric datasets, resolving individual sources well below $0.5 M_{\odot}$, at the peak of the stellar Initial Mass Function, at the distance of the Magellanic Clouds.

The wealth of data sets the basis for comparing massive star clusters in different environments (by metallicity, stellar density, etc.) providing critical insights into the processes that regulate star formation through cosmic history.

At the moment we are far from reaching consensus on what regulates the details of the star formation process. For example, the hierarchical star formation scenario predicts that the age spread is very small for compact clusters and increases with spatial scale [101]. In contrast, the turbulent core model predicts that star formation is continuously active for several Myrs [102]. The relevance of the many different physical processes involved, of the different initial conditions describing the status of the molecular clouds, and feedback from massive stars is not completely understood yet [43]. This is mostly due to the lack of systematic and homogeneous spectroscopic studies that, in principle, should span a large range of conditions. The main product of star formation, i.e. the shape of the IMF, is still a subject of debate. Observationally, the high-mass end ($M \gtrsim 1M_{\odot}$) of the IMF appears to follow the well established “universal” Salpeter’s slope. The $M \simeq 0.5 M_{\odot}$ turnover of the IMF, however, cannot be explained without additional physical assumptions to set the stellar mass scale. Bate [103] and Krumholz et al. [104] have recently suggested that the characteristic mass scale is determined by the mass over which radiative feedback becomes able to suppress fragmentation. On the other hand, early deuterium burning may play a fundamental role, and this may explain why the typical stellar mass is so close to the hydrogen burning limit [43]. The IMF in the brown dwarf regime is still poorly constrained; at the low mass end, we don’t even know how to disentangle e.g. a low mass object that formed in the field from an ejected planet. Binarity, variability, accretion, mass loss are just some of the phenomena that complicate the study of young stellar objects.

Given the short time scales, reconstructing different populations, estimating ages and membership is the first fundamental step. The high extinction caused by the parental molecular clouds makes near-infrared spectroscopy the tool of choice. Massive stars provide us with a range of spectral lines usable to classify them down to 1 subtype (using e.g. He I at 1.70, 2.058, 2.113 μm , the N III complex at 2.115 μm , and He II at 2.1185 μm , the H Brackett series). Knowing the spectral type we can derive extinction, and therefore estimate temperature and luminosity: for targets of known distance, we can put them in the HR diagram. By comparison with isochrones, one can then derive ages and eventually reconstruct the star formation history of embedded regions. The same strategy can be adopted for lower mass stars, still in a Pre-Main-Sequence phase, as described in detail in Section C.5.6.

In addition to studying individual sources, reconstructing the global dynamic status of young clusters is also a key tool for understanding star formation, since different theoretical models

Key Questions:

- How do massive stars form?
- How does feedback from massive stars affect their birth environments?
- What determines whether star clusters will stay bound or dissolve?



Figure 16: HST image of 30 Doradus in the Large Magellanic Cloud, which is a prime target for multi-object spectroscopy of crowded fields using AO.

make different predictions on e.g. velocity dispersion, mass segregation, ejection, and cluster dispersal. Members of our team have started an ambitious program to study massive star clusters of different characteristics (by metallicity, stellar density, etc.) using proper motions. Their targets are located in the Galactic Disk (i.e. Trumpler 14, Westerlund I and II), Galactic Center (Quintuplet and Arches), and in the Magellanic Clouds (30 Doradus, NGC346). These systems, characterized by a high level of internal structure and sub-clustering [105, 106, 107, 108, 109, 110, 111, 112] are ideal laboratories to investigate how star formation events develop and how high and low mass stars affect their mutual evolution. Spanning an age range of few million years, these systems provides snapshots of the early evolutionary phases of stellar clusters.

C.5.5.2 OBSERVATIONAL NEEDS

Observations show that the extinction towards star forming regions is strongly varying from star to star. Experience with VLT/X-shooter shows that a wavelength coverage from U to K enables us to observe the less embedded stars in the optical regime. This enables access to lines like $H\alpha$ allowing a much better determination of the stellar parameters. In fact, stellar atmosphere models [FASTWIND, 113] can be fitted to the spectrum to derive the fundamental stellar parameters based on the shapes of the line profiles [see e.g. 114]. In order to classify OB stars using the absorption lines in the NIR range, a resolution of one thousand is enough. However, for full spectral modeling, including wind features, a $R \gtrsim 4000$ is necessary. Spectra of $SNR \simeq 100 - 200$ allow deriving the effective temperature, mass loss rate from $H\alpha$ or $Br\gamma$ emission (stellar winds, seen in emission, will fill in the $H\alpha$ and $Br\gamma$ absorption lines), rotational velocity, gravity (from the stark-broadened Brackett lines). The massive stars are bright in the H- and K-band, making it easier to achieve high SNR. However, sensitivity requirements are more strict if we want to detect the embedded stars in the optical. An O7 star at a distance of 3 kpc with a $A_V = 10$ mag, will have a magnitude $V = 18$ mag. To obtain a clearer picture of massive stars feedback in the ISM one needs spectrographs

capable of reaching such limits with high SNR in reasonable time.

One would also like to push spectral classification down to much lower masses, e.g. $2-3 M_{\odot}$, targeting stars still in the pre-main sequence (PMS) phase. Just like the most massive stars in their post-main sequence phase, PMS stars can be used for age measurements, once their spectra have been classified, e.g. using the CO absorption at 2.3 micron, Ca lines at 9000 Å to confirm their suspected PMS nature and the classification by Kenyon and Hartmann [115] to derive their temperatures and luminosities. By comparing the ages of the massive stars and the PMS stars we will be able to see whether star formation proceeds differently, in time, at the two ends of the stellar mass spectrum.

For reconstructing the internal dynamics of massive star clusters, the problem is to measure the radial velocities for a large number of stars in crowded environments. Angular resolution of the order of 0.05 to 0.1 arcsec is required to resolve single stars in the core of the clusters, while high SNR ($> 50 - 100$) and medium resolution ($R = 5000 - 10000$) spectra are needed to measure radial velocities dispersions of the order of $\sim 2 - 5$ km/s. Wide spectral range paired with multi-slit capability is needed to efficiently map different regions of the Milky Way and nearby galaxies: infrared coverage will be needed to measure the radial velocities of the highly extinguished massive clusters towards the Galactic center. Optical wavelengths $\lambda\lambda = 390 - 508$ nm can be used to measure radial velocities from the OB stars in the Magellanic Clouds. A dedicated monitoring program (e.g. once a month for one year) would also allow us to obtain the first complete census of the spectroscopic binaries in the crowded cores of the young clusters. Ejection is a natural byproduct of unstable 3-body problems, so the mass spectrum of binaries is a further observational constraint for models of massive star formation. Combined with high-precision relative proper motions, radial velocity data would allow us to determine the 3D dynamics of a complex, young stellar system ($M > \text{few}10^3 M_{\odot}$), a fundamental observational constraint to characterize star formation and the early phase of cluster evolution.

These studies critically need an instrument combining high multiplexing capability, the ability to cover a wide wavelength range and high spatial resolving power to operate in crowded fields with minimal background contamination. Last but not least, for these studies access to the full southern hemisphere is definitely a plus: the Magellanic Clouds are not accessible from Mauna Kea.

C.5.5.3 GMOX REQUIREMENTS

High multiplexing capability is very important to produce the necessary statistics to properly assess the global properties of the clusters. Large spectral coverage is needed to ensure that more extincted clusters can be observed with the same quality. High angular resolution is fundamental to observe as close to the clusters cores as possible.

Parameter	Value	Justification
Bandpass	U-to-K	To measure stellar parameters and v_{rad} over a broad range of cluster extinctions
Resolving Power	$R \simeq 5,000$	To measure radial velocities with ~ 5 km/s precision (cross-correlation) and to allow full atmospheric modeling of massive stars
Field of View	$1 - 5 \text{ arcmin}^2$	To match the typical sizes of galactic and Magellanic Clouds star forming regions
Slit width	$0.4 - 0.04$	To beat crowding and increase sensitivity
Multiplexing Capability	$\simeq 100 - 500$ targets	To increase statistics in very crowded fields
Sensitivity	SNR=8 in 1hr at $I_{AB} = 18$	

Table 12: Summary of requirements for case [C.5.5](#)

C.5.6 STAR FORMATION AND CIRCUMSTELLAR DISCS

C.5.6.1 OPEN PROBLEMS

Planets form in evolving protoplanetary disks around young stars. As most stars form in young open clusters (YOCs) and star forming regions (SFRs), we need to look at these systems to study also planet formation. Galactic YOCs and SFRs provide detailed snapshots of young stars and their disks at similar age; to study their evolution one has to compare regions of different age.

According to the current paradigm, the evolution of the gaseous content of protoplanetary disks plays a key role in the planetary formation process. The migratory path of forming planets is determined by the surface density of gas in the disk. Also planet population synthesis models rely on the radial distribution of the gas surface density [e.g., 116]. The evolution of the gas surface density of circumstellar disks is mostly regulated by two processes: viscous accretion and winds, mainly photoevaporative or disk winds [117]. Driven by turbulence, some disk material is accreted to the innermost regions while angular momentum is transported to the outer parts. At the hot, inner edge of the disk, ionized gas is funneled by the magnetic field to accrete onto the central star (magnetospheric accretion, see [118, 119]). Mass accretion gives rise to characteristic spectral signatures: the shock on the photosphere produces a hot continuum, easily detected in the UV as an excess emission in the Balmer continuum region ($\lambda \lesssim 364$ nm) and as veiling of photospheric absorption features across the entire visible region [120, 121]. At the same time, strong and broad emission lines arise in the optical and near-infrared spectra due to the high velocity of the material infalling on the star [122].

Both observations and models show that the near-UV excess correlates with the total accretion luminosity (L_{acc}) as well as with the luminosity of various emission lines [123, 124, 121]. However, disentangling photospheric spectrum from the accretion emission is not easy. First, the veiling due to accretion makes the photospheric features shallower: if veiling is not taken into account properly, the derived spectral type is earlier than the real one [125]. Second, the accretion continuum makes the spectrum appear bluer, while the reddening makes it redder. The need to assume a reddening law (important to correct the measured UV fluxes) adds uncertainty, as well as the fact that accretion is a highly variable process also on small timescales (minutes to hours, e.g., [126]).

This has strong implications on non-simultaneous observations across different wavelength ranges, since systematic errors due to variability are difficult to take into account. In practice, not only the estimated mass accretion rates but even the most fundamental stellar parameters (effective temperature, radius, luminosity) are often poorly defined, adding large scatter to the HR diagram of coeval populations that in principle should nicely trace theoretical isochrones (with binaries).

The availability of the X-shooter spectrograph at the 8m ESO/VLT telescope has helped astronomers shed some light on this issue. By covering the spectral range from $\lambda \sim 300$ nm to $\lambda \sim 2500$ nm simultaneously with high-sensitivity and medium resolution, X-shooter allows one to beat the degeneracies between the stellar and accretion parameters. Recently, Manara et al. [127] have used X-shooter to clarify the nature of two accreting objects in the $\simeq 1$ Myr Orion nebula cluster (ONC) whose positions on the HR diagram, determined with photometry and spectroscopy

Key Questions:

- What is the age of young stars?
- Are there multiple star formation bursts in young clusters?
- What is the main driver of disk evolution and dispersal?
- How do stars acquire their final mass?
- How does disk evolution depend on metallicity?

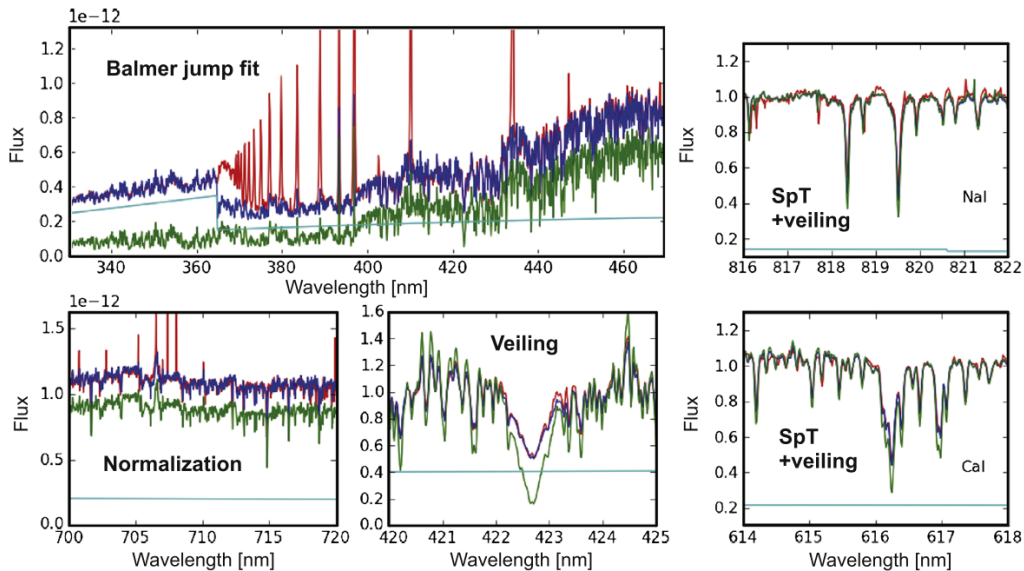


Figure 17: A combination of photospheric and accretion spectra can reproduce the observed emission; line veiling, however, affects the spectral features and biases the stellar type estimates. A global solution is necessary to properly derive the parameters of pre-main-sequence stars. (Adapted from [125]).

over a limited bandpass, were compatible with 30 Myr old isochrones (see Fig. 18). An analysis of the full X-shooter spectra has allowed us to reconstruct the stellar and accretion properties of these two objects, revealing that they were misclassified in the literature. Their newly determined stellar properties place these objects on two completely different positions in the HR diagram, and to an age estimate compatible with the mean cluster age. It is interesting to understand why the two objects were misclassified. In the case of OM1186, the Spectral Type (SpT) had been correctly determined but the stellar luminosity (L_*) was underestimated due to the degeneracy between A_V and L_{acc} derived from broad-band photometry. For the second object, OM3125, the error was in the SpT, due to the narrow wavelength range covered by the spectrum used in previous observations. In this case, the strong veiling of the photospheric signatures led to the assignment of a much earlier SpT.

Other independent works are showing the importance of using broad-band spectra to properly derive stellar and accretion properties of young stars. In particular, Herczeg and Hillenbrand [128] have used mostly Keck/LRIS spectra to show that spectral type classification of young stars is inaccurate if veiling due to accretion is not quantified and considered together with extinction (see Fig.15). The importance of covering a wide spectral range simultaneously is ultimately dictated by the very short timescales on which accretion varies, as short as minutes to hours [126]. An estimate of veiling on a non-simultaneous spectrum does not allow one to achieve the same precision in the determination of stellar parameters; this possibly is the main cause of the longstanding problem with the exceedingly large age dispersion in young clusters.

The UV-excess is surely the most direct tracer of accretion, but the accretion luminosity, and thus the mass accretion rates, can also be derived using the luminosity of various emission lines. Recent works with X-shooter have demonstrated that robust estimates of \dot{M} are obtained, once stellar parameters and extinction have been properly derived, using the luminosity of multiple emission lines [129, 130] instead of the luminosity of a single line. Among the various emission lines that can be used for these estimates, the best correlation between line and accretion luminosity is found for high upper-level Balmer lines (e.g., $H\gamma$) in the blue part of optical spectra

and Paschen series lines, such as the Pa β line in the near-infrared. This line, as well as other near-infrared emission lines, are accurate proxies as their fluxes are less affected by extinction. Moreover, infrared spectroscopy can also be used to probe the substellar regime.

The other main processes driving the evolution of protoplanetary disks are winds, which are best studied spectroscopically through the analysis of forbidden emission lines [131]. High-velocity components of forbidden lines trace jets while the low-velocity component traces slow disk winds, possibly photoevaporated by the high-energy (X-ray and UV) photons coming from the central star [132]. Studying forbidden lines in young stars allows one to determine the physical conditions of these winds, such as temperature and density. An analysis of forbidden emission lines in the Lupus SFR using X-shooter spectra has shown that these winds are slow ($V_{\text{peak}} < 20$ km/s), dense ($n_H > 10^8 \text{ cm}^{-3}$), warm ($T \sim 5000\text{-}10\,000$ K), and mostly neutral as expected either from photoevaporative or disk wind models [133]. Photoevaporation sets the final fate of the disk and fixes the "t=0" for the evolution of planetary systems in the following Gyrs of frictionless regime.

To further understand disk evolution it is necessary to study regions of different ages and environment. Recent studies indicates that disk accretion last longer in environments with lower metallicity, such as in the outskirts of our Galaxy and in the Magellanic Clouds [134]. Such studies may lead to a connection between star and planet formation in our solar neighborhood and other galaxies throughout cosmic history. However, these results require confirmation, relying solely on photometric surveys and a single accretion indicator, the H α line, which is not the most accurate tracer of accretion. It is necessary to accurately determine stellar and accretion parameters of statistically significant samples of targets at different metallicity (i.e. in the Magellanic Clouds) using the same methodology described above for close-by targets (see also Sect. E.3.4).

C.5.6.2 OBSERVATIONAL NEEDS

X-shooter is the best instrument available today to investigate the nature of pre-main-sequence objects, allowing one to determine self-consistently the Spectral Type, extinction and accretion luminosity, the jet/disk wind properties, and the relative importance of these processes. X-shooter, however, is limited by the lack of multi-object capability and operates only in the seeing limited regime.

Great progress would be enabled by a wide-band multi-object spectrograph: young galactic clusters in the Milky Way reach extremely high density (about 30,000 stars/pc³ in the core of the Orion Nebula Cluster) and are therefore ideally suited for multi-slit spectroscopy. Wide band spectral coverage is needed to measure lines from different atomic species with different ionizing conditions, including H recombination lines (the entire Balmer and Paschen series as well as the higher transition Brackett series) and a large number of molecular transitions of H₂ and CO in the near-IR. Resolution should be adequate to resolve the broad H α line ($\Delta\lambda \simeq 100$ km/s) of classical T Tauri stars. Using extremely narrow slits allows one to study the central regions of clusters, characterized by strong and highly non-uniform background, and source crowding. It also allows one to increase spectral resolution to probe the kinematics of the inner regions close to the source of jets and outflows.

C.5.6.3 GMOX REQUIREMENTS

GMOX must have multi-slit capability over a field of view of at least one square arcmin. Very-wide band spectral coverage, U-to-K, allows one to measure the rich spectrum characteristic of young stellar objects. Resolution $R > 5000$ is needed to resolve the broad H α line tracing accretion and

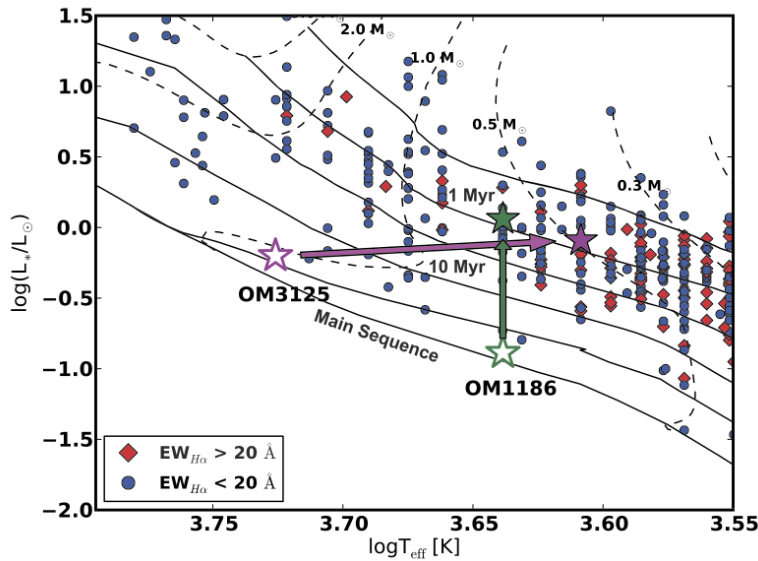


Figure 18: Position on the HR Diagram of the two objects in the Orion Nebula Cluster discussed in the text. The empty stars represent the target stellar parameters reported in the literature, while the positions determined with our method are shown with filled stars. The evolutionary tracks shown in the plot are by [135]. (Adapted from [127]).

jets kinematics. The ability to select narrow slits ($\sim 0.1''$) with AO allows one to penetrate the inner regions of young clusters, minimizing confusion and background.

Parameter	Value	Justification
Bandpass	U-to-K	To disentangle the effects of accretion, extinction to derive accurate stellar parameters
Resolving Power	~ 5000	To resolve accretion tracing lines and obtain jets kinematics
Field of View	$\sim 1 \text{ arcmin}^2$	Matched to typical scale of young star forming regions
Slit width	$\sim 0.1''$	To minimize confusion and background
Multiplexing Capability	$\sim 100\text{s}$ sources	To obtain spectra of all available Pre-Main-Sequence stars in a star forming region
Observing Efficiency	Simultaneous coverage	To avoid systematics due to short timescales variability

Table 13: Summary of requirements for case C.5.6

C.6 LSST TRANSIENTS

By probing 100 times more volume than the recent generations of transient searches such as Pan-STARRS1 and PTF, LSST is going to enable the next level of time domain studies, probing variability both in position and time. Rarely observed events will become commonplace, new and unanticipated events will be discovered. The impact of LSST on astrophysics has been recognized by the latest Decadal Survey; Gemini is expected to play a key role (See Section B), in particular with the spectroscopic followup of transients .

C.6.1 GMOX CAPABILITY FOR LSST FOLLOW-UP OBSERVATIONS

We have made the exercise of going through the high-priority scientific questions that LSST is going to attack, listed in the index of the LSST Science Book, marking those that are well suited for follow-up with a wide-band, moderate resolution spectrograph at Gemini reaching the sensitivity levels of LSST, 24.5 mag per single visit (Figures 19 to 26) rebinning the spectra at somewhat lower resolution. Almost the entire list provides a strong match, with the possible exception of solar system studies dealing with e.g. statistical analysis of multitudes of small bodies scattered across the sky, and the themes of Barionic Acoustic Oscillations and Weak Lensing, typically dealing with scales much larger than the Gemini field of view: (the fundamental BAO length scale, about 150 Mpc, is about 100 times the largest angular scale probed by the unvignetted Gemini field of view). In fact, an instrument like DESI at the Mayall 4-m telescopes, capable of simultaneously measuring 8,000 redshifts over a 8 square degree field of view, seems ideally matched to follow the multitude of LSST transients that will appear on each LSST field. Some of these objects, though, will require an 8m telescope with the ultimate sensitivity provided by extreme AO, either because they are too faint even at their peak or just because all interesting transients eventually fade away. Gemini cannot, and should not compete with e.g. Mayall in terms of very-wide-field coverage and routine monitoring, but can provide the ancillary capability of reaching the faintest sensitivity levels.

5	The Solar System	97
5.1	A Brief Overview of Solar System Small Body Populations	97
5.2	Expected Counts for Solar System Populations	99
5.3	The Orbital Distributions of Small Body Populations	105
5.4	The Main Belt: Collisional Families and Size Distributions	110
5.5	Trans-Neptunian Families and Wide Binaries	115
5.6	The Size Distribution for Faint Objects—"Shift and Stack"	117
5.7	Lightcurves: Time Variability	120
5.8	Overlapping Populations	122
5.9	Physical Properties of Comets	126
5.10	Mapping of Interplanetary Coronal Mass Ejections	127
5.11	The NEA Impact Hazard	128
5.12	NEAs as Possible Spacecraft Mission Targets	132
	References	133

Figure 19: Section of the LSST Science Book related to Solar System science. The highlighted items are well suited to GMOX follow-up observations.

6	Stellar Populations	137
6.1	Introduction	137
6.2	The Magellanic Clouds and their Environs	138
6.3	Stars in Nearby Galaxies	144
6.4	Improving the Variable Star Distance Ladder	146
6.5	A Systematic Survey of Star Clusters in the Southern Hemisphere	150
6.6	Decoding the Star Formation History of the Milky Way	155
6.7	Discovery and Analysis of the Most Metal Poor Stars in the Galaxy	160
6.8	Cool Subdwarfs and the Local Galactic Halo Population	162
6.9	Very Low-Mass Stars and Brown Dwarfs in the Solar Neighborhood	166
6.10	Eclipsing Variables	171
6.11	White Dwarfs	175
6.12	A Comparison of Gaia and LSST Surveys	192
	References	196

Figure 20: Same as Figure 19, but related to the study of stellar populations.

7	Milky Way and Local Volume Structure	201
7.1	Introduction	201
7.2	Mapping the Galaxy – A Rosetta Stone for Galaxy Formation	202
7.3	Unravelling the Secular Evolution of the Bulge and Disk	208
7.4	A Complete Stellar Census	209
7.5	Three-Dimensional Dust Map of the Milky Way	211
7.6	Streams and Structure in the Stellar Halo	216
7.7	Hypervelocity Stars: The Black Hole–Dark Halo Link?	221
7.8	Proper Motions in the Galactic Halo	222
7.9	The Darkest Galaxies	224
7.10	Stellar Tracers of Low-Surface Brightness Structure in the Local Volume	228
7.11	Globular Clusters throughout the Supralocal Volume	235
	References	239

Figure 21: Same as Figure 19, related to the study of the Milky Way.

8	The Transient and Variable Universe	245
8.1	Introduction	245
8.2	Explosive Transients in the Local Universe	247
8.3	Explosive Transients in the Distant Universe	254
8.4	Transients and Variable Stars in the Era of Synoptic Imaging	261
8.5	Gravitational Lensing Events	268
8.6	Identifying Variables Across the H-R Diagram	274
8.7	Pulsating Variable Stars	280
8.8	Interacting Binaries	284
8.9	Magnetic Activity: Flares and Stellar Cycles	290
8.10	Non-Degenerate Eruptive Variables	296
8.11	Identifying Transiting Planets with LSST	299
8.12	EPO Opportunities	302
	References	303

Figure 22: Same as Figure 19, related to the study of transient phenomena.

9	Galaxies	309
9.1	Introduction	309
9.2	Measurements	311
9.3	Demographics of Galaxy Populations	313
9.4	Distribution Functions and Scaling Relations	316
9.5	Galaxies in their Dark-Matter Context	319
9.6	Galaxies at Extremely Low Surface Brightness	330
9.7	Wide Area, Multiband Searches for High-Redshift Galaxies	334
9.8	Deep Drilling Fields	337
9.9	Galaxy Mergers and Merger Rates	338
9.10	Special Populations of Galaxies	340
9.11	Public Involvement	341
	References	342

Figure 23: Same as Figure 19, related to the study of galaxies.

11	Supernovae	379
11.1	Introduction	379
11.2	Simulations of SN Ia Light Curves and Event Rates	381
11.3	Simulations of Core-Collapse Supernova Light Curves and Event Rates	385
11.4	SN Ia Photometric Redshifts	388
11.5	Constraining the Dark Energy Equation of State	391
11.6	Probing Isotropy and Homogeneity with SNe Ia	395
11.7	SN Ia Evolution	395
11.8	SN Ia Rates	397
11.9	SN Ia BAO	399
11.10	SN Ia Weak Lensing	401
11.11	Core-Collapse Supernovae	401
11.12	Measuring Distances to Type IIP Supernovae	403
11.13	Probing the History of SN Light using Light Echoes	404
11.14	Pair-Production SNe	405
11.15	Education and Public Outreach with Supernovae	406
	References	409

Figure 24: Same as Figure 19, related to the study of supernovae.

12	Strong Lenses	413
12.1	Basic Formalism	413
12.2	Strong Gravitational Lenses in the LSST Survey	417
12.3	Massive Galaxy Structure and Evolution	427
12.4	Cosmography from Modeling of Time Delay Lenses and Their Environments	429
12.5	Statistical Approaches to Cosmography from Lens Time Delays	432
12.6	Group-scale Mass Distributions, and their Evolution	434
12.7	Dark Matter (Sub)structure in Lens Galaxies	436
12.8	Accretion Disk Structure from 4000 Microlensed AGN	441
12.9	The Dust Content of Lens Galaxies	442
12.10	Dark Matter Properties from Merging Cluster Lenses	445
12.11	LSST's Giant Array of Cosmic Telescopes	448
12.12	Calibrating the LSST Cluster Mass Function using Strong and Weak Lensing	450
12.13	Education and Public Outreach	455
	References	457

Figure 25: Same as Figure 19, related to the study of strong gravitational lensing.

13	Large-Scale Structure	461
13.1	Introduction	461
13.2	Galaxy Power Spectra: Broadband Shape on Large Scales	462
13.3	Baryon Acoustic Oscillations	468
13.4	Primordial Fluctuations and Constraints on Inflation	476
13.5	Galaxy Bispectrum: Non-Gaussianity, Nonlinear Evolution, and Galaxy Bias	479
13.6	The LSST Cluster Sample	481
13.7	Cross-Correlations with the Cosmic Microwave Background	490
13.8	Education and Public Outreach	494
	References	494
14	Weak Lensing	499
14.1	Weak Lensing Basics	499
14.2	Galaxy-Galaxy Lensing	502
14.3	Galaxy Clusters	506
14.4	Weak Lensing by Large-scale Structure	513
14.5	Systematics and Observational Issues	518
	References	526
15	Cosmological Physics	529
15.1	Joint Analysis of BAO and WL	530
15.2	Measurement of the Sum of the Neutrino Mass	536
15.3	Testing Gravity	540
15.4	Anisotropic Dark Energy and Other Large-scale Measurements	545
15.5	Cosmological Simulations	548
	References	554

Figure 26: Same as Figure 19, related to the study of dark energy, dark matter and new physics.

The most compelling case for LSST follow-up with Gemini is probably provided by exotic sources that emerge from below the detection threshold, rising in brightness over time scales of

hours, or a few days. One can refer to true transients as objects whose character is changed by the event, usually as the result of some kind of explosion or collision, whereas variables are objects whose nature is not altered significantly when they increase in brightness. The 5 or 6 band photometry of LSST will have limited predictive power to constrain the nature of enigmatic transients: medium resolution spectroscopy over a wide-band spectral range is absolutely needed.

A convenient way to represent the basic characteristics of explosive events is to plot the peak luminosity versus characteristic time scale. Figure 27 shows the location of some of them. The absolute magnitudes on the right can be composed with the distance modulus of the local Universe: long-period novae at $V_{abs} \simeq -7$ could be detected at their peak by LSST up to the distance of the Virgo cluster (DM=+31). Spectroscopic followup is within reach.

Supernovae occupy the upper part of the diagram. The spectroscopic light curves of their expanding shells provides us with a 3-dimensional movie of the chemical enrichment of galaxies, including the production and decay of radioactive materials and dust grains which are a prerogative for the existence of life. Supernovae are also fundamental distance indicators and have provided the first direct evidence for cosmic acceleration [136, 137]. This discovery rested on observations of several tens of supernovae at low and high redshift. These samples have been observed with a variety of telescopes, instruments, and photometric passbands. The low-redshift SN Ia measurements that are used both to anchor the Hubble diagram and to train SN Ia distance estimators are themselves compiled from combinations of several surveys using different telescopes and selection criteria. When these effects are combined with uncertainties in intrinsic SN Ia color variations and in the effects of dust extinction, the result is that the current constraints are largely dominated by systematic rather than statistical errors. An instrument allowing one to observe similar supernovae over a wide range of redshifts, minimizing background confusion from the host galaxies, would allow reduction of the systematic uncertainties that eventually propagate into our knowledge of fundamental parameters of the cosmos.

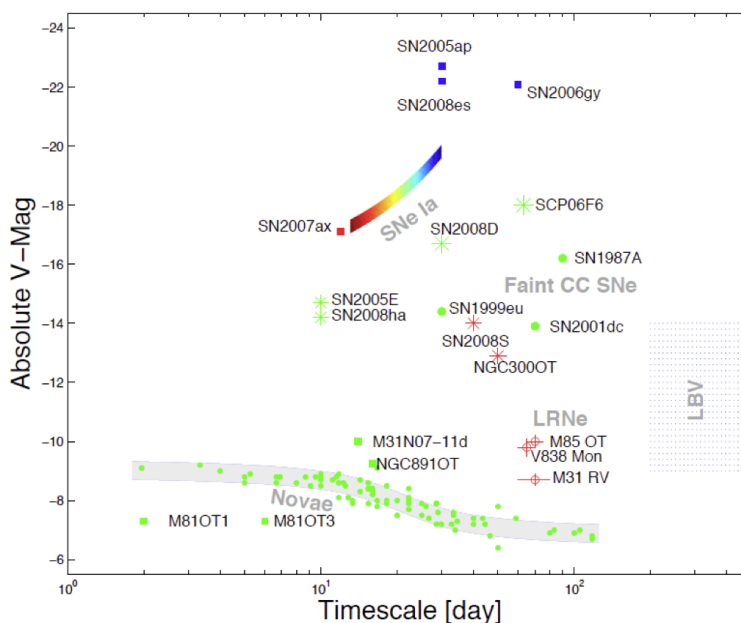


Figure 27: Peak V-band luminosity of known transients, either explosive (supernovae) or eruptive (novae, luminous blue variables - LBVs), as a function of duration, color coded to represent the true color at maximum brightness. Also shown are other peculiar transients (reproduction of Fig.8.1 of LSST Science Book)

Supernovae are also connected to the Gamma-ray bursts (GRBs), the most violent cosmic events associated with the birth of a rapidly spinning stellar black hole. Long duration GRBs probably result from the deaths of certain types of massive stars [138]. Since the explosion is mostly directional (“jetted”) with conical opening angles ranging from less than a degree to a steradian, a detection depends on the location of the observer. The initial emission of gamma rays is followed by an optical afterglow from the interaction of the relativistic debris and the circumstellar medium. An observer outside the cone of the jet misses the burst of gamma-ray emission, but can still detect the subsequent afterglow emission [139], an “off-axis” orphan afterglows. Since the “beaming fraction” (the fraction of sky lit by gamma-ray bursts) is estimated to be between 0.01 and 0.001, the true rate of GRBs is 100 to 1000 times the observed rate. Since a supernova is not relativistic and is spherical, all observers can see the supernovae that accompany GRBs. Understanding the nature of GRBs is another fascinating program that can be attacked by a sensitive wide-band spectrograph at Gemini.

C.6.1.1 OBSERVATIONAL NEEDS

The next generation spectrograph for the Gemini telescope should be able to operate over a very-wide spectral range covering the visible bandpasses, where LSST operates, with extension to the infrared, as dictated by both AO performance and cosmological redshift. The spectra of e.g. supernovae are extremely rich of emission lines, like e.g. $H\alpha$, HeI5570, 10830, CII8729,9812, OI 5577, 6300, 6364, MgI. 4571, SiII 10990, 16450, Si 10824, 11309, CaII 7292, 7325, 8499-8663, FeII 7155, 12570, 15330, 16400, CoII 15430. To track the rest frame optical spectrum up to $z \simeq 2$, beyond the limit of the furthest supernova discovered by the HST, one has to reach the K-band with spectral resolution adequate to reject OH lines.

To trace light curves, the spectrograph must be stable and allow for accurate, absolute spectrophotometric calibration. The ability to rapidly acquire a target minimizes overhead, in particular for programs dealing with relatively bright targets of opportunity or long term monitoring programs, reducing the impact on regularly scheduled observations. Multi-object capability is always a plus, allowing one to e.g. identify the host galaxy if a supernova appears in a remote cluster. Temporal resolution is also a plus, and readout times as short as a few seconds may represent an interesting capability for certain types of transients, like e.g. planetary transits.

C.6.1.2 GMOX REQUIREMENTS

While GMOX requirements have been derived from the whole set of science cases described in Section C, GMOX also fulfills the requirements set for LSST follow-ups. By design, GMOX is indeed the versatile, quickly configurable, medium-resolution, wide-band, high efficiency spectrograph required for maximizing the scientific return of the LSST mission. We envision a perfect and highly productive synergy between GMOX and LSST.

D SCIENCE REQUIREMENTS

As expected for a multi-purpose facility instrument like GMOX, the top-level requirements have been derived not just from a single application case but from a *set* of compelling science cases, taking into account the technical constraints provided by the facilities to be used (Gemini, GeMS) and the current status of technology (DMDs, detectors). Table 19 provides a summary of the requirements, briefly discussed hereafter.

1. **Spectral Coverage:** Extra-wide spectral coverage, from the U-band to the K-band accessible from the ground, emerges as a general requirement. It allows for better science by measuring multiple spectroscopic tracers of each target, disentangling the role played by the various regions contributing to the spectrum. Continuous spectral coverage allows measuring/recovering the redshift of sources with missing or mediocre estimates, e.g. from photo-z methods, and in general to trace similar physical phenomena across cosmic history. Simultaneous coverage is a huge advantage in terms of observing efficiency, but there are cases involving the study variable objects, like transients or accreting Pre-Main-Sequence stars, where simultaneity is scientifically needed. Simultaneous, wide spectral coverage also provides significant advantages from the operational point of view, as one instrument can be permanently mounted at the telescope and overhead is minimized. It also allows one to optimally exploit the best seeing conditions and bright vs. dark time. Our nominal spectral range will be from 350nm to 2.4 μ m.
2. **Multi-object capability:** This capability facilitates another huge gain in observing efficiency. In principle, IFUs are a possibility but they do not cover an extended spectral range AND a wide field of view with high spatial resolution at a reasonable cost. Other more conventional approaches (reconfigurable slits, lenslets) are not well matched to the sharpness provided by extreme adaptive optics at an 8 m telescope, and to the variety of conditions that may be encountered, from poor seeing to extreme Strehl ratio. Therefore, our approach is to use MEMS devices, in particular the Digital Micromirror Devices made by Texas Instruments, as they are commercially available at low cost, are extremely reliable and have pristine cosmetic quality. Using a single DMD per spectrograph arm GMOX can easily take $\simeq 400$ full, well separated spectra in parallel with extremely rapid and accurate target acquisition.
3. **Sensitivity:** Exploiting Adaptive Optics should allow one to reach the ultimate sensitivity achievable from the ground. Spectroscopy in the nearly diffraction limited regime enables the use of extremely narrow slits, reducing the noise due to the sky background to minimum levels. To work with adaptive optics, the spectrograph must be capable of synthesizing and aligning slits of a few micron, matching the diffraction limit of the telescope ($\lambda/D = 25$ mas at 1 μ m). Keeping the field of view entirely within the unvignetted field of view of Gemini (3'1) is also important to minimize thermal background in the K-band. Again, DMDs appear ideally suited for this application.
4. **Efficiency:** To reach the faintest sources, the highest possible throughput must also be pursued. The optics and detectors will therefore require different optimization vs. wavelength and slit sizes. For this reason we envision three spectroscopic arms: Blue (350-589 nm), Red (589-1000 nm, cut at the GeMS laser wavelength) and NIR, the last being split into three channels to cover the Y+J, H and K bands. Also the capability of acquiring a multitude of sky-spectra adjacent to each target, essential for accurate sky-subtraction, provides de-facto and increase by a factor of two in efficiency over systems requiring beam-switching.

5. Spectral Resolution: A resolving power of about $R = 5,000$ emerges as a general requirement. On the other hand, for a slit spectrograph the resolving power is not a fixed parameter, as it depends on the slit width selected by the user. Optimal sampling of the slit on the detector (about 3 pixels/slit) can be achieved only at a central, “nominal” value of the slit width. Narrowing the slit one achieves higher spectral resolutions at the expense of worse sampling, and viceversa. For a Gemini facility instrument, this means that the resolving power may depend on the observing conditions, since to exploit the AO to reach the faintest sources one will use narrow slits thus increasing spectral resolution. We have made the assumption that in 2022 Gemini will routinely operate with some level of AO correction. We have therefore set our nominal resolving power $R \simeq 5000$ for a slit width of 0.25” in the infrared, 0.33” in the Red channel, and 0.41” in the Blue channel. These values generally correspond to what can be routinely achieved with limited AO performance, e.g. with ground layer correction, or in laser-only mode (no tip-tilt).

E GMOX CAPABILITIES

E.1 EXPOSURE TIME CALCULATOR

Using the basic instrument parameters (listed in Table 1) we have developed an exposure time calculator (ETC) to predict GMOX sensitivity across its entire spectral range. To provide generic users with a reliable and well developed Graphic User Interface, we adopted the infrastructure of MOSFIRE XTcalc, a gui based ETC written in IDL by Gwen Rudie, and publicly available at <http://www2.keck.hawaii.edu/inst/mosfire/etc.html>.

We extended the original source code to include optical wavelengths and made all changes required by GMOX and Gemini. The parameters for the Gemini telescope, including the reflectivity of the Ag-coated mirrors and throughput of the science channels of ALTAIR (80%) or GeMS-CANOPUS (70%), were provided by the Gemini team. We assumed the IR sky background at Mauna Kea from the Gemini web page, at zenith with 1.6mm water vapor column. We added the thermal emission of the telescope, assumed to radiate as a blackbody at 280 K with 10% emission. When ALTAIR or GeMS are included, extra emissivity factors of 20% and 30%, respectively, are added. For GMOX we included losses by the DMDs due to a) their Al-coated mirror surface, b) the double pass through the case window with standard AR-coating provided by TI for the Visible range and optimized coating for the IR bands, c) throughput losses due to the gaps between mirrors, and d) the extra background due to the contrast achieved by DMDs (see Section G.2.3.2). We combined the throughput of all optical components in each GMOX channel, including the efficiency of the VPH gratings. For the detector quantum efficiency, we used standard curves for the E2V CCDs and the measured QE curve for IR (see Section G.2.3.2 for details on GMOX’s throughput). Figure 28 shows our best prediction for the total throughput curves, from telescope aperture to detectors included, in the three basic GMOX configurations: with Gemini only, with ALTAIR and with GeMS. Finally, to be conservative in our sensitivity estimates, we added an extra 15% throughput loss to account for slit losses and all other unknown. This extra factor is not shown in Figure 28.

We used typical dark current and read noise figures of advanced CCDs and IR Focal Plane Arrays, the latter driven in non-destructive readout mode to bring the readout noise down to 3.75 electrons using Fowler 16 sampling; this is the default value for MOSFIRE ETC.

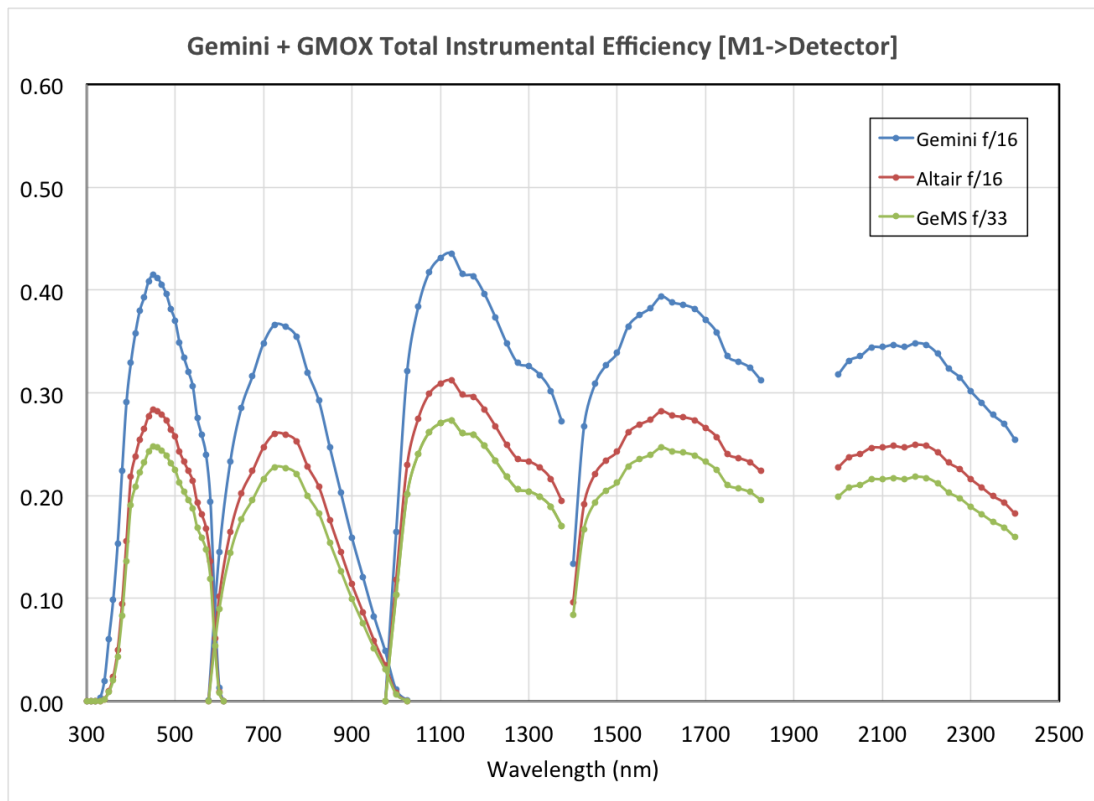


Figure 28: GMOX total on-sky throughput, from the telescope to the detectors. The three sets of lines represent, for each filter, the total throughput without AO (top), with ALTAIR (middle, assuming 80% gray transmission) and GeMS (bottom, assuming 70% gray transmission).

E.2 SENSITIVITY ESTIMATES

Given the wide range of conditions in which GMOX can operate, from relatively mediocre natural seeing to nearly diffraction-limited MCAO conditions, the variety of configurations (pure Gemini, ALTAIR, GeMS) and the choices of slit size, it is hard to encapsulate in a few parameters the results of the calculation. We will thus refer to three representative cases:

1. good seeing (0.6" in the V-band) with moderate AO correction. Here we assume "ground-layer" AO correction or a "seeing enhanced mode", where the size of the PSF at visible wavelengths is reduced by 50% (see Section F.1). We consider this to be the typical case, encountered during average seeing, when the guide stars are far from the target field, or when using ALTAIR with the wide-field corrector, or when the AO system is operated without tip-tilt correction.
2. relatively poor seeing (0.8 – 1.0" in the V-band) without AO correction.
3. excellent seeing (0.4" in the V-band) and full AO correction. In these conditions, occurring about 20% of the time, the AO provides high Strehl ratios (> 70%) either at the center of the field (ALTAIR) or over the full field in the IR (GeMS).

Case 2 corresponds to the nominal configuration, with $0.41'' \times 0.41''$ slits for the Blue arm, $0.33'' \times 0.33''$ for the Red arm and $0.25'' \times 0.25''$ for all channels of the Near-IR arm, i.e. to 5×5 , 4×4 and 3×3 micromirrors/slit for the Blue, Red and Near-IR arms, respectively. With this setup, the resolving

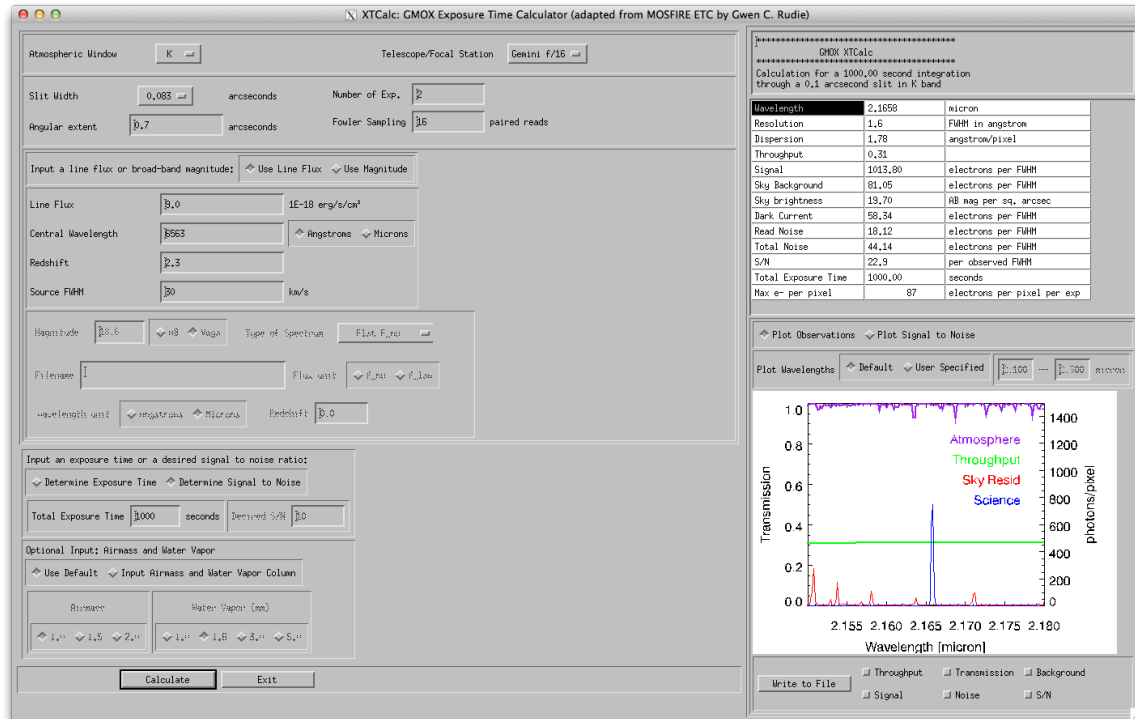


Figure 29: Screen capture of the XTCalc Gui developed for MOSFIRE and adapted to GMOX, for the default case of an emission line.

power is the nominal $R = 5,000$ on each module except for the YJ channel, where it drops to about $R = 3880$. Since in Case 1 and 3 the slits are respectively expanded and reduced, the resolving power decreases and increases. In practice, depending on the seeing and on the availability of the tip-tilt stars, these conditions can be found simultaneously across the field when the AO system is in operation. Also the same source can be observed in a certain condition (e.g. diffraction limited) in the IR and in another condition (e.g. seeing limited) in the Blue. As we will see, GMOX can naturally adapt to optimally match the science requirements (resolving power, sensitivity, spatial resolution...) to the observing conditions.

For our estimates we considered square slits with size equal to the PSFs (slit losses are accounted for in the ETC). We assumed an integration time of 3,500 s split over 2 exposures of 1,800s; we adopted $\text{SNR} = 5$ per resolution element. Since the ETC returns the SNR per spectral pixel (i.e. coadded over the cross dispersion direction), we requested $\text{SNR} = 5$ divided the square root of the number of spectral pixels under the slit (a value also reported in Tables 15 and 16). The resolving power decreases as the slit width increases, following a relation that we have assumed to be linear (Table 14). This implies that in the visible range the sensitivity per resolution element to a flat continuum spectrum increases with the slit width as the resolution decreases, while in the infrared, where the background is stronger, the sensitivity per resolution element increases with narrower slit widths. ALTAIR and GeMS have comparable performance, ALTAIR being superior in terms of higher throughput and correspondingly lower emissivity at IR wavelengths, while GeMS is capable of synthesizing narrower slits with less sky background. With extreme AO correction, GeMS is ultimately superior.

Resolving Power vs. Slit Sampling

Mirrors/slit	slit width		Blue		Red		IR	
	f/16	f/33	$R (\lambda/\Delta\lambda)$	Pixel/slit	$R (\lambda/\Delta\lambda)$	Pixel/slit	$R (\lambda/\Delta\lambda)$	Pixel/slit
1	0.083"	0.040"	22,500	0.60	18,000	0.75	13,500	0.92
2	0.167"	0.080"	11,250	1.20	9,000	1.50	6750	1.83
3	0.250"	0.120"	7500	1.80	6000	2.25	4500	2.75
4	0.333"	0.160"	5625	2.40	4500	3.00	3375	3.67
5	0.417"	0.200"	4,500	3.00	3600	3.75	2700	4.58
6	0.500"	0.240"	3750	3.60	3000	4.50	2250	5.50
7	0.583"	0.280"	3214	4.20	2571	5.25	1929	6.42
8	0.667"	0.320"	2812	4.80	2250	6.00	1687	7.33
9	0.750"	0.360"	2500	5.40	2000	6.75	1500	8.25
10	0.833"	0.400"	2250	6.00	1800	7.50	1350	9.17
11	0.917"	0.440"	2045	6.60	1636	8.25	1227	10.1
12	1.000"	0.480"	1875	7.20	1500	9.00	1125	11.0

Table 14: GMOX spectrograph characteristics.

GMOX at f/16: Gemini North and South without AO; Gemini North with ALTAIR

Field of View Sampling	171" × 90" 83 mas/micromirror		IR Arm		
	Blue arm 3500 – 5890 Å	Red Arm 5890 – 9700 Å	YJ: 0.97 – 1.35 μm	H: 1.46 – 1.81 μm	K: 1.83 – 2.45 μm (K)
	Nominal: Enhanced 0.3" Seeing at V				
Mirrors/slit	5	4	3	3	3
Slit Width	0.42"	0.33"	0.25"	0.25"	0.25"
$R = \lambda/\Delta\lambda$	4500	4500	3700	4500	4500
sampling (pixel/slit)	3	3	2.75	2.75	2.75
AB limit mag.	23.3	23.0	23.0	23.4	22.1
	Regular Seeing: 0.6" Seeing at V				
Mirrors/slit	12	10	8	8	8
Slit Width	1.00"	0.83"	0.67"	0.67"	0.67"
$R = \lambda/\Delta\lambda$	1875	1800	1590	1930	1930
sampling (pixel/slit)	7.2	7.5	7.3	7.3	7.3
AB limit mag.	23.6	23.2	23.1	23.0	22.1
	ALTAIR: FWHM = 0.05" at J				
Mirrors/slit	3	2	1	1	1
Slit Width	0.25"	0.16"	0.08"	0.08"	0.08"
$R = \lambda/\Delta\lambda$	7500	9000	11100	13500	13500
sampling (pixel/slit)	1.8	1.5	0.9	0.9	0.9
AB limit mag.	23.2	22.9	23.0	23.5	22.5

Table 15: Summary of baseline configurations achievable with GMOX in the various channels for our three representative cases: nominal/enhanced seeing (with Altair throughput), regular seeing (without Altair throughput) and extreme AO correction (with Altair throughput). For each case, we list the number of mirrors opened to synthesize a slit (row 1), corresponding to different slit widths in the sky, depending on the f/# of the telescope and AO system (row 2). The resolving power is then derived from the baseline configuration, set to $R = 4, 500$ and 3 pixels/slit for the Blue channel and red channel, and 2.75 pixels/slit for the IR channels (row 3). The sampling (pixels/slit) is reported in row 4. Finally, in row 5 we report the limit magnitude providing SNR=5 per resolution element in 3600s integration, split in two exposures of 1800s each.

GMOX at f/33: Gemini South with GEMS

Field of View Sampling	85" × 45" 40 mas/micromirror				
	Blue arm 3500 – 5890 Å	Red Arm 5890 – 9700 Å	IR Arm		
			YJ: 0.97 – 1.35 μm	H: 1.46 – 1.81 μm	K: 1.83 – 2.45 μm (K)
	Nominal: GLAO 0.3" Seeing at V				
Mirrors/slit	10	8	6	6	6
Slit Width	0.40"	0.32"	0.24"	0.24"	0.24"
$R = \lambda/\Delta\lambda$	2250	2250	1850	2250	2250
sampling (pixel/slit)	8	6	5.5	5.5	5.5
AB limit mag.	23.3	22.9	22.9	23.3	21.9
	GEMS: FWHM = 0.05" at J				
Mirrors/slit	3	2	1	1	1
Slit Width	0.12"	0.8"	0.04"	0.04"	0.04"
$R = \lambda/\Delta\lambda$	7500	9000	11100	13500	13500
sampling (pixel/slit)	1.8	1.5	0.9	0.9	0.9
AB limit mag.	23.1	22.8	22.8	23.4	22.5

Table 16: same as Table 15 for the case of GeMS with enhanced seeing and extreme AO.

E.3 EXAMPLES OF GMOX GUARANTEED TIME PROGRAMS

In Section C we have highlighted some of the big science questions that astronomers will be asking at the time GMOX will be available. From those questions we have derived the general requirements of the instrument and estimated its performance. We can now reverse the point of view, envisioning a scenario in which an instrument with the capabilities predicted for GMOX is available to the community. We then ask the questions: what could a typical user propose to observe if GMOX existed? What kind of observing proposals, beyond those dealing with the aforementioned big questions, could the Gemini TAC expect to receive once GMOX is available? To answer these questions, we have crafted a few examples derived from the expertise of our science team. They can be regarded as possible examples of guaranteed time programs tailored to illustrate the versatility of our instrument concept.

E.3.1 GALACTIC OUTFLOWS

There is now good evidence that galaxies with high star-formation rates are the source of large galactic-scale winds that carry enriched material out of the galaxies. These are seen as blue-shifted absorption features in galactic spectra. GMOX will be able to map this distribution in 3-D velocity/space by observing favorable asterisms of background galaxies. This will enable us to understand the dynamical evolution of the winds, how they are accelerated by the galaxy, and how they interact with the surrounding medium, giving us new insights into the enrichment of the IGM and on the possible feedback mechanisms that control the inflow of material back onto galaxies.

Constraining the properties of galactic outflows is crucial in defining the whole picture of galaxy evolution. However, properties such mass outflow rate, location, maximum velocity, and total gas column density are not well-constrained by observations of optical and ultraviolet resonance lines in galaxy spectra. The existing studies place entire galaxies in the slits and hence cannot resolve the flows and relate them back to the detailed local properties of the driving sources [140, 141]. GMOX can perform the first spatially resolved “down the barrel” study of galactic outflows in local face-on spatially resolved galaxies. We plan to use individual bright young star-clusters scattered throughout the disk, as background sources to sample multiple sight-lines, pro-

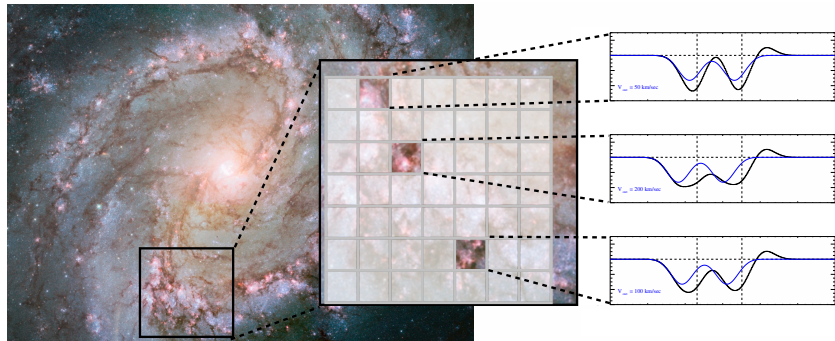


Figure 30: HST image of M83, degraded to $0.5''$ resolution with a footprint of the GMOX FoV superimposed. The three windows highlight three star clusters, where slits can be placed. The three mock spectra, show the blue shifted NaD doublet, with three out-flow velocities (50, 100 and 200 km/sec respectively), seen at GMOX resolving power $R=4000$.

viding us with a 3D mapping of the properties of the blue shifted outflowing gas.

The nearby face-on grand design spiral M83 is a prime target, as its proximity and orientation allow for detailed observations of a starburst and 3D mapping of its outflow. The 2D spiral disk structure has already been extensively mapped at high resolution at all wavelengths accessible from space and from the ground (Chandra, FUSE, GALEX, HST, Spitzer, Herschel, CO, VLA, and HI at 21cm). The combination of this wealth of data provides an excellent complement to this experiment for quantifying star formation and its feedback into the ISM. GMOX is the ideal instrument for obtaining high resolution ($R \sim 5000$), high SNR spectra of a magnitude limited ($V < 18$ mag) sample of star clusters in M83 (see Fig. 30). For a target with $V \sim 18$ mag (Vega), one hour integration with a $0.33''$ slit at $R \sim 5000$, will yield a SNR of ~ 60 per spectral pixel, and higher than 100 per resolution element.

E.3.2 EXOPLANETS IN THE GALACTIC BULGE

Most of the exoplanets discovered to date are nearby, –within ~ 500 pc of the Sun. But, as a result, the frequency and the physical properties of planets in different galactic environments (metallicity, stellar age, density, etc.) remain poorly constrained. The farthest exoplanets discovered were identified in the Galactic Bulge by the SWEEPS program, through continuous monitoring of 180,000 stars for 7 days with HST [142]. SWEEPS identified 16 candidate planets with orbital periods between 0.45 and 4.2 days and orbital radii $R < 1R_{\text{Jup}}$. Taking into account recent results that hot Jupiters can have radii up to $2 R_{\text{Jup}}$ [143], the total number of planet candidates increases to 35. However, photometric transit observations alone are insufficient to distinguish between planetary, brown-dwarf, and low-mass stellar companions because these all have similar radii. Radial-velocity (RV) measurements provide unambiguous confirmation since the expected RV amplitude is ~ 28 km/s due to a $0.1 M_{\odot}$ companion of a $1 M_{\odot}$ star, and ~ 2.8 km/s for a planet of $10 M_{\text{Jup}}$. Indeed, [142], used the FLAMES-UVES combination to confirm the planetary nature of 2 brightest candidates, thus demonstrating the feasibility of the RV technique.

Among the 35 candidates, 15 are brighter than $V = 22.5$ mag, and GMOX, because of its high image quality and throughput, can be used for a systematic RV study of this entire sample. Since the SWEEPS field is comparable to the GMOX FoV, all the planet candidates can simultaneously be observed with GMOX, allowing us to determine the physical properties (such as mass and radii) of exoplanets in the Galactic bulge, and whether the planetary frequency in the Galactic bulge is similar to the local neighborhood's. The high multiplexing efficiency makes it possible to obtain in one shot all the spectra for the Bulge candidate planet host in our sample, thus assuring a great degree of homogeneity in the data.

E.3.3 EXTREME HORIZONTAL BRANCH STARS IN GALACTIC GLOBULAR CLUSTERS

Horizontal Branch (HB) stars consist of a helium burning core of $\approx 0.5 M_{\odot}$ surrounded by a hydrogen burning shell and a hydrogen envelope of varying mass. The range of hydrogen envelope masses is thought to result from a spread in mass loss on the previous red giant branch (RGB) phase, a process very poorly understood. The temperature of an HB star (at a given metallicity) depends on its envelope radius, i.e. mass: the cooler HB stars have more massive envelopes. The hotter and least massive HB stars (Extreme HB, EHB), at the blue end of the HB, have too little envelope mass to sustain hydrogen shell burning. They dominate the UV flux in old stellar populations and are visible at cosmic distances. Understanding their properties and evolution is vital for interpreting the integrated UV light from old galaxies, and may hold the key to solving the long-standing "UV-upturn problem", the raise of far-UV flux with decreasing wavelength found in giant ellipticals.

The origin and evolution of EHB stars in GGCs is still hotly debated, since these stars cannot be explained within the framework of canonical stellar evolution models. Several competing formation scenarios have been proposed; the first is the hot flasher scenario, where the EHB progenitor has lost a significant amount of mass during the RGB phase, most likely due to stellar collisions or close binary interactions. This enhanced mass loss triggers a thermonuclear flash during the early white dwarf cooling phase, leading to extensive mixing of nuclear burning products, such as carbon and nitrogen [144, 145, 146, 147]. A second evolutionary channel is the He-enhanced scenario, where the high temperatures of EHBs are attributed to a greatly enhanced star initial He abundance [148]. Finally, some EHB stars in GGCs have been suggested to form via the merger of two He-rich white dwarfs [149]. Among the field population, the majority of EHB stars are found in short-period binary systems, with periods less than 10 days [150]. This forms a contrast with the apparent scarcity ($\leq 25\%$) of close binaries in GGCs found by [151, 152], on the basis of the radial velocities measured for EHB stars in three clusters. If EHB binaries in clusters are indeed as rare as current measurements suggest, this would indicate an evolutionary history where an initial He enhancement plays a dominant role, or point towards the binary fraction of EHB stars in GGCs decreasing with time due to the high stellar densities in these systems [151]. On the other hand, spectroscopic studies of ~ 150 HB stars in ω Cen showed that some EHB stars are Carbon enhanced [153], and that moreover there is well-defined positive correlation between the atmospheric Helium and Carbon abundances, including Carbon abundances up to a hundred times solar. Given the fact that He-enhanced scenario does not predict any metal enhancement, our results point toward the Hot flasher scenario for at least the most Helium-enriched stars of the sample, see Fig. 31.

Another massive GGC, NGC 2808, shows a well-populated EHB, with stars lying below the canonical zero-age HB in a UV - visual color-magnitude diagram [155]. NGC 2808, as well as ω Cen, are suspected to have a He-enhanced stellar sub-population which forms the bluest main-sequence. These He-enriched stars could be the progenitors of the EHB stars observed in these two clusters. However, spectra of the blue (and supposedly He-enriched) main sequence stars in ω Cen reveal a carbon abundance of only $[C/M] = 0.0$ [156] Thus the Hot flasher and He-enrichment scenarios make markedly different, and testable, predictions for the Helium and Carbon abundances of the blue hook stars. Other massive GGCs show extended HBs with a substantial fraction of EHB stars and the signature of multiple generations of stars, such as NGC 6441 and NGC 6338 [157]. Understanding the origin of EHBs in GGCs is then important not only for a mature understanding of the late evolution of low-mass stars, but also in the context of the interpretation of the multiple stellar populations observed in quite a few GGCs.

The main challenge in characterizing the EHB populations in GGCs is due to the faintness

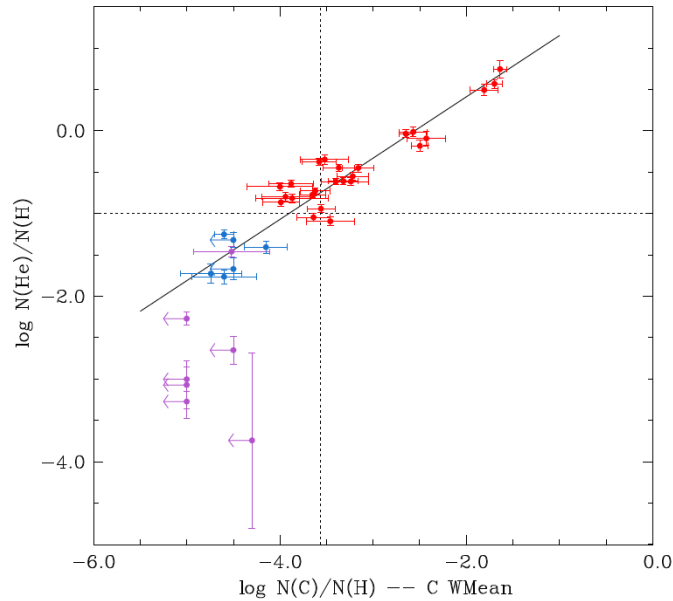


Figure 31: Helium abundance vs. the mean carbon abundance. This diagram shows an obvious relation between the abundances of the two elements, which is illustrated by the linear regression (black solid line) based on the 30 stars for which a carbon abundance was obtained. Dotted lines indicate the solar helium and carbon abundances. [Adapted from 154, , Fig.7].

of the targets ($18 < V < 21$ mag) and to the extreme crowding of the field (from 5 to 20 stars per arcsec² outside the cluster core). Moreover, Nitrogen lines have never been detected or had meaningful upper limits derived for EHB stars in any GGCs due to their relative weakness. We specifically searched for them in FORS2 spectra of ω Cen EHB stars, but were limited by the rather low spectral resolution (2.6 Å) and high noise level of the data. Most of the EHB stars for which spectra have been collected are in the outskirts of the clusters. In ω Cen, the ~ 150 HB stars with spectra from FORS2, FLAMES and VIMOS on the VLT telescope are all located at a distance of more than 3 arcminutes from the cluster center (core radius, $r_c \sim 1.5'$). Thanks to the high spatial resolution of GMOX we would be able to sample EHB stars closer to the cluster core, or inside the half-mass radius in other GGCs. This will allow us to sample a larger number of targets. In ω Cen for example, about 20 EHB stars could be observed with 1 GMOX pointing at a distance of $\sim 1'$ from the cluster center, and 10-15 objects inside the half-mass radius ($r_h \sim 5'$). If including hot HB stars, we will be able to sample 30-40 stars per pointing.

Using GMOX, with an exposure time of 1h (including overheads) we can reach a Signal to Noise (S/N) ratio ranging from 20 (visual) to 35 (blue). This means that with four spectra a S/N 40-70 can be reached. These spectra will be at least a factor of two more accurate than the FLAMES and FORS2 spectra and they will allow us to measure Carbon and Nitrogen abundances down to 1% by mass. By observing different fields around the cluster core and up to the half mass radius we will be able to sample ≈ 250 EHB stars with 3 nights of observations. The other massive GGCs are smaller ($r_c < 1'$) but still have a substantial fraction of EHBs and hot HBs outside the cluster core. In the case of NGC 2808 for example, there are ≈ 200 EHB stars outside the cluster core. These could be observed again with different GMOX pointings in a 2-3 night campaign.

Spectral coverage in the blue and visual will provide the opportunity to observe simultaneously lines of both Carbon (CIII: 4647, 4650, 4651, 4665, 5696 Å; CIV: 4658, 5801, 5811 Å) and Nitrogen (NII: 4040, 4240 Å, NIII: 4634, 4640 Å) in the HB stars. Coverage in the near-infrared is

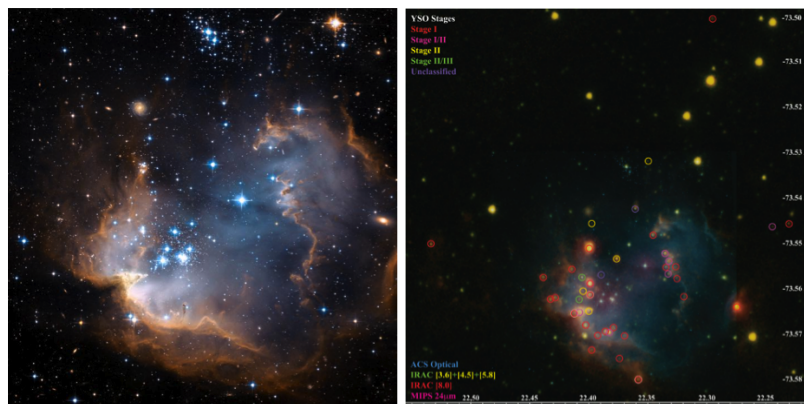


Figure 32: HST image (left), and Spitzer/HST combined image (right) of NGC 602 in the Small Magellanic Cloud from [164]. This region can fit into the GMOX For and spectra of all YSO candidates and young massive stars can be obtained in one night.

needed to constrain the possible occurrence of cool, low-mass companions that may contaminate the results. A resolution $R > 3500$ is required in the entire spectral coverage.

E.3.4 CHARACTERIZING YOUNG STELLAR OBJECTS IN THE MAGELLANIC CLOUDS

GMOX in 1 hr can detect with minimal confusion the continuum of a T Tauri star in the LMC at $SNR \simeq 5$, opening the possibility of studying in detail Pre-Main-Sequence stars (PMS) outside the Milky Way. The Spitzer SAGE-LMC [158], SAGE-SMC [159], and Herschel HERITAGE [160] programs have surveyed the LMC and SMC with relatively high spatial resolution ($\sim 2'' - 30''$) at IR wavelengths, up to $500 \mu\text{m}$. Thousands of PMS stars and Young Stellar Objects (YSOs) have been identified [161, 162, 163, 164, 165, 166] creating the largest and most complete census of young stars in an extragalactic environment. Confusion, contamination, and reddening vs. temperature degeneracy, however, hamper progress when using only photometry, even from HST. Spectroscopy allows us to characterize the spectral type, measure accretion, and discriminate between optically bright YSOs and post-asymptotic giant branch stars, as demonstrated by [167] using the AAOmega spectrograph. These spectra span the $3700\text{--}8800 \text{ \AA}$ range with $R \sim 1300$, well within the GMOX range. Unlike AAOmega, GMOX will be capable of taking spectra in the youngest, richest and most crowded clusters like NGC 602 (Fig. 32), allowing detailed studies of star formation in low metallicity environments.

E.4 GMOX IN THE CONTEXT OF OTHER MAJOR FACILITIES

It is not possible to encapsulate in a single figure of merit the strengths of GMOX and compare them with the spectrographs operating at other 8-m class telescopes. Figure 33 shows the area covered by GMOX in a Resolving Power vs. Wavelength diagram, against the areas occupied by the spectrographs at Keck and VLT. GMOX occupies the central part of the field, matching the parameters of several other instruments. Diagrams of this type do not capture all weaknesses or strengths of each instrument, but convey the message that GMOX is not a niche instrument but a most powerful workhorse.

It is more appropriate to limit the comparison to multi-slit and IFU instruments, designed to work on narrow fields like those delivered by the Gemini telescopes. Spectroscopic observations of dense fields using long-slit or multi-object spectrographs based on either fibers or punched plates are problematic, if not impossible in the case of an AO-fed system. Working with plates drilled with slit widths below $0.5''$ poses very strong requirements to the long-term geometrical stability of the focal plane, besides the obvious inconvenience of doing pre-imaging weeks in

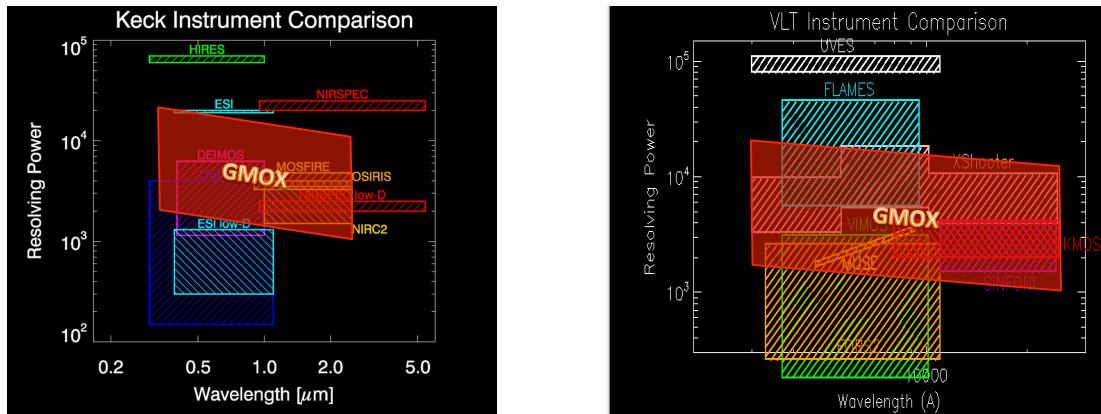


Figure 33: Illustration of the parameter space “spatial resolution” vs. “field coverage” for the complement of spectrographs at Keck (left) and VLT (right), with the area covered by GMOX.

advance and having to guess the optimal width vs. realistic seeing conditions. Increasing the slit size decreases resolution, increases the background and source confusion, which combine to limit sensitivity and data quality. To minimize problems, one concentrates on the brightest, most isolated sources. Better results can be achieved with modern instruments like MOSFIRE, having the capability of moving slits across the field, but the number of slits is limited (up to 46 in the case of MOSFIRE) and the physical size of the devices makes this approach optimal for relatively wide fields, e.g. about 6×6 arcmin in the case of MOSFIRE. Given these limitations, a general consensus has emerged that IFU instruments are better tailored for observations of crowded fields. It is therefore instructive to compare GMOX with current IFU instruments, following the excellent summary provided by Tim-Oliver Husser in his recent PhD Thesis at the University of Göttingen.

There are three main approaches to Integral Field Spectroscopy:

- I Lenslet array - An array of micro-lenses splits up the image and the light from each is dispersed by a spectrograph [168]. An example for this kind of IFU is the SAURON instrument [169] at the 4.2 m William Herschel Telescope on La Palma.
- II Fibers - The most common technique for IFUs uses a bundle of optical fibers in the image plane, which transfer the light to the spectrograph [170]. A major problem with this approach is the gaps between the fibers, i. e. the spatial coverage is not contiguous. This disadvantage can be overcome by using lenslets in front of the fibers, which focus all their light into the fibers [171]. Examples are the Potsdam Multi-Aperture Spectrophotometer (PMAS, see [172]) at the 3.5m telescope on Calar Alto, or two existing instruments at the VLT: ARGUS [173], the IFU mode of the FLAMES+Giraffe spectrograph, and the Visual and IR Multi-Object Spectrograph (VIMOS, see [174]).
- III Image-slicer - The need for fibers can be eliminated by using segmented mirrors, which divide the image into slices that are then laid out end to end and transferred to the spectrograph [175]. An IFU of this type called SINFONI [176] is attached to one of the VLT telescopes. A more recent example is MUSE [177].

Table 17 and 18 show a list of IFUs in the optical and IR domain operating at 8m class telescopes, plus the next generation of IFUs planned for the 30-m class telescopes. Figure 34 illustrates how these instruments cover the pixel/slit size vs. field size parameter space. There is an

obvious “main sequence” due to the anticorrelation between field coverage and spatial resolution. A few instruments stand out for their larger field of view: MUSE and SINFONI at VLT and the future IFU for the ELT (preliminary requirements). JWST/NIRSpec stands out for its large field of view in MSA mode (represented by a square), while NIRSpec/IFU falls within the main sequence. Most of the IFUs operate in the Infrared fed by Adaptive Optics. IFUs working in the visible are generally operated in seeing limited conditions. GMOX is represented by red and blue squares, to indicate that it covers both the visible and the IR wavelength range. The slit size can be tuned to adapt to both seeing limited and AO conditions (again, with fine tuning on each individual source). The field coverage is typically 2-3 orders of magnitudes larger than IFUs with similar spatial resolution.

Overall, the main competitors of GMOX will be MUSE in the visible and JWST/NIRSpec-MSA in the IR. MUSE is an extraordinary instrument: first a field slicer divides the focal plane into sub-fields that are sent to 24 identical IFUs (Laurent et al., 2010), where secondary image slicers split further the slits feeding the light to the spectrographs. Each of the 24 spectrographs has a $4K \times 4K$ CCD detector with $15 \mu\text{m}$ pixels. The wavelength coverage is 4650\AA to 9300\AA with a spectral resolution of $\Delta\lambda=2.6$, i.e. $R = 1770$ at the blue end and $R = 3590$ at the red end. Two different modes are available: in the wide field mode (WFM), the field of view is $60'' \times 60''$ with a spatial resolution of $0.2''$, while for the narrow field mode (NFM) is $8'' \times 8''$ and $0.025''$ respectively, requiring an adaptive optics system under development. For both modes, the number of spatial pixels is 300×300 .

In comparison to MUSE, GMOX covers a much wider spectral range with higher spectral resolution; at GeMS, GMOX has the same field of view of MUSE, otherwise the field is four times larger. In terms of sensitivity, in the current wide-field mode MUSE has no losses associated with an AO bench but has more reflections: overall the losses may compensate each other. MUSE delivers typical images of $0.7''$ [9]; if GeMS is just able to provide a 50% reduction of the natural PSF, GMOX should outperform MUSE on individual sources. Of course, MUSE will still produce unique science each time an IFU is strictly needed to map every single pixel in the field, unless a Hadamard Spectroscopy IFU mode is implemented on GMOX.

In what concerns JWST/NIRSpec, there are obvious advantages from operating in space: much lower background and continuous spectral coverage from 1 to 5 micron. Still, GMOX has its own strengths: spectral coverage across the visible range, higher spectral resolution ($R \simeq 5000$ vs. $R \simeq 2700$, nominal values), a larger number of slits (2.1 million mirrors in a single DMD against the 250,000 shutters in the set of 4 MSA) and narrower slits: a $200 \times 450\text{mas}$ shutter covers an area 56 times larger than a $40 \times 40\text{mas}$ mirror at GeMS. In practice, GMOX has the spatial resolution of the NIRSpec IFU with the field coverage of the NIRSpec MSA. Concerning sensitivity, the dark sky continuum observed on Mauna Kea can be approximated as a 5800K gray body times the atmospheric transmission, scaled to produce $18.2 \text{ mag/arcsec}^{-2}$ in the H band, (Maihara et al. 1993 PASP, 105, 940). By comparison, the sky brightness in space ranges from $\simeq 4 \times 10^{-19} \text{ erg cm}^{-2} \text{ s}^{-1} \text{ \AA}^{-1} \text{ arcsec}^{-1}$ (low-zodi) to $\simeq 1.2 \times 10^{-18} \text{ erg cm}^{-2} \text{ s}^{-1} \text{ \AA}^{-1} \text{ arcsec}^{-1}$ (high-zodi), corresponding to 1/5th to 1/15-th of the dark-sky continuum on the ground. The smaller slit size, together with the larger aperture, makes GMOX on Gemini competitive with JWST/NIRSpec over the $\simeq 80\%$ fraction of the near-IR spectrum unaffected by telluric lines.

Another practical advantage of GMOX is the higher filling factor ($\simeq 91\%$ for the DMD, $\simeq 64\%$ for the MSAs). The presence of a wide gap between slits in NIRSpec MSAs means that only a fraction of the sources in a field will be optimally aligned within the “sweet spot” of each aperture; multiple exposure will thus be needed to acquire all interesting targets that could have been observed simultaneously if the gap were minimal, as in the case of GMOX. This represents a substantial operational overhead. The 5% gap between DMD mirrors increases throughput, allows one

to use multiple elements to modulate the slit width, and simplifies data processing and analysis. Ease of scheduling and availability contribute to make GMOX a precious resource complementary to JWST/NIRSpec.

Instrument	Type	Range [Å]	Resolution	Field of View	Pixel Size
VLT-ARGUS	II	3700 – 9500	5600-46000	12"×7" 6.6"×4.2"	0.52" 0.30"
Gemini-GMOS	I	4000 – 11000	630–4300	5"×7"	0.2"
Subaru-Kyoto 3DII	I	3600 – 9200	1200	3.6"×2.8"	0.096"
VLT-VIMOS	II	4000 - 11500	200–3000	13"×13" –54"×54"	0.33" –0.67"
VLT-MUSE	III	4650 – 9300	2.6 Å	60"×60" 8"×8"	0.2" 0.025"
GMOX	MEMS	3650 -24000	4500	90"×45"	$n \times 0.083''$

Table 17: Selection of available IFUs for the visible domain in comparison to GMOX. The types are (I) lenslets, (II) fibers and (III) image-slicer.

Instrument	Type	Range [μm]	Resolution	Field of View	Pixel Size
VLT-KMOS	III	0.8-2.5	1800-4200	24 × 2.8" × 2.8" 0.2"	
VLT-SINFONI	III	1.1 – 2.45	1500–4000	8"×8"	0.25"
	III	1.1 – 2.45	1500–4000	3"×3"	0.1"
	III	1.1 – 2.45	1500–4000	0.8"×0.8"	0.025"
Keck-OSIRIS	I	1.0 – 2.4	3400-3800	up to 0.45"×1.28"	0.02"
	I	1.0 – 2.4	3400-3800	up to 1.68"×2.24"	0.035"
	I	1.0 – 2.4	3400-3800	up to 2.4"×3.2"	0.05"
	I	1.0 – 2.4	3400-3800	up to 4.5"×6.4"	0.10"
Gemini-NIFS	III	0.94 – 2.4	5000-6000	3"×3"	0.103"×0.04"
GMT-IFS	III	0.9 – 2.5	5000-10000	0.53"×0.27"	0.006"
	III	0.9 – 2.5	5000-10000	1.06"×0.54"	0.012"
	III	0.9 – 2.5	5000-10000	2.20"×1.125"	0.025"
	III	0.9 – 2.5	5000-10000	4.40"×2.25"	0.050"
ELT-IFU ^{*a}	TBD	0.5 – 2.4	5000-20000	0.2" – 10"	0.004"-0.040"
TMT-IRIS	I, III	0.8 – 2.5	4000-8000	0.064"(BB)[0.458"(NB)]×0.512"	0.004"
	I, III	0.8 – 2.5	4000-8000	0.144"(BB)[1.008"(NB)]×1.154"	0.009"
	I, III	0.8 – 2.5	4000-8000	1.1"×2.275"	0.025"
	I, III	0.8 – 2.5	4000-8000	2.2"×4.55"	0.050"
JWST-NIRSpec	MEMS	0.6 - 5	100, 1000, 2700	3.6'×3.4'	0.2"×0.46"
JWST-NIRSpec	III	0.6 - 5	100, 1000, 2700	3.0"×3.0"	0.1"×3"
GMOX	MEMS	3650 -24000	1500-15000	90"×45"	$n \times 0.083''$

Table 18: Same as Table 17

^aRequirements from

https://www.eso.org/sci/facilities/eelt/docs/ESO-191883_2_Top_Level_Requirements_for_ELT-IFU.pdf

In the future, most of the new developments will presumably concentrate on the instrumentation for the 30m-class telescopes, that will approach their first light at the same time as GMOX. GMOX will probably remain unique among 8m class telescopes. At some point in the next decade the new facilities will start operating with Adaptive Optics, outperforming Gemini at IR wavelengths. It is quite possible, however, that the technological advances allowing 30m telescopes to reach their diffraction limit in the near IR, requiring e.g. $4^2 = 16$ times more actuators, will en-

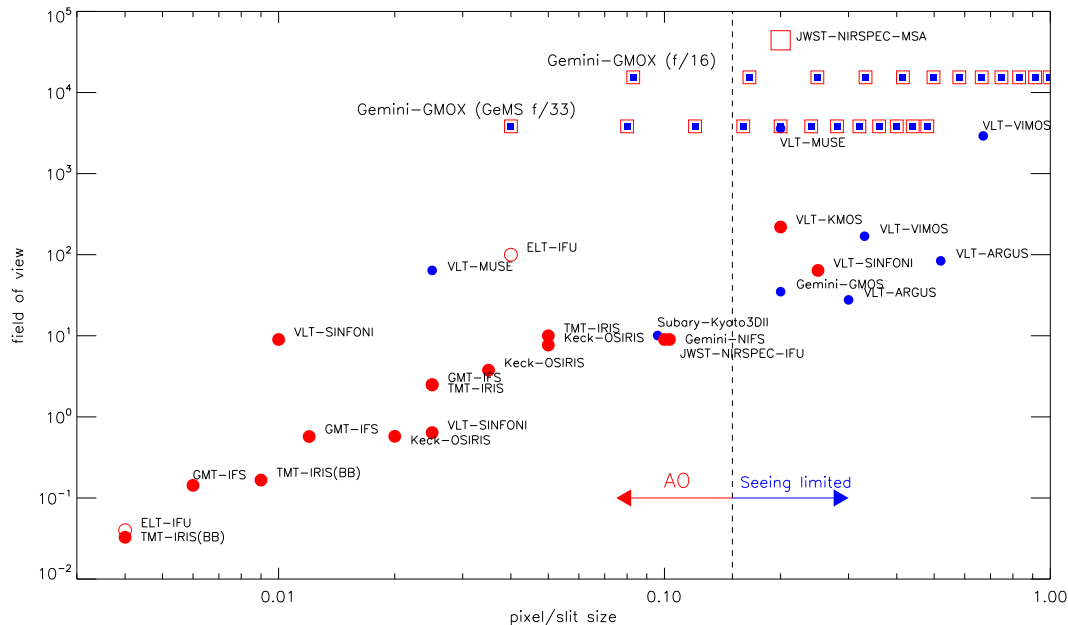


Figure 34: illustration of the spatial resolution vs. field coverage achieved by current and future IFUs at 8-m and 30-m class telescopes, plus JWST. Blue and red colors indicate visible and infrared spectral range, respectively. The vertical line is indicative, representing the region that separates AO vs. non-AO optimized systems.

able 8m telescopes like Gemini to push their diffraction limited performance well into the visible regime; 8m telescopes could then play a critical, complementary role to the 30m telescopes. GMOX is able to take full advantage of these new capabilities, and can remain a formidable workhorse for Gemini till the end of the next decade and beyond.

F CONCEPT OF OPERATIONS

Versatility and ease of operations are key features of GMOX. The instrument can adapt to the variety of seeing conditions and AO performance encountered at the focal plane of Gemini without changing its opto-mechanical configuration, except for the DMD pattern: from the hardware point of view, the “reaction time” of GMOX is nearly instantaneous. This means that during the night GMOX can perform a large variety of observations, limited only by the efficiency of the ancillary systems, adaptive optics in particular.

F.1 GEMINI AO AND GMOX

An Adaptive Optics System like ALTAIR on Gemini-North achieves the highest Strehl ratio using natural guide stars (NGS). For best performance, the natural star has to be brighter than $V \sim 13$ and within $\sim 25''$ from the target; with these restrictions NGS-AO is viable only for a limited number of targets. Using a laser guide star (LGS), the natural guide star is needed only for tip-tilt correction, relaxing the requirements on its brightness ($V \lesssim 17$) and distance from the target (up to about $60''$). Still, especially at high galactic latitudes, this is often not enough. The popular “deep fields” (Hubble, GOODS, Chandra, Candelas, Frontier Fields...) surveyed at multiple wavelengths

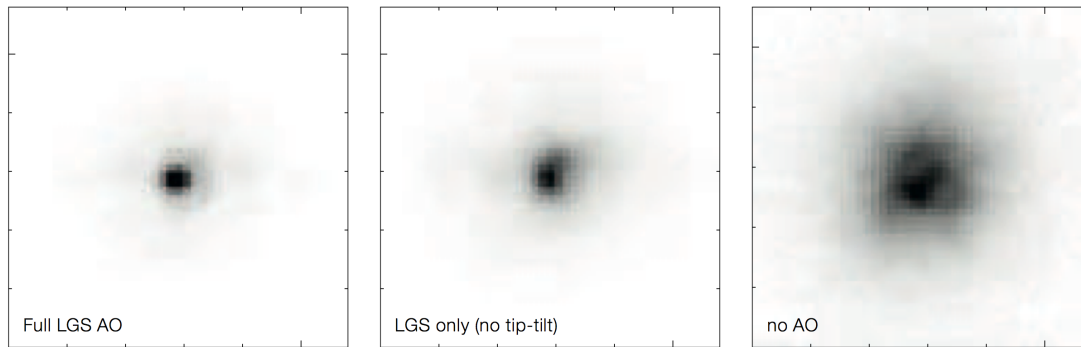


Figure 35: NAOS performance measured on CONICA in the K-band for full LGS-AO (left), and without tip-tilt (center). The seeing limited PSF (right) is shown for reference. With full LGS-AO, the Strehl ratio was 22% and the $FWHM \sim 85$ mas. Without tip-tilt, the Strehl ratio was reduced to 10 % and the FWHM increased to 130 mas. For comparison, the K-band FWHM without AO is 300 mas. (from Davies et al, 2008, ESO Messenger 131, 7)

to study galaxy formation and evolution are especially problematic: to minimize scattered light from nearby sources, they are usually selected in regions with the minimum number of even moderately bright stars.

To overcome these limitations one can increase the complexity of the AO systems, developing e.g. a Multi-Conjugate AO system like GeMS on Gemini-South, delivering excellent correction over a $\sim 85'' \times 85''$ field of view. But even with GeMS, the sky coverage is not 100% and the actual Strehl ratio depends on the availability, brightness and distance of multiple tip-tilt stars. The opposite approach is to reduce complexity and accept a somewhat modest wavefront correction, but over most of the sky. This is the case of Ground Layer AO systems, that correct for the common turbulence located near the entrance pupil of the telescope neglecting the uncorrelated higher altitude contributions. When most of the atmospheric turbulence lies in the ground layers, GLAO substantially improves the image quality over a large field. This is the strategy adopted e.g. by the SAM AO system at the SOAR telescope, which delivers $0.4''$ images in the I band on about 50% of the nights. At Gemini, this type of approach is implemented on Gemini-North with the Field Lens Option, a convex lens that conjugates ALTAIR to the ground level rather than at high altitude. The field covered by the ALTAIR Field Lens is $50''$ diameter, limited by the size of the lens itself, but the unvignetted field delivered by ALTAIR is $120''$ in diameter. It may be possible to upgrade the field lens to deliver larger field of view.

An even simpler approach has been developed at ESO, the so-called “seeing enhanced mode” [178]. Starting with the fact that with GLAO the sky coverage increases as the acceptable Strehl ratio decreases, one can take the extreme position of ignoring the tip-tilt star and work with the laser only. In good seeing conditions, always needed for any type of AO, the higher order correction provided by the laser will tend to concentrate the flux in the core of the PSF. The tip-tilt jitter, left uncompensated, will broaden the PSF core on top of the extended halo; a small broadening of the PSF core is enough to significantly degrade the Strehl ratio, but in fact the FWHM still remains much better than the seeing limit (Fig 35). Dispensing completely with tip-tilt correction has the huge advantage of 100 % sky coverage. Seeing enhanced AO can be regarded as the guaranteed minimum improvement achievable with an all-sky AO system; while its performance can be disappointing from an imaging perspective, for slit spectroscopy the reduction of the FWHM is a strength to be exploited.

GMOX design parameters are largely driven by the telescope focal ratio, the physical size of

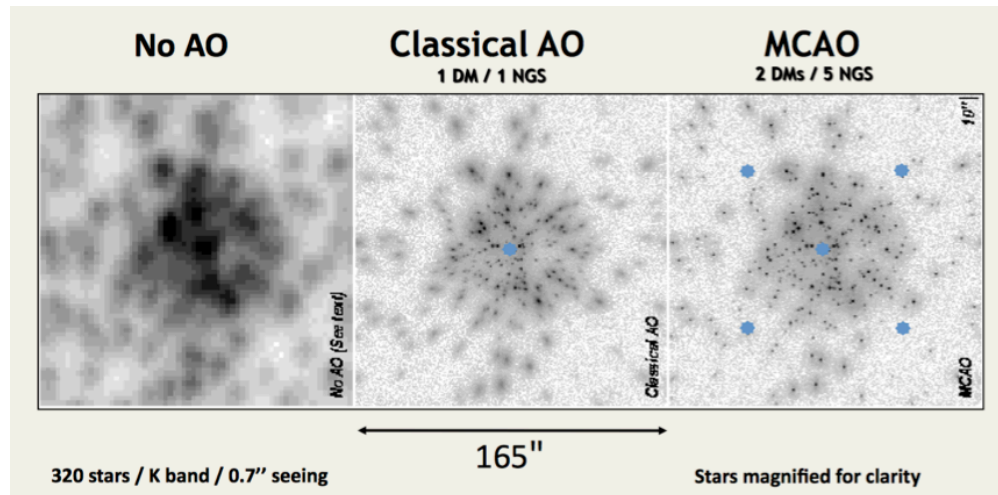


Figure 36: Summary of AO performance in different regimes. GMOX can adapt to each source, adjusting the position of the slit and its width “on-the-fly” for optimal signal-to-noise. (from https://www.noao.edu/meetings/ao-aas/talks/Christou_Gemini_AO_AAS.pdf).

the DMDs and the size of the latest generation of detectors. There is little room for tuning. The fact that they nicely match the unvignetted field of view of Gemini, the field of view delivered by GeMS and (potentially) by ALTAIR and the core of the diffraction limited PSF can be regarded as a fortuitous: GMOX can optimally exploit the enhanced image quality provided by the AO systems, regardless of the achieved level of correction. The illustrative cases shown in Figure 36, i.e., seeing limited, classical AO, and MCAO, as well as any other type of performance delivered e.g. with a GLAO system, are all good matches for GMOX. A simple field acquisition image is enough to optimally position the slits on targets, with widths that can be matched to the FWHM of individual targets, variable across the field and in wavelength. Hereafter we will consider three different observing conditions to illustrate how the instrument can be optimally operated. In principle, these conditions could be obtained on the same night following the vagaries of observing conditions or the sudden appearance of a target of opportunity.

F.2 NORMAL SEEING CONDITIONS, PARTIAL AO CORRECTION

In about 50% of the nights the V-band seeing at Gemini is between 0.8'' and 0.4''. In these conditions the AO provides a substantial reduction of the FWHM over the full field of view, by a factor $\simeq 2 - 2.5$. A FWHM ranging from 0.2'' to 0.4'' from *K* to *U* is considered typical for e.g. Ground-Layer AO correction. It is reasonable to assume that partial AO correction, or some sort of “seeing enhanced mode” will represent the standard observing condition of GMOX; in fact, the nominal slit widths and resolution have been tuned around these conditions. Dispensed from the need to find a natural guide star in the immediate vicinity of the target, GMOX can thus operate at $R \simeq 5,000$ over the full wavelength range. As shown in Figure 3, the mean half-light radius of galaxies at redshift $z > 2$ is in the range 0.2'' to 0.4'', so partial AO correction is entirely adequate for spectroscopic studies of these sources. With GEMS this size will correspond to resolving powers of $R \simeq 2,500$.

Depending on the size/brightness of the target and on the science goals, the slit width can be adapted to match the broader PSF, reducing slit losses but degrading spectral resolution, or made narrower to preserve or even push the resolving power above nominal values. The assignment

of the optimal slit width for each individual source in the field can be made in real time by an algorithm using the field acquisition image to extract positions and FWHM or half-light radii, and a functional form for the FWHM vs. slit size relation.

Since these seeing conditions are statistically the most frequent, GMOX can perform ultra-deep observations split over several nights, reaching $SNR > 10$ at $m(AB) = 25$ in 40 hours (see Figure 14). Binning the reduced spectra could push this limit to levels not far from those achieved by JWST/NIRSpec at full $R = 3,000$ resolution.

F.3 POOR/BAD SEEING CONDITIONS

In about 30% of the nights the V-band seeing at Gemini is worse than $0.8''$. When the seeing is worse than $\simeq 0.8''$, GMOX can simply bypass the AO system to maximize throughput.

Since the lack of AO correction mostly impacts the potential performance of the IR channel, observations in natural seeing may focus primarily on spectroscopy in the visible range or on spectroscopy of sources that do not require AO correction. These include **spectroscopy of bright QSOs, stellar spectroscopy in the Milky Way bulge and halo, and immediate follow-up of LSST transients**. In this case, the spectroscopic visible channels will be *prime*, the IR (and the field imaging cameras) *secondary*. On the other hand, IR observations may turn out to be more valuable in bright time and the IR channel would then be *prime*. **Low mass pre-main sequence objects in nearby star forming regions and bright $z \sim 6$ QSOs** ($J_{AB} \sim 21$) represent typical classes of IR sources that can be targeted in these conditions. To maintain the resolving power above $R \simeq 1,000$, needed for acceptable OH subtraction, IR observations should in any case avoid slits of the order of $1''$ (at $f/16$). The slits in the *secondary* channels can be kept identical to preserve the source area being observed (possibly the default case for extended sources), tuned to match the $\lambda^{-1/5}$ variation of the seeing with wavelengths (possibly the default case for point sources), or adjusted to achieve some different resolving power. It is also possible to observe any target sequentially with different slit widths, e.g. $5''$ for initial flux calibration and $1''$ for science.

When the visible channels are *prime*, they tend to drive long integrations on the CCDs keeping the object at the same position under the slit. Moves to correct for bad pixels, to observe in nod-shuffle mode, or to sample the slit in the spectral direction will require minimal overhead, driven by the telescope slew time, guide star acquisition and detector readout time, while the re-configuration of the DMDs will be, again, instantaneous. Viceversa, if the IR channel is *prime* it may be preferable to nod more frequently for optimal sky subtraction. In general, the *secondary* channel and the imaging cameras will take data in parallel with readout times compatible with the *prime* setup, i.e. integration times and frequency of telescope slews. Since the target flux will be known, e.g. from the target acquisition images, setting the optimal readout parameters should be done automatically. All field images will be processed in real time to monitor slit alignment and changes of atmospheric conditions. They may also be taken in different filters, if scientifically valuable.

F.4 EXCELLENT SEEING CONDITIONS, FULL AO CORRECTION

In the 20% of the nights with excellent seeing conditions, the AO systems can achieve their ultimate performance allowing GMOX to unleash its full potential. At GeMS, it could be possible to select slit widths as small as 41mas , enabling the deepest observations of unresolved point sources in crowded fields such as the **Large Magellanic Clouds, Globular Clusters, etc.**

Extreme AO correction improves the FWHM across the full spectral range, but the gain will always be larger in the near-IR and marginal in the UV. Therefore, the IR channel will always be

prime. If the source density is high enough, the tip-tilt stars can be monitored by GMOX's field cameras, otherwise GeMS has to remain in charge. In the first case, GMOX can take data in the Blue channel, otherwise the dichroic in GeMS will prevent wavelengths shorter than 5900 Å to reach GMOX. It is therefore possible that in the most exquisite seeing conditions GMOX will be incapable of taking spectra shortward of 6000 Å.

As a final remark, we must notice that GMOX will always be able to take hundreds of spectra and 3 multi-color images in parallel. If a program requires the acquisition of one or a few spectra, nothing prevents one from pointing to random sources "on the fly", selected just on the basis of colors (e.g. from LSST) or kinematics (from Gaia) or any other criterion. While proposers can always select multiple targets of lower priority in their fields, the Observatory may fill-in with other targets whenever possible, implementing a policy similar to the "pure parallel" mode that has been so successful on *HST*. If an average observation lasts 1 hour and takes 400 spectra, one will end up with hundreds of thousand spectra per year. Despite its small field of view, GMOX can be rightfully considered as one of the "massively multiplexed spectrographs" of the next generation.

F.5 OBSERVING MODES

GMOX observations will be carried out following observing templates implementing different observing strategies. Planning tools, based on those developed for JWST/NIRSpec, will be provided to facilitate users to craft their observations. A standard observing template could contain the following steps:

- Telescope pointing; guide and AO setup
After pointing the telescope to a target, one performs the standard operations of guide star acquisition and AO control loop initialization. These procedures are not controlled by the GMOX GUI.
- Target Acquisition: Basic DMD setup
A typical GMOX observation starts with the 3 imaging channels taking in parallel an acquisition image of the field. Since the mapping of the celestial field on both the DMD and the detectors has been calibrated, i.e. the Pixel-to-DMD maps are supposed to be always available, it is sufficient to use just one of these images to drive the selection of the slits on each DMDs. If a finding chart is at hand, target acquisition can be as simple as point-and-click on the target in the "prime" image, the one where it has been detected with the highest signal to noise. The operator may have predefined the slit width on the basis of the science case, or just adopt a value adequate to the current observing conditions. The control system automatically determines the centroid of the selected source and set/accept the slit width; tilting the relative group of micromirrors is instantaneous and the science integration can begin (Figure 37). The total acquisition time will largely depend on the overhead associated with acquiring and displaying a short image; exposures of 10–20 s in broad-band should generally be adequate to identify typical spectroscopic targets, or at least reference sources nearby. We should remark that if the telescope pointing is just adequate, say within a few arcseconds, there is no need for extra moves to put the source "under the slit", no matter how narrow it is: it is the slit that follows the source with great accuracy. Overall, with some optimization of the Graphic User Interface, it should be possible to start science integrations within 60s.

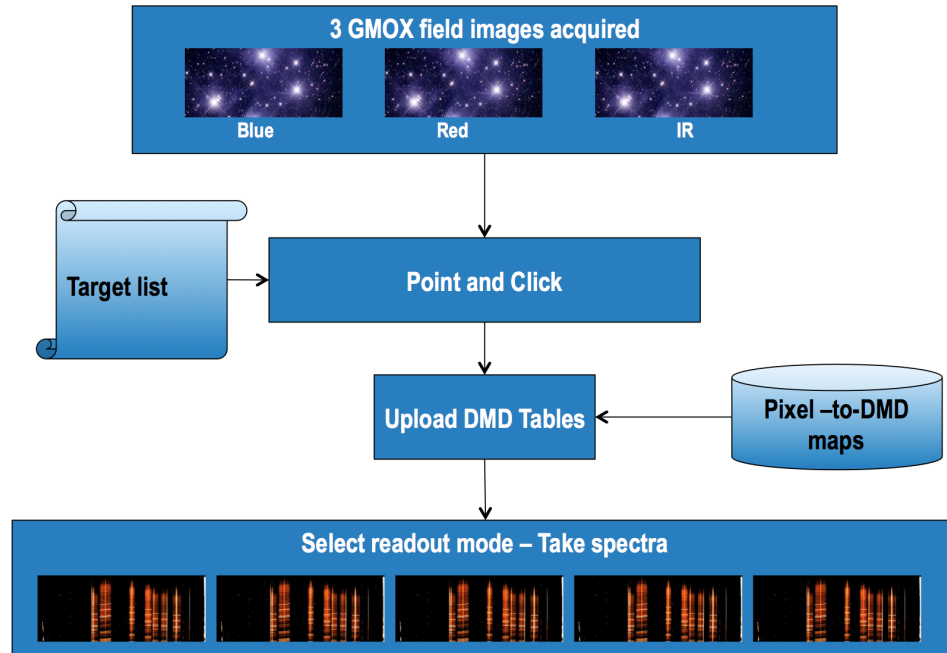


Figure 37: Flow diagram of the basic target acquisition of GMOX, applicable for single sources like e.g. immediate followup of transients and targets of opportunity.

- Target acquisition: advanced DMD setup

The basic scheme discussed in the previous point can be refined adding a set of functions to handle more complex cases, like the acquisition of faint and/or multiple targets. First, the acquisition images may be processed to remove bias, correct for flat field and mark saturated bad pixels that may affect the measure of the centroids. Second, on the cleaned image(s) an automatic routine (SExtractor or similar) can be run to build a catalog of sources to be cross-matched with the target catalog provided by the user. SExtractor would return, together with the centroids, the size of the targets; both information can be used to automatically fine-tune the slit widths, according to predefined criteria and constraints like e.g. the range of acceptable resolving powers, to optimally match the science goal to the actual seeing conditions or AO performance. The importance of accurate centroiding and slit width tuning is nicely illustrated by Figure 2 of Sánchez-Janssen et al. 2014 (REF A&A 566, A2 (2014)) showing the fraction of transmitted flux, as a function of FWHM-to-slit width ratio, when a Gaussian point source is displaced perpendicular to the slit by a fractional amount of the slit width, $\Delta x = (x - x_0)/w$. The plot only shows the minimal loss, accounting only for geometrical effects.

If the field is heavily crowded, it will be necessary to carefully craft the input catalog to prevent spectral overlap, as usual with a multi-slit spectrograph. However, unlike conventional instruments, DMDs allow one to override any preset targets with a simple mouse click. All these operations, with the exception of any last minute manual intervention, can be made automatic, with execution time depending only on the capability of the control system; again, once the configuration file has been created, the slit set up is instantaneous. Also, in this case the duration of the setup depends mostly on the overheads; since the field images have limited pixel size, image processing analysis should proceed quickly. Setting the optimal slits for hundreds of targets, if their list has been previously prioritized, should not take more

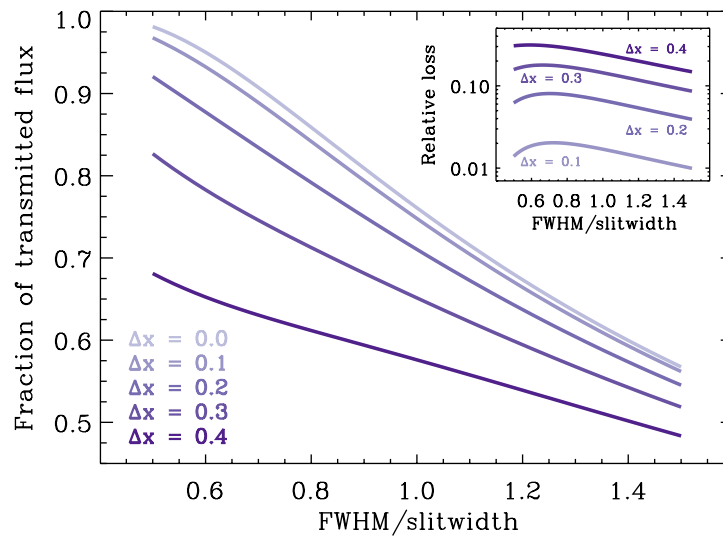


Figure 38: Fraction of transmitted flux as a function of FWHM-to-slit width ratio for a Gaussian point source that is displaced perpendicular to the slit by a fractional amount of the slitwidth, $\Delta x = (x - x_0)/w$. The inset panel shows the flux loss relative to the case where the object is perfectly centered within the slit. A slit length $l = 10w$ is assumed. (from Sánchez-Janssen et al. 2014 (REF A&A 566, A2 (2014)))

than 2 or 3 minutes.

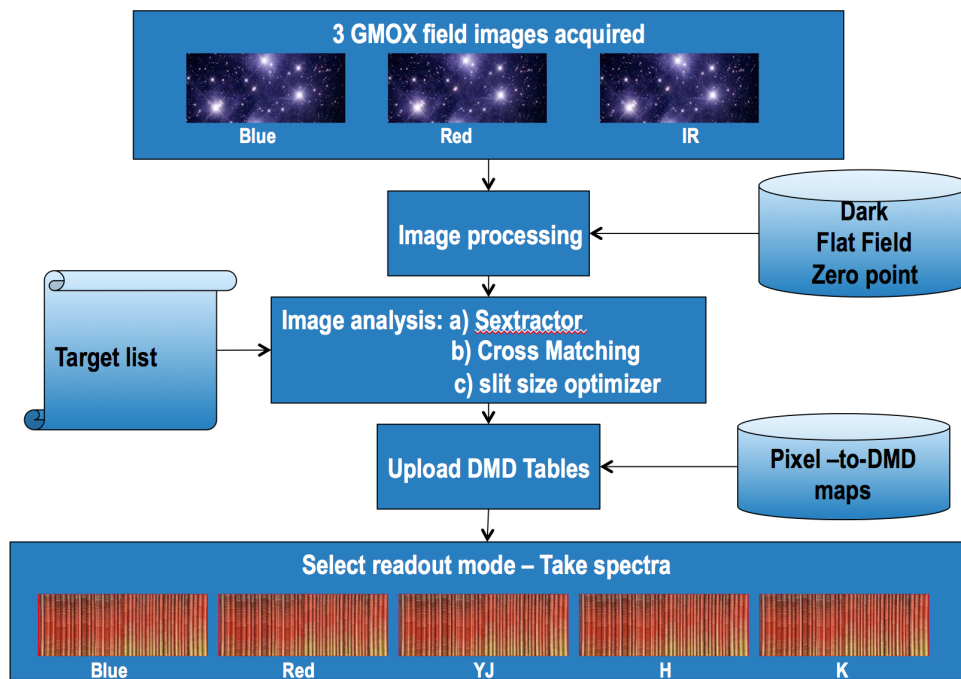


Figure 39: Flow diagram of the advanced target acquisition of GMOX, to be used with faint and/or large numbers of targets.

A further refinement, probably mandatory in the early days of operation, is to take three short check-out images in parallel before starting long science exposures; the imaging channels will show the full field with each selected target masked by a dark spot, or a bar; in our

experience with IRMOS at KPNO, the symmetry of the PSF wings leaking from both sides of the slits provides a formidable tool to immediately assess the quality of the alignment. Further fine tuning could still be possible at this point, but should not be needed.

- Science Exposures: Integration on both the imaging and the spectroscopic channel proceed in parallel. The mode of operation is typically driven by the “prime” spectroscopic channel(s). Selecting an exposure of e.g. 900 s for the Blue and Red channels, followed by a dithering move, means that the IR spectroscopic channels can match the length of the CCD integration with a sequence of multiple short ramps, say 6×150 seconds. The imaging channels can be used in multiple ways, e.g. a) to monitor the slits, taking a frame every few seconds; b) to perform deep integration, possibly in a variety of filters; and c) for guiding or tip-tilt control, in subarray mode. The imaging channels can also provide absolute flux calibration: absolute spectrophotometry with GMOX is easy to implement.

The acquisition strategy can be refined to allow for a) source dithering, moving the telescope and slit pattern a few pixels away to remove bad/hot pixels; b) slit sub-samplings (both along the dispersion and cross-dispersion directions) to smooth the detector response and allow for better subtraction of the OH lines; and c) nod-and-shuffle on the CCD channels for improved removal of OH lines. Observing templates can implement different strategies, allowing the operator to pick up the science program best matched to the observing conditions without hardware reconfiguration.

Generally, a science image will contain both sources and sky spectra, all paired with the appropriate flat fields and line images. For IRMOS we have developed in IDL a data processing pipeline that can automatically process the data. As long as calibration images are available, processing of the spectra can proceed in parallel and be made nearly automatic. Final calibration will require data relative to telluric standard stars.

F.6 NON-STANDARD OBSERVING MODES, HADAMARD TRANSFORM SPECTROSCOPY

GMOX can be easily configured as an IFU performing Hadamard Transform Spectroscopy. In a Hadamard Transform Spectrograph (HTS), the telescope focal plane is projected onto a set of N long slits (e.g. a $180'' \times 90''$ field can be split into $N = 180$ slits each $180'' \times 0.5''$). Of these slits, $N/2$ are open and $N/2 - 1$ are closed. The “barcode” is built following the terms in the first row of an $N \times N$ Hadamard matrix (an orthogonal matrix whose entries are either +1 or -1). Spectra received by the $N/2$ open slits will turn out badly superimposed, as if one had taken a slitless spectrograph randomly masking half of the field. But by changing the bar code N times, i.e. scanning the full Hadamard matrix row by row, and reading each image one can eventually reconstruct the full datacube in (x, y, λ) [see ref. 179, for a demonstration with IRMOS at Kitt Peak]. This is because each row of the Hadamard matrix represents an orthogonal vector on the N -dimensional space probed by each pixel. Moreover, the inversion is analytic and immediate thanks to the symmetry of the Hadamard matrix. Producing a HTS datacube takes the same time needed to scan the field with a single long-slit, but the exposure time on-source at the end is $N/2$ (90 times, in our example) longer. The gain achieved in signal-to-noise (Fellgett advantage) is $\sqrt{N}/2$ ($=6.7$ for $N = 180$) when detector noise dominates. If a strong emission line is present in a limited portion of the spectrum, the Fellgett advantage at the line peak is even higher.

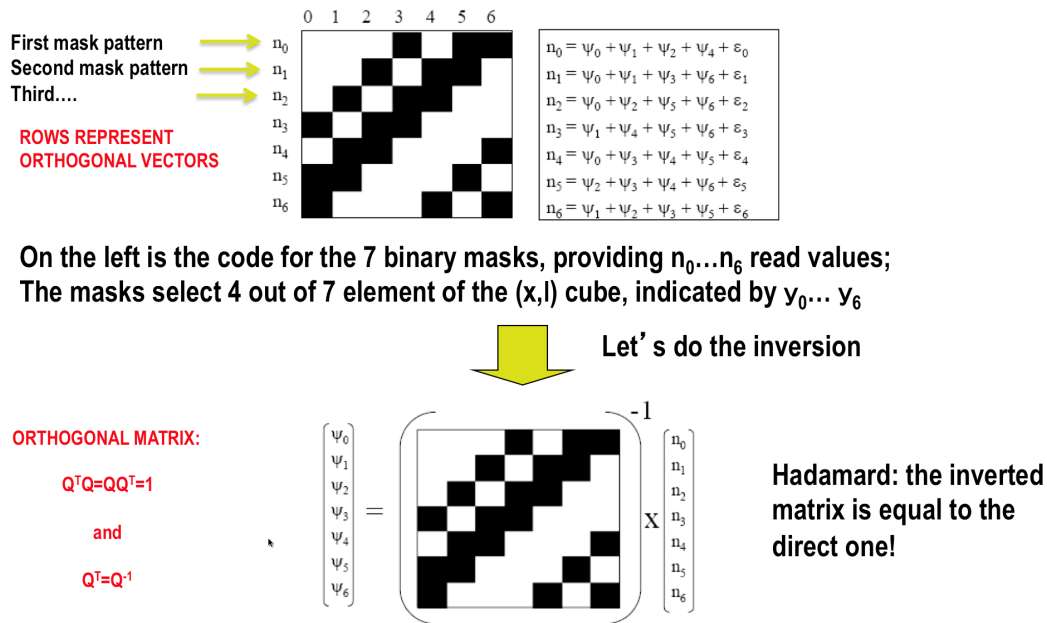


Figure 40: Schematic of Hadamard transform spectroscopy for a single pixel. A set of 7 images is acquired, providing 7 values ($n_0 \dots n_6$) for a given pixel. The flux collected each time has been modulated by a mask at the focal plane, allowing only a certain combination of “spaxels” to be integrated. For example, $n_0 = \psi_0 + \psi_1 + \psi_2 + \psi_4$, where ψ_i represents the points in the sky, each at a certain wavelength, that the spectrograph directs onto the same pixel. The set of 7 images provides, for each pixel, a system of linear equations in 7 unknowns that can be immediately inverted thanks to the orthogonality of the matrix. We have therefore $\psi_0 = n_0 + n_1 + n_2 + n_4$, and so on (neglecting a global multiplicative constant).

The Fellgett advantage decreases when the sky brightness is high, so a HTS is especially efficient over narrow or medium passbands lacking strong airglow lines. For GMOX, it may be more practical to put gratings tailored to specific spectral regions, e.g. the Ha+[NII] region, on the filter wheels of the relative imaging channels. Then, by simply loading a set of predefined slit patterns on the DMDs and driving the detector readout time in-sync with the DMD patterns, GMOX is transformed into an IFU spectrograph. Having three channels in parallel, one could for example produce three IFU datacubes showing the 3-d kinematics of ionized Hydrogen in $H\beta$ (Blue Channel), $H\alpha$ (Red Channel) and $Br\gamma$. Three lines allow one to reconstruct the density, temperature and foreground extinction of each kinematic component of the ionized gas, over the full field of view of GMOX. **This capability is unparalleled by any other existing or planned instrument.**

GMOX can be operated in many other ways. Spectroscopy of transiting planets may require real-time monitoring of atmospheric transmission: in this case, the imaging channels can provide photometry of a large number of nearby stars to achieve high precision. Also, bright sources can be masked out to study their surrounding nebulosity, or companions, allowing for a “spectro-coronographic” mode. The list may continue, and we have no doubt that our colleagues will find more creative ways of exploiting the versatility of GMOX to enable a wide range of exciting discoveries.

F.7 CALIBRATION STRATEGY

GMOX operations require preliminary mapping of the transformation between the different focal planes: telescope, DMDs, and detectors. Other calibration steps, e.g. dark, flat field and the

dispersion solution are similar to those typically performed with multi-slit spectrographs. We discuss these calibration steps in some detail below.

- **Initial Calibration: Mapping Imaging Detectors vs DMDs (minimum cadence: 1 per week)**
The three modules will take in parallel a calibration image to set the correspondence between the DMD mirrors and the pixels of the three imaging cameras. This requires turning-on a flat-field lamp(s) of the Calibration Unit and then directing a grid of DMD mirrors (“pinholes”) to the camera channels (Figure 41). Each image is immediately processed to extract the centroid of the pinholes on the imaging detectors, allowing one to create the 2-d polynomial function mapping the DMD on the CCD, and vice-versa. This operation can be completed within a few minutes and made automatic. A check of the focusing of the cameras on the DMD planes can also be performed at this point.

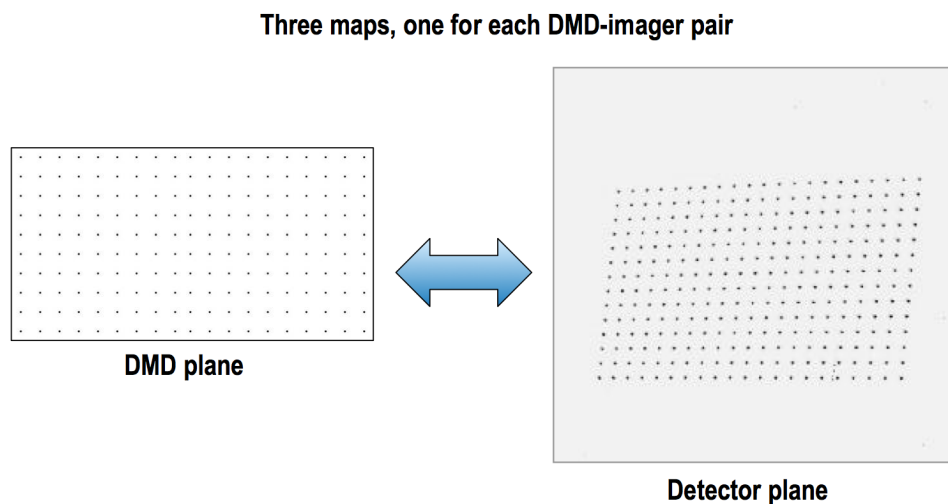


Figure 41: Illustration of the strategy to create the DMD-to-Detector map. The regular, known grid of pinholes is created on the DMD plane and imaged on the imaging channels. The image on the right is an actual calibration image of IRMOS at KPNO, showing strong field distortion generated by the off-axis optical layout.

- **Initial Calibrations: DMDs vs. sky (minimum cadence: 1 per month)**
The second part of the initial calibration is the mapping of the DMDs and detectors on the sky. This requires observing a known asterism, in parallel on each imaging channel. During commissioning it will be necessary to observe an astrometric reference field to map field offset, rotation and distortion of each channel. Once this information is at hand, it is possible to find the cross-correspondence between DMDs and detector of the different channels. Routine checks can be performed on any field to validate the offset values. The correct focusing of the telescope focal plane on the DMD plane can also be checked at this point.
- **Darks, flats, dispersion solutions (minimum cadence: daily)**
Darks and flats will be needed for each detector; darks can be taken during daytime and in parallel for all 8 detectors. Flats for the 3 imaging detectors can be taken in “full-imaging” mode (all DMDs “on”) during day-time. For the spectroscopic channels the simplest approach is to take flats and arcs for each DMD/slit configuration used on the previous night; this operation can be performed hours later, as long as flexure between the DMDs and detectors is negligible. Other approaches may eventually become viable. In the case of JWST,

which benefits from a stable space environment and needs to minimize the actuation of moving parts, the plan is to derive the flats from an extensive set of global calibration data. Vice-versa, in the case of IRMOS at Kitt Peak, both flats and arc lamps are acquired "on the fly" at the end of each exposure, before reconfiguration of the the DMD pattern, due to alignment instability of the system. Assuming the light sources are adequate, these exposures can be quite short (10S) and the entire procedure can be made automatic.

- Flux calibration (minimum cadence: 2 daily)
Spectrophotometric standard stars can be used to obtain the intrinsic response function of the instrument and derive an absolute flux calibration of the science data. These observations will need to be performed with a wide slit aperture (5") in order to measure most of the flux of the standard. We will be able to identify a set of suitable standard stars covering the full spectral range of GMOX by leveraging Gemini expertise, as well as HST and JWST calibration plans, where spectrophotometric calibration is performed from the UV to the NIR at the 5% accuracy level.
- Telluric correction (minimum cadence: 1 per science observation)
Red and NIR spectra are affected by telluric absorption lines. Since these atmospheric absorption lines vary with time and often do not scale linearly with airmass, it will be necessary to observe a telluric standard star at a similar airmass, with the same setup used for the science target and close in time to the science observation. GMOX "point-and-click" mode allows one to minimize this type of overhead. Note that the blue channel does not require telluric correction.
- Other modes:
Different observing modes may require dedicated calibration files. For example, in the Nod & Shuffle mode, each frame requires darks taken following the same shuffling pattern as the science data to remove bias pattern, dark current and charges trapped on pixels that do not shuffle charges efficiently (charge build-up). This observation mode, on the other hand, is sensitive to the flat field errors. Depending on the characteristics of the detector, flat fields taken with an internal lamp may have significant fringing. Fringing, however, is removed by the science data since the sky is subtracted using the same pixels. If the fringing is stronger than the pixel-to-pixel variations, it may be appropriate to avoid flat fielding, especially if the data have been dithered.

Calibration Step	Method	Frequency (minimum)	Frequency (goal)
GMOX geometry: DMD vs Detector	Cal. Flat Field on DMD grid	Every week	Every few months
Astrometry: DMD vs Sky	Astrometric Field	Every month	Every year
Spectroscopy: Flat Fields	Cal. Flat Field on DMD pattern	End of night/daytime	Every week
Spectroscopy: Dispersion solution	Cal. Arcs on DMD pattern	End of night/daytime	Every week
Spectroscopy: telluric correction	Telluric standard stars	2-3 times per night	2-3 times per night
All detectors: dark and bad-pixel map	Dark shutter	Every week	Every few months
Imaging Detectors: Flat Field	Cal. Flat Field	End of night/daytime	Every week

Figure 42: Cadence of the calibration steps required by GMOX.

G TECHNICAL REQUIREMENTS AND A FEASIBLE INSTRUMENT DESIGN

In this section we outline the instrument concept and demonstrate its feasibility. We start with an overview of the top-level technical requirements. This is followed by a brief discussion of performance trades. We then provide an overview of the design including a discussion of how GMOX would integrate with the adaptive optics systems on both Gemini North and South. Then the optical, mechanical, electrical, and software aspects of GMOX are presented to demonstrate feasibility. And finally, we discuss design options and technical risks.

It is important to note that this is a feasibility study, not a conceptual design study, and the level of detail presented here is intended only to demonstrate feasibility. There are numerous details that have been left to future phases of the design.

G.1 TOP-LEVEL REQUIREMENTS

The top-level technical requirements for GMOX are derived from two sources: the science cases and the observatory requirements. Each science case requires a basic set of instrument parameters, e.g. bandpass, resolving power, and efficiency. The observatory requirements fall into one of two categories; environmental and instrumental. The environmental requirements describe the environment the instrument will operate in, while the instrumental requirements define the optical, mechanical, thermal, and electrical constraints imposed by the telescope.

We have summarized these requirements in three tables. Table 19 summarizes the science-driven instrument requirements; Table 20 lists the Observatory environmental requirements; Table 21 details the observatory instrument requirements.

G.2 INSTRUMENT DESIGN

To provide the highest sensitivity with very wide and simultaneous spectral coverage, in addition to the flexibility to fine-tune slit widths in real time, we have baselined an instrument with three arms and five spectroscopic channels. We use the term “arm” here to denote a functionally complete spectrograph module containing: (1) any fore-optics needed to modify the beam ahead of the slit, (2) a DMD-based programmable slit array, (3) a collimator, (4) one or more dispersing channels with a grating, camera, and science-grade detector, and (4) an acquisition/slit-viewing camera. Our baseline approach would employ a single channel in the Blue and Red arms, and three channels in the NIR arm to cover the Y+J, H, and K bands. Fig. 2 provides a simplified schematic view of the GMOX optical layout, showing the three arms split by dichroic mirrors.

G.2.1 ADAPTIVE OPTICS MODES

GMOX is designed with Adaptive Optics (AO) in mind and takes full advantage of the capabilities offered by GeMS on Gemini South and ALTAIR on Gemini North. Here we describe how we intend to integrate GMOX with GeMS and ALTAIR.

G.2.1.1 GMOX WITH GEMS

The Gemini Multi-Conjugate Adaptive Optics System (GeMS) provides adaptive optics correction for instruments on Gemini South. The system uses five laser beacons and a suite of natural guide stars to measure and compensate for atmospheric distortions over a bandpass of $0.8\mu\text{m} < \lambda < 2.4\mu\text{m}$. GeMS is mounted on Port 4 of the Instrument Support Structure (ISS) and takes the native $f/16$ telescope beam and produces a nominal $f/32$ corrected output, which is then directed to the

Req. ID	Description	Value	Units	Comments	Traceable to
REQ-1100	Bandpass				
	<i>visible</i>				
REQ-1101	blue	365 - 589	nm	AO sodium line between Blue/Red Channel	C.4.3, C.4.4, C.4.5, C.5.1, C.5.2, C.5.3, C.5.4, C.5.5, C.5.6
REQ-1102	red	589 - 970	nm	Red cutoff driven thermal IR	C.4.3, C.4.4, C.4.5, C.5.1, C.5.2, C.5.4, C.5.5, C.5.6
	<i>near infrared</i>				
REQ-1103	Y+J	970 - 1350	nm		C.4.1, C.4.2, C.4.3, C.4.4, C.4.5, C.5.1, C.5.2, C.5.3, C.5.4, C.5.5, C.5.6
REQ-1104	H	1460 - 1810	nm		C.4.1, C.4.2, C.4.3, C.4.4, C.4.5, C.5.2, C.5.3, C.5.4, C.5.5, C.5.6
REQ-1105	K	1930 - 2450	nm		C.4.1, C.4.2, C.4.3, C.4.4, C.4.5, C.5.3, C.5.4, C.5.5, C.5.6
REQ-1200	Resolving power				
	<i>visible</i>				
REQ-1201	blue	4000		minimum	C.4.3, C.4.4, C.5.1, C.5.2, C.5.3, C.5.4, C.5.5, C.5.6
REQ-1202	red	4000		minimum	C.4.3, C.4.4, C.5.1, C.5.2, C.5.4, C.5.5, C.5.6
	<i>near infrared</i>				
REQ-1203	Y+J	4000		minimum	C.4.1, C.4.2, C.4.3, C.4.4, C.5.1, C.5.2, C.5.3, C.5.4, C.5.5, C.5.6
REQ-1204	H	4000		minimum	C.4.1, C.4.2, C.4.3, C.4.4, C.5.2, C.5.3, C.5.4, C.5.5, C.5.6
REQ-1205	K	4000		minimum	C.4.1, C.4.2, C.4.3, C.4.4, C.5.3, C.5.4, C.5.5, C.5.6
REQ-1300	Total Efficiency (non-AO)				
REQ-1301	Total on-sky efficiency	20	%	median (over 50% of each bandpass)	C.4.1, C.4.2
REQ-1400	Field of view				
REQ-1401	AO Mode	36	arcsec ²	rectangular field preferred	C.4.1, C.4.2, C.5.1, C.5.2, C.5.3, C.5.4
REQ-1402	Natural Seeing	1	arcmin ²	rectangular field preferred	C.4.5, C.5.5
REQ-1500	Slit Width				
REQ-1501	AO Mode	100	marcsec		C.4.1, C.4.2, C.5.1, C.5.2, C.5.3, C.5.4
REQ-1502	Natural Seeing	300	marcsec		C.4.5, C.5.5
REQ-1600	Multiplex capability				
REQ-1601	Minimum spatial sampling	1	arcsec	between any two targets	C.4.3, C.4.4, C.4.5, C.5.1, C.5.2, C.5.3, C.5.4, C.5.5, C.5.6
REQ-1602	Minimum number of targets	4			C.4.3, C.4.4, C.4.5, C.5.1, C.5.2, C.5.3, C.5.4, C.5.5, C.5.6
REQ-1700	Observing Efficiency				
REQ-1701	Science target acquisition time	5	min		All SCs
REQ-1702	Tip/Tilt target acquisition time	5	min		All SCs
REQ-1800	Calibration				
REQ-1801	Calibration source	8 spectral lines per channel, minimum		> 10 lines across the detector is desirable	All SCs
REQ-1900	Reliability				
REQ-1901	Operability	95	%		All SCs
REQ-1902	Instrument lifetime	10	yrs		All SCs

Table 19: GMOX science driven instrument requirements.

Req. ID	Description	Value	Units	Comments	Traceable to
REQ-2100	Telescope Operations Environment				
REQ-2101	Altitude	0 to 4,300	m		ICD-G0013
REQ-2102	Ambient air temperature	-15 to +25	C		ICD-G0013
REQ-2103	Ambient air temperature step	+/-25	C		ICD-G0013
REQ-2104	Ambient light	Night time observing to normal lighting conditions			ICD-G0013
REQ-2105	Relative humidity	0 - 100	%	see footnote in ICD-G0013	ICD-G0013
REQ-2106	Wind speed	0 to 33	m/sec		ICD-G0013
REQ-2107	Gravity orientation	Any			ICD-G0013
REQ-2108	Vibration (PSD, minimum integrity)	0.0008, 20 to 1000 Hz	g ² /Hz	all axes, see footnote in ICD-G0013	ICD-G0013
REQ-2109	Shock	10	g		ICD-G0013
REQ-2110	Seismic base acceleration	0.4, 0.5 to 100 Hz	g	any axis	ICD-G0013
REQ-2111	Seismic acceleration at cass	2.0g, 0.5 to 100 Hz	g	any axis	ICD-G0013
REQ-2112	Mechanical interface	ISS or handling cart			ICD-G0013
REQ-2113	Cleanliness	Occasional wind blown dust, sand and insects			ICD-G0013
REQ-2200	Instrument Operating Environment				
REQ-2201	Altitude	0 to 4,300	m		ICD-G0013
REQ-2202	Ambient air temperature <i>Median air temperature</i>	-15 to +20	C	see footnote in ICD-G0013	ICD-G0013
REQ-2203	Mauna Kea	0	C		ICD-G0013
REQ-2204	Cerro Pachon	9	C		ICD-G0013
REQ-2205	Ambient air temperature rate of change	+/- 0.8	C/hr	see footnote in ICD-G0013	ICD-G0013
REQ-2206	Relative humidity	0 - 90	%	see footnote in ICD-G0013	ICD-G0013
REQ-2207	Wind speed	0 to 5	m/sec		ICD-G0013
	<i>Gravity component limits</i>				
REQ-2208	X	+/- 1.0	g		ICD-G0013
REQ-2209	Y	+/- 1.0	g		ICD-G0013
REQ-2210	Z	-1 to 0	g	see footnote in ICD-G0013	ICD-G0013
REQ-2213	Vibration (PSD)	1x10 ⁻⁵ , 20 to 1000 Hz	g ² /Hz	6dB/octave drop-off to 2000 Hz	ICD-G0013
REQ-2214	Shock	10	g		ICD-G0013
REQ-2215	Seismic base acceleration	0.4, 0.5 to 100 Hz	g	any axis	
REQ-2216	Seismic acceleration at cass	2.0g, 0.5 to 100 Hz	g	any axis	ICD-G0013
REQ-2217	Mechanical interface	ISS or handling cart			ICD-G0013
REQ-2218	Cleanliness	Occasional wind blown dust, sand and insects			ICD-G0013
REQ-2300	Transportation/shipping				
REQ-2301	Altitude	0 - 15,500	m		ICD-G0013
	<i>Ambient air temperature (induced by packing)</i>				
REQ-2302	low diurnal limits	-25 to -33	C	see footnote in ICD-G0013	ICD-G0013
REQ-2303	high diurnal limits	33 to 71	C	see footnote in ICD-G0013	ICD-G0013
REQ-2304	Temperature shock	+/- 35	C		ICD-G0013
REQ-2305	Relative humidity	0 - 100	%	with condensation	ICD-G0013
REQ-2306	Wind speed	0 to 67	m/sec		ICD-G0013
REQ-2307	Gravity orientation	Any			ICD-G0013
	<i>Vibration</i>				
REQ-2308	PSD	0.015 (10 to 40 Hz) 0.00015 @ 500Hz	g ² /Hz		ICD-G0013
REQ-2309	Shock	15	g	all axes, see footnote in ICD-G0013	ICD-G0013
REQ-2310	Cleanliness	Occasional wind blown dust, sand and insects			ICD-G0013

Table 20: Observatory environmental requirements.

Req. ID	Description	Value	Units	Comments	Traceable to
REQ-3100	Instrument volume, mass, and loading				
REQ-3101	Volume: science ports 1,3,5	see Gemini dwg: 89-GP-1000-0004			ICD 1.5.3/1.9
REQ-3102	Mass	2000	kg		ICD 1.5.3/1.9
REQ-3103	CG	1000	mm	from ISS mechanical interface	ICD 1.5.3/1.9
REQ-3104	Out of balance	500	Nm	with respect to telescope elevation axis	ICD 1.5.3/1.9
REQ-3105	<i>Loads on instrument mount bosses</i>				
REQ-3106	Tension	10,000	N		ICD 1.5.3/1.9
REQ-3107	Shear	10,000	N		ICD 1.5.3/1.9
REQ-3108	Moment	1,000	Nm		ICD 1.5.3/1.9
REQ-3109	Fastener load torque	68	Nm		ICD 1.5.3/1.9
REQ-3110	Fastener induced loads	80	%	of torque load	ICD 1.5.3/1.9
REQ-3200	Optical interface				
REQ-3201	ISS port optical clear diameter	400	mm		ICD 1.5.3/1.9
	<i>Focus location</i>				
REQ-3202	f/16	300	mm	with respect to ISS mount interface	ICD 1.5.3/1.9
REQ-3203	f/32	300	mm	Gemini South with GeMS	ICD 1.5.3/1.9
	<i>Input f/#</i>				
REQ-3204	Gemini-S + AO mode (GEMS)	F/33.2			TBD
REQ-3205	Gemini-S non-AO mode	f/16			ICD 1.5.3/1.9
REQ-3206	Gemini-N AO mode (ALTAIR)	f/16			TBD
REQ-3207	Gemini-N non-AO mode	f/16			ICD 1.5.3/1.9
REQ-3300	Electronic interface				
REQ-3301	ISS system services	see ICD 1.9 to 3.6			ICD 1.5.3/1.9
REQ-3302	Ampacity	75	%	of published values for 30 C rise	ICD 1.5.3/1.9
REQ-3400	Thermal interface				
REQ-3401	Enclosure type	insulated and thermally conditioned			ICD 1.5.3/1.9
REQ-3402	Unconditioned heat release from instrument	100	W	max goal	ICD 1.5.3/1.9
REQ-3403	Unconditioned heat conducted to ISS	50	W		ICD 1.5.3/1.9
REQ-3404	Component temperatures (environmentally exposed)	2	C	above ambient	ICD 1.5.3/1.9
REQ-3500	Adaptive optics control				
	<i>NGS Loop RTC Feedback</i>				
REQ-3501	Feedback coordinates	two degrees of freedom per each of three guidestars			Gemini AO Staff
REQ-3502	Frame rate	400	fps	minimum	Gemini AO Staff
REQ-3503	Latency	2.5	ms	maximum	Gemini AO Staff

Table 21: Observatory instrument requirements.

science instruments by a fold mirror integral to the ISS. GeMS was commissioned in 2011, is used routinely, and produces images close to the diffraction limit in the near infrared, with uniform quality over a two square arcminute field.

There are several compatibility considerations with GMOX and GeMS, however, as we will see, they are all manageable and we do not see any show-stoppers with regard to the use of GMOX with GeMS. The most obvious consideration is that the plate scale of GeMS is half of that from the telescope native beam, and here we simply accept the loss in field size rather than exchange optics internal to GMOX to compensate for the transition from AO to non-AO operations.

The primary compatibility consideration is that the GMOX bandpass is wider than for GeMS. Visible light that would feed the blue and red arms of GMOX is used by GeMS for AO correction; in particular for the natural guide stars and tip-tilt-focus correction. Therefore, as currently configured, GeMS would not be able to deliver visible light to GMOX. Two things have to happen to correct this and both are possible, and straightforward.

First, the dichroic that establishes the science beam bandpass would have to be replaced by a "notch" dichroic. The notch dichroic would pass all light from the telescope to GMOX with the exception of light in a narrow bandpass centered on the sodium laser wavelength, 589 nm. By doing this, the functionality of the laser guide star (LGS) loop is retained, but the functionality of the natural guide star (NGS) loop, which is to correct for tip-tilt-focus and anisoplanatic modes, is lost.

To convince ourselves the notch dichroic can be built, we contacted Infinite Optics and they produced a very preliminary coating design for which the reflectivity is shown in Fig. 43. As shown in the plot, the reflectivity is quite uniform over the bandpass and with a proper antireflection coating on the back side of the dichroic, the transmission should be of order 95%, except of course for the region around 589 nm where the coating is highly reflective and the transmission drops to zero.

Second, the functionality of the NGS loop has to be re-established, and this would be done in part by GMOX and in part by the Acquisition and Guiding Unit. GMOX would provide feedback from one of its three slit viewing cameras to correct for tip-tilt and anisoplanatic modes. And the Acquisition and Guiding Unit would correct for slow focus changes; a feature that is currently planned for the NGS2 upgrade on GeMS in any case. The tip-tilt and anisoplanatic mode correction with GMOX would use the same On-Detector Guide Window (ODGW) technology used by GSAOI with GeMS. The fact that GSAOI can provide its own tip-tilt and flexure correction is significant for GMOX in that it means the hooks are already in the real time controller (RTC) software to accept correction signals from the science instrument, rather than GeMS.

With regard to the dichroic, it is fortuitous that there exists a two-position dichroic exchange mechanism in GeMS, and currently only one of the two dichroics is used. This leaves open the possibility of using the un-used slot for the notch dichroic. In this way, GeMS could be operated in its normal mode with no impact on existing instruments, but still be able to serve GMOX by simply swapping dichroics using the mechanism that presently exists.

Additionally, a minor, yet easily solved, issue is that the atmospheric dispersion corrector (ADC) internal to GeMS is not designed for the broader bandpass of GMOX. However, the GeMS ADC is not mounted permanently in the science beam; it is inserted and removed by an automated linear mechanism. Therefore, for GMOX operations, the ADC would simply be translated out of the science beam and atmospheric dispersion correction would take place internal to GMOX; GMOX has one ADC for each arm.

Lastly, in GeMS there is a portion of the optical path that is not seen by the wavefront sensor (WFS) and imperfections in the optics not seen by the WFS produce aberrations that are not corrected by the AO loop. These non-common-path aberrations (NCPA) can be corrected but re-

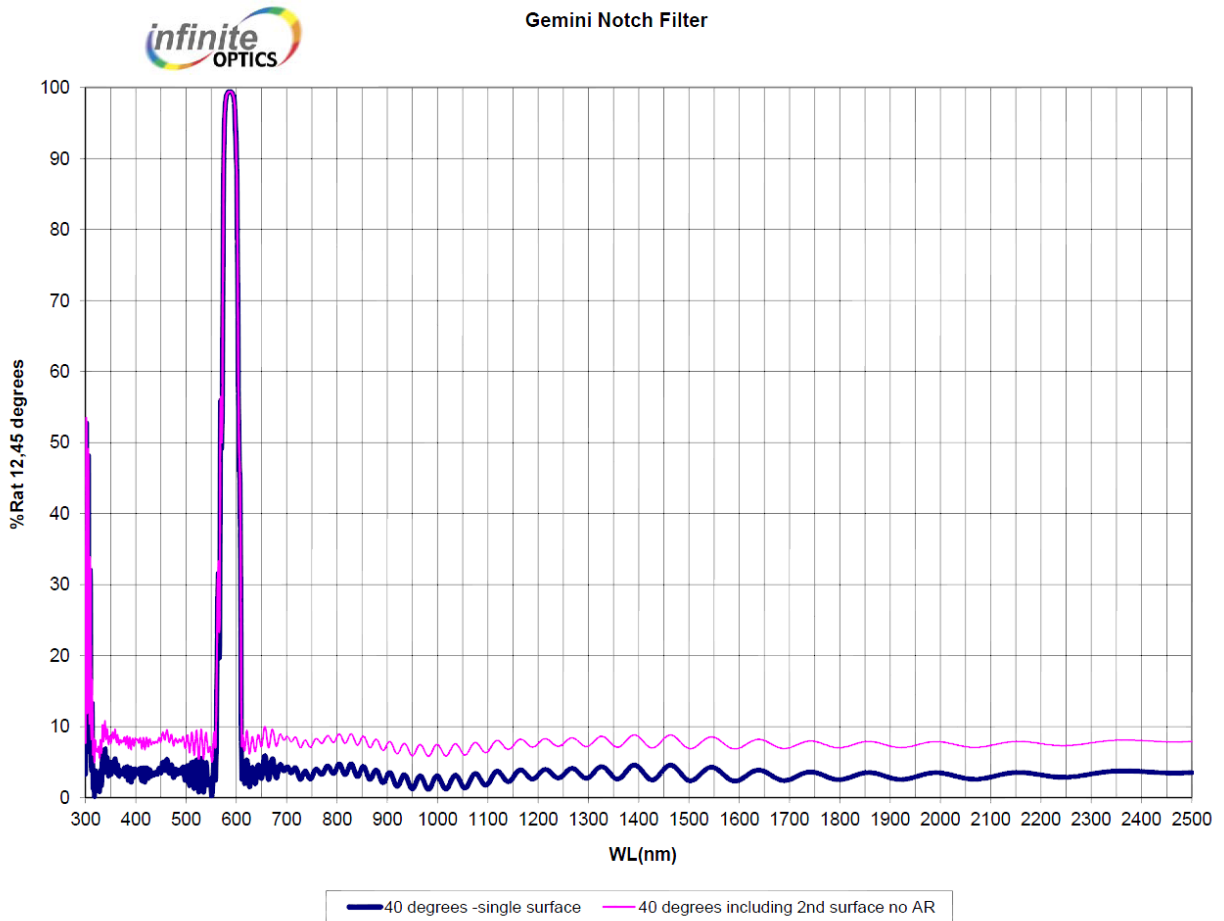


Figure 43: Reflectivity as a function of wavelength for a notch dichroic tuned to reflect only the sodium laser line at 589 nm. The pink curve includes reflection off the rear surface of the dichroic, which would be reduced with a proper AR coating. This data is based on a preliminary coating design by Infinite Optics.

quire analysis input from the science instrument. The present method of correction utilizes two out-of-focus images, one on either side of focus, to build a distortion map that is added to the profile of the deformable mirror. Therefore GMOX must provide the capability to capture defocused images, and there a number of ways to do this.

G.2.1.2 GMOX WITH ALTAIR

ALTAIR is the facility AO instrument at the Gemini North telescope. It provides compensation for atmospheric distortion using a combination of natural guide stars, a single laser guide star conjugate to ground, and a peripheral wavefront sensor (PWFS). The LGS mode provides high-order correction while the NGS provides tip-tilt and focus correction. Tip-tilt and focus can also be corrected using the PWFS. As with GeMS, focus correction is required to compensate for density fluctuations in the sodium layer of the atmosphere, which alters the apparent object distance of the laser guide star. ALTAIR has a bandpass covering $1.0\mu\text{m} < \lambda < 2.5\mu\text{m}$, similar to GeMS. And like GeMS, ALTAIR uses the visible light for the NGS loop.

The compatibility considerations for GMOX with ALTAIR are very similar to that with GeMS. How to recover the visible part of the spectrum being the primary consideration. However, as with GeMS, ALTAIR employs a two-position dichroic exchange mechanism, and like GeMS, only one position is used presently. We understand there are plans to utilize the second position for a sodium-line notch dichroic that would allow ALTAIR to be used for visible science. Such an upgrade would be ideal for GMOX. Although it is not clear what the bandpass of this new dichroic will be. In any event, we know, based on the preliminary design work by Infinite Optics, that a broad-band dichroic (covering U to K band) with a narrow notch at 589 nm is possible, and one could imagine replacing the new notch dichroic with one suitable for GMOX with minimal, if any, impact on existing science instruments.

With the visible light being passed to GMOX, the NGS loop is lost, and tip-tilt and focus correction would have to be handled by the PWFS. This is adequate for GMOX since the LGS+P1 mode provides a factor of two reduction in the width of the native point spread function, and this is in-line with science requirements for GMOX in AO operations. It may be possible, with some improvement in the Strehl ratio, to use the ODGW functionality of GMOX and we will explore this possibility. In this case we would only use the PWFS for focus compensation.

As with GeMS, the ADC is not optimized for visible wavelengths and we would not want to use it with GMOX. However, since the ADC is removable from the optical path this is not an issue. GMOX has an ADC for each arm of the spectrograph, each being optimized for its respective bandpass.

Non-common path aberrations would be corrected in the same way described for GeMS.

G.2.2 OPTICAL DESIGN

The UV to near-IR wavelength coverage of GMOX requires a multi-channel instrument, and we have adopted a three-arm design (see Fig. 2). This provides many benefits:

1. High throughput resulting from optimized coatings, materials, and detectors.
2. Full simultaneous spectral coverage.
3. The ability to optimize slit widths based on delivered PSFs in each arm.
4. The ability to optimize ADCs separately for each arm.

Channel	WL (nm)	R	Slit width			Grating		Spectral length		Beam \emptyset (mm)	Camera		
			arcsec	mirrors	pixels	angle	l/mm	mm	pixels		f/#	FL (mm)	FOV (deg)
Blue	320.0	3132	0.417	5	3.0	20.1	1493	80.9	8085.2	101	1.834	183.4	23.3
	458.5	4500											
	589.0	5765											
Red	589.0	3681	0.333	4	3.0	18.0	772.5	78.2	7815.6	101	2.293	230.8	18.9
	797.2	5000											
	1000.0	6250											
Y+J	970.0	2757	0.250	3	2.75	11.3	337.5	29.8	2976.3	81	2.802	227.1	16.7
	1160.6	3300											
	1350.0	3837											
H	1460.0	4461	0.250	3	2.75	16.9	354.3	29.5	2947	81	2.802	227.0	16.6
	1636.8	5000											
	1810.0	5530											
K	1930.0	3962	0.250	3	2.75	15.3	240.0	29.4	2942	81	2.802	227.0	16.6
	2191.9	4500											
	2450.0	5030											

Table 22: GMOX first-order optical design parameters.

5. Design flexibility in terms of beam size, grating parameters, etc., per arm.
6. No grating exchange mechanisms or articulated cameras required.
7. Modularity in terms of assembly, alignment, and testing of individual arms.

The three arms for GMOX are created using two dichroic beamsplitters ahead of the telescope focal plane and any other optics in the instrument. The first dichroic splits near 589 nm, reflecting the blue channel bandpass and transmitting the red and NIR. The second dichroic would split near $1\mu\text{m}$, reflecting the red channel bandpass and transmitting the NIR light. All arms include an atmospheric dispersion corrector, although it is likely the NIR arm could use the GeMS ADC during AO operation, and no ADC correction under natural seeing. The NIR arm employs an additional pair of dichroics to split the light into Y+J, H, and K bandpasses.

Considering the top-level requirements outlined in Sec. G.1 and the format of the baseline science detectors, we have developed the set of design parameters summarized in Table 22. These parameters fall out of calculations based on inputs such as bandpass, resolution, slit width, detector pixel size, and projected slit width on the detector. These calculations assume $10\mu\text{m}$ pixels for all channels, with the nominal slit widths sampled by 3 detector pixels for the blue and red channels, and 2.75 pixels for the NIR channels. The results provide a reasonable starting point and serve as the basis for the conceptual optical design we have developed for GMOX.

The optical design can be broken into six major functional modules:

1. A fore-optics assembly to split the beam into three arms and steer the light properly into the reimaging optics.
2. A reimager for each arm, including an ADC, to relay the telescope image surface onto the DMD array with the necessary focal reduction.
3. A DMD array for each arm which serves as a real-time, multi-object slit selector, as well as reflecting acquisition and guide stars into a slit viewing channel.
4. An off-axis Schmidt collimator.

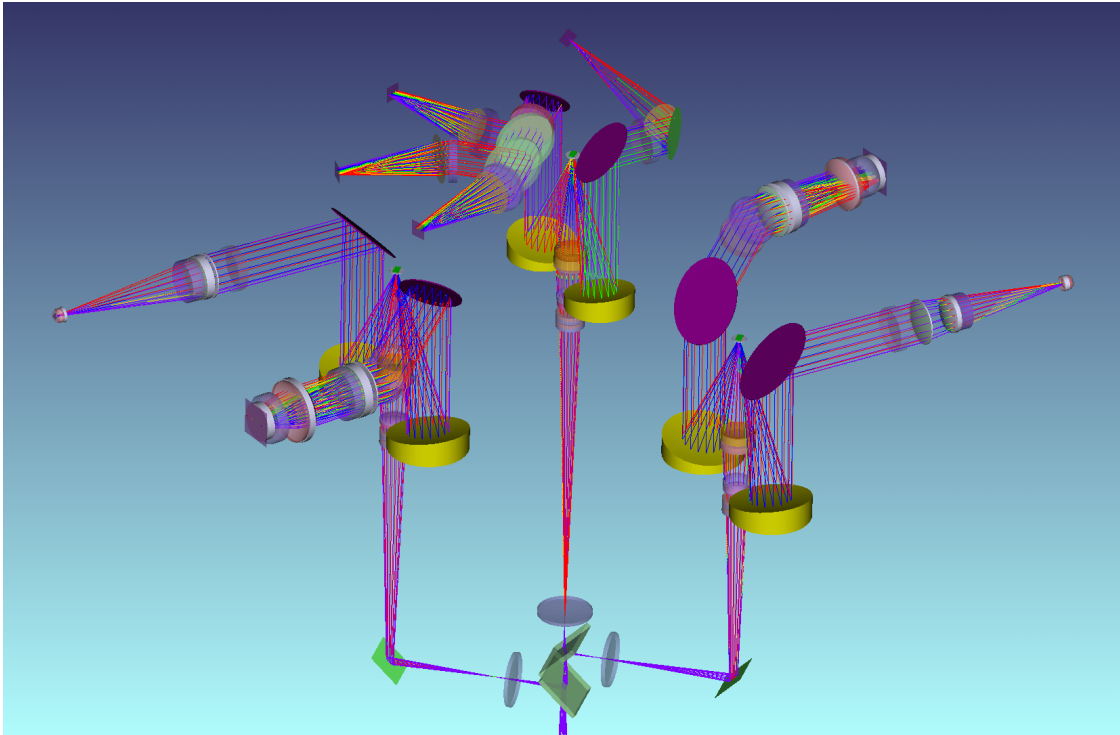


Figure 44: GMOX optical layout. In this view the ISS is off the bottom edge of the figure, the blue arm is to the left, the red arm is to the right, and the NIR arm is in the center.

5. A spectroscopic channel (or channels) per arm with a disperser, reimaging lens, and detector.
6. An acquisition/imaging channel per arm to provide real-time slit-viewing or parallel deep imaging capability.

In the sections that follow, we describe each of these optical modules in detail.

G.2.2.1 FORE-OPTICS

The optical layout of GMOX is shown in Figure 44. In this view the ISS is just off the bottom edge and light from the telescope travels from bottom to top. The beam enters from the bottom via the ISS port at either $f/16$ for $f/33.2$, depending on the site and AO operation. It first encounters the blue dichroic, tilted 45 degrees, which reflects light shortward of 589 nm into the blue arm and transmits light longward of 589 nm, out through the K-band. Immediately following the blue dichroic is the red dichroic, tilted 45 degrees opposite to the blue dichroic. The red dichroic reflects light shortward of 1000 nm into the red arm, and transmits longer wavelengths though to the NIR arm. There is only 300 mm between the mounting surface of the ISS and the telescope focal surface, and it was our desire to split the beam ahead of the telescope focus to facilitate field lenses in each arm with coatings optimized for each arm. With the long edge of the rectangular field oriented along the tilt axis of the dichroics, there was just enough room to get both the blue and red dichroics ahead of the telescope focal surface.

Immediately after the dichroics is a field lens in each arm, which serves to create a pupil within the reimager. In addition to providing an accessible location for a cold stop in the NIR arm, it also minimizes the beam footprint within the reimager lens, allowing the reimager optics to squeeze

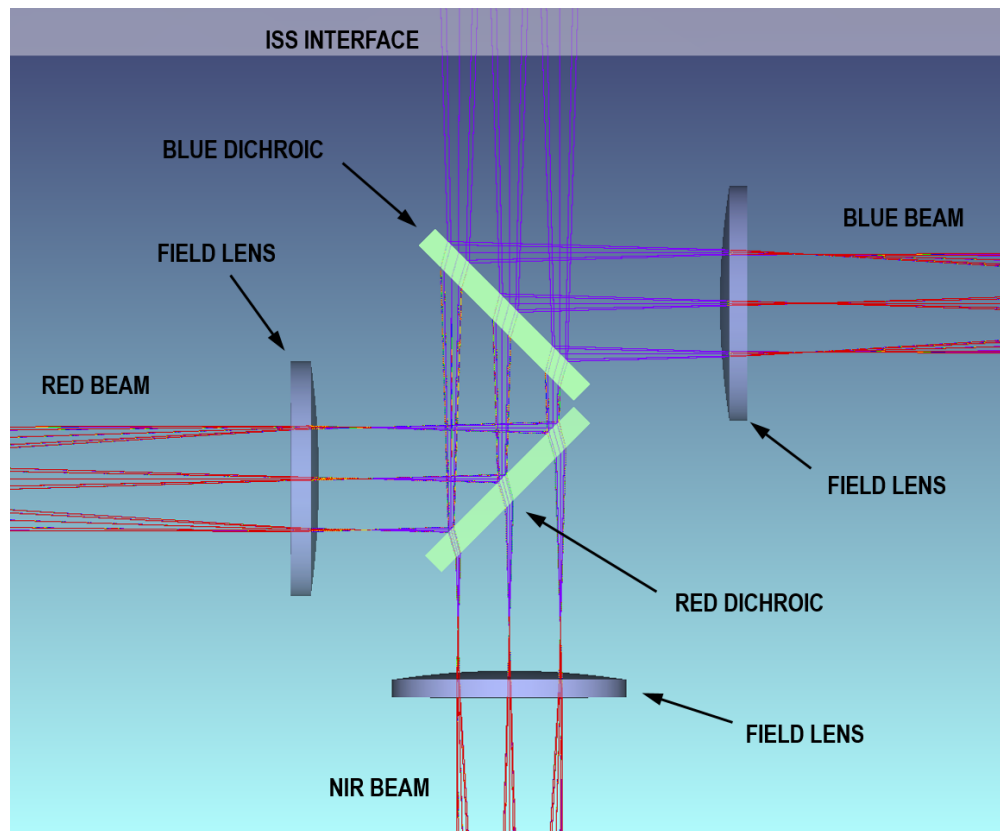


Figure 45: Detail of the GMOX central optics assembly, that part of the fore optics assembly which includes the blue and red dichroic beamsplitters and the three field lenses. The ISS interface to the instrument is at the top of the figure, with light traveling from top to bottom. The blue arm is split off to the right by the first dichroic, and the red arm is split off to the left by the second dichroic.

between the mirror pairs of the Schmidt collimators. The final elements making up the fore-optics are two fold mirrors which bend the red and blue arms 90 degrees and bring them parallel with the straight-through path of the NIR arm. Figure 45 shows the details of the fore optics assembly minus the two fold mirrors, which we refer to as the central optics assembly.

G.2.2.2 REIMAGERS

After passing through the fore-optics, the beam enters the reimager. A focal reduction of $4\times$ is needed to fit the $171'' \times 90''$, $f/16$ field ($85'' \times 45''$ at $f/33$) onto the DMD. The field lens forms a pupil at the reimager, minimizing the beam diameter and therefore, the diameter of the reimager optics. The 5-element reimagers for the red and blue arms use a closely-spaced doublet-singlet-doublet lens configuration, providing high throughput and allowing the lens elements to be mounted in a single barrel. For the NIR arm, the reimager will be housed within the cryostat and cold; therefore we employ a similar design with air-spaced lenses, with the addition of a plane parallel window serving as the entrance into the cryostat. A cold stop will be installed at the location of the pupil; unfortunately, switching between the $f/16$ and $f/33$ beams causes the pupil size and location to change, and this will require a cryogenic exchange mechanism for the cold stop. Finally, for the NIR reimager we employ a biconic surface on the first lens in order to correct for the significant astigmatism that results from passage of a converging beam (even at $f/16$) through

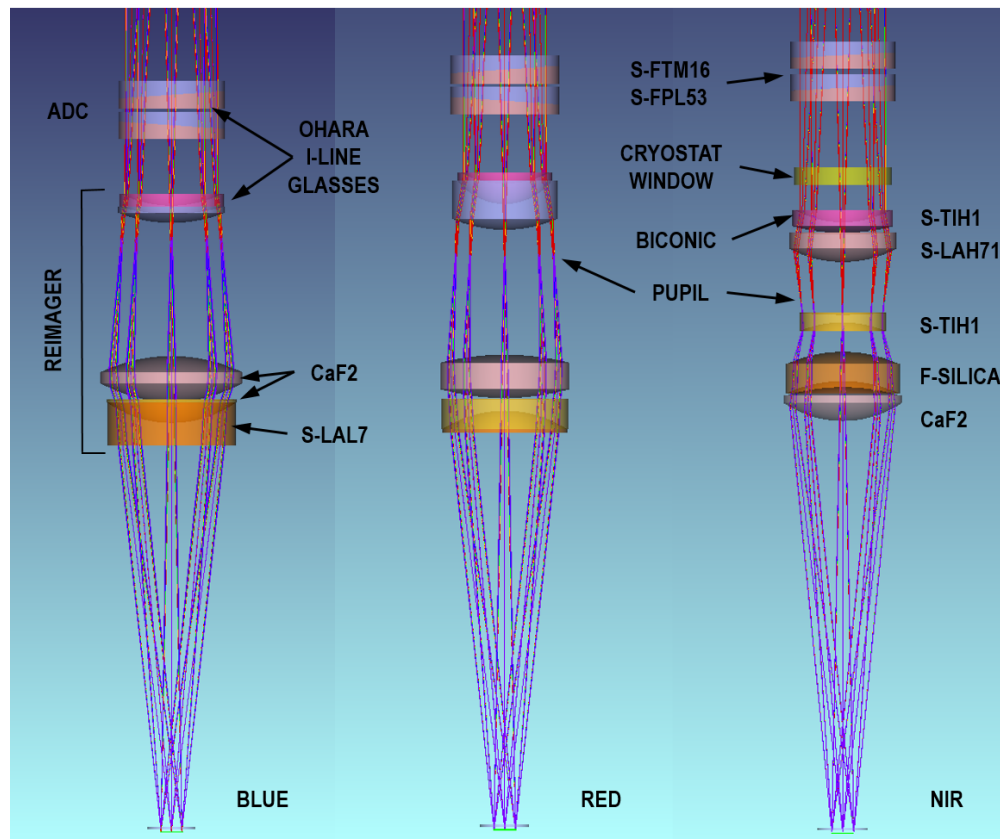


Figure 46: Details of the three reimager optics assemblies, including the atmospheric dispersion corrector ahead of each reimager lens. Here light is traveling from top to bottom in each panel.

two tilted, plane parallel optics (the dichroic beamsplitters). Figure 46 shows the optical layout of each reimager assembly.

The beam exits the reimager at $f/4.1$, and comes to focus on the DMD with a scale of $0.083''$ per micromirror. The DMD is rotated 45 degrees with respect to the “horizontal” plane of the optics; this is due to the fact that the micromirrors tilt along their diagonal. The effect is a 45 degree rotation of the field after reflection off of the DMD; see Figure 47.

G.2.2.3 DIGITAL MICROMIRROR DEVICE

A digital micromirror device, or DMD, is a silicon chip carrying on its top surface up to 8 million microscopic mirrors arranged in a rectangular array. The mirrors can be individually tilted ± 12 degrees to an ON or OFF state. In typical projection applications, the mirrors in the ON state reflect light from a projector lamp into a lens, making the corresponding pixels appear bright on the screen. Mirrors in the OFF state direct the light elsewhere, making the pixels appear dark. To vary brightness levels, each mirror can be toggled on and off very quickly, and the duty cycle determines the intensity on screen. Since the mirrors can switch at several KHz, it is possible to change multiple “photograms” per second. Each photogram can be further split in sync with cyclic RGB color illumination (e.g. filtering the projection lamp through a spinning wheel, or using LEDs) to produce a color movie. This is the principle of the so-called “DLP technology”.

Texas Instruments leads this market, producing several types of DMDs. For GMOX we would baseline the 2048×1080 pixel “CINEMA-2K” device (Fig. 48) because of its large ($13.7 \mu\text{m}$) mirror

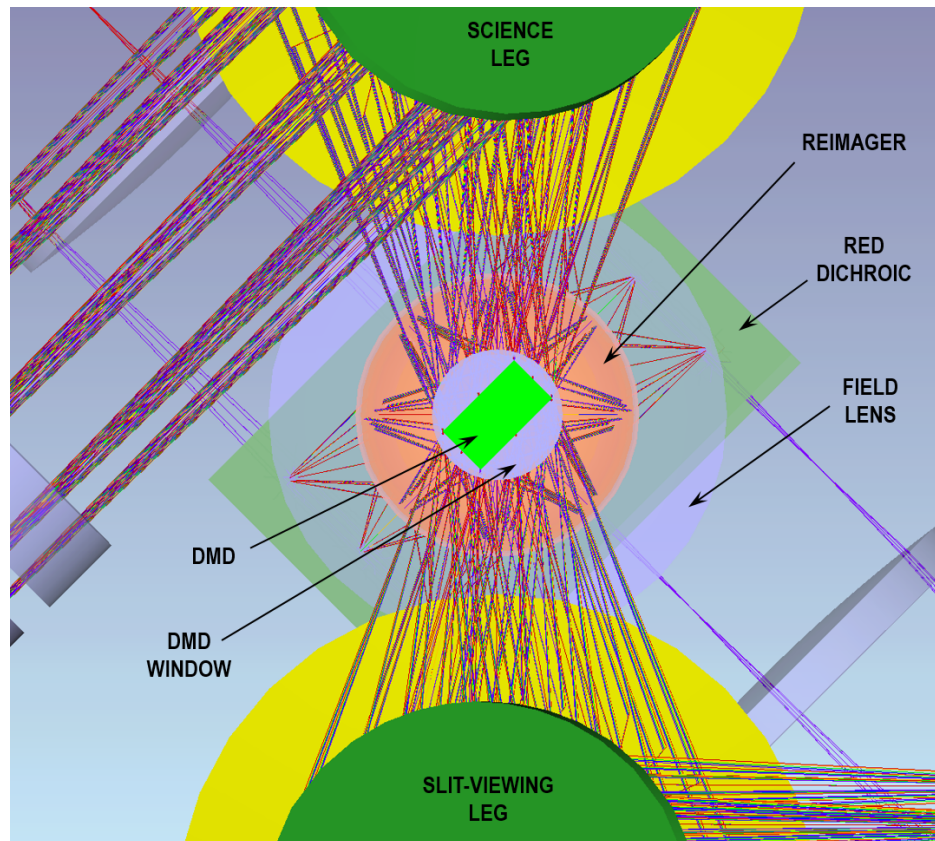


Figure 47: View from the back side of the NIR DMD, showing the 45 degree orientation of the field with respect to the beams reflected off the DMD.

size. This is the same device considered by ESA for the SPACE mission conceived by the PI of this GMOX proposal [180], selected in 2008 and later blended into Euclid.

With tens of millions of parts produced, each one having micromirrors operating flawlessly for trillions of on/off cycles, DMDs are regarded as the most reliable mechanical devices ever built. The consumer market dictates their cosmetic and image quality to be pristine and stable for the entire lifetime of the device, estimated in decades. When DMDs first appeared on the market about 20 years ago, image contrast (fraction of light leaking when mirrors are OFF) was an issue, but it now reaches JWST specs, $\approx 1 : 2500$ or about 8.5 magnitudes [181].

Two instruments have been built in the past based on DMDs: RITMOS (PI Ninkov, [182]) and IRMOS (PI MacKenty, [183]); the former working at visible wavelengths, the latter in the near-IR at the 4 m Mayall telescope at Kitt Peak. Both PIs are members of this proposing team. Recently, a NASA grant (PI Ninkov, RIT) has been awarded to evaluate the performance of Cinema DMDs after window replacement, needed to enhance far-UV transmission. RIT should be able to deliver to GMOX a set of DMDs with improved A/R coatings to further increase total throughput. Still, our sensitivity estimates have been based on the currently standard TI window A/R coatings, except for the NIR arm where we assume a replacement window with a proper coating for the bandpass.

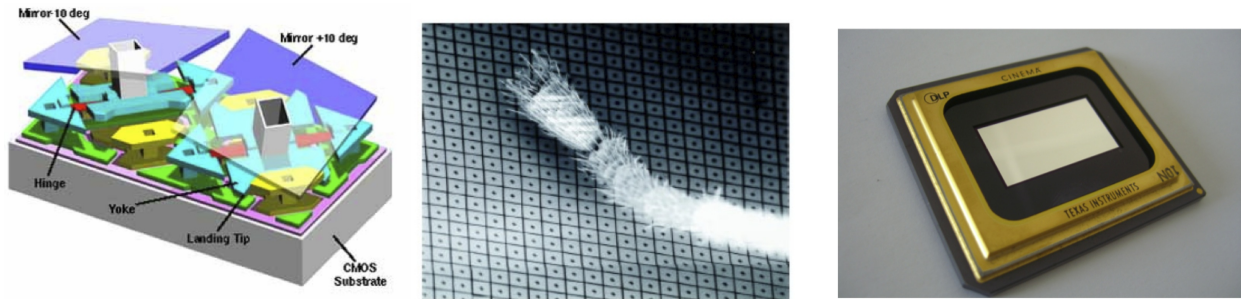


Figure 48: Left: Typical substructure of a TI DMD; Center: An early DMD array with an ant leg for comparison; Right: Packaged DMD CINEMA (2048 × 1080) device.

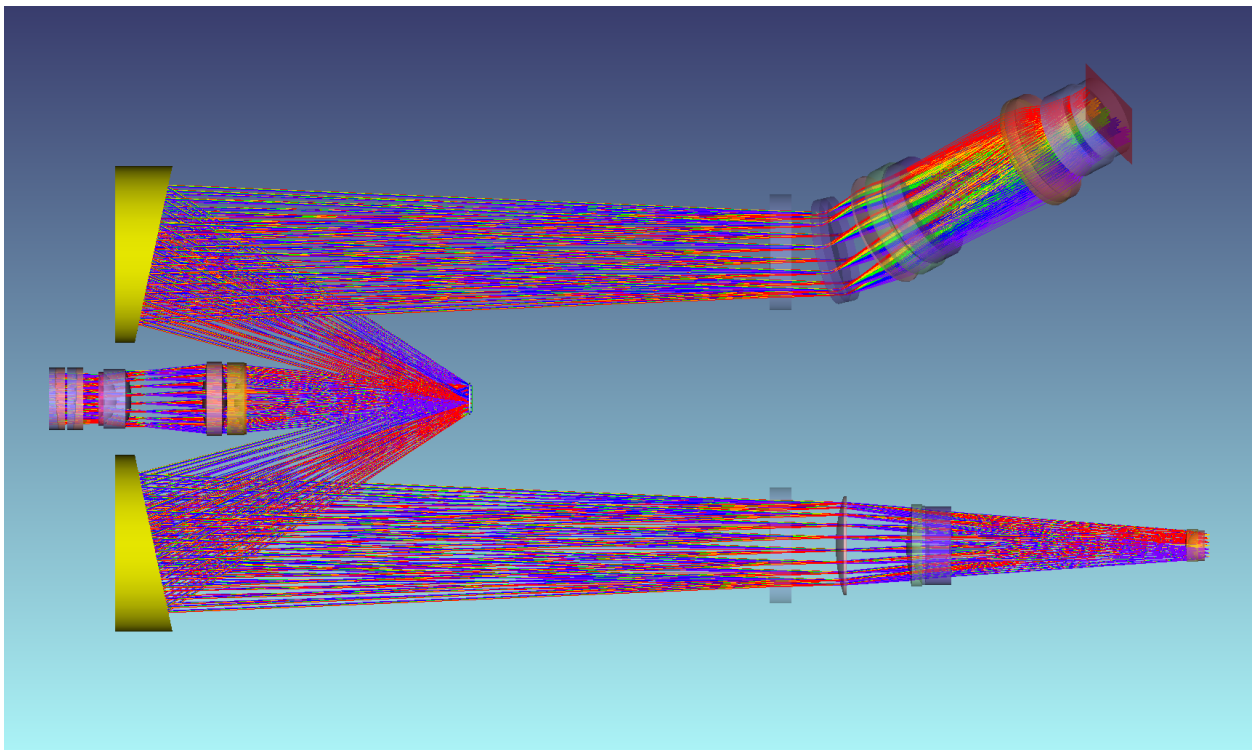


Figure 49: Optical detail for a DMD-based spectrograph, using a refractive reimager ahead of the DMD and a Schmidt collimator with discrete off-axis optics per DMD mirror state. Both output beams, ON and OFF (dispersing and slit-viewing), are shown unfolded here for clarity.

G.2.2.4 OFF-AXIS SCHMIDT COLLIMATORS

To provide parallel spectroscopic and acquisition/imaging channels, we have adopted a symmetric design (Fig. 49). The parallel channels use the ON and OFF reflected beams at ± 24 degrees relative to the incident beam, which is normal to the plane of the DMD. The relatively fast $f/4.1$ beam, the large field angles into the DMD (~ 15 degree full field of view), and the inherent angle between the normal to the DMD and its plane of reflection, led to an off-axis, modified Schmidt design for the collimators. Both collimators in a particular arm are identical, producing a 101 mm collimated beam in the red and blue arms, and a 81 mm beam in the NIR arm. Unlike a classic Schmidt, the mirrors are conic (oblate ellipsoid) rather than spherical, which alleviates the need for a field flattener in front of the DMD. Also, the collimator pupil is offset from the usual location at the center of curvature of the mirror where the corrector resides, driven primarily by the need to have a pupil at the reimager. The benefit is the reduced size of the dispersers and camera optics downstream. The blue and red collimators employ a single aspheric corrector, while the tighter imaging requirements of the NIR channels require a dual corrector design. The first element of the dual corrector is a typical Schmidt corrector with optical axis coincident with the mirror axis, while the axis of the second corrector is centered on the axis of the collimated beam. The collimators are folded to fit the available instrument volume.

G.2.2.5 SPECTROSCOPIC CHANNELS

The spectroscopic channels are comprised of VPH grating dispersers, refractive camera lenses, CCD detectors in the red and blue arms, and HgCdTe detectors in the NIR arm. In addition, the NIR arm contains two dichroics immediately after the collimator corrector in order to split the light into Y+J, H, and K channels. The blue and red spectroscopic cameras, shown in Figure 50, employ all-refractive designs based on the SDSS/BOSS spectrographs. The all-refractive NIR cameras are shown in Figure 51. The three cameras employ similar designs, each with six air-spaced elements.

G.2.2.6 SLIT-VIEWING CHANNELS

Each arm of GMOX is equipped with a slit-viewing camera, which images any light not sent to the spectroscopic channels by the DMD mirrors. These cameras would be used for acquisition (field identification, target selection, etc.), fine guiding, tip-tilt feedback for the AO system, and parallel science imaging. The optical designs for the cameras are rather straightforward, all-refractive systems, shown in Figure 52.

G.2.3 OPTICAL PERFORMANCE

G.2.3.0.1 IMAGE SIZE There are three distinct image plane locations in GMOX where we must ensure the imaging performance of the optics is sufficient. These are: (1) the surface of the DMD, (2) the detectors of the spectroscopic cameras, and (3) the detectors of the acquisition/slit-viewing cameras. The imaging chain begins with the telescope, and Figure 53 shows the spot diagrams for the telescope focal surface, located 4 m behind the vertex of the primary mirror, with a radius of curvature of 1.915 m concave toward the primary. Across the GMOX field of view, the telescope design delivers consistent 0.05" images. With each DMD mirror subtending 0.083", we see that the first link in the imaging chain is capable of delivering spot diameters 0.6x the size of a single DMD mirror.

The function of the reimagers is to relay the curved telescope focal surface onto the flat surface of the DMD arrays, with a (de)magnification of 4x. This maximizes the field of view while the

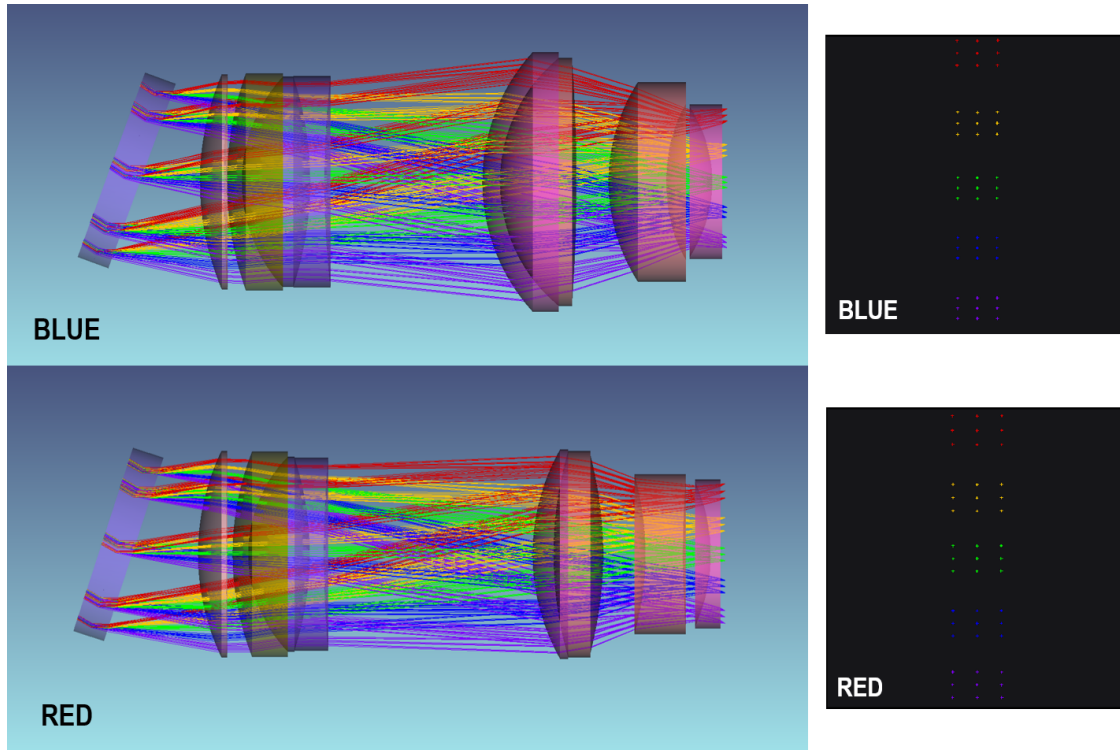


Figure 50: Details of the visible spectroscopic cameras. The optical designs are based on those for the SDSS/BOSS spectrograph cameras. The tilted plane parallel elements at the left edge are the VPH gratings; light propagates left to right. The black squares at the right show the format of the spectra on each detector. A 3 x 3 grid of points representing the full field were ray-traced at each of five wavelengths across the respective bandpass. The dispersion direction is top to bottom (long to short wavelengths) both in the optical layouts and detector formats.

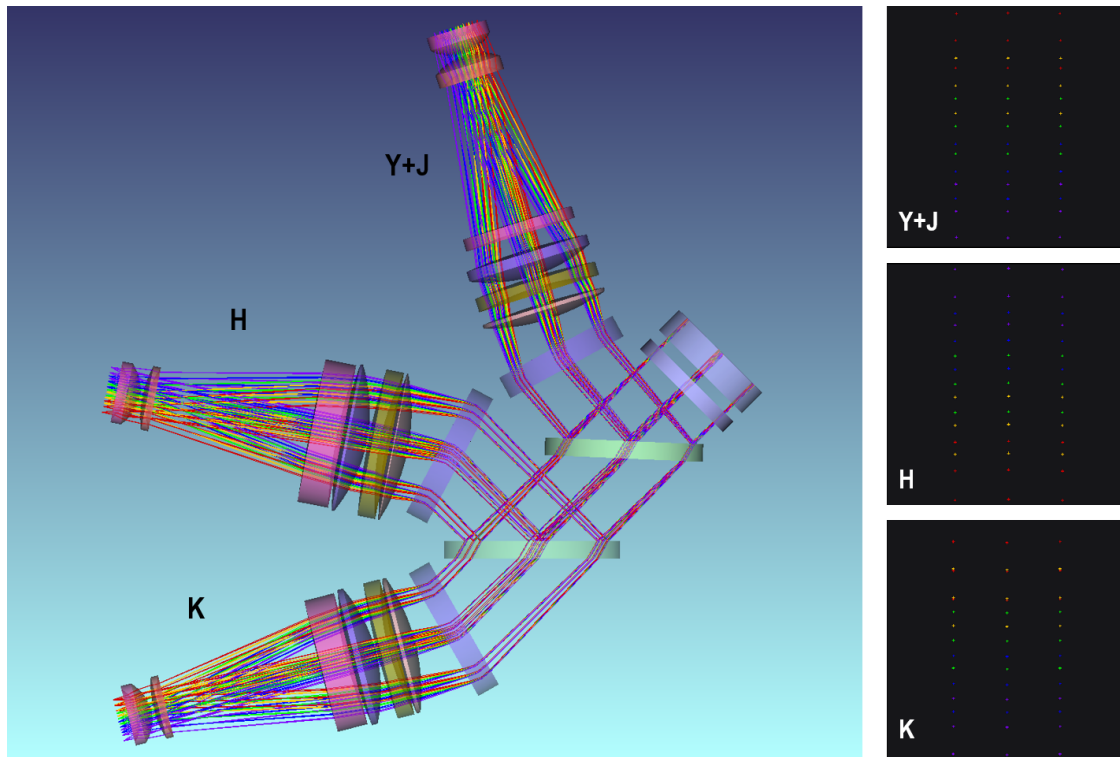


Figure 51: Details of the NIR spectroscopic channel optics. The all-refractive cameras employ an air-spaced, 6-element optical design. Two dichroics split the beam into the three channels between the dual aspheric Schmidt corrector and the VPH gratings. The black squares at the right of the figure show the format of the spectra on each detector. A 3 x 3 grid of points representing the full field were ray-traced at each of five wavelengths across the respective bandpass. The dispersion direction is top to bottom (long to short wavelengths).

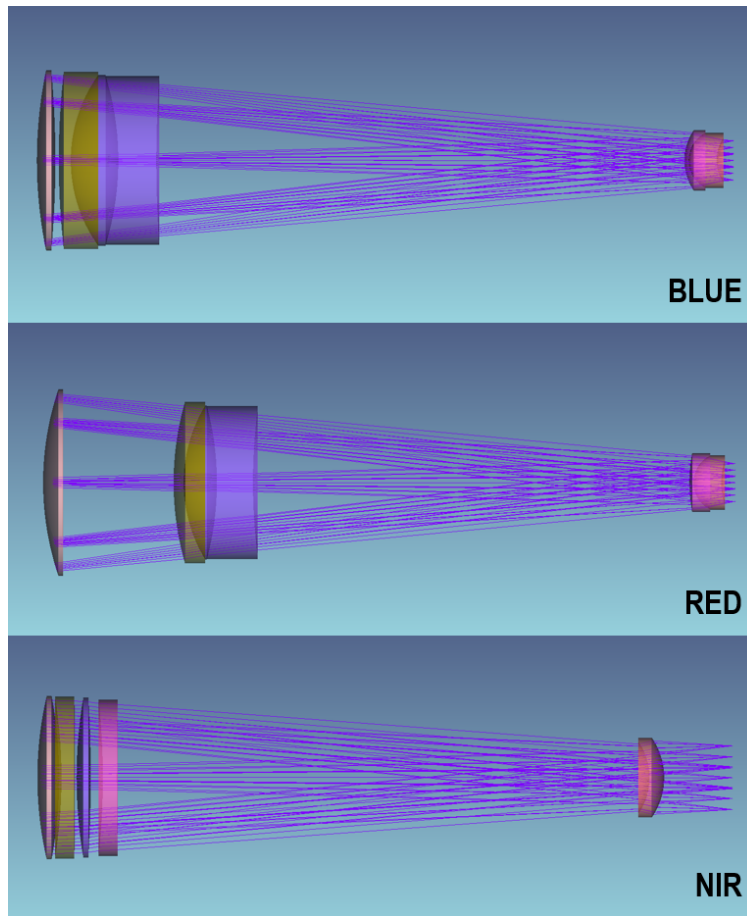


Figure 52: Details of the slit-viewing camera optics.

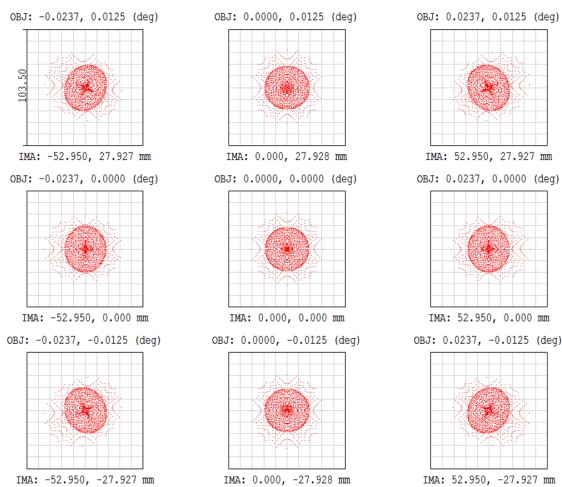


Figure 53: Spot diagrams at the telescope focal surface, representing the full GMOX bandpass. The boxes are $103.5 \mu\text{m}$ square, equivalent to a 2×2 array of DMD mirrors projected to the telescope focal surface. The RMS diameter is a consistent $32 \mu\text{m}$ ($0.05''$) across the $170.6'' \times 90.0''$ field of view of GMOX.

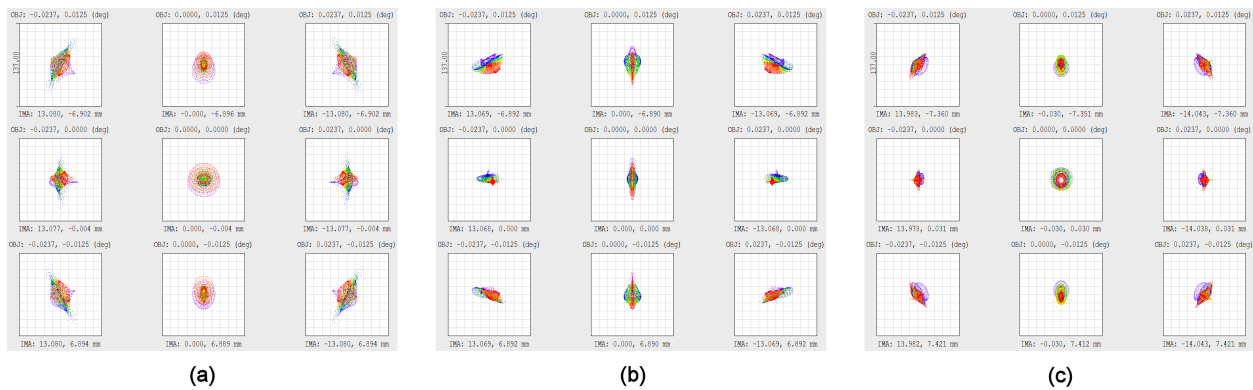


Figure 54: Spot diagrams at the DMD for the (a) blue, (b) red, and (c) NIR arms. These spots represent the imaging performance of the three reimagers over the full field and bandpass of each arm. All boxes are $137 \mu\text{m}$ square, corresponding to a 10×10 array of DMD mirrors. The wavelengths and average RMS spot radius are as follows: (a) 330-589 nm, $13.85 \mu\text{m}$; (b) 589-1000 nm, $10.72 \mu\text{m}$; (c) 970-2400 nm, $8.71 \mu\text{m}$.

resulting $f/4$ beam provides sufficient clearance between the incident and reflected beams at the DMD. The reimagers should produce image sizes that are small enough (approximately half or less than half of the slit width) to not blur the images and add to the slit losses beyond that already resulting from the native (or AO-corrected) image widths. Figure 54 shows the full bandpass spots sizes delivered by the reimagers at each DMD. In the figure the boxes represent a 10×10 array of micromirrors. With nominal slit widths of 5, 4, and 3 micromirrors (blue, red, and NIR arms, respectively), the reimagers as designed meet their performance objective. Note that in all of the spot diagrams shown here, the telescope is included in the Zemax model used to produce the images.

The DMD image plane is reimaged by a Schmidt collimator and spectroscopic camera combination onto the corresponding science detector, with the wavelengths dispersed by the VPH gratings. Figure 55 shows the spots produced by the blue and red arms at the science detectors. Instead of showing a 3×3 panel of spot diagrams for individual wavelengths across each bandpass, here we have overlaid five wavelengths at each field position in order to convey the imaging performance of the spectroscopic channels in a more compact format. The centroid for each wavelength and field position was used to center the spot in the box corresponding to the particular field position. In reality, the overlaid wavelengths in each box would be widely separated (dispersed) at the detector plane. Figure 56 shows similar spot diagrams for the three NIR science channels: Y+J-band, H-band, and K-band.

Similarly, in the three slit-viewing channels the DMD is reimaged onto the detector by the combination of a Schmidt collimator and slit-viewing camera. Figure 57 shows the spots at the slit-viewing detectors for each arm. For this study we have targeted a pixel format of $2\text{k} \times 1\text{k}$ for the slit-viewing cameras, i.e., one pixel per DMD mirror. For the blue and red arms the assumed pixel size is $12 \mu\text{m}$ (Andor fast-readout camera); for the NIR it is $18 \mu\text{m}$ (H2RG). Keeping in mind the nominal slit widths of five, four, and three micromirrors (blue, red, and NIR arms, respectively), likely the imaging performance of the slit-viewing optics is adequate for the purposes of acquisition and guiding, certainly at this early stage of the design process. For the purposes of calibration and mapping of DMD mirror position to slit-viewing detector pixel, however, it is likely we would want to tighten up the PSF's a bit, particularly in the blue arm. As it stands, the camera designs are not difficult and there is certainly room to improve the imaging performance without a significant increase in complexity or cost.

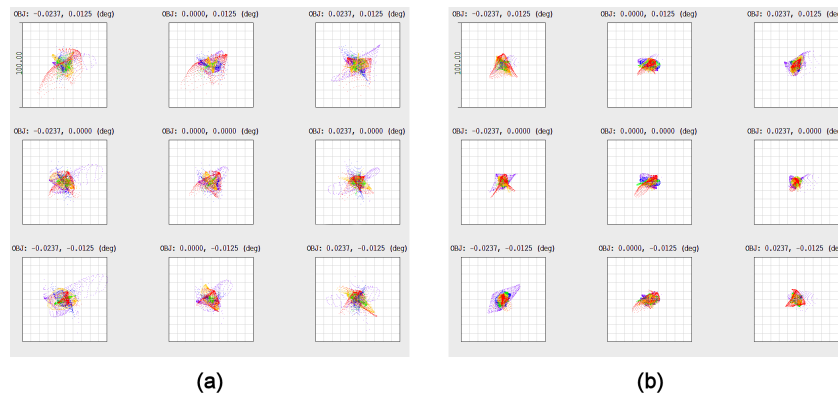


Figure 55: Spot diagrams at the spectroscopic detectors for the (a) blue, and (b) red arms. For each field position, spots from five wavelengths spanning the full bandpass have been overlaid, in order to show the image sizes in a more compact format. In reality, these wavelengths are dispersed across the length of the spectrum. All boxes are 100 μm square, corresponding to a 10 x 10 array of detector pixels. The wavelengths and average RMS spot radius are as follows: (a) 330-589 nm, 10.03 μm ; (b) 589-1000 nm, 6.70 μm .

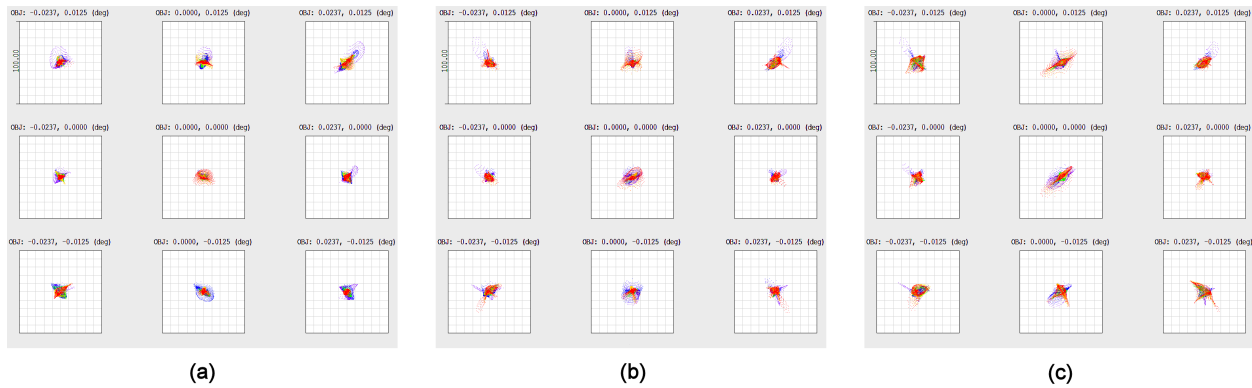


Figure 56: Spot diagrams at the NIR spectroscopic detectors for the (a) Y+J-band, (b) H-band, and (c) K-band channels. For each field position, spots from five wavelengths spanning the full channel bandpass have been overlaid, in order to show the spectroscopic image sizes in a more compact format. In reality, these wavelengths are dispersed across the length of the spectrum. All boxes are 100 μm square, corresponding to a 10 x 10 array of detector pixels. The wavelengths and average RMS spot radius are as follows: (a) 0.97-1.35 μm , 5.07 μm ; (b) 1.46-1.81 μm , 5.18 μm ; (c) 1.93-2.4 μm , 6.53 μm .

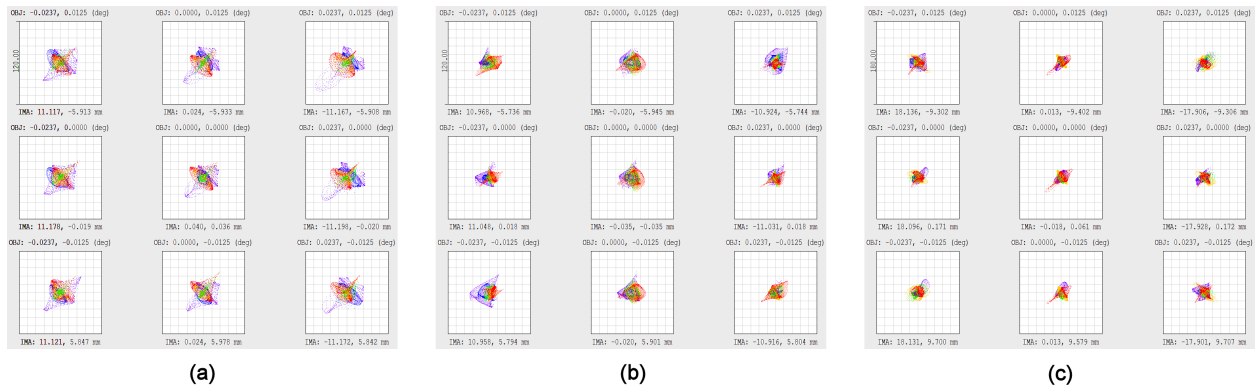


Figure 57: Spot diagrams at the slit-viewing detectors for the (a) blue, (b) red, and (c) NIR arms. These spots represent the imaging performance over the full field and bandpass: (a) 330-589 nm; (b) 589-1000 nm; (c) 0.97-2.40 μm . For the blue and red arms the boxes are 120 μm square; for the NIR arm the boxes are 180 μm square. This corresponds to a 10 \times 10 array of detector pixels in all cases. The average RMS spot radius in each arm across the field is: (a) 12.64 μm ; (b) 8.81 μm ; (c) 10.30 μm .

G.2.3.1 THROUGHPUT

We have constructed a detailed instrumental throughput (efficiency) model for the five spectroscopic channels and three slit-viewing/imaging channels of GMOX. Our model considers all GMOX instrumental effects except slit loss (seeing) and scattered light. This includes: anti-reflection coatings; mirror reflectivities (Al, Ag, Au); glass internal transmission; dichroic performance based on measured curves from the BOSS dichroics produced by JDSU; reflectivity, fill factor, and window transmission in double pass for the DMD's (assumes a replacement window for the NIR); and grating efficiencies based on the first-look, unoptimized design curves from Kaiser Optical (which include manufacturing tolerances). Figure 58 shows a plot of the resulting efficiency estimates for the five spectroscopic channels, and Figure 59 shows the plot for the slit-viewing channels. Note that for the slit-viewing channels we have not assumed any filter transmission curves (losses).

For the QE of the blue and red spectroscopic detectors, we adopted values published in the datasheet for the CCD290-99 (e2v document A1A-778871 Version 1, March 2014). Specifically, we used the curve corresponding to the astro multi-2 AR coating for standard (blue) and deep depletion (red) silicon at -100°C . For the NIR detector QE, we refer to the QE curves for a WFIRST-AFTA (H4RG-10) SCA published by Teledyne [184]. QE curves are plotted for each of the 16 bands of a developmental SCA; we have conservatively chosen values from the lower $\sim 25\%$ of the curves.

G.2.3.2 DMD CONTRAST

DMDs are not ideal devices: some of the light that diverted to the off-beam may leak to the on-beam, increasing the background and degrading sensitivity. This problem, generally referred to as “loss of contrast”, has been often mentioned as a drawback of DMDs. About 15 years ago, NASA down-selected to the Micro-Shutter-Array technology for JWST/NIRSpec against Digital-Micromirror-Devices on the basis of the higher achievable contrast; the spec was 1:2500, i.e. less than one background photon out of 2,500 had to leak to the science channel.

For commercial applications, in particular for projection devices, achieving high contrast is mandatory: digital movie theaters in particular require the highest dynamic range of illumination. In the years since, Texas Instruments has made great progress: the latest generations of

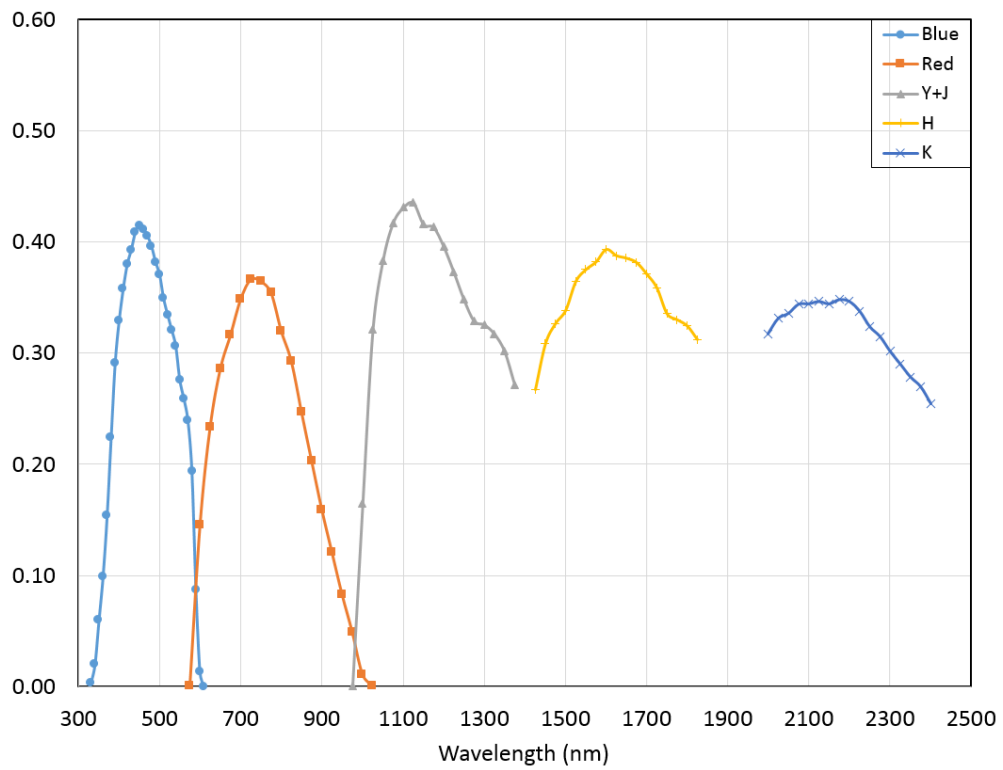


Figure 58: Instrumental throughput estimates for the five spectroscopic channels of GMOX. Telescope and Adaptive Optics systems are not included.

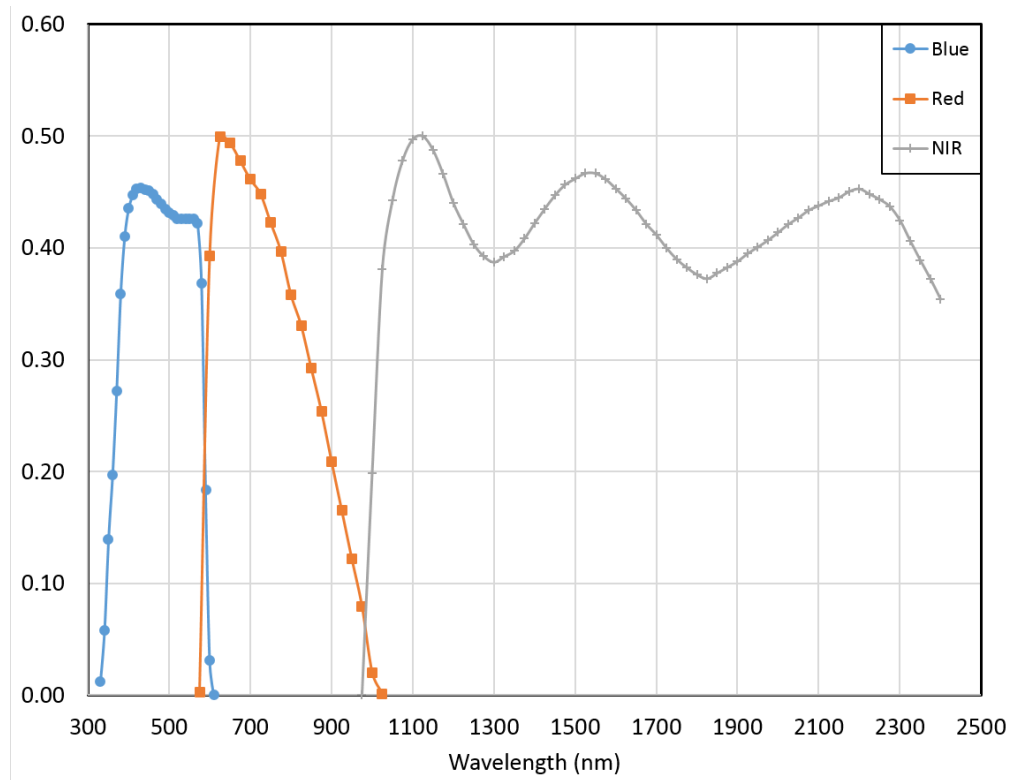


Figure 59: Instrumental throughput estimates for the three imaging/slit-viewing channels of GMOX. Telescope and Adaptive Optics systems are not included.

“dark” DMDs are compliant with the industrial standards set by the Digital Cinema Initiatives. In particular, DMDs are compliant with the sequential contrast requirement, expressed as *“The sequential contrast ratio is computed by dividing the white luminance (of a peak white field) by the black luminance (of a black field). The nominal (reference) value is required to have a minimum sequential contrast of 2000 : 1”* (REF. http://www.dcinovies.com/archives/spec_v1/DCI_Digital_Cinema_System_Spec_v1.pdf). Measuring the full-on vs. full-off contrast in stationary conditions is appropriate also of astronomical applications, as the spectroscopic channel typically sees a stationary, nearly uniform full-off field (the exceptions being the slits open to the targets).

Contrast is inherently a characteristic of the integrated systems, as it strongly depends on the $f/\#$, on the illumination angle, on having a telecentric vs. non-telecentric beam, on the size and location of the pupil, on the illumination overfill, optical ghosts, etc., plus scattering and diffraction from the DMD itself. The values quoted by projector vendors have increased from 1:400 for the early generations of projectors to 1:13,000 for the most recent ones. Projectors, however, operate with optical layouts and operating conditions quite different from an astronomical spectrograph: they blast the DMD with an enormous number of photons and push the $f/\#$ to the limit ($\approx f/2.8$) to increase output luminosity. This at the expense of degraded contrast, which can be recovered by timing the intensity of the illuminating source: a “dynamic iris” is now used to decrease brightness when the scene is dark.

Direct measures of the intrinsic DMD contrast are difficult, scarce and often refer to obsolete devices. Illuminating a Cinema DMD at $f/3$, Zamkotsian et al. (Proc. SPIE 7932, Emerging Digital Micromirror Device Based Systems and Applications III, 79320A (February 11, 2011); doi:10.1117/12.876872) measured at visible wavelengths a native contrast 1:2,300 comparing adjacent mirrors. At NASA Goddard we are measuring much higher values: using a Agilent Cary 5000 spectrophotometer illuminating the DMD from the normal direction, the faint background scattered by a square of $\approx 100,000$ mirrors tilted off is comparable to the signal reflected by ≈ 2 pixels tilted on. We estimate a contrast $\approx 1 : 50,000$ at visible wavelengths in conditions similar to those encountered by an astronomical spectrograph. The contrast should improve at longer wavelengths, as the scattering contribution from the aluminum mirrors decreases with the square of the wavelength.

To understand the optical properties of DMDs, it is also interesting to consider their diffraction pattern. A DMD is basically a 2D grating with faces blazed at 45° . The diffraction orders follow the orthogonal orientation of the grating, and therefore are centered around the perpendicular axis for normal illumination; their location depends on the wavelength but not on the tilt angle of the mirrors. Their intensity, however, is modulated by an envelope determined by the Fourier transform of the tilted mirrors, peaking along the diagonal at 24° from the normal. Switching between the on- and off-state is, in rigorous terms, a shift of the envelope. Figure 60 shows two examples of DMD diffraction pattern, stretched in intensity to illustrate the richness of the geometry. The plots clarify why TI has developed mirrors tilting along the diagonal, to minimize the contribution of unwanted diffracted light, i.e. to increase contrast. Our simple model has several limitations: a) spectrographs don't have the DMD at the pupil plane but at the focal plane, and the correlated beam is spread over just a few adjacent mirrors, with non-uniform intensity, b) the model assumes a plane wave, while the actual beam is converging and not telecentric, so that each mirror receives a different cone of light; c) in broad-band the orders are smoothed and not visible. Direct measures are needed, and our group is pursuing this key aspect with experimental setups at RIT, JHU and Goddard under an independent NASA funded program.

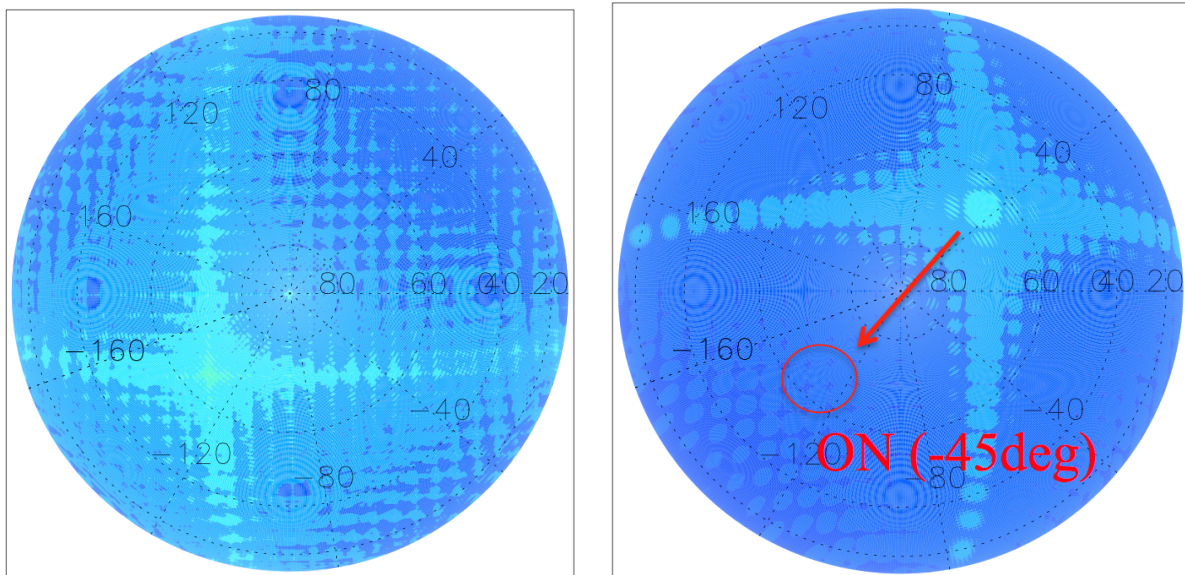


Figure 60: Left: Orthographic polar projection (view from the top, illumination direction) of the diffraction pattern generated by a DMD device with 3 mirrors tilted to the “ON” beam. The intensity has been stretched to illustrate the pattern. Right: Diffraction pattern created by one single mirror tilted in the “OFF” direction, 48° away from the “ON” beam.

Let’s assume our measured contrast 1:50,000. If all DMD mirrors are tilted-on, the spectrograph will see a slitless spectrum of the sky. The worse case will be the H band, with a sky brightness of 14.5 magnitudes per square arcsecond. Our $0.1''$ pixel sampling reduces this value by 5 magnitudes, so the full-on background is equivalent to 19.5 mag/pixel. We then tilt all mirrors off. The contrast 1:50,000 produces an attenuation of 11.75 magnitudes, bringing us to 31.25mag. The Zero Point for the H band is about 10^{10} ph/s/m²/micron. Assuming a bandpass of $0.35\mu\text{m}$ and a 50 m^2 telescope with 30% throughput, this corresponds to 4.5×10^{10} ph/s, that diluted by 27.25mag implies 0.015 e/s/pix of sky background, which is just slightly higher than our assumed dark current. Assuming an equivalent readout noise (after multiple non destructive samples) of 3.5 e/pixel, GMOX in the H-band becomes background limited after about 1500s. We have included this effect in our ETC.

G.2.4 MECHANICAL DESIGN

The GMOX mechanical design is driven by several key requirements. First, the instrument must fit within the control volume specified by Gemini. Second, the instrument structure must be stiff so as to minimize flexure. Third, it must have the requisite mass and CG to balance the ISS, and ultimately the telescope. And fourth, the design must be conducive to ease of optical alignment; at least relatively so.

As discussed in Sec. G.2.2, the odd hammerhead shaped control volume drives the optical layout, and that in turn drives the mechanical layout. Figure 61 shows a very conceptual design for GMOX placed within the instrument control volume of Port-1. The instrument has dimensions of 1266 mm in “X”, 2831 mm in “Y”, and 1912 mm in “Z”. To maximize stiffness, the mechanical structure is designed such that the base of the instrument consumes nearly all of the available volume near the interface to the ISS. This maximizes the footprint on the ISS surface making for a very stiff structure, one that can adequately handle the bending moments induced by the vary-

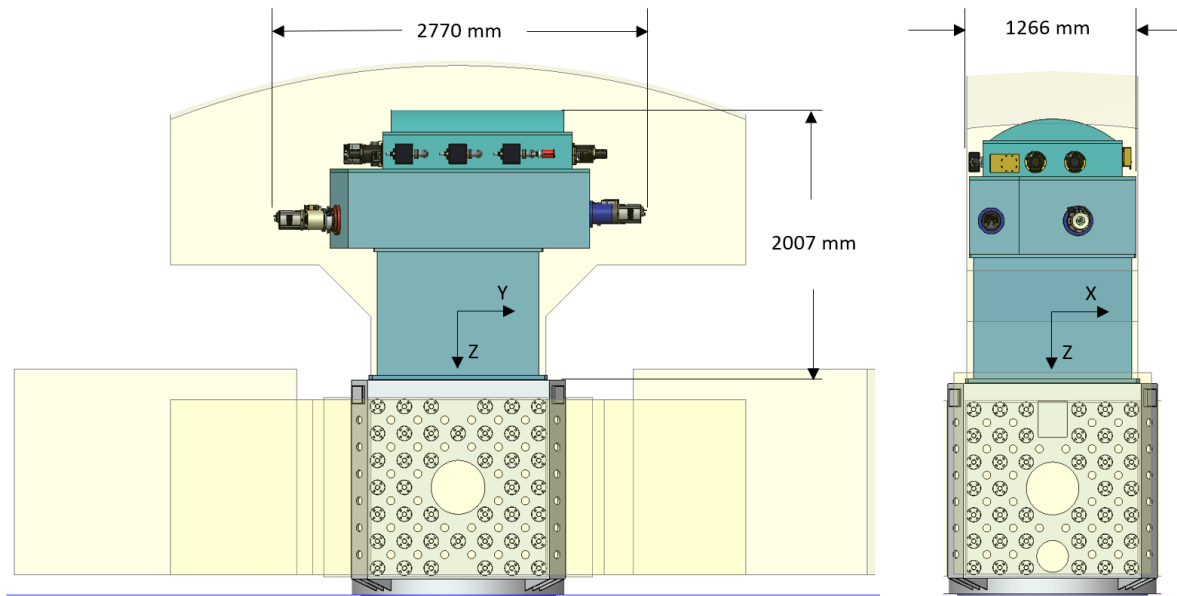


Figure 61: Rendering showing the side-view and end-view of GMOX mounted on the ISS within the Gemini specified instrument control volume.

ing gravity load. In the X-direction, the instrument consumes nearly all of the 1300 mm width available within the control volume.

The conceptual mechanical layout of GMOX is shown in Fig. 62. The instrument is divided into three primary opto-mechanical modules: the Lower Bench, the Upper Bench, and the NIR Cryostat. Each of these is described in more detail below. This layout is advantageous from an opto-mechanical alignment perspective since the reference datums that locate one module to another are all parallel, and parallel surfaces can be readily machined to high precision with integral locating features to precisely align one module to the next.

In this initial conceptual design, we have assumed aluminum for the structural material, which keeps the instrument light. A bit too light for the requirement. The mass of the instrument, as shown, is 1659 kg, with a center of gravity (CG) located 1095 mm from the ISS interface. To achieve the required 2000 kg mass with a CG 1000 mm from the ISS, ballast has been added in the form of two *mass towers*, which reside inside the lower bench; see Figure 63. The towers are bolted directly to the ISS so as not to increase instrument flexure. Another means of adding additional mass to the instrument would be to construct the structural components from steel. Steel has three times the density and three times the stiffness. To first-order, steel provides no benefit from a flexure perspective in a case like this where the loading is strictly gravity. But it would solve the mass problem for certain.

There are, however, practical considerations with respect to the trade between steel and aluminum. Steel structures can be welded with less distortion than aluminum and that eases fabrication. Aluminum, on the other hand has a higher thermal conductivity, by a factor of four, and that is advantageous from the perspective of the temporal stability of the instrument, since changing thermal gradients due to changing weather can shift optics. Aluminum is also easier to machine. Of course, the coefficient of expansion of aluminum is nearly a factor of two greater than steel, so steel wins in that regard. These considerations would be looked at more carefully in the next phase of development.

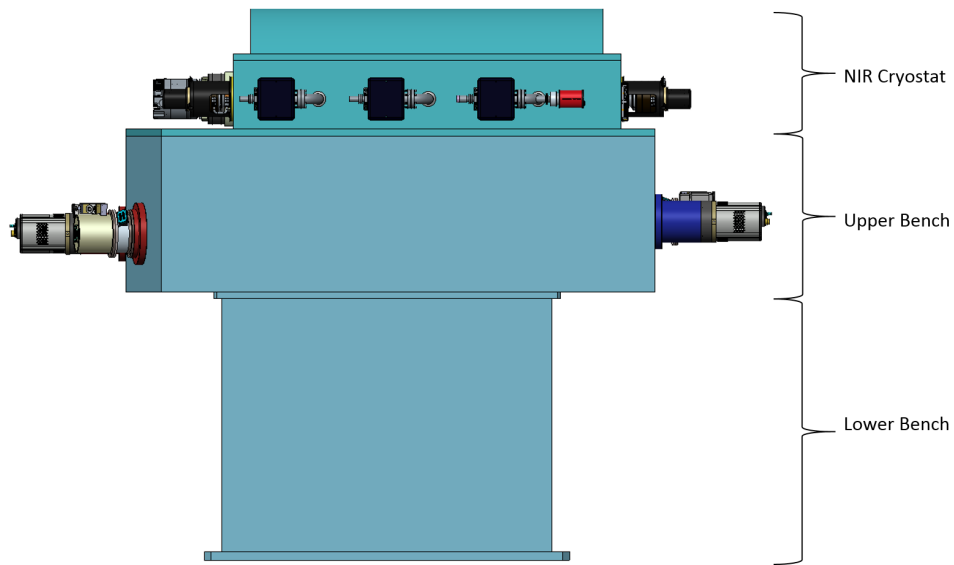


Figure 62: GMOX side-view. Mechanically, the instrument is composed of three stacked modules: the lower bench, the upper bench, and the near infrared cryostat.

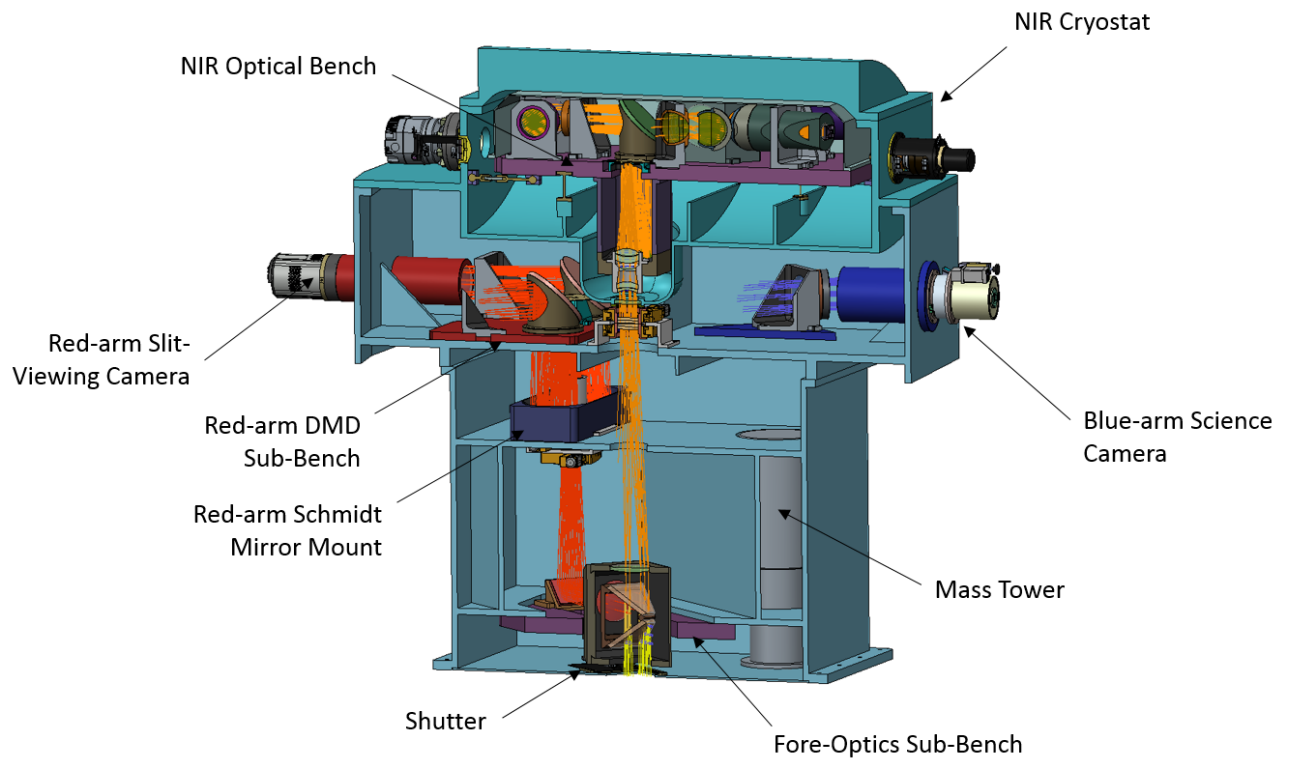


Figure 63: Rendering showing a section view of GMOX.

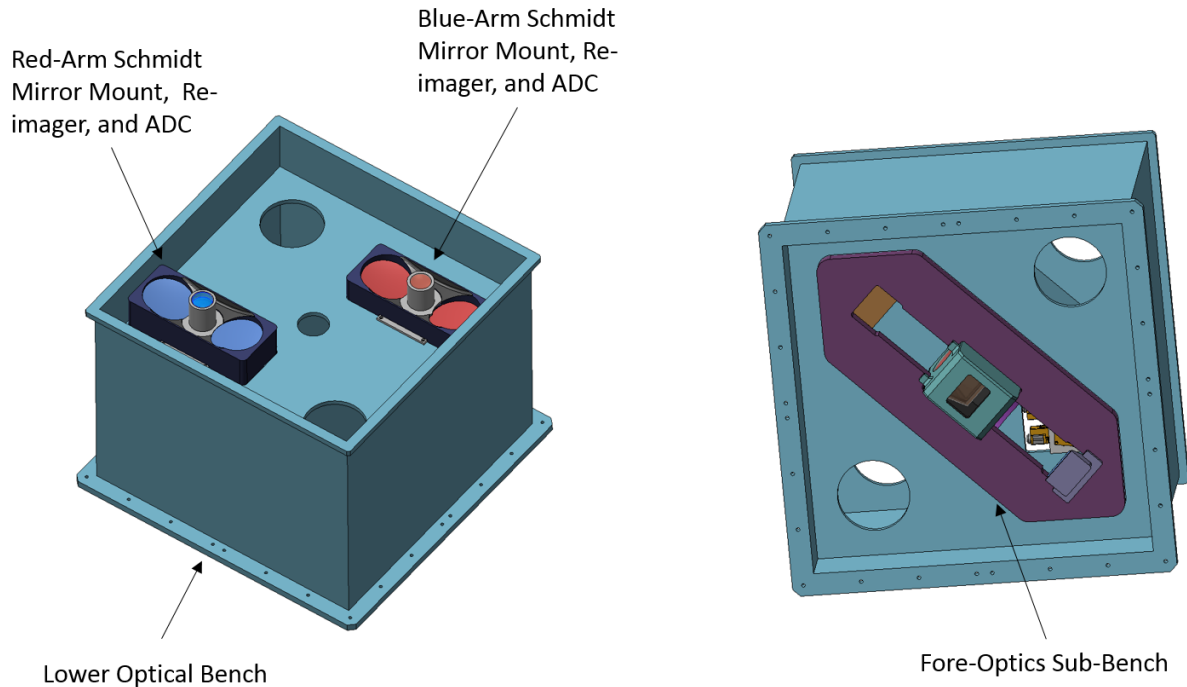


Figure 64: Rendering of the lower optical bench showing the placement of the Left: red and blue arm Schmidt mirror cells and ADCs, and Right: the fore-optics sub-bench.

G.2.4.1 THE LOWER BENCH

The lower bench serves as the base of the instrument. Within the lower bench there are two *levels*; see Fig. 64. On the lower level, all the instrument fore-optics are mounted including the shutter, field lenses for all three arms, the beam splitters for the red and blue arms, as well the fold mirrors that redirect the red and blue beams along a path that is normal to the ISS and parallel to the near infrared beam in the center. All of these optics are mounted to the fore-optics sub-bench, which attaches to the *bottom* side of the lower level. On the top side of the upper level, the Schmidt collimator mirror assemblies for the red and blue arms are mounted, along with their integrated re-imaging optics and atmospheric dispersion correctors.

The top-most surface of the lower bench interfaces to the bottom of the upper bench. Locating features, i.e. dowels, would precisely locate the two benches relative to one another, and the bolted joint around the perimeter flange of the lower bench would securely fasten the two benches together. This will be a very stiff connection.

The bottom-most surface of the lower bench interfaces to the ISS. A flange around the perimeter of the bench circumscribes the outermost pattern of 12 mm threaded holes in the ISS. As envisioned, 28 of those threaded holes would be use to fasten the lower bench to the ISS.

To accommodate trim-weights, two large holes are provided on each level of the lower bench. These holes create two tall volumes in which the mass towers described above would reside. The mass towers would bolt directly to the ISS using the existing array of 12 mm threaded holes.

As just described, the fore-optics are mounted on a sub-bench. This allows for a more orderly arrangement of the optics, one that is more conducive to precision fabrication and alignment.

The fore-optics sub-bench comprises three opto-mechanical assemblies: a central-optics assembly consisting of the field lenses for all three arms, and both dichroic beam splitters, and two fold mirrors. Should tip-tilt control be required for inter-arm flexure control, and it most likely

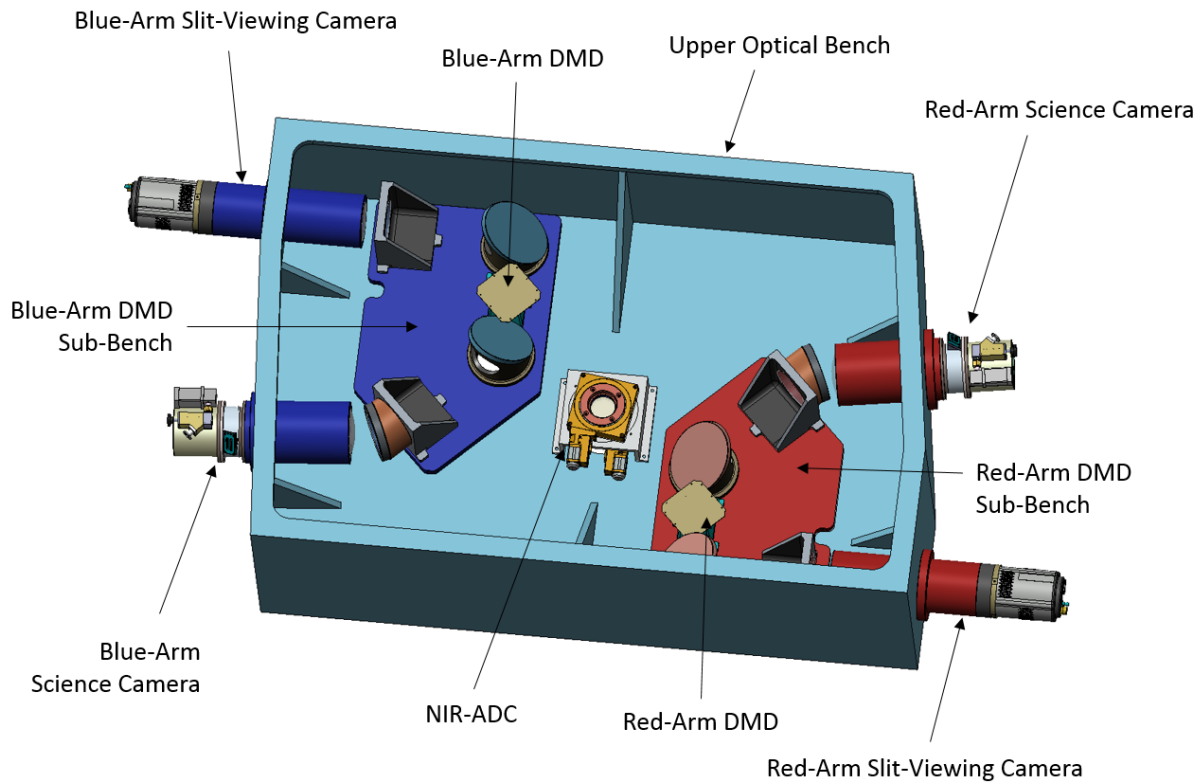


Figure 65: Rendering of the upper optical bench showing the placement of the red and blue arm sub-benches, and the ADC for the NIR arm.

will, we would implement that control at the fold mirrors; most certainly using piezo actuators. Each of these assemblies would be pinned to the sub-bench. And the fore-optics sub-bench itself would be pinned and bolted to the lower bench. Nominal shims at the interfaces to the sub-bench would allow for adjustment to accommodate manufacturing tolerances.

Similarly, each of the two collimator mounts locates a pair of Schmidt collimator mirrors. The reimaging optics attach to the mirror mount, as does the atmospheric dispersion corrector. Like the fore-optics bench, nominal shims would be integral to the design, and would be tailored to accommodate manufacturing tolerances. The collimator assemblies would be pinned and bolted to the top side of the upper level of the lower bench.

G.2.4.2 THE UPPER BENCH

The upper bench is the mechanical reference for the red and blue arm DMDs, Schmidt correctors, and gratings, as well as the fold mirror for both the spectroscopic and slit-viewing legs. It is also the interface to which the science and slit-viewing cameras attach for the red and blue arms. And it is the reference for the near infrared arm atmospheric dispersion corrector. Figure 65 shows the arrangement.

There are two sub-benches in the upper bench. One containing the DMD, correctors, folds and grating for the red arm, and a second for the same components of the blue arm. Again, as with the components in the lower bench, we have opted to mount these components to sub-benches rather than directly to the bench itself to ease alignment verification. Nominal shims would be used where placement tolerances exceed manufacturing tolerances, and those would be adjusted

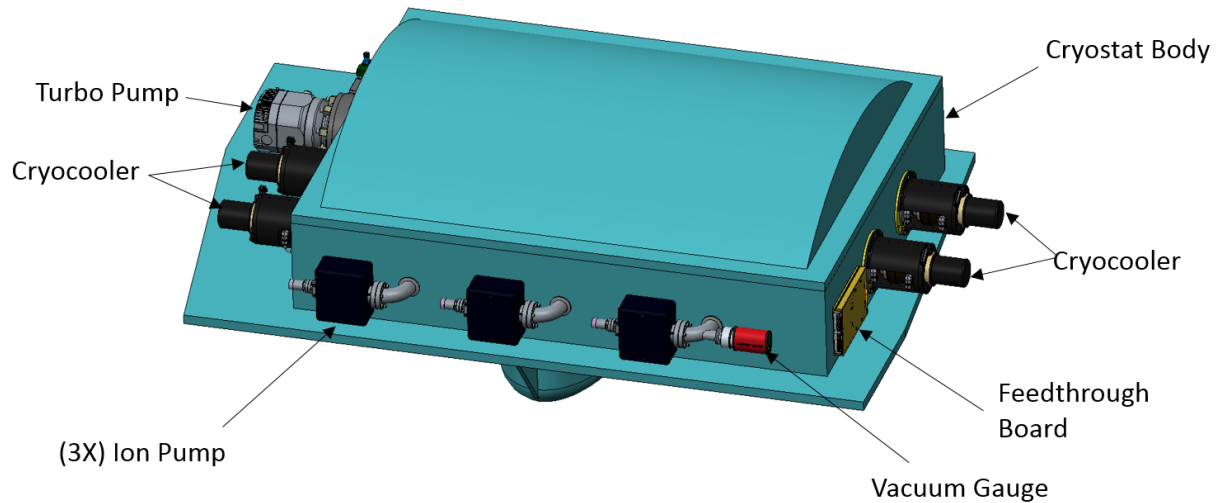


Figure 66: Rendering showing a conceptual design for the NIR cryostat.

based on as-built dimensions.

The top of the upper bench interfaces to the near infrared cryostat. And that interface would be pinned. The bottom side interfaces to the lower bench as discussed above.

G.2.4.3 THE NEAR INFRARED CRYOSTAT

The near infrared cryostat houses all of the optics in the near infrared arm, except for the NIR atmospheric dispersion corrector. Figure 66 shows a rendering of the assembly. The form factor is rectangular and squat, very similar in fact to the APOGEE cryostat for SDSS. This form factor is driven not only by the layout of the optics and the desire to minimize the volume, but also to allow ease of mounting for pumps and cryocoolers, which is readily accommodated by the four flat side-walls around the perimeter. A protrusion at the bottom of the cryostat body accommodates the Schmidt mirror assembly. This bump-out is required to encompass these optics without interfering with optical components from the red or blue arms housed in the upper bench. A small, 70 mm diameter, window in the center of the protrusion allows the near infrared light into cryostat.

The cryostat is a welded aluminum (6061-T6) structure consisting of two components: the cryostat body, and the cryostat lid. In general, the plates are thick, ranging from 12 mm to 25 mm. A large machined flange surrounding the body of the cryostat interfaces to the upper bench and that interface would be pinned for repeatable alignment. This pinned interface also serves as the placement reference for the location of the cold optical bench inside.

The remaining particulars of the cryostat design, including the vacuum and thermal details are described here:

- The Opto-mechanical Layout – All the optics in the near infrared cryostat are mounted to a single optical bench. Figure 67 shows the arrangement. Optics are mounted in logical subassemblies in a fashion similar to the visible arms. Camera lenses would be mounted in barrels, each barrel being mounted to an angle bracket that is kinematically attached to the bench. Each grating would be mounted to the face of its corresponding lens barrel. The Schmidt correctors would also be mounted in a barrel-to-right-angle-bracket arrangement.

As can be seen in the rendering the packaging of the spectral leg is tight, especially in the spectroscopic leg in the region around the dichroics. Clearance exists between the compo-

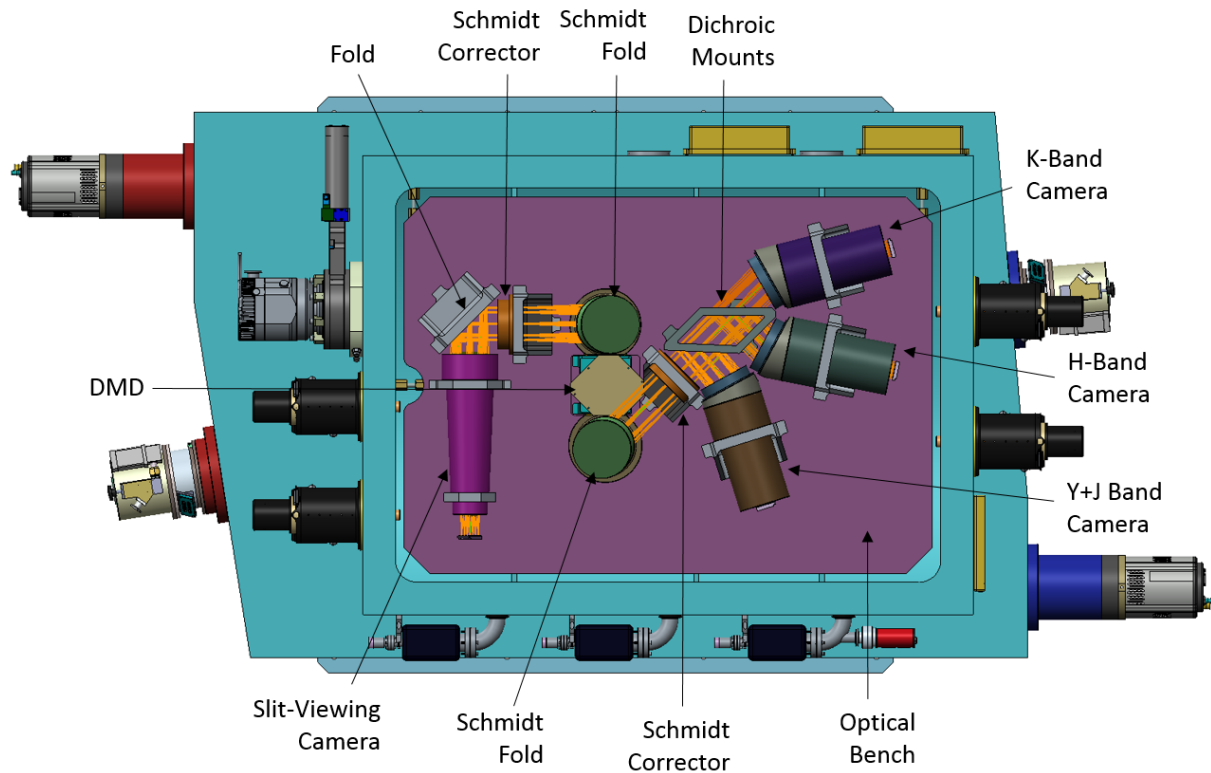


Figure 67: Rendering showing a conceptual design for the NIR cryostat.

nents but we would like more, and in the next iteration of the optical layout we would work to create a bit more separation between the dichroics and the gratings. This should be possible.

On the subject of clearance, the most glaring problem is the DMD board. It interferes with both Schmidt fold mounts as well as the Schmidt corrector mount on the spectroscopic leg. Clearly the DMD board will have to be revised, and this is possible. Although the level of effort is not yet known. It *should* not be significant as the board contains mostly traces with very few components. We should note that clearance in the visible arms is similarly problematic, albeit not nearly as severe. Therefore the modification to the board layout would be done in such a way that the board would work for all three arms.

- The Vacuum System – The cryostat volume is roughly 500 liters and would be pumped under steady-state operation using a bank of three Varian 20 liter/sec Star Cell ion pumps located on the side of the cryostat body. Combined with the cryopumping provided by the Sterling coolers a pressure of less than a microTorr should be readily achievable.

For roughing, we have found that pumping is far more efficient with the turbo mounted directly to the cryostat, instead of in a pump cart with a sufficiently long, and low conductance, hose connecting it to the cryostat. As such, a dedicated 240 liter/sec turbo pump would be permanently affixed to the body of the cryostat. And a gate valve would isolate the pump from the vacuum space during normal operation.

Pressure inside the cryostat would be monitored using a Pfeiffer MPT 200 combination (Pirani/Cold Cathode) gauge, which measures vacuum from atmospheric pressure down well into the high vacuum regime.

- The Thermal Design – To mitigate thermal background and achieve the desired detector performance, the near infrared optics and the detectors must be cooled. The temperatures to which they must be cooled will differ, however. For the optics, 120K will be sufficient to mitigate thermal background, as predicted by the direct integration of the blackbody over 2π sterad and demonstrated e.g. by MOSFIRE (McLean, I.S., Steidel, C.C. et al. 2012 “MOSFIRE, the Multi-Object Spectrometer For Infra-Red Exploration at the Keck Observatory” SPIE Procs, 8446 17) .

However, if needed, the DMD could operate at a higher temperature without adversely impacting background. The DMD sits on the focal plane and each pixels of the IR channel sees a tiny fraction of its surface, with almost a 1:1 correspondence between mirror and detector pixel; accounting for the area and assuming an average emissivity $\epsilon \simeq 10\%$ mainly do to the gaps between the mirrors, the maximum operating temperature needed to keep its thermal contribution up to $2.5 \mu\text{m}$ below a nominal 0.001 e/s/pixel dark current level is $T_{DMD} = 200\text{K}$ (Figure 68). Note that this temperature is lower than the operating temperature of the DMD on IRMOS ($\simeq 288 \text{ K}$) and this, and the lack of a cold shield in front of the detector to prevent stray light, is probably the cause of the higher background experienced by that instrument; GMOX will be immune to this problem. Operating the DMD at 120 K is more than adequate for the thermal design and RIT has demonstrated that DMDs can operate at this temperature. We plan to verify the RIT results in the coming months at JHU. And should it be determined that a higher DMD temperature is required it would be possible to do so without adversely impacting the thermal background, up to a temperature, $T_{DMD} = 200\text{K}$, provided the remaining optics and structure are held at 120 K.

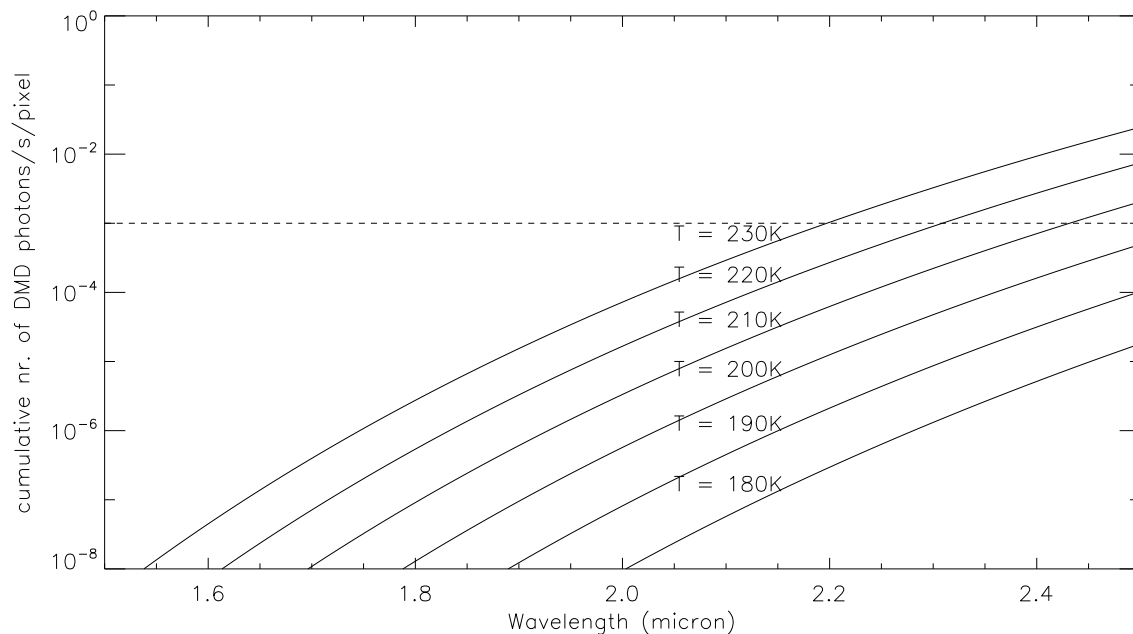


Figure 68: Total number of photons/s emitted by the GMOX DMDs reaching a pixel in the IR channel vs. DMD temperature. The dashed line at 0.001 e/s/pixel is representative of the dark current level.

The detectors would operate at a temperature of 77K. Hence, there will be two thermal regimes in GMOX, one for the optics, and one for the detectors.

The optical bench will be mounted to the body of the cryostat on titanium post flexures and cooled by a pair of Sunpower Cryotel GT coolers; one at each end of the bench. A radiation shield covers the entire top and sides of the optical bench. Multi-layer insulating blankets would be applied to the outer surfaces of the shield, the bottom of the bench, and the Schmidt mirror support.

The total heat load on the optics, radiative and conductive, is expected to be of order 15W. Assuming a large gradient along the thermal straps connecting the coolers to the bench, say 15 K, the Cryotel GTs would run at roughly 105 K, and at that temperature the lift is 22 W, or 44 W for two coolers. Therefore cooling may be possible using a single cooler. However, two coolers has its advantages. Specifically, more uniform cooling since cooling from each end of the bench reduces thermal gradients, and more importantly, the coolers can run at lower power, where the vibrational energy transmitted to cryostat is truly negligible.

For the detectors, two additional cryocoolers would be used. One for the three science channel detectors, and a second for the slit-viewing detector. It may be that one cooler could be used for all four detectors, but given the dispersed placement of the detectors, two will likely be required. Further analysis is needed to determine if one is sufficient.

- The Sunpower Cryotel GT Cooler – We would use the Sunpower Cryotel series coolers for the GMOX near infrared dewar, both for cooling the optics and the detectors. This choice stems from several key advantages the Sunpower cooler has over other technologies, including very long lifetime, compact form factor, and minimal heat dissipation to the ambient, at least by cryocooler standards.

The only negative to the Sunpower coolers is vibration, and this is a significant consideration for astronomical instruments. The self-contained unit vibrates from the linear piston motion internal to the unit. Even with passive damping, the unit vibrates at its fundamental mode of 60 Hz, at the level of 400 mG, and to a lesser degree at harmonics of 60 Hz. However, Sunpower has recently developed an active damping control system for the Cryotel units. When combined with a properly designed mount, the vibrational energy transmitted to the cryostat is negligible. Recent test results from the cryostats for the Subaru Prime Focus Spectrograph (PFS) cameras show vibration levels of order 1 mG at the cryostat with the cooler running at full power.

A photograph of the Cryotel GT assembly used for the PFS cameras is shown in Fig. 69. As shown, the cooler is mounted in a housing and supported axially, as well as laterally, on springs. A welded stainless bellows provides a soft transition from the base of the cooler to the *cup* at the front of the unit. In this photo the active damping motor is housed inside the gold cover at the rear of the unit (right side of the photo). We are grateful to Gerry Luppino for sharing the bellows mounting concept used here, which provided the basis for this design.

Heat generated by the coolers would be removed by facility glycol coolant. Dissipation from the Cryotel GT when operating at full power is roughly 250 W and with a glycol flow rate of 1 l/min the expected temperature rise of the body of the cooler is of order 10 K, small enough to produce only a minimal amount of convective heat leak to the dome. From experience, we know that only a small portion of the body of the cooler reaches this elevated temperature; most of the surface runs at ambient. The 4 l/min required by the four coolers can readily be supplied by the Gemini facility.

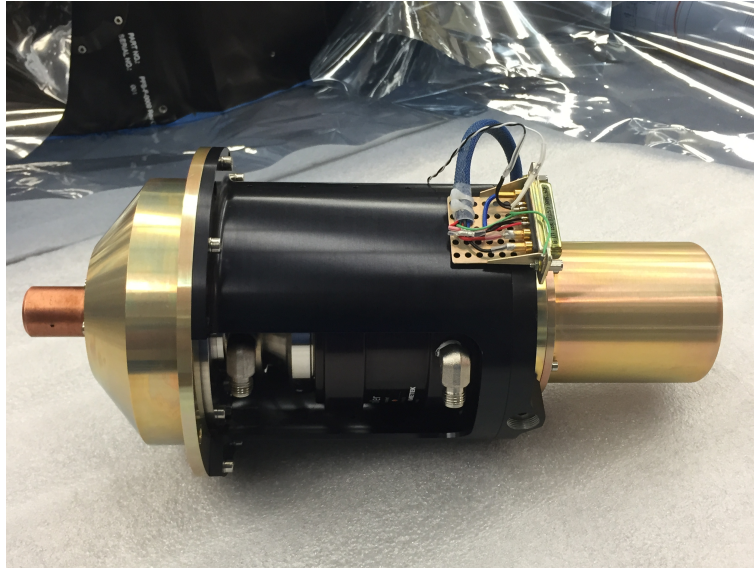


Figure 69: Photograph of the Sunpower Cryotel GT used on the Subaru Prime Focus Spectrograph camera cryostats. The active damping motor is housed inside the gold cover at the rear of the unit (right side in this figure)

- The Structural Design – An initial finite element analysis study was conducted to guide the design of the cryostat. The results show that the vessel is structurally sound with the maximum displacement being 0.6 mm at the window location. Around the perimeter of the cryostat, the displacements are much lower and range from 20 μm to 200 μm depending on the location.

In terms of the structural integrity of the design, the analysis shows that the Von Mises stresses are less than 50 MPa everywhere, with one stress concentration at 48 MPa in a non-welded region. This level of stress is reasonable for a first-cut of the design. The allowable stress as per the ASME Pressure Vessel code is 55 MPa in a weld-region for welded 6061-T6, and 100 MPa in a non-welded region. Therefore, the design as-is looks reasonable.

Contour plots for the displacement magnitude and Von Mises are shown in Fig. 70

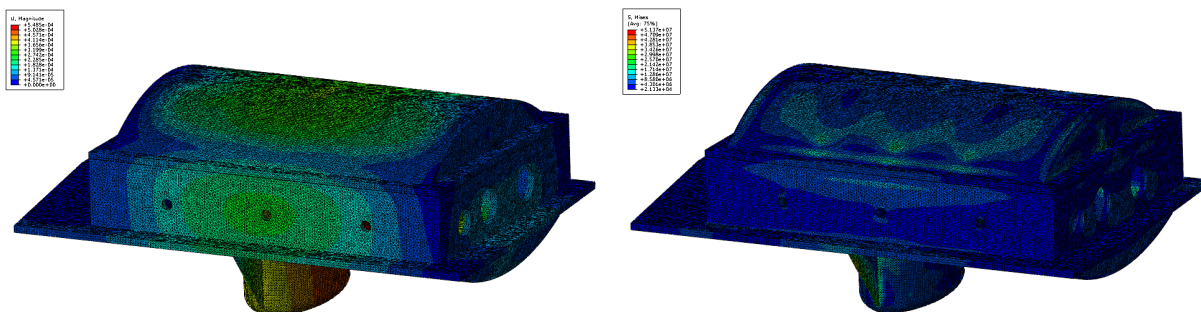


Figure 70: Preliminary finite element analysis results for the Left: displacements and, Right stresses within the cryostat structure.

G.2.4.4 OPTICAL MOUNTS

GMOX contains both refractive and reflective optics, all of which are of modest size, i.e. 200 mm in diameter or less. We will mount these optics in a fashion typical for most astronomical instruments. Here we describe briefly the types of mounts that will be used and where they will be used. Note that for this effort – a feasibility study – we have not modeled mounts for every optic, and those that have been modeled are simply representations of what the mount would look like. More detail would be added in the next phase of the design.

What follows is a brief description of the optical mounts used in various subassemblies throughout the instrument. As a rule, optics would be mounted by dead-reckoning, i.e. without adjustment. We rely on manufacturing accuracy to guarantee accurate placement of the optics. And where tolerances do not permit this approach, shims between the “mount” and the “cell” would be used to facilitate a one-time adjustment of the optic.

- The Central Optics – The “Central Optics” subassembly contains the field lenses for all three arms, as well as the red and blue dichroics; three lenses and two mirrors. This assembly will track ambient temperature therefore we would likely use athermalized cells for the lenses, or possibly a cell with integral flexures ([185]). A soft O-ring in a retainer would compress the lens slightly in the axial direction seating it against the base of the cell. The cell would most certainly be constructed of aluminum, and would have a radial pattern of Teflon plugs bored to fit the lens outer diameter with a reasonable clearance; reasonable with respect to the decenter tolerance. Since the field lenses have minimal power, we do not expect tight tolerances on placement.

The field lenses would be mounted in the central optics frame. The aluminum frame is a four sided box with precision bores on each of three faces to locate the respective lens cells, and an opening at the bottom to allow light to enter from the telescope.

The two dichroics would mount to a single triangular shaped frame with openings for light to enter and egress. Three Teflon or Delrin buttons on the face of the frame would locate the face of each mirror. A spring-loaded retention scheme would be used to constrain the optic axially, and bumpers and spring plungers would locate and constrain the optic laterally. The dichroic frame would mount to a thick plate that is precisely located to the face of the central optics frame.

The central optics is mounted to the fore-optics sub-bench via a three point pseudo-kinematic mount. In Figure 71 the fore-optics sub-bench is shown on the left, and details of the central optics assembly are shown on the right.

- Red and Blue Arm Fold Mirrors – Each fold mirror will be three-point mounted on Teflon or Delrin pads to a 45 degree aluminum mount block. A spring-loaded frame, or spring-loaded tabs, would hold the mirror to the block. Bumpers would register the mirror laterally with a spring-retention feature to load the mirror against the bumper. Each fold mirror assembly would be mounted to the fore-optics bench on three points, and pinned for accurate and repeatable placement.

Should tip-tilt motion control be required for flexure compensation we would alter this design somewhat. In all likelihood the three pads that locate the face of the mirror would be replaced by piezo-driven actuators and the lateral constraint would be replaced by a membrane flexure attached to the rear of the mirror.

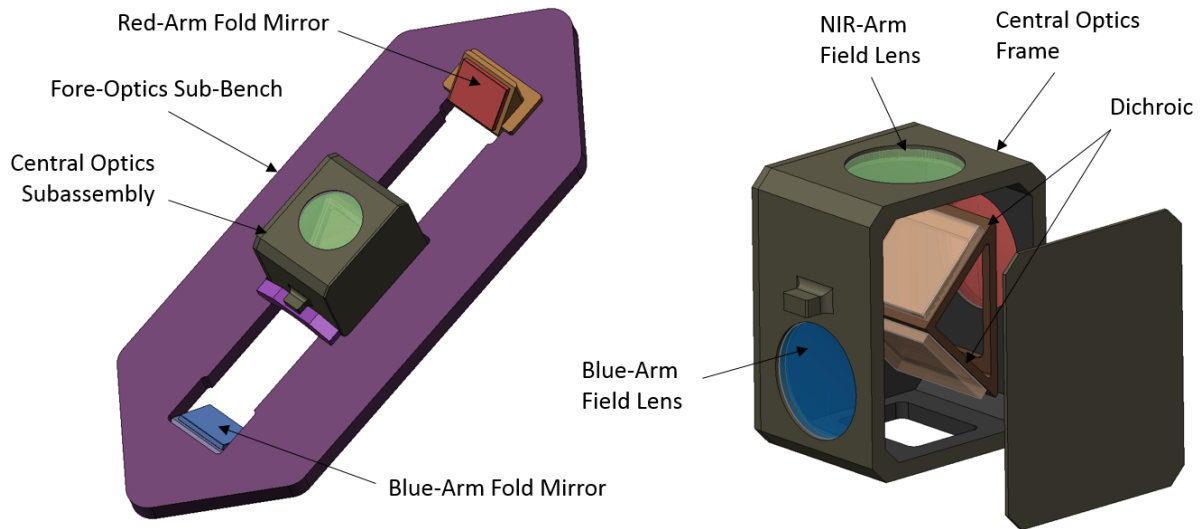


Figure 71: Left, rendering of the fore-optics sub-bench, and Right, rendering of the central optics sub-assembly.

- Schmidt Mirror Mounts – Each arm of the spectrograph contains a Schmidt collimator. However, GMOX only uses two small footprints of the entire Schmidt primary. Therefore, to conserve space and reduce mass, we use a segmented primary consisting of the two corections of the mirror illuminated by the optics. This complicates matters opto-mechanically in that these segments must then be mounted and realigned as they were in the original parent blank. To do this, we will mount the two segments in a single rectangular cell with two round pockets precisely located to achieve the correct segment spacing. Alignment fiducials, i.e. flats or reference marks applied by the optician, would be used to re-orient the segments. The aluminum cell would either be athermalized to match the coefficient of expansion of the mirror material, fused silica, or we would use flexures to accommodate the differential expansion. In the near-infrared arm the large thermal excursion demands that we do the latter, and for commonality in design, we would likely adopt the same approach for all three arms. As with the other optical mounts, the mirrors would be retained on-axis by compliant constraints.
- Reimager Lenses – The reimaging lenses, located roughly at the apex of the Schmidt primary, will be mounted in round athermalized or flexured cells, then stacked end-to-end with spacers to set the relative distance from lens-to-lens. Again, for the near-infrared arm, as with the Schmidt mirror segments, we would use flexure cells to accommodate the radial differential expansion between the lens and cell diameters, and compliant flexured retainers to constrain each lens on-axis. For commonality we would likely do the same for the red and blue arms. The reimager would be attached directly to the Schmidt mirror cell and located by a hole in the center of the cell. A flange on the outer diameter of the reimager would be used to attach the assembly, and a nominal shim at that interface could be tailored to account for manufacturing tolerances.
- Red and Blue Arm DMD Sub-Bench – In each arm, the DMD, two fold mirrors, two correctors and the VPH grating are mounted on a common plate, the DMD sub-bench; see Fig. 72. The DMD is mounted atop a pyramid-shaped base, which is attached to the top side of the

plate at three points. Locating pins in the plate would register the mount. The correctors would be mounted in either athermalized or flexured cells and attached to a right-angle mount fixed at three points to the bench. A large boss on the bottom of the corrector mount serves as a placement reference. The folds mount in a similar fashion. In all cases, spring retention features would be used to retain the optics along their axis.

The entire sub-bench would be affixed to the upper bench at three, or possibly four, points. Four points may be needed given the form-factor of the sub-bench. It goes without saying, that a four point mount would require a tight constraint on co-planarity of the four-point surface on both sides of the interface. o the ambient

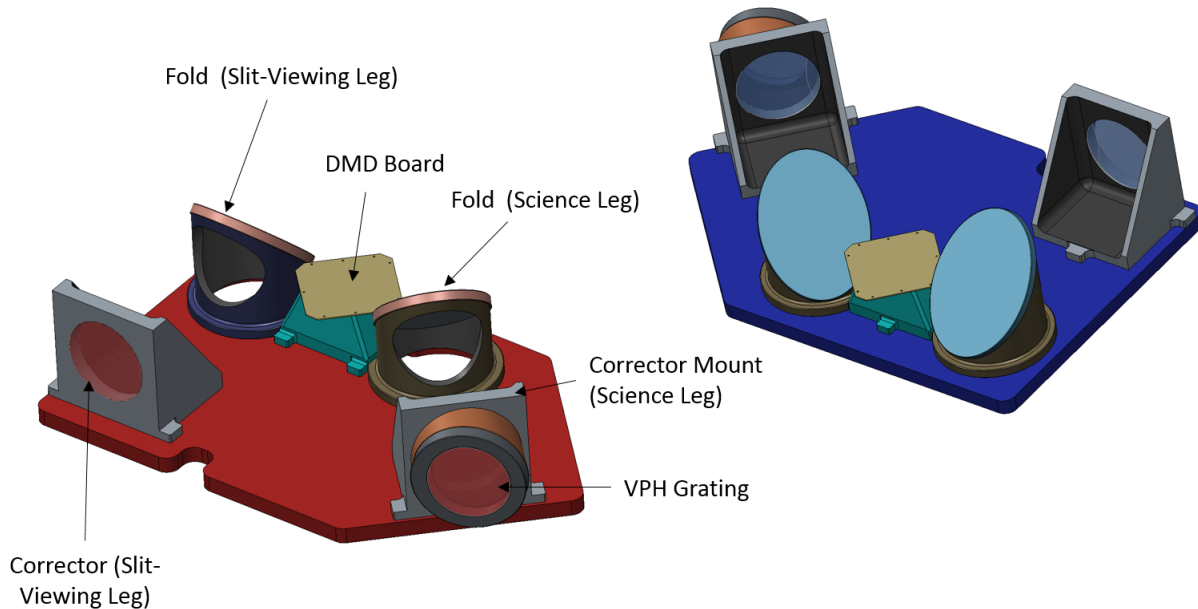


Figure 72: Lower Left: rendering of the red-arm DMD sub-bench, and Upper Right: rendering of the blue-arm DMD sub-bench, which is nearly identical to the red arm.

- **The Camera Lens Mounts: Visible Arms** – There are four visible band-pass cameras in GMOX. The lens mount concepts used for these cameras would be similar and based on heritage from past camera designs that have proven successful, in particular the lens mounts for the SDSS and BOSS spectrographs; see [186]. However we do not envision fluid-couple lenses for either the contact triplets or doublets as was used in the SDSS and BOSS spectrographs. Instead we would likely use Sylgard-184.

As with the SDSS and BOSS cameras, lenses would be mounted in athermal cells comprised of a metal cell with a radial pattern of Teflon plugs bored to fit the as-built diameter of the lens. An O-ring contact between the lens and axial retainer would provide sufficient compliance to accommodate differential expansion in the axial direction. Lens cells would be aligned in a barrel and spacers would set the lens-to-lens distances.

- **The Camera Lens Mounts: Near Infrared Arm** – For the near infrared arm, lenses would be mounted in aluminum flexure cells as was done for the WHIRC (Meixner et al. [187]) and FourStar (Persson et al. [188]) near infrared cameras. This concept is described in detail in Smee [185]. In this scheme, lenses are centered by a radial pattern of flexures, which accommodate the differential contraction between the aluminum cell and glass lens as the temper-

ature drops from room temperature to cryogenic temperature. Axial retention is provided by spring force, either from belleville springs or from a thin disk with integral flexures. The latter is more appropriate for small lenses (less than 100 mm in diameter), and the former is more appropriate for large lenses.

A photograph showing several applications of this technique is shown in Fig. 73.

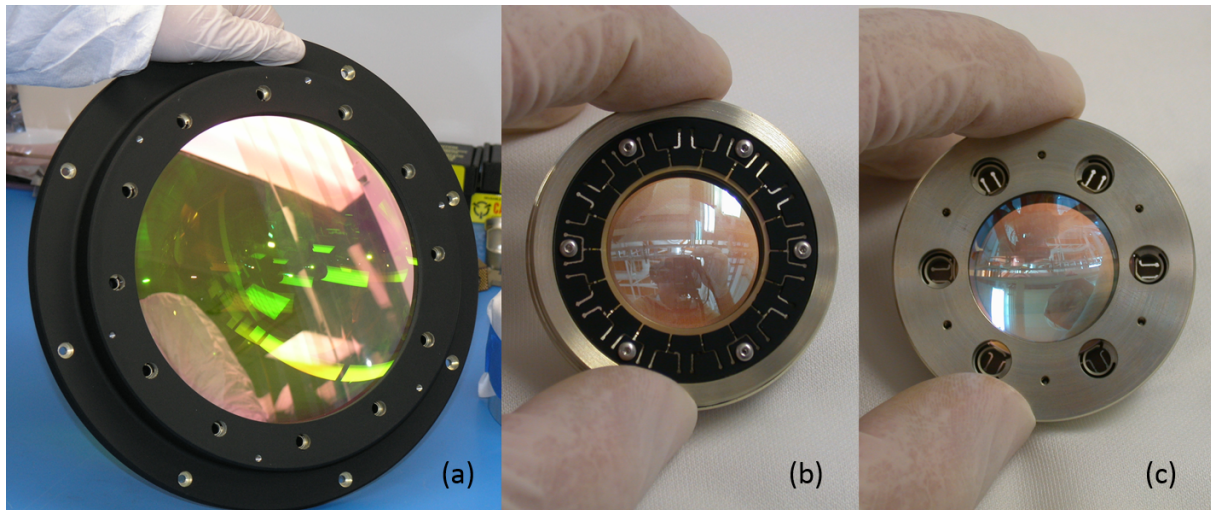


Figure 73: (a) FourStar, lens L6, a 200 mm diameter calcium fluoride lens that operates at 200K, (b) Front side of WHIRC camera lens, L3, a 30 mm diameter fused silica lens which operates at 77K, and (c) the back side of WHIRC lens, L3.

G.2.4.5 DETECTOR MOUNTS

Cooled detectors, such as the e2v CCD290-99, or the Teledyne HxRG detectors would be mounted in a vacuum environment and cooled to operating temperature by closed cycle refrigeration. Detectors typically have mounting features in the base of the package and it is these features that would be referenced to the detector mount. The detector mount material would be chosen to match the coefficient of thermal expansion of the detector package. Fine threaded adjustments behind the mount facilitate a one-time adjustment of tip, tilt, and piston of the detector. Compliant thermal straps, such as indium, would connect the mount to the cold-plate of the dewar. A heater on the mount would be used to facilitate fine control of the detector temperature. And a thermostat in the heater circuit would prevent an over temperature condition. We would adopt this basic design philosophy for all the science cameras, both visible and near infrared, but again, the details will depend on the particulars of the camera design, which won't be well understood until the design progresses further.

In the case of the slit-viewing cameras, the detectors would be packaged by the vendor, Andor. However, if it were determined that building the slit-viewing camera around a sensor such as the e2v LGSD or NGSD CMOS detector, which does not come in a packaged configuration such as the Anodor 4k, then we would likely use many of the design principles outlined above to mount the device. Cooling requirements for sCMOS sensors are not as demanding of course so some of the thermal details would change.

G.2.4.6 FLEXURE

We had hoped to be able to say something quantitative about flexure in this report. However other priorities precluded it. What we can say is that, qualitatively speaking, the design should be very stiff given the design of the optical bench. The lower bench is broad and short, and should be very stiff. The upper bench is similar, as is the cryostat.

A detailed finite element analysis would be done during the conceptual design phase. Certainly we anticipate some level of inter-arm flexure. If significant we would compensate for it, most likely using tip-tilt control of the fold mirrors in the red and blue arms.

G.2.4.7 INSTRUMENT INTEGRATION

As configured, the logical sequence for integrating GMOX is to assemble and verify subsystems at the subsystem level and then integrate these modules into their larger parent assemblies. We would verify subsystems as we go, and this verification would largely be a metrology exercise, but also a functional checkout of mechanisms and sensors. Below is an outline of the procedure for each of the three main components of the instrument: the Lower Bench, the Upper Bench, and the NIR cryostat.

1. Integrate Lower Bench.

- (a) Verify lower bench reference feature locations and sizes.
- (b) Fore-Optics Sub-Bench
 - i. Assemble central optics components without lenses or lens cells and install on fore-optics bench.
 - ii. Assemble fold mirror mounts to fore-optics bench.
 - iii. Verify optical references with respect bench references.
 - iv. Remove opto-mechanics, install lens cells, and reassemble.
 - v. Install fore-optics sub-bench to lower bench.
 - vi. Verify placement via metrology.
 - vii. Shim as needed to account for manufacturing tolerances.
- (c) Red and Blue Schmidt Mirror Cells
 - i. Verify cell features via metrology.
 - ii. Install mirrors.
 - iii. Assemble and install reimaging optics.
 - iv. Verify placement of optics.
 - v. Integrate ADCs and verify performance.
 - vi. Install mirror cell subassemblies to lower bench.
 - vii. Verify placement via metrology.
 - viii. Shim as needed to account for manufacturing tolerances.

2. Integrate Upper Bench.

- (a) Verify upper bench reference feature locations and sizes.
- (b) Red DMD Sub-Bench

- i. Verify sub-bench reference feature locations and sizes.
 - ii. Assemble mirror mounts without optics.
 - iii. Verify opto-mechanical references with respect to bench references.
 - iv. Remove opto-mechanics, install mirrors, DMD, correctors, and VPH grating.
 - v. Install sub-bench to upper bench.
 - vi. Verify placement via metrology.
 - vii. Shim as needed to account for manufacturing tolerances.
- (c) Blue DMD Sub-Bench
- i. Verify sub-bench reference feature locations and sizes.
 - ii. Assemble mirror mounts without optics.
 - iii. Verify opto-mechanical references with respect to bench references.
 - iv. Remove opto-mechanics, install mirrors, DMD, correctors, and VPH grating.
 - v. Install sub-bench to upper bench.
 - vi. Verify placement via metrology.
 - vii. Shim as needed to account for manufacturing tolerances.
- (d) Red Science Camera
- i. Verify lens and cell dimensions
 - ii. Assemble lenses into cells
 - iii. Assemble cells into lens barrel
 - iv. Verify placement via metrology and adjust shims as needed to compensate for machining tolerances.
 - v. Verify performance optically
 - vi. Install camera to upper bench
- (e) Blue Science Camera
- i. Verify lens and cell dimensions
 - ii. Assemble lenses into cells
 - iii. Assemble cells into lens barrel
 - iv. Verify placement via metrology and adjust shims as needed to compensate for machining tolerances.
 - v. Verify performance optically
 - vi. Install camera to upper bench
- (f) Red Slit-Viewing Camera
- i. Verify lens and cell dimensions
 - ii. Assemble lenses into cells
 - iii. Assemble cells into lens barrel
 - iv. Verify placement via metrology and adjust shims as needed to compensate for machining tolerances.
 - v. Verify performance optically
 - vi. Install camera to upper bench
- (g) Blue Slit-Viewing Camera
- i. Verify lens and cell dimensions

- ii. Assemble lenses into cells
 - iii. Assemble cells into lens barrel
 - iv. Verify placement via metrology and adjust shims as needed to compensate for machining tolerances.
 - v. Verify performance optically
 - vi. Install camera to upper bench
 - (h) Near Infrared ADC
 - i. Verify optical dimensions
 - ii. Assemble optics into mounts
 - iii. Verify stage performance
 - iv. Install ADC to upper bench
3. Integrate Upper Bench Onto Lower Bench.
4. Integrate NIR Cryostat.
- (a) Verify cryostat vacuum performance (i.e. vacuum integrity)
 - (b) Verify cold plate reference feature locations and sizes.
 - (c) Verify opto-mechanical mounts.
 - (d) Assemble mounts to optical bench without optics.
 - (e) Verify critical opto-mechanical reference features. Adjust shims as needed to compensate for machining tolerances.
 - (f) Remove mounts, install optics, and reassemble onto optical bench.
 - (g) Integrate DMD and DMD electronics, and verify performance.
 - (h) Integrate detectors.
 - (i) Install optical bench into cryostat.
 - (j) Verify bench placement and adjust as necessary.
 - (k) Pump down and verify thermal performance.
5. Integrate NIR Cryostat Onto Upper Bench.
6. Perform System Level Functional Testing.

G.2.5 ELECTRICAL DESIGN

The GMOX electrical system, as presently envisioned, would be broken down into a number of electrical subsystems, which are described in more detail below. Electronics components would fall into one of three major functional areas: 1) instrument control and monitoring; 2) detectors and detector readout; and 3) DMD control. Each of these is described in some detail below.

At a very high level, the instrument control architecture would consist of a control computer which communicates with a detector server, for reading all the camera detectors and processing images, and three Arm Control Units (ACUs), which are responsible for control functions and sensor readout. Figure 74 illustrates the configuration. The GMOX control computer would host the control GUI and would be a coordinated development effort with Gemini to ensure compatibility with facility software standards. The control computer would be the primary observer interface, with GUIs for setting up observing parameters, and GUIs to provide instrument status feedback to the user.

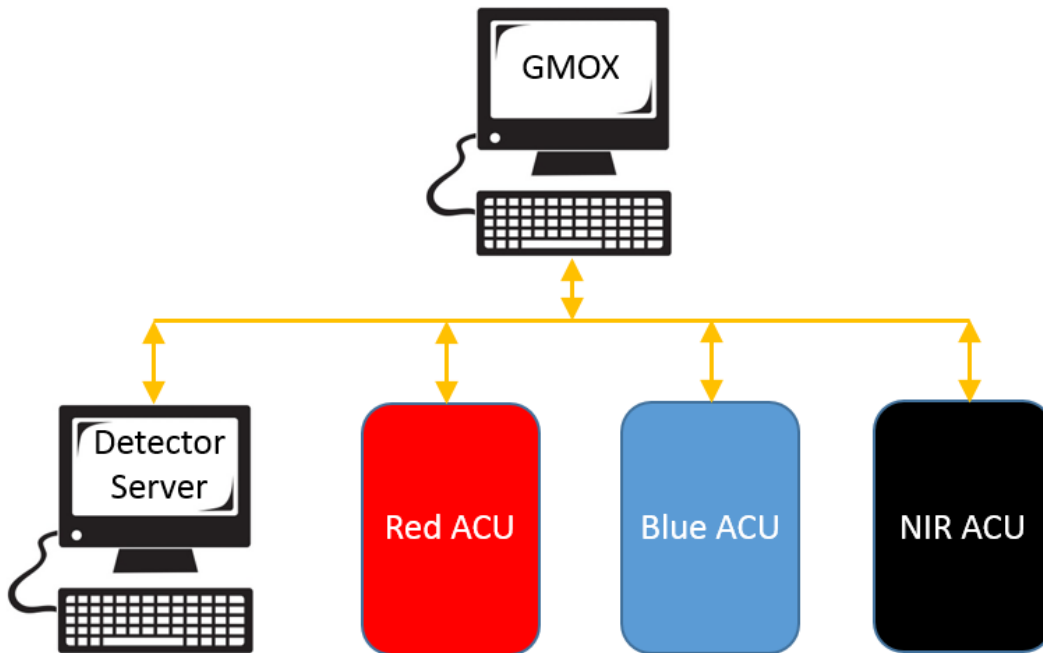


Figure 74: Schematic representation of the GMOX control instrument control architecture. A master control computer communicates with a detector server, dedicated to detector readout and data processing, and three Arm Control Units, one for control of each of the spectrograph arms.

G.2.5.1 ELECTRONICS FOR INSTRUMENT CONTROL AND MONITORING

Each arm of GMOX will have several subsystems that must be controlled and monitored, including a DMD, an ADC, a tip-tilt fold mirror for flexure control, a cryocooler for cooling the science detector, an ion pump for the science detector dewar, a heater for detector temperature control, as well as a number of temperature sensors for monitoring the health of these subsystems and for heater control. The electronics required for these systems will be packaged in an Arm Control Unit (ACU) and there will be one ACU for each arm. Figure 75 shows a schematic representation of the ACU for one of the visible arms. The near infrared ACU would be similar, but will require additional cryocooler controllers and a larger ion pump controller. In addition, the near infrared ACU would not have a fold mirror controller.

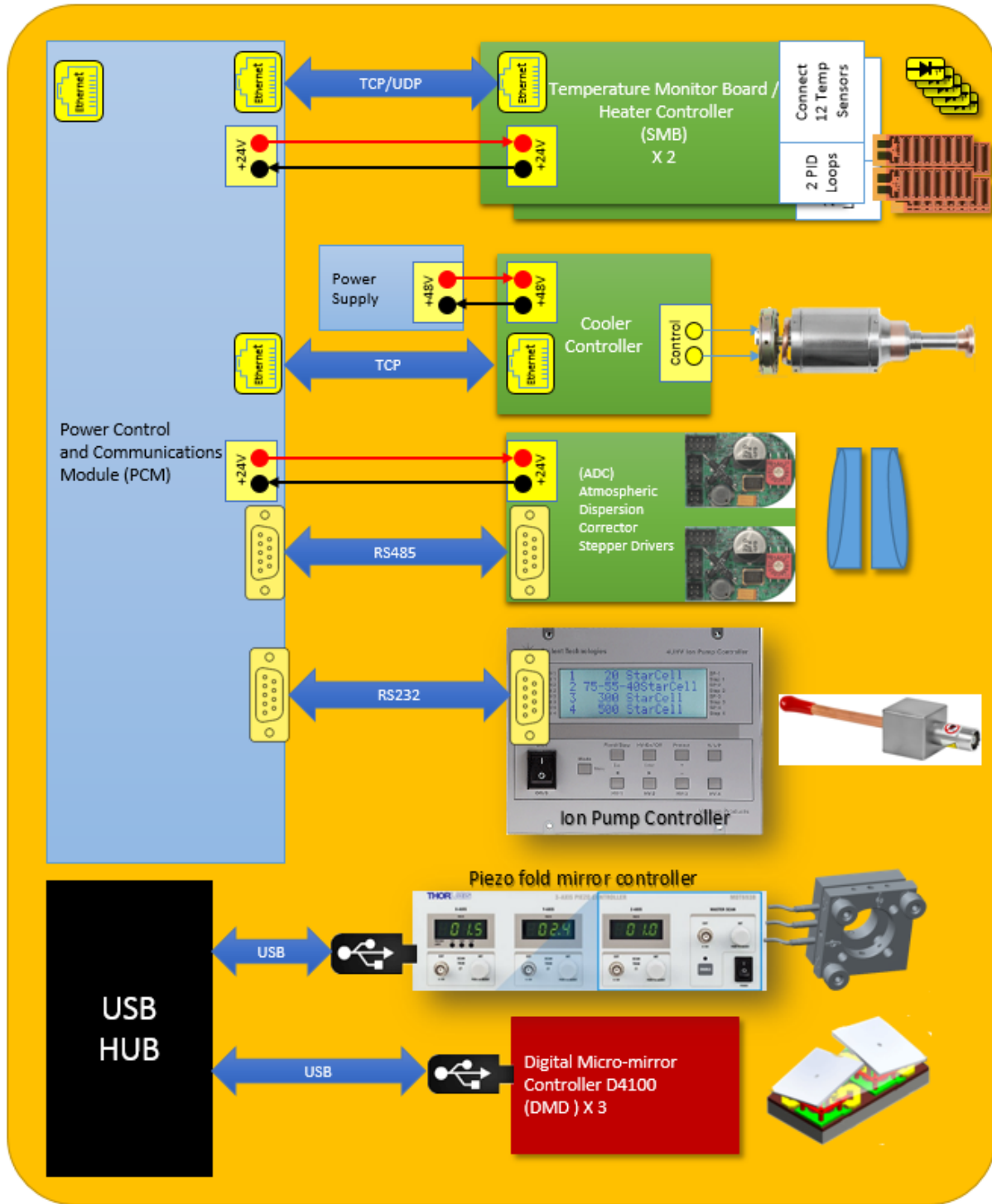


Figure 75: Schematic representation of the Arm Control Unit (ACU) for a visible arm of the spectrograph. The near infrared arm ACU would be similar.

Power and communication within an ACU will be handled by a Power Control Module (PCM), a custom printed circuit board built by JHU for the JWST project, and later used on the Prime Focus Spectrograph (PFS) for Subaru. This 125 mm x 125 mm board has a four port Ethernet switch

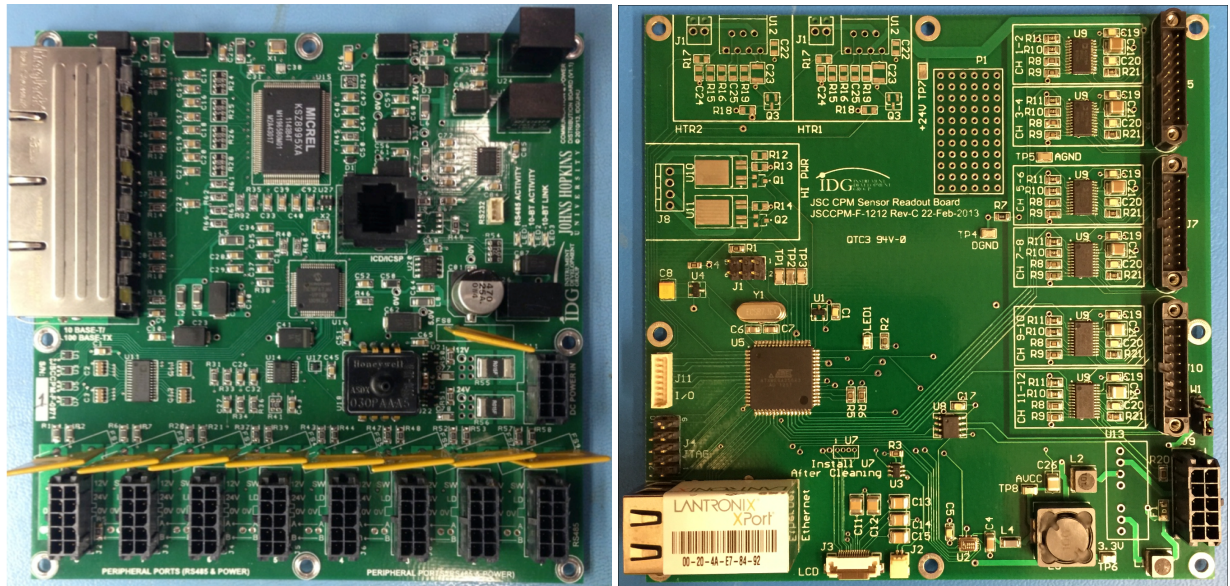


Figure 76: Left: Photograph of the Power Control Module (PCM), and Right: Photograph of the Temperature Monitor Board. The size of each board is 125 mm x 125 mm. Both boards were developed for JWST.

for communication to other modules such as the temperature control board, and eight channels of RS485/RS232 communication and power control/monitoring for peripherals operated by DC power at 12 V or 24V, such as the stepper motor controller for the ADC.

Temperature monitoring and heater control will be handled by the Temperature Monitor Board (TMB). This board is also custom built, with heritage from JWST and PFS. It has the same form-factor as the PCM board so the two boards can be stacked in a compact configuration. The TMB will read up to 12 sensor channels, and can control two PID heater channels at up to 100 W per channel. A limiting resistor sets the heater channel power, therefore for low power applications such as detector thermal control, the power can be easily reduced to a lower level. The board communicates via the Ethernet protocol.

Photographs of the PCM and TMB are shown in Fig. 76. These two boards would handle the bulk of the control and monitoring for each arm of the spectrograph.

The remaining electronics within the ACU would be off-the-shelf components unless further study dictates otherwise.

G.2.5.2 DETECTOR READOUT SYSTEM

As presently envisioned, the detector readout system would be separate from the instrument control system. This arrangement is typical of most astronomical instruments. Images would be acquired and stored on a single server and this server would also host the data reduction pipeline. Figure 77 shows a schematic representation of the configuration. Details of the detector electronics for the various cameras are described in more detail below.

G.2.5.3 DETECTORS FOR THE VISIBLE SCIENCE ARMS: CCDs

Based on the current optical design concept, the required detector size for the blue arm is 78.5 mm (spectral) x 12.9 mm (spatial), and for the red arm is 78.7 mm (spectral) x 16.1 mm (spatial). And

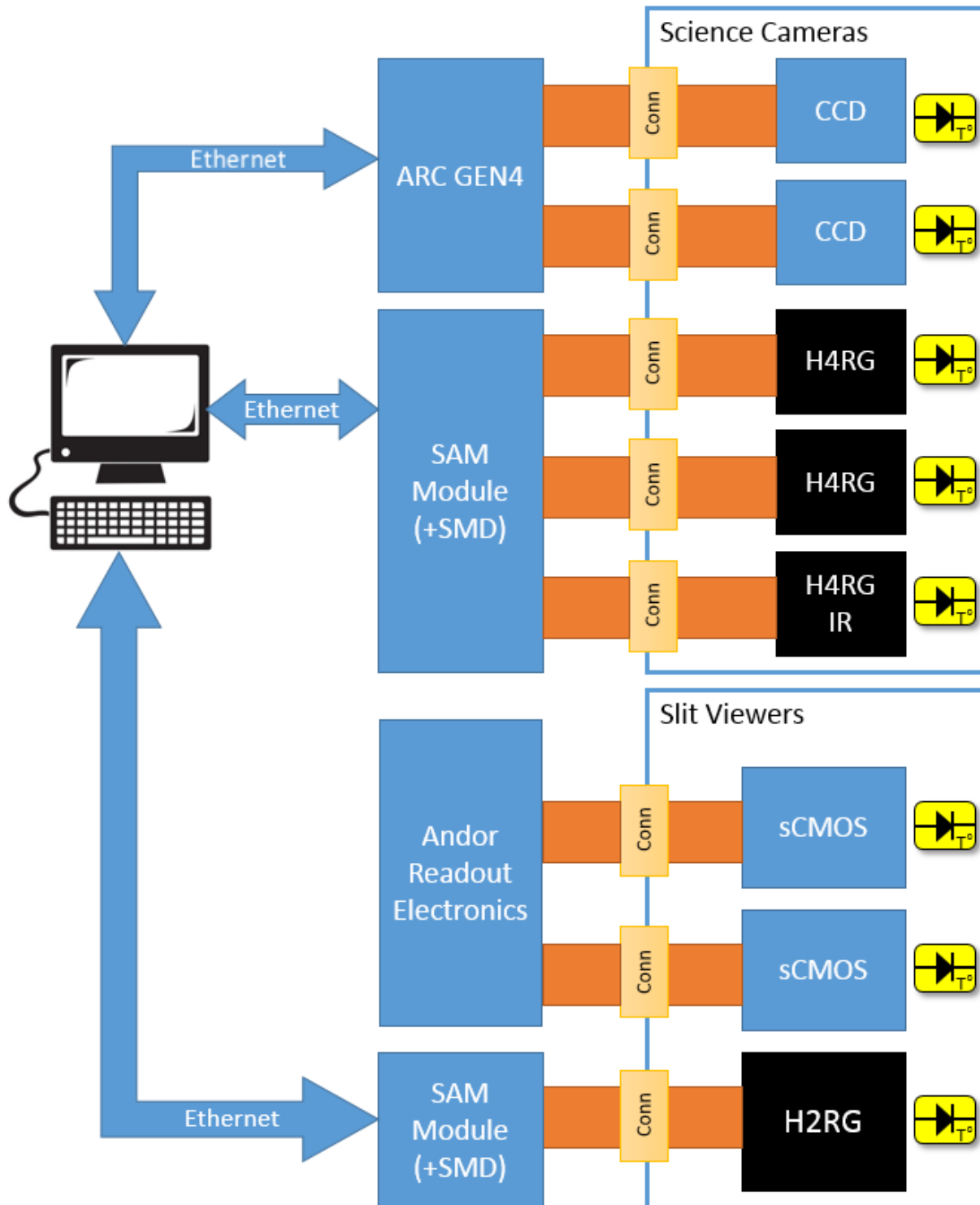


Figure 77: Schematic representation of the detector readout system. Images are acquired and stored by a single server, which also hosts the data reduction pipeline.

we want to sample the slits with three pixels ideally. Therefore we require pixels that are $10\mu\text{m}$ for the nominal slit widths defined above (5 mirrors wide in the blue, and 4 mirrors wide in the red).

For the GMOX visible science channels we would use large format charge coupled devices (CCDs). Today, CCDs are readily available in formats large enough to image GMOX spectra without the need to butt multiple detectors together. This has the advantage of no gaps in the spectra (or field depending on how the detectors are butted), and eliminates the complexity of adjusting two detectors such that their surfaces are in the same plane.

We have investigated CCDs offered by two commercial vendors: e2v, and Semiconductor Technology Associates (STA). Both can provide high quality CCDs in suitable formats for GMOX, and both are just large enough to capture the entirety of the spectra for all field positions. However, the standard large formats are square, not rectangular, hence, there will be many unused pixels in the spatial direction. Certainly large format rectangular CCDs can be made (e.g. the $3\text{k} \times 8\text{k}$ CCDs made by e2v for the MODS spectrograph) but they would be very costly. In any case, the extra pixels do not pose a problem.

The CCD of choice from e2v would be the CCD290-99, which is a $9.2\text{k} \times 9.2\text{k} \times 10\mu\text{m}$ pixel pitch with 2.5 e⁻ readnoise (at 50 kHz read rate) and 2 e⁻/pixel/hour dark current (at -100 C). The CCD290-99 is available in both standard and deep depletion silicon for optimal quantum efficiency (QE) in either the blue or red bandpass, respectively. They also offer multiple coating options to further enhance the QE.

Semiconductor Technology Associates offers the STA1600, a $10.5\text{k} \times 10.5\text{k} \times 9\mu\text{m}$ pixel device, with comparable specs as the e2v CCD290-99 (2 e⁻ readnoise at 50 kHz and 3 e⁻/pixel/hour dark current). However, they do not offer a deep depletion version of this detector.

Our preference for GMOX is the e2v CCD290-99 given the option for the higher QE, deep depletion device for the red channel, and e2v's sterling reputation for delivering quality detectors on schedule. With regard to quality and schedule, STA may be quite good but we do not have any direct experience with STA in this regard.

G.2.5.4 CCD READOUT ELECTRONICS

The e2v CCD 290-99 detector is a 16-channel device. We have investigated two off-the-shelf controllers for this application, the first manufactured by Semiconductor Technology Associates Inc. (STA), and the second by Astronomical Research Cameras Inc. (ARC). Both controllers are comparably priced, however the ARC controller is expandable to 32 channels and could be used to read both visible science detectors. The STA controller is limited to 16 channels.

Two significant strengths of the STA controller are that it uses Ethernet communication, and digital correlated double sampling (DCDS). Currently ARC is producing their Gen. III controller, and plans to release an FPGA based Gen. IV controller in early 2016. The current ARC controllers use fiber optics and a PCI interface board for communication. The Gen. III controller uses correlated double sampling (CDS), while the Gen. IV controller will use DCDS, and will communicate via Ethernet. The flexibility of the Ethernet communication is a definite plus for the STA controller, but it is twice as expensive as the ARC controller. The Gen. IV ARC controller with DCDS and Ethernet communication, while not in production yet, would offer a potential cost savings (should we choose to read both detectors from a single controller). Therefore we have chosen the ARC Gen. IV controller as the baseline for this study.

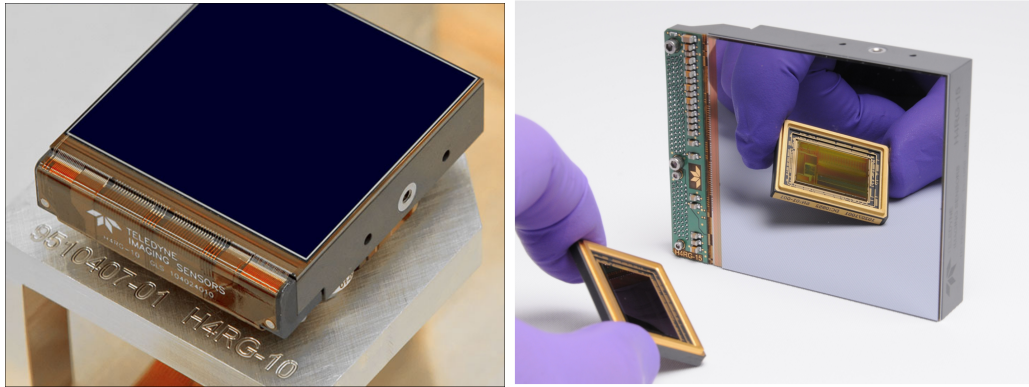


Figure 78: Photographs of the Teledyne H4RG-10 (Left) and H4RG-15 (Right) HgCdTe detectors. Both detectors have 4096×4096 pixels. The H4RG-10 has $10\mu\text{m}$ pixels and the H4RG-15 has $15\mu\text{m}$ pixels. The gloved hand in the foreground of the H4RG-15 shows the new hermetic package for the sidecar signal processing ASIC used in the SMD module described below in the text.

G.2.5.5 DETECTORS FOR THE NEAR INFRARED ARM; HgCdTe DETECTORS

There are only two possible vendors for the near infrared detectors: Teledyne and Raytheon. Each offers HgCdTe (mercury, cadmium, telluride) devices commercially and each has significant experience building science grade devices. The largest arrays currently available, from either company, are 4096×4096 pixels. Hence, the optical design has been tailored to work with this format. As described above, the near infrared arm is split into three channels, each having one $4k \times 4k$ detector, and the number of pixels, the slit width, and the pixel sampling of the slit, dictate the resolving power in each channel.

Teledyne offers two detector options that are viable for GMOX. One is the WFIRST format detector, the H4RG-10, funded by and being developed for NASA. This format is $4k \times 4k$ and the pixels are $10\mu\text{m}$. The second is the H4RG-15, a $4k \times 4k$ device with $15\mu\text{m}$ pixels. Each device can be read out by Teledyne's sidecar ASIC. A photo of the two devices is shown in Fig. 78, along with the "Sidecar" signal-processing ASIC chip we will discuss in the electronics section. The cost of an H4RG-10 science grade device, which is our baseline, is \$930k.

Raytheon is also funded to develop HgCdTe devices for WFIRST, the Astro-4k.10. They also have plans to produce an Astro-4k.15, a $15\mu\text{m}$ pixel detector for the ground based community and hope to have funding to build prototypes in calendar year 2016. The Astro-4k detectors are being built using two different molecular beam epitaxy (MBE) approaches: MBE on cadmium zinc telluride (CZT), and MBE on silicon. The advantage of MBE on silicon is lower cost. The disadvantage is reduced performance, however Raytheon claims they are very close to producing detectors of comparable performance to MBE on CZT.

Given the maturity of Teledyne's technology, and readout options, the detector of choice for the near infrared channels is the H4RG-10, $2.5\mu\text{m}$ cutoff material. Teledyne plans to be in flight production for the H4RG-10 in less than two years. In addition the specs for the H4RG-10 are slightly better than the H4RG-15. The read noise for the H4RG-10 is $2/3$ that of the H4RG-15, and the QE is slightly better at shorter wavelengths. The dark current is the same for the two detectors.

The specs for the H4RG-10 are given in Table 23. Updates to the H4RG-10 performance from a new series of detectors might be released before year end. For now, Teledyne is releasing these specs to interested parties considering the procurement of these detectors. Due to the developmental nature of these detectors, these specs are projected performance based on best effort, and

are not guaranteed.

G.2.5.6 NEAR INFRARED DETECTOR READOUT ELECTRONICS

For reading the H4RGs, the baseline detector for the near infrared channels, we would use the Teledyne Sidecar ASIC Module (SMd) and the Sidecar Acquisition Module (SAM). The SMd is a second-generation package of the Sidecar ASIC and it is just now becoming available. It will use a relatively new column-grid-array (CGA) technology, which is similar to the standard ball-grid-array (BGA) mounting which is used for microprocessors and other products with very large numbers of contacts in a dense array, but the balls are replaced with relatively thin columns; the result is a system with greatly improved tolerance to the thermal mismatch between the ceramic package and the composite laminate circuit board. The SAM replaced the old Jade 2 card. It provides voltages and clocking to the ASIC and handles communications with the ASIC and host computer. The SAM will work with Windows or Linux and communicates via USB 2.0, Camera Link, or GigE Vision protocol.

The sidecar can be mounted immediately behind the detector, or in close proximity to it, and it would operate at the detector temperature. It dissipates only about 150 mW at 100 kHz readout rate; that power scales very nearly linearly with the frequency. In addition, it requires only 3.3 VDC at very small current to operate, and generates complete telemetry of voltages and operating state internally. A short flex cable connects the Sidecar and detector. A multi-layer flex cable would route the signals from the Sidecar to a hermetic feedthrough on the dewar. A cable on the outside of the dewar would carry the signals to the Sidecar Acquisition Module (SAM), which communicates with the host computer.

If we were to adopt the Astro-4k detectors instead of the H4RG, we would not be able to use the Teledyne electronics for readout. In that case we would use either a Clark controller, which is what Raytheon is using now, or a customized ARC controller. ARC controllers would also be an option for reading the H4RG. The Australian National University and the University of Hawaii are using ARC controllers for reading Teledyne's HxRG detectors, including the H4RG.

G.2.5.7 SLIT-VIEWING CAMERA DETECTORS

The slit-viewing cameras in GMOX provide two distinct functions. First, they provide imaging feedback for the DMD, from which the configuration of the slit can be verified. And second, one of the cameras is used to provide real-time tip-tilt feedback to the adaptive optics real time controller (RTC). If all the slit-viewing camera were required to do is image the DMD, the slit-viewing cameras would be technically straight-forward and relatively inexpensive. But the need to provide real-time feedback, at a sampling rate of up to 400 Hz, requires that the slit-viewing cameras operate at high frame-rate, and with low read noise, which adds greatly to the technical complexity and cost; specifically for the detector.

For the visible arms of GMOX we require a detector that has a large format, 2k x 1k, (sufficient to map the DMD), with low read noise ($< 10 e^-$ preferably), a fast frame rate of 400 frames per second, and high QE ($> 70\%$). In slit-viewing mode we would read the full frame, while in tip-tilt control mode we would read "regions of interest" centered on, nominally, three natural guide stars. Reading several regions of interest rather than the full frame minimizes processing and increases the sampling rate.

At present, few options exist in the way of suitable detectors for either the visible or the near infrared arm. For the near infrared arm, the obvious option, and the baseline for GMOX, is the Hawaii H2RG, although, in principle, a Raytheon VIRGO 2K array would suffice as well. The

Parameter	Unit	Best effort value	Goal
Array format ⁽¹⁾	pixel	4096 x 4096	4096 x 4096
Read-out integrated circuit (ROIC)		H4RG-10	H4RG-10
Pixel pitch	μm	10	10
Power Dissipation ⁽²⁾	mW	≤ 10	≤ 10
Detector Material		HgCdTe	HgCdTe
Detector Substrate		CdZnTe, removed	CdZnTe, removed
Cutoff wavelength (50% of peak QE) @77K	μm	2.5	2.5
Mean Quantum Efficiency (QE) at 800 nm	%	≥ 70	≥ 80
Mean Quantum Efficiency (QE) at 1,000 nm	%	≥ 70	≥ 80
Mean Quantum Efficiency (QE) at 1,230 nm	%	≥ 70	≥ 80
Mean Quantum Efficiency (QE) at 2,000 nm	%	≥ 70	≥ 80
Median Dark current: @ 0.5 V bias and 77 K	e-/s	≤ 0.05	≤ 0.01
Median Readout Noise, correlated double sampling (CDS) at 100 kHz pixel readout rate	e-	≤ 20	≤ 12
Total noise ⁽³⁾	e-	≤ 10	≤ 6
Well Capacity at 0.5 V bias	e-	≥ 60,000	≥ 80000
Interpixel capacitance (single nearest neighbor)	%	≤ 2	≤ 1
Total pixel crosstalk (nearest neighbor) by cosmic ray hit	%	≤ 3	≤ 2
Latency ⁽⁴⁾	%	≤ 0.5	≤ 0.1
Operability ⁽⁵⁾	%	≥ 95	≥ 99
Cluster ⁽⁶⁾ : Total bad pixels in clusters as a percentage of array	%	≤ 2	≤ 0.5
SCA Flatness ⁽⁷⁾ using molybdenum or equivalent package	μm	≤ 25	≤ 10

Table 23: Published specifications for the Teledyne H4RG-10 focal plane array. The readout circuit offers various options; with 32 channels, the full array can be read in about 1 second. Due to the developmental nature of these detectors, these specs are projected performance based on best effort, and are not guaranteed.

HxRG detectors were developed with windowed readout in mind and multiple windows are possible, albeit with some customization of the ASIC software. In low noise mode at 400 kHz, reading with the Sidecar ASIC, three 10×10 sub-arrays can be read out in 2.6 ms (384 Hz sampling) in a read-reset-read sequence, providing a single correlated double sample (CDS) read per window. The CDS readnoise with the Sidecar ASIC, in “slow” mode, is expected to be roughly 15 e-. Therefore, with 0.5 ms overhead for calculating centroids, we can meet the 400 Hz requirement for tip-tilt control using guidestars ranging from 12th to 15.5th magnitudes, depending on the number of pixels used to measured the centroid (note that GMOX can guide in “white light”). The second value provides an interesting reference point, as basically every 2MASS star is viable for guiding in the IR. According to Hutchings et al. (2002), there are about 2 stars brighter than 15.5 every 8.4 square arcminutes at the galactic pole; at least one guide star should therefore be available over a large fraction of the sky.

In the visible arm, there are multiple options. One option would be the $1760 \times 1680 \times 24\mu\text{m}$ pixel LGSD CMOS sensor being developed for the European Southern Observatory (ESO) by e2v Technologies [189]. This detector is not currently available commercially but is in development. It is being developed with wavefront sensing in mind and offers impressive performance: a fast frame rate of 700 frames per second, low read noise (< 3 e-), and high QE ($> 90\%$). A smaller version of this detector has been developed, the 880×840 pixel NGSD CMOS device, a quarter-sized prototype of the larger LGSD CMOS detector. e2v Technologies expects to progress to the full-size LGSD device subject to contract from ESO in the following year. One would hope that on the timescale of GMOX the LGSD CMOS sensor would be available commercially. Currently, e2v does not have a cost estimate for the LGSD CMOS sensor.

A second option for the visible arms is Teledyne’s HyViSI technology. Although with a factor of three higher readnoise it is far less attractive. The HyViSI detectors use the same ROIC (readout integrated circuit) as the HxRG series detectors with a silicon detector layer for visible bandpass sensitivity. Teledyne quotes read noise of 8-10 e- CDS readnoise for their HyViSI using the Sidecar ASIC for readout in slow mode. According to Teledyne, readnoise at this level should be achievable at readout rates up to 500 kHz. The cost of a HyViSi detector is roughly \$275k.

A third option for the visible arms is a variant of the Onyx sCMOS sensor from e2v. This sensor would be a 1980×1080 format with $5.3\mu\text{m}$ pixels. It is a front-illuminated detector with a microlens design providing approximately 80% QE at 600 nm. The full array can be read out at 60 frames per second with 14-bit resolution and > 400 frames per second with 8-bit resolution. While it may be a bit limiting given an 8-bit output is required to achieve $> 400\text{fps}$, it should be noted that the 8-bit range can be configured to cover either the low light range (low read noise)

Calculating the Guide Star Magnitude:

The Zero Point in the H band is 9.56×10^9 ph/s/m²/μm. If we assume

- wide bandpass from 1 to $2.5\mu\text{m}$ ($\Delta\lambda = 1.5\mu\text{m}$),
- 50m^2 telescope area with 40% total throughput ($A_{eff} = 20 \text{m}^2$),
- 400KHz frame rate ($t_{exp} = 2.5 \times 10^{-3} \text{s}$),
- centroid estimated over 5 pixel diameter ($RON = 15 \times \sqrt{19} = 65 \text{e}$)
- SNR=8 ($Signal = 65 \times 8 = 500 \text{e}$)

we have a guide star magnitude

$$m = -2.5 \log(500/7.5 \times 10^8) = 15.44$$

If we instead assume that the centroid has to be estimated over the full 100×100 pixel window then the magnitude drops to about H=12.0.

or the full well depth of the sensor. It should also be relatively straightforward to switch between different bit-depths/frame rates. However it appears that reading multiple regions of interest, or windows, is not possible with this device, which imposes additional computational overhead as the entire array must be read to extract the guidestar positions. A commercial company, Andor Technology, based in the United Kingdom, will be offering this sensor in a packaged configuration in the near future. The cost for such a system is roughly \$25,000.

And yet a fourth option for the visible arms, also from Andor Technology, is based on a custom sensor built initially for the DKIST solar telescope. This options is our current baseline. It is a large area sCMOS detector with a 4096 x 4096 pixel array, and a 12 μ m pixel pitch. The QE for the back-illuminated version of this device is > 80%, and they are targeting < 3 e- read noise. The full-resolution frame rate is 80 frames per second (16-bit). However for GMOX we would only need to read the central 1024 rows, which increases our effective frame rate to 320 frames per second. Furthermore, multiple regions of interest can be read with this sensor, hence we would only read rows containing the guidestar windows, which further increases the frame rate. The cost for this sensor packaged with readout electronics from Andor is approximately \$200,000 for a back-illuminated sensor. Note, this price is based on a current limited view of potential in the astronomy market. If future demand for the device increases, the price would be expected to drop.

G.2.5.8 SLIT-VIEWING CAMERA READOUT ELECTRONICS

The choice of electronics for the slit-viewing cameras is, of course, driven by the detector. For the near infrared arm, we would use Teledyne's Sidecar ASIC. It is the logical choice given the demanding processing requirements. However, one could imagine using a customized ARC controller.

For the two visible arms, the choice of electronics depends on the detector ultimately chosen. If we were to use the e2v LGSD CMOS, we would likely use electronics provided by e2v Technologies. If we were to use Teledyne's HyViSI detector, we would then use their Sidecar ASIC for readout. Lastly, if we were to use either the latest Onyx CMOS or the Andor-4k sCMOS sensor, the readout electronics would be provided by Andor in a packaged configuration.

G.2.5.9 DMD ELECTRONICS

The DMDs are controlled by two commercially available boards based on the DLP Discovery 4100 chipset from Texas Instruments: a formatter board and a DMD board. The DMD resides in a socket on the DMD board, which communicates over an LVDS (Low Voltage Differential Signal) bus with the formatter board through an impedance matched flexible printed circuit cable (FPC). A block diagram of the configuration is shown in Fig. 79.

For GMOX, the baseline would be to use electronics provided by VISITECH (www.visitech.no). VISITECH is a Norwegian company that specializes in lithography systems that utilize DLP technology from Texas Instruments. We have purchased a development package including electronics and a Cinema 2K DMD from VISITECH already so we have experience working with this vendor. VISITECH produces custom formatter boards based on the TI Discover 4100 chipset, and have developed a custom formatter board for the LUXBEAM Cinema DC2K DMD. A photograph of the formatter and DMD boards is shown in Fig 80 along with a photograph of a DMD 0.7 XGA and its associated electronics on an optical bench; the older DMD 0.7 XGA electronics are very similar to those provided by VISITECH.

An issue with these electronics is that they are not designed to operate in a cryogenic environment. Although tests have shown the the DMD board, and the DMD itself, will function at least

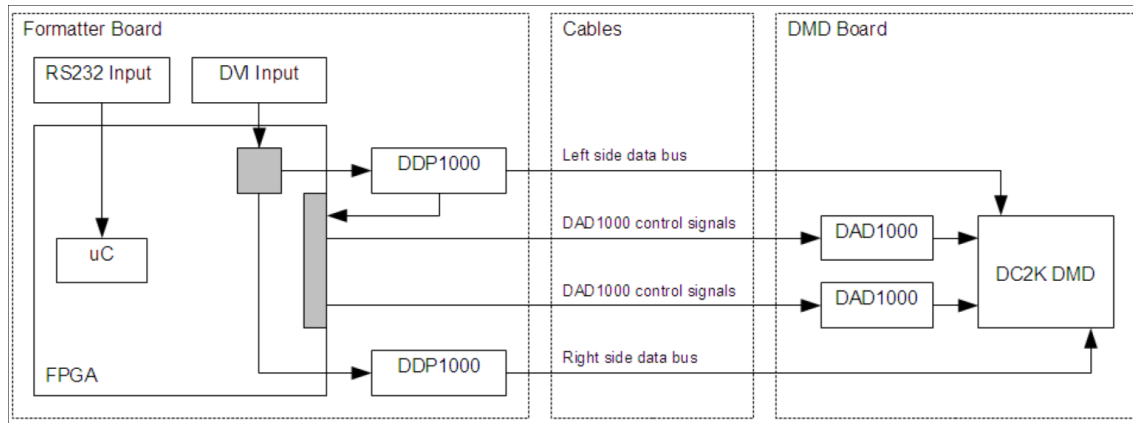


Figure 79: Block diagram of the formatter and DMD board. The formatter communicates with the DMD board over a flexible printed circuit.

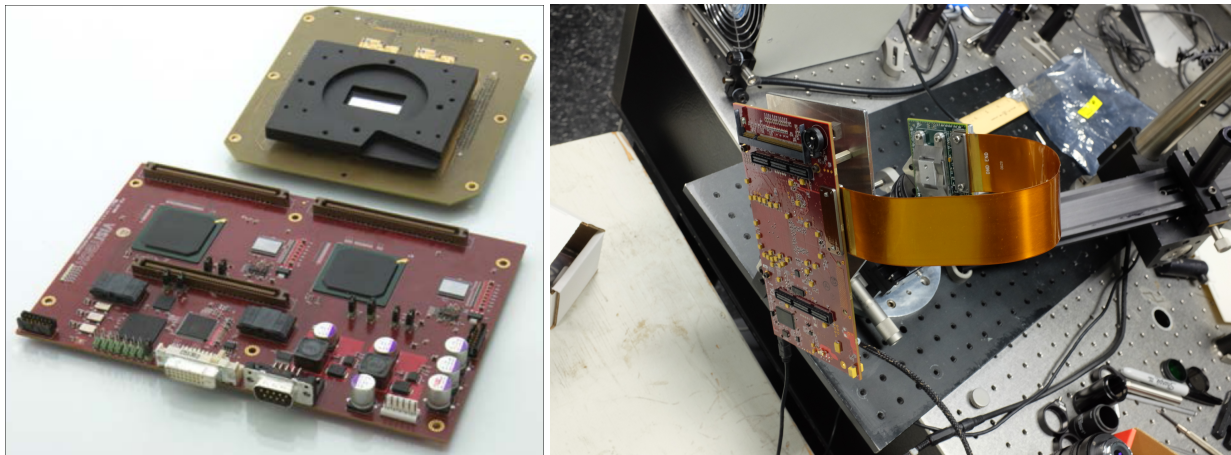


Figure 80: Left: Photograph of the VISITECH LUXBEAM DC2K formatter board (foreground) and DMD boards (background), and Right: Photograph of the Texas Instruments Discovery 4100 Development kit configured with an older DMD 0.7 XGA.

down to 130K (and quite probably lower than this since the tests conducted were not limited by the DMD or the DMD board but rather by the test cryostat).

As for the formatter board, it has been shown to fail at temperatures below -40°C . There are three possible solutions to this problem. One is to house the formatter board in an insulated and heated box on the outer surface of the cryostat radiation shield. We believe this is likely the simplest approach. The board dissipates only 2.7 W so this should not be that challenging. A second option is to locate the board outside the cryostat but still in close enough proximity to the DMD to such that a cable with the appropriate impedance can be used. A third option is to develop a custom board that will operate at cryogenic temperatures. The latter could be very costly but may not be out of the question.

G.2.5.10 COMMERCIAL VERSUS CUSTOM BOARDS

The electrical scheme described here is a mix of custom and commercial off-the-shelf electronics. Certainly one could devise a workable scheme consisting entirely of off-the-shelf electronics, or

all custom PCBs. Off the shelf components offer clear advantages in terms of cost, ease of support, and in most cases ease of replacement. Custom electronics offer the advantage of tailored performance, size, form factor, interface control, etc. What we have proposed is a balance between the two approaches.

We have chosen to adopt two custom PCBs that were developed for previous projects given the performance, size, and cost advantages they offer. One of them, the power control module (PCM) described above, satisfies a unique requirement; the ability to communicate with multiple devices having disparate communication protocols through a single, modern protocol, TCP/IP. The second, the temperature monitor board (TMB) also described above, has the advantage of offering up to 12 channels of temperature readout, two channels of heater control, and up to four analog input channels for sensor readout. The production cost of a these boards, for production runs of order ten units, is of approximately \$750, far less than a Lakeshore controller, which costs approximately \$4000.

In general, whether to use off-the-shelf electronics or custom boards is a common consideration on instrument projects. A significant concern, in either case, is obsolescence, either of box-level electronics (e.g. Lakeshore controllers and the like) or board-level component parts. And given the pace of technology today we are seeing obsolescence at a higher rate than in the past. Parts available at the beginning of the project design phase may not be available when the design is complete. For this reason we have chosen to produce critical, and commonly used, electronics in-house, since obsolescence at the component level, while a nuisance, typically only requires a minor change to a PCB layout, which is often more palatable than modifying interfaces.

G.2.6 INSTRUMENT SOFTWARE DESIGN

G.2.6.1 OVERVIEW OF CONTROL SOFTWARE ARCHITECTURE

The GMOX instrument control software will employ a middleware architecture whereby a server and client peripheral devices interact via a SQL Server Command and Telemetry database. Devices will stream telemetry via User Datagram Protocol (UDP) packets. The database, acting as the hyphen in “Client – Server”, provides a “disconnected” software architecture that allows the server and peripherals (client subsystems) to focus on their respective tasks and not be burdened with handshaking and polling operations. This disconnected model also allows subsystems to be taken off-line without interrupting the overall Instrument software operation, and provides for a much more fault tolerant system than a conventional polling type system.

GMOX instrument control software tasks will be divided up into four main components. They are:

- A Command and Telemetry Database
- A Server Application
- A Web Application (Graphical User Interface)
- Firmware

A detailed description of each of these components is provided here.

1. The GMOX Command and Telemetry Database – The command and telemetry database will reside on a computer that is mounted in an electronics control rack. It consists of a self-contained Microsoft SQL Server relational database. The database serves as an interface

between the Server App and the Web App. The database is also a repository for device configuration and system parameter storage.

- (a) Telemetry: The server will include an independent process that listens for UDP telemetry broadcast packets from subsystems and stores telemetry data in a queryable Telemetry Archive Table. A web application will read telemetry from the database and present it on display pages that can indicate temperature, pressure and other instrument statuses for human consumption.
 - (b) Commanding: Commands can either be generated by a user from a web page's Graphical User Interface (GUI) or via a running server application. Commands are added as indexed, time-stamped records to the database Command table. A separate server thread reads and parses commands as they accumulate in the database Command table and then routes them to their appropriate subsystem for execution.
2. GMOX Server Application – The server application is a multi-threaded application that is primarily responsible for reading and routing commands from the database command table. It also provides for critical health and safety monitoring of the Instrument hardware. Incoming UDP telemetry is decoded and stored in the Telemetry database table. The server application will contain numerous classes that act as drivers for each subsystem e.g. motor controllers, temp controllers etc.
 3. GMOX Web Application – The Web application serves as a graphical user interface. It allows users to execute GMOX commands and monitor GMOX telemetry. The web application does not communicate directly with the server application; it only interfaces with the GMOX database. The user can have multiple instances of browsers loaded with web application pages. This is useful for monitoring several telemetry pages simultaneously.
 4. Firmware – Whenever possible devices will have firmware that offloads the burden of work from the server computer. The idea is to keep the commanding of subsystems as quick and simple as possible and have as much functionality built into the subsystem as possible.

G.2.6.2 COMMUNICATIONS

All devices will be connected using Ethernet. In cases where an off-the-shelf device demands an RS-232 connection, we will incorporate an RS-232 to Ethernet converter. All devices will receive IP addresses via DHCP from a rack mounted router. IP's will be assigned based on the subsystem's MAC address. If supported, devices will be configured to stream telemetry data in UDP packets. If a device doesn't support UDP there will be a server thread running that polls the device and adds its telemetry to a separate UDP stream. Commanding of devices will primarily use TCP/IP or in some cases UDP if only one protocol is supported.

G.2.6.3 DMD CONTROL SOFTWARE

Building on the legacy of IRMOS, GMOX can be operated by dedicated software connecting the main components via a command/control system implemented on top of a TCP/IP socket layer [183]. The existing IRMOS Operating System provides a command sequencer, telemetry collection, and separate threads for the operation of the subsystems. The user interacts via a GUI component (see Fig. 81) allowing direct control of the instrument, status monitoring, data display and quick look analysis. Tools to create and position slits and perform simple calibrations are provided. The

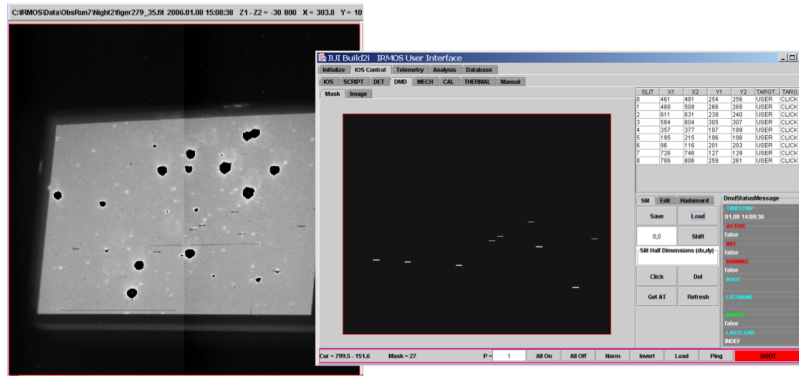


Figure 81: IRMOS GUI screen captures. Left: Preimaging of a science field with selected IRMOS slits. This control image was obtained with the spectrographic channel in imaging mode (no grating) projecting the “negative” slit pattern. Right: Screenshot of the IRMOS User Interface window used for slit mask assignments. The slits are seen in DMD coordinates (hence the rectangular 848x600 pixel window). The slit definition table is in the upper right (science data from [190]).

original IRMOS software was mainly written in JAVA, allowing the major components to operate on different platforms. The IRMOS GUI provides an excellent template for GMOX and will be made available to Gemini to speed up the development of the instrument GUI.

G.2.6.4 DETECTOR READOUT SOFTWARE

We strongly prefer open-source over closed-source, mostly to lower dependence on proprietary systems. When timing constraints allow we prefer coding in an interpreted scripting language, these days python, both for flexibility and to make the code accessible to more programmers.

The API for the science detectors will fundamentally be to provide integrations as FITS files.

The baseline HxRG controller set is the Teledyne SAM and ASIC, driven over the SAM Ethernet link. The science detectors have no extreme timing requirements, so we expect to reuse an existing pure python module which wraps the Teledyne Linux library. This exposes both up-the-ramp and Fowler-sampled readouts, as well as control over the ASIC registers. Standard ASIC firmware should be sufficient.

The baseline CCD controller is the ARC boardset. The science API requirements are straightforward, so we expect to only need to call and wrap a few low-level ARC API classes.

The slit-viewers obviously have tighter requirements given the 400 Hz frame-rate. The standard HxRG ASIC code only supports reading out one window per read but can be modified, and in fact has been for certain customers, to read multiple windows. These modifications would likely be contracted to Markus Loose, as he has the expertise and has explicitly expressed an interest in doing it.

The code for reading the sCMOS slit-viewing would depend somewhat on the vendor chosen for the sensors. But assuming the Andor 4K x 4k, the code would likely be developed in concert with the vendor, with the vendor providing the low-level code.

G.2.6.5 DEVELOPMENT TOOLS

For the instrument control software, we would use either a Windows based system incorporating Visual Studio, C#, Sql Server and IIS given our experience with this system and its broad support, or we could use Linux, Apache, MySQL and Python (LAMP). Both systems will provide the functionality that we need. For the detector readout software we would likely use Python.

G.2.7 DATA REDUCTION SOFTWARE CONSIDERATIONS

For IRMOS we have developed a basic pipeline in IDL allowing to extract calibrated spectra from data taken with a DMD as slit selector. We plan to utilize this IDL script as a convenient example for the development of the GMOX pipeline; however, we will adopt the Python environment, leveraging on the development of tools for the analysis of JWST/NIRSpec spectra at STScI. We plan to adopt an Agile software development approach, recently implemented with success at STScI for the development of the algorithms for the JWST data analysis tools.

G.2.8 PERFORMANCE TRADES

As the overall study progressed, the operation of GMOX in conjunction with Gemini facility AO became a primary focus of the technical development effort and consumed a large fraction of our available resources. Key design decisions were made based on an evolving understanding of Gemini interfaces and operational requirements – specifically in the area of AO – and as a result several trades studies we intended to look at in some detail, including eliminating the blue arm and eliminating K-band, were not evaluated. However, two areas not initially identified for trade studies did involve significant research and technical consideration, and these are described in the following paragraphs.

G.2.8.1 FIELD OF VIEW

After a fair amount of consideration we adopted a baseline for the GMOX field of view of 90" x 171" in all modes (Gemini-North and Gemini-South) except for the AO mode in the south, where the field will be 45" x 85". This represents a compromise between design complexity and science capability. To maintain the 90" x 171" field with GeMS would require either a zoom-lens reimager for each channel, or a large insertable focal reducer near the telescope focus. Both of these options would be rather complex and certainly add cost.

G.2.8.2 NIR DETECTOR SELECTION

The WFIRST infrared detectors being developed separately by both Teledyne and Raytheon utilize a 4k x 4k x 10 μm pixel format. We chose to investigate the use of this format over the 4k x 4k x 15 μm pixel format as it offers several advantages. First, NASA is funding both Teledyne and Raytheon to develop these detectors for WFIRST, and that development funding should lessen the cost of those detectors for projects like GMOX. Second, since Raytheon has funding to work on the WFIRST detectors but NOT on the Astro-4k.15, this offers us a more mature option to Teledyne's detectors than the Astro-4k.15. And third, the smaller pixel size reduces the focal length of the NIR cameras, reducing the size of the cryostat, which eases packaging considerations. After weighing the two options we adopted the 10 μm pixel format as the baseline for GMOX.

G.2.9 TECHNICAL RISKS

Several technical risks have been identified with the GMOX concept, although none are significant. We discuss each of them here, and summarize what we feel are the top five risks in a risk registry in Section H.4.1.

1. Slit-viewing camera detectors – For adaptive optics with GMOX, the slit-viewing camera must do more than simply produce static images of the DMD to verify the configuration of

the “slits”. This camera must also provide rapid, real-time, feedback on the location of three, and preferably four, guidestars. The frame-rate required is upwards of 400 Hz. Therefore every 2.5 ms the positions of three guidestars must be sent to the AO real-time controller. With such short exposures the photon count will be small (of order a few hundred photons per pixel for a 15th magnitude guide star), and read-noise is an important consideration. As is processing time, and to reduce processing time, and to enhance the frame-rate, it is sensible, and in fact desirable, to read sub-arrays around the guidestars rather than the entire detector. Hence, we require a large format, low noise, high frame-rate detector system with very low latency and the ability to read multiple regions of interest.

Finding a detector that satisfies these requirements is challenging. However, several options are available as discussed in Sec. G.2.5.7, and more will become available in the next few years. Therefore, we feel the risk is moderate at this point.

2. Cryogenic operation of DMDs – IRMOS operates an early DMD at $\simeq -40\text{C}$, but this does not seem to be sufficient for ultimate performance in the K-band. We estimate that 200 K is adequate. Recently, it has been demonstrated that modern DMDs are fully functional down to 130 K [191], so there is plenty of margin. On the other hand, operating the IR DMD at 120 K would facilitate the cryogenic design. We do not anticipate the additional ten degrees will matter, but this needs to be verified and we have plans to do so in the near term.
3. DMD window replacement – We have based our sensitivity estimates on the standard coatings provided by Texas Instruments. It is possible, however, to change the window with another having multi-layer coatings for optimal throughput, and we would very much like to tailor the coating of each DMD for the channel it is used in.

Co-I Z. Ninkov (RIT) is actively pursuing methods to replace the standard window. This activity is funded by a NASA Science and Technology program (SAT) led by Ninkov. The main goals of the program are 1) to verify the feasibility of window replacement on Cinema DMD to increase throughput beyond the visible wavelengths; 2) to develop radiation hard readout electronics suitable for space applications. Recently, NASA has expanded the scope of the program to include testing of Cinema DMD devices in a relevant environment to raise their technological maturity to TRL6; this in order to include DMDs as a suitable asset for space missions before the 2020 Decadal Survey.

Concerning window replacement, a number of companies have been contacted and L-1 Standard and Technology has been selected as the prime contractor for this effort. This company has extensive experience with the DMD 07 XGA (1024 x 768, 13.68 μm pixel pitch) window removal and has successfully substituted the original windows with a variety of materials. We do not believe the Cinema DMDs pose any special new challenge with respect to the smaller DMDs L-1 is already familiar with. Three other companies have been contacted to provide different windows (in particular Sapphire for UV transmission) and their coating. At the same time, RIT has started an independent program to gain similar window replacement capabilities. To assess the performance of DMDs with the different windows, NASA Goddard has started a program to characterize the optical behavior of DMDs with different windows, using their new Agilent Cary5000 UV-VIS-IR spectrophotometer to measure DMD reflectivity, diffracted and scattered light. RIT is also performing independent test with their own ellipsometer.

All these activities are in progress at this time. The first replacement windows have been delivered; RIT has produced their first window-replaced DMDs; GSFC has performed the

first measures on original DMDs to establish a baseline and optimize their methodology. Test plans for radiation, vibration, acoustic tests are also being finalized for TRL6 qualification. Interest in this program has been expressed by other groups working with DMDs for non-astronomical applications. We expect that GMOX and future projects exploiting DMDs will greatly benefit from this NASA funded program.

Therefore, while there is some risk that swapping the window on the Cinema DMD proves challenging, we feel this risk is modest, given the successes to date with the DMD 07 XGA, which has similar packaging.

4. Instrument flexure:

- a) Flexure between spectrograph arms – The telescope pointing can be used to keep the targets within their slits, but only on a single arm. Differential flexures between arms will need to be controlled or compensated in order to keep all three arms simultaneously locked onto the targets. The fold mirrors on the blue and red arms could be used as fine-steering mirrors, driven by feedback from the slit viewing camera to maintain alignment with the slits.
- b) Changes in alignment between a slit-viewing camera and its corresponding DMD – This will lead to target acquisition nightmares. The mapping between slit camera pixels and DMD micromirrors needs to be very stable (or predictable). The obvious mitigation is a very stiff design, confirmed of course by analysis.

5. Manufacturability of the near-IR gratings – The line frequencies of the near-IR gratings in the strawman design are low for the VPH domain. We have contacted Kaiser Optical Systems and they feel the low line frequencies in the NIR are likely not an issue given that the viable line frequency decreases as wavelength increases.

6. Grating efficiency in the visible arms – The line frequency of the blue grating is high compared to similar gratings we've built for this bandpass based on the first-pass design by Kaiser Optical. This leads to reduced efficiency near the edges of the bandpass.

The line frequency is also a bit high for the red grating, and like the blue grating, this leads to reduced efficiency at the edge of the bandpass, albeit not as severe as in the blue, and mainly at the short wavelength end of the bandpass.

7. Availability of H4RG detectors – Teledyne Imaging Sensors has recently started taking orders for their Hawaii H4RG-15 (15 μm pixel format) detectors, and they are presently developing the H4RG-10 (10 μm pixel format) for the WFIRST program. These designs draw on heritage from the H2RG sensor which has been used successfully in many instruments. There have been technical challenges however with the H4RG-15 and delivery of functioning science grade devices has been delayed. Despite the delays it appears Teledyne has managed to solve these technical challenges and we expect to see first-article science grade detectors delivered by the end of 2015. The present status of the H4RG-10 program is not known. While we are reasonably confident that Teledyne will be delivering science grade devices on the timescale of GMOX, the inherent complexity of fabricating such devices compels us to flag delivery of the H4RG as a risk.

As an alternative to the H4RG, Raytheon's pending HgCdTe Astro-4k.10 is an option. The Astro-4k.10 is being funded by NASA for the WFIRST program. It has the same 4k x 4k x 10 μm pixel format as the H4RG-10. The device is being built in two flavors: MBE (Molecular Beam Epitaxy) on CdZnTe and MBE on silicon. The latter being less expensive but with

reduced performance, albeit possibly acceptable. The former adheres to the MBE approach used by Teledyne for the H4RG and should have comparable performance. They anticipate availability on the timescale of GMOX. Raytheon has substantial heritage in HgCdTe technology and has produced numerous devices for astronomy.

J ACKNOWLEDGMENTS

The authors of this study are deeply indebted to the many colleagues and collaborators who provided critical insights on almost every aspect of this work. In particular, we acknowledge Stephen Goodsell, Pascale Hibon, Bernadette Rambold, Madeline Close and the entire GIFS Study Team of Gemini for advice and support especially with understanding the AO systems; Suresh Sivanandam at Dunlap Institute is acknowledged for helpful discussions, while we look forward to partner in the GMOX proposing team for the coming call. D. Apai (U. Arizona), S. Beckwith (Berkeley), S. Heap (NASA-GSFC), M. Kasper (ESO), S. Kassin (STScI), J. Mather (NASA Goddard), A. Miotello (Leiden), A. Rest (STScI), K.B. Schmidt (UC Santa Barbara), M. Stiavelli (STScI), D. Vorobiev (RIT) and F. Zerbi (INAF) are especially acknowledged for key insights on the capabilities of GMOX.

BIBLIOGRAPHY

- [1] National Research Council, *New Worlds, New Horizons in Astronomy and Astrophysics* (The National Academies Press, 2010), ISBN 978-0-309-15799-5.
- [2] National Research Council, *Optimizing the U.S. Ground-Based Optical and Infrared Astronomy System* (The National Academies Press, 2015), ISBN 978-0-309-37186-5.
- [3] Gemini's Science and technology Advisory Committee, *Report 2012b* (Gemini, 2012).
- [4] A. Zitrin, T. Broadhurst, et al., MNRAS **413**, 1753 (2011), *Strong-lensing analysis of MS 1358.4+6245: New multiple images and implications for the well-resolved $z \approx 4.92$ galaxy.*
- [5] D. Coe, A. Zitrin, et al., ApJ **762**, 32 (2013), *CLASH: Three Strongly Lensed Images of a Candidate $z \approx 11$ Galaxy.*
- [6] R. J. Bouwens, G. D. Illingworth, et al., Nature **469**, 504 (2011), *A candidate redshift $z \sim 10$ galaxy and rapid changes in that population at an age of 500 Myr.*
- [7] R. S. Ellis, R. J. McLure, et al., ApJ **763**, L7 (2013), *The Abundance of Star-forming Galaxies in the Redshift Range 8.5-12: New Results from the 2012 Hubble Ultra Deep Field Campaign.*
- [8] B. E. Robertson, R. S. Ellis, S. R. Furlanetto, and J. S. Dunlop, ApJ **802**, L19 (2015), *Cosmic Reionization and Early Star-forming Galaxies: A Joint Analysis of New Constraints from Planck and the Hubble Space Telescope.*
- [9] R. Bacon, J. Brinchmann, et al., ArXiv e-prints (2014), *The MUSE 3D view of the Hubble Deep Field South.*
- [10] A. Zitrin, I. Labbe, et al., ArXiv e-prints (2015), *Lyman-alpha Emission from a Luminous $z=8.68$ Galaxy: Implications for Galaxies as Tracers of Cosmic Reionization.*
- [11] T. Treu, K. B. Schmidt, et al., ApJ **775**, L29 (2013), *The Changing Ly α Optical Depth in the Range $6 < z < 9$ from the MOSFIRE Spectroscopy of Y-dropouts.*
- [12] M. Trenti, M. Stiavelli, and J. Michael Shull, ApJ **700**, 1672 (2009), *Metal-free Gas Supply at the Edge of Reionization: Late-epoch Population III Star Formation.*
- [13] D. Sobral, J. Matthee, et al., ApJ **808**, 139 (2015), *Evidence for PopIII-like Stellar Populations in the Most Luminous Lyman- α Emitters at the Epoch of Reionization: Spectroscopic Confirmation.*
- [14] X. Fan, M. A. Strauss, et al., AJ **132**, 117 (2006), *Constraining the Evolution of the Ionizing Background and the Epoch of Reionization with $z \sim 6$ Quasars. II. A Sample of 19 Quasars.*
- [15] G. D. Becker, J. S. Bolton, et al., ArXiv e-prints (2014), *Evidence of patchy hydrogen reionization from an extreme Ly α trough below redshift six.*
- [16] D. J. Mortlock, S. J. Warren, et al., Nature **474**, 616 (2011), *A luminous quasar at a redshift of $z = 7.085$.*
- [17] J. S. Bolton, M. G. Haehnelt, et al., MNRAS **416**, L70 (2011), *How neutral is the intergalactic medium surrounding the redshift $z = 7.085$ quasar ULAS J1120+0641?*
- [18] G. De Rosa, B. P. Venemans, et al., ApJ **790**, 145 (2014), *Black Hole Mass Estimates and Emission-line Properties of a Sample of Redshift $z \sim 6.5$ Quasars.*
- [19] X.-B. Wu, F. Wang, et al., IAU General Assembly **22**, 51223 (2015), *Discovery of a 12 billion solar mass black hole at redshift 6.3 and its challenge to the black hole/galaxy co-evolution at cosmic dawn.*
- [20] G. R. Meurer, T. M. Heckman, and D. Calzetti, ApJ **521**, 64 (1999), *Dust Absorption and the Ultraviolet Luminosity Density at $z \sim 3$ as Calibrated by Local Starburst Galaxies.*
- [21] D. P. Stark, R. S. Ellis, et al., ApJ **697**, 1493 (2009), *The Evolutionary History of Lyman Break Galaxies Between Redshift 4 and 6: Observing Successive Generations of Massive Galaxies in Formation.*
- [22] R. J. Bouwens, G. D. Illingworth, et al., ApJ **793**, 115 (2014), *UV-continuum Slopes of $> 4000 z \sim 4-8$ Galaxies from the HUDF/XDF, HUDF09, ERS, CANDELS-South, and CANDELS-North Fields.*
- [23] K. Duncan, C. J. Conselice, et al., MNRAS **444**, 2960 (2014), *The mass evolution of the first galaxies: stellar mass functions and star formation rates at $4 \lesssim z \lesssim 7$ in the CANDELS GOODS-South field.*
- [24] B. Salmon, C. Papovich, et al., ArXiv e-prints (2014), *The Star-Formation Rate and Stellar Mass Relation of Galaxies at*

- 3.5 $z \leq 6.5$ in CANDELS.
- [25] M. Dickinson, J. Kartaltepe, et al., *Are starbursts really mergers at high redshift? A kinematic investigation*, NOAO Proposal (2013).
- [26] P. Madau and M. Dickinson, *ARA&A* **52**, 415 (2014), *Cosmic Star-Formation History*.
- [27] M. L. Balogh, S. L. Morris, et al., *ApJ* **527**, 54 (1999), *Differential Galaxy Evolution in Cluster and Field Galaxies at $z \sim 0.3$* .
- [28] G. Kauffmann, T. M. Heckman, et al., *MNRAS* **341**, 33 (2003), *Stellar masses and star formation histories for 10^5 galaxies from the Sloan Digital Sky Survey*.
- [29] D. J. Croton, V. Springel, et al., *MNRAS* **365**, 11 (2006), *The many lives of active galactic nuclei: cooling flows, black holes and the luminosities and colours of galaxies*.
- [30] L. Fan, A. Lapi, G. De Zotti, and L. Danese, *ApJ* **689**, L101 (2008), *The Dramatic Size Evolution of Elliptical Galaxies and the Quasar Feedback*.
- [31] M. Vestergaard and P. S. Osmer, *ApJ* **699**, 800 (2009), *Mass Functions of the Active Black Holes in Distant Quasars from the Large Bright Quasar Survey, the Bright Quasar Survey, and the Color-selected Sample of the SDSS Fall Equatorial Stripe*.
- [32] M. S. Owers, W. J. Couch, P. E. J. Nulsen, and S. W. Randall, *ApJ* **750**, L23 (2012), *Shocking Tails in the Major Merger Abell 2744*.
- [33] T. D. Rawle, B. Altieri, et al., *MNRAS* **442**, 196 (2014), *Star formation in the massive cluster merger Abell 2744*.
- [34] H. Ebeling, L. N. Stephenson, and A. C. Edge, *ApJ* **781**, L40 (2014), *Jellyfish: Evidence of Extreme Ram-pressure Stripping in Massive Galaxy Clusters*.
- [35] G. De Lucia, S. Weinmann, et al., *MNRAS* **423**, 1277 (2012), *The environmental history of group and cluster galaxies in a Λ cold dark matter universe*.
- [36] M. Brodwin, S. A. Stanford, et al., *ApJ* **779**, 138 (2013), *The Era of Star Formation in Galaxy Clusters*.
- [37] Y. Koyama, T. Kodama, et al., *MNRAS* **403**, 1611 (2010), *Panoramic $H\alpha$ and mid-infrared mapping of star formation in a $z = 0.8$ cluster*.
- [38] M. Postman, D. Coe, et al., *ApJS* **199**, 25 (2012), *The Cluster Lensing and Supernova Survey with Hubble: An Overview*.
- [39] J. Lotz, M. Mountain, et al., in *American Astronomical Society Meeting Abstracts #223* (2014), vol. 223 of *American Astronomical Society Meeting Abstracts*, p. #254.01.
- [40] M. S. Owers, S. W. Randall, et al., *ApJ* **728**, 27 (2011), *The Dissection of Abell 2744: A Rich Cluster Growing Through Major and Minor Mergers*.
- [41] W. Karman, K. I. Caputi, et al., *A&A* **565**, A5 (2014), *Rest-frame ultraviolet spectra of massive galaxies at $z \sim 3$: evidence of high-velocity outflows*.
- [42] P. Madau and M. Dickinson, *ARA&A* **52**, 415 (2014), *Cosmic Star-Formation History*.
- [43] M. R. Krumholz, *Phys. Rep.* **539**, 49 (2014), *The big problems in star formation: The star formation rate, stellar clustering, and the initial mass function*.
- [44] B. G. Elmegreen, in *EAS Publications Series*, edited by C. Charbonnel and T. Montmerle (2011), vol. 51 of *EAS Publications Series*, pp. 31–44.
- [45] A. Adamo, J. M. D. Kruijssen, et al., *MNRAS* **452**, 246 (2015), *Probing the role of the galactic environment in the formation of stellar clusters, using M83 as a test bench*.
- [46] K. E. Johnson, A. K. Leroy, et al., *ApJ* **806**, 35 (2015), *The Physical Conditions in a Pre-super Star Cluster Molecular Cloud in the Antennae Galaxies*.
- [47] J. M. D. Kruijssen, *MNRAS* **426**, 3008 (2012), *On the fraction of star formation occurring in bound stellar clusters*.
- [48] P. G. van Dokkum and C. Conroy, *Nature* **468**, 940 (2010), *A substantial population of low-mass stars in luminous elliptical galaxies*.
- [49] D. Calzetti, R. Chandar, et al., *ApJ* **719**, L158 (2010), *A Method for Measuring Variations in the Stellar Initial Mass Function*.
- [50] M. Cappellari, R. M. McDermid, et al., *Nature* **484**, 485 (2012), *Systematic variation of the stellar initial mass function in early-type galaxies*.
- [51] J. E. Andrews, D. Calzetti, et al., *ApJ* **767**, 51 (2013), *An Initial Mass Function Study of the Dwarf Starburst Galaxy NGC 4214*.
- [52] B. C. Whitmore, R. Chandar, and S. M. Fall, *AJ* **133**, 1067 (2007), *Star Cluster Demographics. I. A General Framework and Application to the Antennae Galaxies*.
- [53] S. G. Boutloukos and H. J. G. L. M. Lamers, *MNRAS* **338**, 717 (2003), *Star cluster formation and disruption time-scales*

- I. *An empirical determination of the disruption time of star clusters in four galaxies.*
- [54] A. Jordán, D. E. McLaughlin, et al., *ApJS* **171**, 101 (2007), *The ACS Virgo Cluster Survey. XII. The Luminosity Function of Globular Clusters in Early-Type Galaxies.*
- [55] R. Chandar, B. C. Whitmore, et al., *ApJ* **719**, 966 (2010), *The Luminosity, Mass, and Age Distributions of Compact Star Clusters in M83 Based on Hubble Space Telescope/Wide Field Camera 3 Observations.*
- [56] N. Bastian, I. S. Konstantopoulos, et al., *A&A* **541**, A25 (2012), *Spectroscopic constraints on the form of the stellar cluster mass function.*
- [57] D. Calzetti, A. L. Kinney, and T. Storchi-Bergmann, *ApJ* **458**, 132 (1996), *Dust Obscuration in Starburst Galaxies from Near-Infrared Spectroscopy.*
- [58] J. E. Dale, *New A Rev.* **68**, 1 (2015), *The modelling of feedback in star formation simulations.*
- [59] I. Cabrera-Ziri, N. Bastian, et al., *MNRAS* **441**, 2754 (2014), *Constraining globular cluster formation through studies of young massive clusters - II. A single stellar population young massive cluster in NGC 34.*
- [60] L. Bianchi, Y. Kang, et al., *Advances in Space Research* **53**, 928 (2014), *The role of ultraviolet imaging in studies of resolved and unresolved young stellar populations. M31 and M33.*
- [61] L. Bianchi, Y. B. Kang, et al., *Ap&SS* **335**, 249 (2011), *Young stellar populations in the local group: an HST and GALEX comprehensive study.*
- [62] L. Bianchi, B. Efremova, et al., *AJ* **143**, 74 (2012), *A Treasury Study of Star-forming Regions in the Local Group. I. HST Photometry of Young Populations in Six Dwarf Galaxies.*
- [63] A. Renzini and F. Fusi Pecci, *ARA&A* **26**, 199 (1988), *Tests of evolutionary sequences using color-magnitude diagrams of globular clusters.*
- [64] G. Piotto, A. P. Milone, et al., *ArXiv e-prints* (2014), *The Hubble Space Telescope UV Legacy Survey of Galactic Globular Clusters. I. Overview of the Project and Detection of Multiple Stellar Populations.*
- [65] B. N. et al, *mnras* **436**, 2852 (2013).
- [66] G. Piotto, A. P. Milone, et al., *AJ* **149**, 91 (2015), *The Hubble Space Telescope UV Legacy Survey of Galactic Globular Clusters. I. Overview of the Project and Detection of Multiple Stellar Populations.*
- [67] S. Villanova, G. Piotto, and R. G. Gratton, *A&A* **499**, 755 (2009), *The helium content of globular clusters: light element abundance correlations and HB morphology. I. NGC 6752.*
- [68] R. Gratton, C. Sneden, and E. Carretta, *ARA&A* **42**, 385 (2004), *Abundance Variations Within Globular Clusters.*
- [69] T. Decressin, G. Meynet, et al., *A&A* **464**, 1029 (2007), *Fast rotating massive stars and the origin of the abundance patterns in galactic globular clusters.*
- [70] A. D’Ercole, E. Vesperini, et al., *MNRAS* **391**, 825 (2008), *Formation and dynamical evolution of multiple stellar generations in globular clusters.*
- [71] N. Bastian, H. J. G. L. M. Lamers, et al., *MNRAS* **436**, 2398 (2013), *Early disc accretion as the origin of abundance anomalies in globular clusters.*
- [72] E. Vesperini, S. L. W. McMillan, F. D’Antona, and A. D’Ercole, *MNRAS* **429**, 1913 (2013), *Dynamical evolution and spatial mixing of multiple population globular clusters.*
- [73] A. Bellini, J. Anderson, et al., *ApJ* **797**, 115 (2014), *Hubble Space Telescope Proper Motion (HSTPROMO) Catalogs of Galactic Globular Clusters. I. Sample Selection, Data Reduction, and NGC 7078 Results.*
- [74] S. Ortolani, A. Renzini, et al., *Nature* **377**, 701 (1995), *Near-coeval formation of the Galactic bulge and halo inferred from globular cluster ages.*
- [75] M. Zoccali, A. Renzini, et al., *A&A* **399**, 931 (2003), *Age and metallicity distribution of the Galactic bulge from extensive optical and near-IR stellar photometry.*
- [76] W. I. Clarkson, K. C. Sahu, et al., *ApJ* **735**, 37 (2011), *The First Detection of Blue Straggler Stars in the Milky Way Bulge.*
- [77] E. Valenti, M. Zoccali, et al., *A&A* **559**, A98 (2013), *Stellar ages through the corners of the boxy bulge.*
- [78] J. P. Fulbright, A. McWilliam, and R. M. Rich, *ApJ* **636**, 821 (2006), *Abundances of Baade’s Window Giants from Keck HIRES Spectra. I. Stellar Parameters and [Fe/H] Values.*
- [79] J. P. Fulbright, A. McWilliam, and R. M. Rich, *ApJ* **661**, 1152 (2007), *Abundances of Baade’s Window Giants from Keck HIRES Spectra. II. The Alpha and Light Odd Elements.*
- [80] K. Cunha and V. V. Smith, *ApJ* **651**, 491 (2006), *Chemical Evolution of the Galactic Bulge as Derived from High-Resolution Infrared Spectroscopy of K and M Red Giants.*
- [81] A. Lecureur, V. Hill, et al., *A&A* **465**, 799 (2007), *Oxygen, sodium, magnesium, and aluminium as tracers of the galactic bulge formation.*

- [82] C. I. Johnson, R. M. Rich, et al., *AJ* **148**, 67 (2014), *Light, Alpha, and Fe-peak Element Abundances in the Galactic Bulge*.
- [83] M. López-Corredoira, A. Cabrera-Lavers, and O. E. Gerhard, *A&A* **439**, 107 (2005), *A boxy bulge in the Milky Way. Inversion of the stellar statistics equation with 2MASS data*.
- [84] D. M. Nataf, A. Udalski, et al., *ApJ* **721**, L28 (2010), *The Split Red Clump of the Galactic Bulge from OGLE-III*.
- [85] C. Wegg and O. Gerhard, *MNRAS* **435**, 1874 (2013), *Mapping the three-dimensional density of the Galactic bulge with VVV red clump stars*.
- [86] E. Athanassoula, *MNRAS* **358**, 1477 (2005), *On the nature of bulges in general and of box/peanut bulges in particular: input from N-body simulations*.
- [87] I. Martínez-Valpuesta, I. Shlosman, and C. Heller, *ApJ* **637**, 214 (2006), *Evolution of Stellar Bars in Live Axisymmetric Halos: Recurrent Buckling and Secular Growth*.
- [88] G. Kordopatis, G. Gilmore, et al., *AJ* **146**, 134 (2013), *The Radial Velocity Experiment (RAVE): Fourth Data Release*.
- [89] R. M. Rich, D. B. Reitzel, C. D. Howard, and H. Zhao, *ApJ* **658**, L29 (2007), *The Bulge Radial Velocity Assay: Techniques and a Rotation Curve*.
- [90] C. D. Howard, R. M. Rich, et al., *ApJ* **688**, 1060 (2008), *The Bulge Radial Velocity Assay (BRAVA). I. Sample Selection and a Rotation Curve*.
- [91] A. Kunder, A. Koch, et al., *AJ* **143**, 57 (2012), *The Bulge Radial Velocity Assay (BRAVA). II. Complete Sample and Data Release*.
- [92] M. Ness, K. Freeman, et al., *ApJ* **756**, 22 (2012), *The Origin of the Split Red Clump in the Galactic Bulge of the Milky Way*.
- [93] K. Freeman, M. Ness, et al., *MNRAS* **428**, 3660 (2013), *ARGOS - II. The Galactic bulge survey*.
- [94] M. Ness, K. Freeman, et al., *MNRAS* **430**, 836 (2013), *ARGOS - III. Stellar populations in the Galactic bulge of the Milky Way*.
- [95] M. Ness, K. Freeman, et al., *MNRAS* **432**, 2092 (2013), *ARGOS - IV. The kinematics of the Milky Way bulge*.
- [96] M. Zoccali, O. A. Gonzalez, et al., *A&A* **562**, A66 (2014), *The GIRAFFE Inner Bulge Survey (GIBS). I. Survey description and a kinematical map of the Milky Way bulge*.
- [97] A. E. García Pérez, J. Johnson, et al., in *American Astronomical Society Meeting Abstracts* (2015), vol. 225 of *American Astronomical Society Meeting Abstracts*, p. 319.06.
- [98] R. K. Saito, D. Minniti, et al., *A&A* **544**, A147 (2012), *Milky Way demographics with the VVV survey. I. The 84-million star colour-magnitude diagram of the Galactic bulge*.
- [99] Y. Chen, L. Girardi, et al., *MNRAS* **444**, 2525 (2014), *Improving PARSEC models for very low mass stars*.
- [100] D. M. Nataf, O. A. Gonzalez, et al., *ArXiv e-prints* (2015), *Interstellar Extinction Curve Variations Toward the Inner Milky Way: A Challenge to Observational Cosmology*.
- [101] B. G. Elmegreen, in *IAU Symposium*, edited by R. de Grijs and J. R. D. Lépine (2010), vol. 266 of *IAU Symposium*, pp. 3–13.
- [102] J. C. Tan, M. R. Krumholz, and C. F. McKee, *ApJ* **641**, L121 (2006), *Equilibrium Star Cluster Formation*.
- [103] M. R. Bate, *MNRAS* **392**, 1363 (2009), *The importance of radiative feedback for the stellar initial mass function*.
- [104] M. R. Krumholz, R. I. Klein, and C. F. McKee, *ApJ* **740**, 74 (2011), *Radiation-hydrodynamic Simulations of the Formation of Orion-like Star Clusters. I. Implications for the Origin of the Initial Mass Function*.
- [105] E. Sabbi, M. Sirianni, et al., *AJ* **133**, 44 (2007), *Past and Present Star Formation in the SMC: NGC 346 and its Neighborhood*.
- [106] E. Hennekemper, D. A. Gouliermis, et al., *ApJ* **672**, 914 (2008), *NGC 346 in the Small Magellanic Cloud. III. Recent Star Formation and Stellar Clustering Properties in the Bright H II Region N66*.
- [107] D. A. Gouliermis, R. de Grijs, and Y. Xin, *ApJ* **692**, 1678 (2009), *A New Diagnostic Method for Assessment of Stellar Stratification in Star Clusters*.
- [108] D. A. Gouliermis, J. M. Bestenlehner, W. Brandner, and T. Henning, *A&A* **515**, A56 (2010), *Recent star formation at low metallicities. The star-forming region NGC 346/N66 in the Small Magellanic Cloud from near-infrared VLT/ISAAC observations*.
- [109] E. Sabbi, D. J. Lennon, et al., *ApJ* **754**, L37 (2012), *A Double Cluster at the Core of 30 Doradus*.
- [110] T. Do, G. D. Martinez, et al., *ApJ* **779**, L6 (2013), *Three-dimensional Stellar Kinematics at the Galactic Center: Measuring the Nuclear Star Cluster Spatial Density Profile, Black Hole Mass, and Distance*.
- [111] A. Stolte, B. Hußmann, et al., *ApJ* **789**, 115 (2014), *The Orbital Motion of the Quintuplet Cluster – A Common Origin for the Arches and Quintuplet Clusters?*
- [112] I. Platais, R. P. van der Marel, et al., *AJ* **150**, 89 (2015), *HST Astrometry in the 30 Doradus Region: Measuring Proper*

- Motions of Individual Stars in the Large Magellanic Cloud.*
- [113] J. Puls, M. A. Urbaneja, et al., *A&A* **435**, 669 (2005), *Atmospheric NLTE-models for the spectroscopic analysis of blue stars with winds. II. Line-blanketed models.*
- [114] L. E. Ellerbroek, A. Bik, et al., *A&A* **558**, A102 (2013), *ASTROBJ₂RCW36/ASTROBJ₂: characterizing the outcome of massive star formation.*
- [115] S. J. Kenyon and L. Hartmann, *ApJS* **101**, 117 (1995), *Pre-Main-Sequence Evolution in the Taurus-Auriga Molecular Cloud.*
- [116] W. Benz, S. Ida, et al., *Protostars and Planets VI* pp. 691–713 (2014), *Planet Population Synthesis.*
- [117] R. Alexander, I. Pascucci, et al., *ArXiv e-prints* (2013), *The Dispersal of Protoplanetary Disks.*
- [118] L. Hartmann, *Accretion Processes in Star Formation* (1998).
- [119] L. Hartmann, *Accretion Processes in Star Formation: Second Edition* (Cambridge University Press, 2009).
- [120] E. Gullbring, L. Hartmann, C. Briceño, and N. Calvet, *ApJ* **492**, 323 (1998), *Disk Accretion Rates for T Tauri Stars.*
- [121] G. J. Herczeg and L. A. Hillenbrand, *ApJ* **681**, 594 (2008), *UV Excess Measures of Accretion onto Young Very Low Mass Stars and Brown Dwarfs.*
- [122] J. Muzerolle, N. Calvet, and L. Hartmann, *ApJ* **550**, 944 (2001), *Emission-Line Diagnostics of T Tauri Magnetospheric Accretion. II. Improved Model Tests and Insights into Accretion Physics.*
- [123] J. A. Valenti, G. Basri, and C. M. Johns, *AJ* **106**, 2024 (1993), *T Tauri stars in blue.*
- [124] N. Calvet and E. Gullbring, *ApJ* **509**, 802 (1998), *The Structure and Emission of the Accretion Shock in T Tauri Stars.*
- [125] C. F. Manara and L. Testi, *Ap&SS* **354**, 35 (2014), *The imprint of accretion on the UV spectrum of young stellar objects: an X-Shooter view.*
- [126] G. Costigan, A. Scholz, et al., *MNRAS* **427**, 1344 (2012), *LAMP: the long-term accretion monitoring programme of T Tauri stars in Chamaeleon I.*
- [127] C. F. Manara, G. Beccari, et al., *A&A* **558**, A114 (2013), *Accurate determination of accretion and photospheric parameters in young stellar objects: The case of two candidate old disks in the Orion Nebula Cluster.*
- [128] G. J. Herczeg and L. A. Hillenbrand, *ApJ* **786**, 97 (2014), *An Optical Spectroscopic Study of T Tauri Stars. I. Photospheric Properties.*
- [129] E. Rigliaco, A. Natta, et al., *A&A* **548**, A56 (2012), *X-shooter spectroscopy of young stellar objects. I. Mass accretion rates of low-mass T Tauri stars in σ Orionis.*
- [130] J. M. Alcalá, A. Natta, et al., *A&A* **561**, A2 (2014), *X-shooter spectroscopy of young stellar objects. IV. Accretion in low-mass stars and substellar objects in Lupus.*
- [131] P. Hartigan, S. Edwards, and L. Ghandour, *ApJ* **452**, 736 (1995), *Disk Accretion and Mass Loss from Young Stars.*
- [132] E. Rigliaco, I. Pascucci, et al., *ApJ* **772**, 60 (2013), *Understanding the Origin of the [O I] Low-velocity Component from T Tauri Stars.*
- [133] A. Natta, L. Testi, et al., *A&A* **569**, A5 (2014), *X-shooter spectroscopy of young stellar objects. V. Slow winds in T Tauri stars.*
- [134] G. De Marchi, N. Panagia, and M. Romaniello, *ApJ* **715**, 1 (2010), *Photometric Determination of the Mass Accretion Rates of Pre-main-sequence Stars. I. Method and Application to the SN 1987A Field.*
- [135] F. D’Antona and I. Mazzitelli, *ApJS* **90**, 467 (1994), *New pre-main-sequence tracks for M less than or equal to 2.5 solar mass as tests of opacities and convection model.*
- [136] A. G. Riess, A. V. Filippenko, et al., *AJ* **116**, 1009 (1998), *Observational Evidence from Supernovae for an Accelerating Universe and a Cosmological Constant.*
- [137] S. Perlmutter, G. Aldering, et al., *ApJ* **517**, 565 (1999), *Measurements of Ω and Λ from 42 High-Redshift Supernovae.*
- [138] S. E. Woosley and J. S. Bloom, *ARA&A* **44**, 507 (2006), *The Supernova Gamma-Ray Burst Connection.*
- [139] J. E. Rhoads, *ApJ* **487**, L1 (1997), *How to Tell a Jet from a Balloon: A Proposed Test for Beaming in Gamma-Ray Bursts.*
- [140] K. A. Kornei, A. E. Shapley, et al., *ApJ* **758**, 135 (2012), *The Properties and Prevalence of Galactic Outflows at $z \sim 1$ in the Extended Groth Strip.*
- [141] R. Bordoloi, S. J. Lilly, et al., *ApJ* **794**, 130 (2014), *The Dependence of Galactic Outflows on the Properties and Orientation of zCOSMOS Galaxies at $z \sim 1$.*
- [142] K. C. Sahu, S. Casertano, et al., *Nature* **443**, 534 (2006), *Transiting extrasolar planetary candidates in the Galactic bulge.*
- [143] J. D. Hartman, G. Á. Bakos, et al., *ApJ* **742**, 59 (2011), *HAT-P-32b and HAT-P-33b: Two Highly Inflated Hot Jupiters Transiting High-jitter Stars.*
- [144] S. Cassisi, H. Schlattl, M. Salaris, and A. Weiss, *ApJ* **582**, L43 (2003), *First Full Evolutionary Computation of the Helium Flash-induced Mixing in Population II Stars.*

- [145] M. Castellani, V. Castellani, and P. G. Prada Moroni, *A&A* **457**, 569 (2006), *Hot flashers and He dwarfs in galactic globulars*.
- [146] T. M. Brown, A. V. Sweigart, et al., *ApJ* **562**, 368 (2001), *Flash Mixing on the White Dwarf Cooling Curve: Understanding Hot Horizontal Branch Anomalies in NGC 2808*.
- [147] M. M. Miller Bertolami, L. G. Althaus, K. Unglaub, and A. Weiss, *A&A* **491**, 253 (2008), *Modeling He-rich subdwarfs through the hot-flasher scenario*.
- [148] F. D'Antona, V. Caloi, and P. Ventura, *MNRAS* **405**, 2295 (2010), *The evolutionary status of the blue hook stars in ω Centauri*.
- [149] Z. Han, *A&A* **484**, L31 (2008), *A possible solution for the lack of EHB binaries in globular clusters*.
- [150] P. f. L. Maxted, U. Heber, T. R. Marsh, and R. C. North, *MNRAS* **326**, 1391 (2001), *The binary fraction of extreme horizontal branch stars*.
- [151] C. Moni Bidin, M. Catelan, and M. Altmann, *A&A* **480**, L1 (2008), *Is a binary fraction-age relation responsible for the lack of EHB binaries in globular clusters?*
- [152] C. Moni Bidin, S. Moehler, et al., *A&A* **498**, 737 (2009), *A lack of close binaries among hot horizontal branch stars in globular clusters. M 80 and NGC 5986*.
- [153] S. Moehler, S. Dreizler, et al., *A&A* **526**, A136 (2011), *The hot horizontal-branch stars in ω Centauri*.
- [154] M. Latour, S. K. Randall, et al., *ApJ* **795**, 106 (2014), *A Helium-Carbon Correlation on the Extreme Horizontal Branch in ω Centauri*.
- [155] T. M. Brown, A. V. Sweigart, et al., *ApJ* **562**, 368 (2001), *Flash Mixing on the White Dwarf Cooling Curve: Understanding Hot Horizontal Branch Anomalies in NGC 2808*.
- [156] G. Piotto, S. Villanova, et al., *ApJ* **621**, 777 (2005), *Metallicities on the Double Main Sequence of ω Centauri Imply Large Helium Enhancement*.
- [157] A. Bellini, G. Piotto, et al., *ApJ* **765**, 32 (2013), *The Intriguing Stellar Populations in the Globular Clusters NGC 6388 and NGC 6441*.
- [158] M. Meixner, K. D. Gordon, et al., *AJ* **132**, 2268 (2006), *Spitzer Survey of the Large Magellanic Cloud: Surveying the Agents of a Galaxy's Evolution (SAGE). I. Overview and Initial Results*.
- [159] K. D. Gordon, M. Meixner, et al., *AJ* **142**, 102 (2011), *Surveying the Agents of Galaxy Evolution in the Tidally Stripped, Low Metallicity Small Magellanic Cloud (SAGE-SMC). I. Overview*.
- [160] M. Meixner, P. Panuzzo, et al., *AJ* **146**, 62 (2013), *The HERSCHEL Inventory of The Agents of Galaxy Evolution in the Magellanic Clouds, a Herschel Open Time Key Program*.
- [161] B. A. Whitney, M. Sewilo, et al., *AJ* **136**, 18 (2008), *Spitzer Sage Survey of the Large Magellanic Cloud. III. Star Formation and ~1000 New Candidate Young Stellar Objects*.
- [162] R. A. Gruendl and Y.-H. Chu, *ApJS* **184**, 172 (2009), *High- and Intermediate-Mass Young Stellar Objects in the Large Magellanic Cloud*.
- [163] M. Sewilo, L. R. Carlson, et al., *ApJ* **778**, 15 (2013), *Surveying the Agents of Galaxy Evolution in the Tidally Stripped, Low Metallicity Small Magellanic Cloud (SAGE-SMC). III. Young Stellar Objects*.
- [164] L. R. Carlson, M. Sewilo, et al., *A&A* **542**, A66 (2012), *Identifying young stellar objects in nine Large Magellanic Cloud star-forming regions*.
- [165] K. A. Romita, L. R. Carlson, et al., *ApJ* **721**, 357 (2010), *Young Stellar Objects in the Large Magellanic Cloud Star-forming Region N206*.
- [166] M. Sewilo, R. Indebetouw, et al., *A&A* **518**, L73 (2010), *The youngest massive protostars in the Large Magellanic Cloud*.
- [167] D. Kamath, P. R. Wood, and H. Van Winckel, *MNRAS* **439**, 2211 (2014), *Optically visible post-AGB/RGB stars and young stellar objects in the Small Magellanic Cloud: candidate selection, spectral energy distributions and spectroscopic examination*.
- [168] R. Bacon, G. Adam, et al., *A&AS* **113**, 347 (1995), *3D spectrography at high spatial resolution. I. Concept and realization of the integral field spectrograph TIGER*.
- [169] R. Bacon, Y. Copin, et al., *MNRAS* **326**, 23 (2001), *The SAURON project - I. The panoramic integral-field spectrograph*.
- [170] S. C. Barden and R. A. Wade, in *Fiber Optics in Astronomy*, edited by S. C. Barden (1988), vol. 3 of *Astronomical Society of the Pacific Conference Series*, pp. 113–124.
- [171] J. R. Allington-Smith, R. Content, R. Haynes, and I. J. Lewis, in *Optical Telescopes of Today and Tomorrow*, edited by A. L. Ardeberg (1997), vol. 2871 of *Society of Photo-Optical Instrumentation Engineers (SPIE) Conference Series*, pp. 1284–1294.
- [172] M. M. Roth, A. Kelz, et al., *PASP* **117**, 620 (2005), *PMAS: The Potsdam Multi-Aperture Spectrophotometer. I. Design, Manufacture, and Performance*.

- [173] L. Pasquini, G. Avila, et al., *The Messenger* **110**, 1 (2002), *Installation and commissioning of FLAMES, the VLT Multifibre Facility*.
- [174] O. Le Fèvre, M. Saisse, et al., in *Instrument Design and Performance for Optical/Infrared Ground-based Telescopes*, edited by M. Iye and A. F. M. Moorwood (2003), vol. 4841 of *Society of Photo-Optical Instrumentation Engineers (SPIE) Conference Series*, pp. 1670–1681.
- [175] R. Content, in *Optical Telescopes of Today and Tomorrow*, edited by A. L. Ardeberg (1997), vol. 2871 of *Society of Photo-Optical Instrumentation Engineers (SPIE) Conference Series*, pp. 1295–1305.
- [176] F. Eisenhauer, R. Abuter, et al., in *Instrument Design and Performance for Optical/Infrared Ground-based Telescopes*, edited by M. Iye and A. F. M. Moorwood (2003), vol. 4841 of *Society of Photo-Optical Instrumentation Engineers (SPIE) Conference Series*, pp. 1548–1561.
- [177] R. Bacon, M. Accardo, et al., in *Society of Photo-Optical Instrumentation Engineers (SPIE) Conference Series* (2010), vol. 7735 of *Society of Photo-Optical Instrumentation Engineers (SPIE) Conference Series*, p. 8.
- [178] R. Davies and M. Kasper, *ARA&A* **50**, 305 (2012), *Adaptive Optics for Astronomy*.
- [179] D. J. Fixsen, M. A. Greenhouse, J. W. MacKenty, and J. C. Mather, *Spectroscopy using the hadamard transform* (2009), URL: <http://dx.doi.org/10.1117/12.810499>.
- [180] A. Cimatti, M. Robberto, et al., *Experimental Astronomy* **23**, 39 (2009), *SPACE: the spectroscopic all-sky cosmic explorer*.
- [181] F. Zamkotsian, P. Lanzoni, et al., in *Society of Photo-Optical Instrumentation Engineers (SPIE) Conference Series* (2010), vol. 7731 of *Society of Photo-Optical Instrumentation Engineers (SPIE) Conference Series*, p. 30.
- [182] R. D. Meyer, K. J. Kearney, et al., in *Ground-based Instrumentation for Astronomy*, edited by A. F. M. Moorwood and M. Iye (2004), vol. 5492 of *Society of Photo-Optical Instrumentation Engineers (SPIE) Conference Series*, pp. 200–219.
- [183] J. W. MacKenty, M. A. Greenhouse, et al., *Irmos: an infrared multi-object spectrometer using a mems micro-mirror array* (2003), URL: <http://dx.doi.org/10.1117/12.461484>.
- [184] E. C. Piquette, W. McLevige, J. Auyeung, and A. Wong, in *Society of Photo-Optical Instrumentation Engineers (SPIE) Conference Series* (2014), vol. 9154 of *Society of Photo-Optical Instrumentation Engineers (SPIE) Conference Series*, p. 2.
- [185] S. A. Smee, in *Society of Photo-Optical Instrumentation Engineers (SPIE) Conference Series* (2010), vol. 7739 of *Society of Photo-Optical Instrumentation Engineers (SPIE) Conference Series*, p. 3.
- [186] S. A. Smee, J. E. Gunn, et al., *AJ* **146**, 32 (2013), *The Multi-object, Fiber-fed Spectrographs for the Sloan Digital Sky Survey and the Baryon Oscillation Spectroscopic Survey*.
- [187] M. Meixner, S. Smee, et al., *PASP* **122**, 451 (2010), *Design Overview and Performance of the WIYN High Resolution Infrared Camera (WHIRC)*.
- [188] S. E. Persson, D. C. Murphy, et al., *PASP* **125**, 654 (2013), *FourStar: The Near-Infrared Imager for the 6.5m Baade Telescope at Las Campanas Observatory*.
- [189] M. Downing, J. Kolb, et al., in *Society of Photo-Optical Instrumentation Engineers (SPIE) Conference Series* (2014), vol. 9154 of *Society of Photo-Optical Instrumentation Engineers (SPIE) Conference Series*, p. 0.
- [190] D. F. Figer, J. W. MacKenty, et al., *ApJ* **643**, 1166 (2006), *Discovery of an Extraordinarily Massive Cluster of Red Supergiants*.
- [191] K. Fourspring, Z. Ninkov, et al., *Testing of digital micromirror devices for space-based applications* (2013), URL: <http://dx.doi.org/10.1117/12.2006121>.
- [192] J. Vernet, H. Dekker, et al., *A&A* **536**, A105 (2011), *X-shooter, the new wide band intermediate resolution spectrograph at the ESO Very Large Telescope*.